Exploration of Novel Fuels for Gas Turbine (ENV-406)

Modeling of T60 Test Rig with Diesel & Biodiesel Fuels

Mémoire

Mina Youssef

Maîtrise en génie mécanique

Maître ès sciences (M.Sc.)

Québec, Canada

Résumé

Dans cette thèse, un modèle numérique a été proposé pour simuler la combustion liquide des carburants conventionnels et non-conventionnels, en particulier le mélange de biodiesel B20. La matrice de test numérique constitue de quatre cas d'écoulement réactifs c.à.d. avec combustion et d'un cinquième avec injection liquide sans combustion (écoulement non-réactif). Les modèles sont calculés à l'aide du logiciel FLUENT™ v.14 en 3D et a l'état stationnaire. Les flammes de diffusion turbulentes sont modélisées en utilisant l'approche de flammelette laminaire stable, avec une fonction de densité de probabilité jointe (PDF). La Validation est effectuée en comparant les mesures expérimentales disponibles avec les résultats obtenus de la CFD.

L'aérodynamique de la chambre de combustion, ainsi que les températures de parois extérieures sont captures avec un degré de précision satisfaisant. La validation des principaux produits de combustion, tels que : CO_2, H_2O et O_2, montre des résultats satisfaisants pour tous les cas d'écoulement réactifs, mais certaines incohérences ont été relevées pour les émissions de CO.

On pense que le banc d'essai (la géométrie de la chambre de combustion et son état de fonctionnement) n'est pas suffisamment adéquat pour la combustion de combustibles liquides. D'autre part, et d'un point de vue numérique, l'approche de flammelette laminaire stable a été trouvé raisonnablement hors mesure de saisir les effets profonds du non-équilibre chimique qui sont souvent associés au processus de lente formation d'un polluant, comme le CO.

Abstract

In this thesis, a CFD model was proposed to simulate the liquid combustion of conventional and non-conventional biodiesel fuels, in particularly the B20 biodiesel blend. The numerical test matrix consists of four reacting flow cases, and one non-reacting liquid fuel injection case. The models are computed using FLUENT™ v.14 in a 3D steady-state fashion. The turbulent non-premixed diffusion flames are modeled using the steady laminar flamelet approach; with a joint presumed Probability density function (PDF) distribution. Validation is achieved by comparing available experimental measurements with the obtained CFD results.

Combustor aerodynamics and the outer wall temperatures are captured with a satisfactory degree of accuracy. Validation of the main combustion products, such as: CO_2, H_2O, and O_2, shows satisfactory results for all the reacting flow cases; however, some inconsistencies were found for the CO emissions.

It is believed that the test rig (combustor geometry and operating condition) is not sufficiently adequate for burning liquid fuels. On the other hand, from a numerical combustion point of view, the steady laminar flamelet approach was found not reasonably able to capture the deep non-equilibrium effects associated with the slow formation process of a pollutant, such as CO.

Table of Contents

LIST OF FIGURES

LIST OF TABLES

ABBREVIATIONS

Symbol	Description
AGR	Automated Grid Refinement
ASTM	American Society for Testing and Materials
BC	Boundary Condition
BML	Bray-Moss-Libby model
B-S	Burke Schumann
CFD	Computational Fluid Dynamics
CFM	Coherent flame model
CMC	Conditional Modeling Closure
CRIAQ	Consortium for Research and Innovation in Aerospace in Quebec
CRW	Continuous Random Walk
DNS	Direct Numerical Simulation
DPM	Discrete phase model
DRW	Discontinuous Random Walk
DSF	Deterministic Separate Flow
EDC	Eddy Dissipation Concept
EPA	Environmental Protection Agency
FAAE	Fatty Acid Alkyl Esters
FAME	Fatty Acid Methyl Esters
FFA	Free Fatty Acids

GRI	Gas Research Institute
ID	Inner Diameter
LEM	Linear Eddy model
LES	Large Eddy Simulation
LHF	Locally Homogenous Flow
LISA	Linearized Instability Sheet Atomization
MB	Methyl Butanoate
MD	Methyl Decanoate
N-S	Navier Stokes
NSERC	Natural Science and Engineering Research Council of Canada
OD	Outer Diameter
ODE	Ordinary Differential Equations
PDE	Partial Differential Equations
PDF	Probability Density Function
ppm	particle per million
RANS	Reynolds-Averaged Navier-Stokes
RDM	Reitz & Diwakar Model
RRC	Rolls-Royce Canada
RSM	Reynolds stress model
RT-KH	Rayleih Taylor-Kelvin Helmholtz
RWM	Random Walk Model
SD	San Diego mechanism

SDE	Langevin Stochastic Differential Equations
SMD	Sauter mean diameter
SMR	Sauter mean Radius
SSF	Stochastic Separated Flow
TAB	Taylor-Analogy breakup
UHC	Unburnt Hydrocarbon

NOMENCLATURE

Symbol	Description	Units
μ_t	Turbulent eddy viscosity	kg/(m.s)
k	Turbulent kinetic energy	m^2/s^2
ε	Eddy dissipation rate	m^2/s^3
δ_{ij}	Kronecker symbol	n/a
Γ	normally distributed random number	n/a
$\tau_{\text{int}eraction}$	Eddy-particle interaction time	s
$\tau_{cros\sin g}$	Particle crossing time	s
$\tau_{particle}$	Particle relaxation time	s
τ_e	Eddy lifetime	s
$\sqrt{\overline{u'^2}}$	local RMS value of the fluctuating velocity	m/s
η	Wave amplitude	m
k	Wave number	m^{-1}
λ	Wavelength	angstrom
ω	Complex wave growth rate	s^{-1}
T_{Taylor}	Taylor parameter	n/a
p_i	Internal pressure at any point on the droplet surface	Pa

p_A	External aerodynamic pressure	Pa
p_σ	Surface tension pressure	Pa
U_{inj}	Injection velocity	m/s
δ_0	Sheet film thickness	m
θ	Spray angle	degree
U_{rel}	Relative velocity	m/s
ν	Kinematic viscosity	m^2/s
σ	Surface tension	N/m
t_b	Breakup time	s
L_b	Breakup length	m
μ_l	Dynamic viscosity	Pa.s
a_{cc}	Droplet acceleration	m/s^2
$C_{RT}, C_\mu, c_F, c_k, c_d, c_b$	Model constant	n/a
y	Distortion parameter	n/a
B_1	Model constant	n/a
$\dot{m}_p$	Particle mass flow rate	kg/s
R	Universal gas constant	kJ/(kmol.K)
$\triangle h_v$	Latent heat of vaporization	J/kg

p_F	Partial vapor pressure	Pa
β	Dimensionless parameter	n/a
C_p	Heat capacity	J/(kg.K)
ρ	Density	kg/m^3
C_D	Drag coefficient	n/a
Y_k	Mass fraction of the k^{th} species	n/a
X_k	Mole fraction of the k^{th} species	n/a
n_k	Number of moles	mol
C_xH_y	General hydrocarbon	n/a
A/F	Air to fuel ratio	n/a
Mw	Molecular weight	kg/mol
ϕ	Equivalence ratio	n/a
Z	Mixture fraction	n/a
ν_F, ν_O, ν_P	stoichiometric coefficients of fuel, oxidizer and products	n/a
RR	Reaction rate	mol/(m^3.s)
Q	Heat release	J
$\Delta h^o_{f,k}$	Heat of formation of the k^{th} species	kJ/mol

h	Enthalpy	J
D	Diffusion coefficient	m^2/s
$\widetilde{Z''^2}$	Favre-averaged mixture fraction variances	n/a
α , γ	Model coefficient	n/a
χ	Scalar dissipation	s^{-1}
x_i	Spatial variable	m
a_s	Strain rate	s^{-1}
$erfc^{-1}$	Inverse of the complementary error function	n/a
S	Source term	n/a
Δt	Integral time step	s
ε_p	Particle emissivity	n/a
σ	Stefan-Boltzmann constant	W/(m^2.K^4)
G	Incident radiation coefficient	n/a
Q_c	Convective heat transfer	W/m^2
Q_r	Radiative heat transfer	W/m^2
Q	Volume flow rate	m^3/s
χ_q	Scalar dissipation at flame quenching	s^{-1}
St	Stokes number	n/a
FN	Flow number	m$^{7/2}$/kg$^{1/2}$

Sc_{kt}	turbulent Schmidt number	n/a
Le	Lewis number	n/a
Sc	Schmidt	n/a
$\Pr$	Prandtl number	n/a
Nu	Nusselt number	n/a
Oh	Ohnesorge number	n/a
Re	Reynolds number	n/a
We	Weber number	n/a
Sh	Sherwood number	n/a
B_M	Spalding number	n/a
t_m	Momentum response time of a particle	s
t_c	Time between particles collisions	s
t_r	Particle response time	s
t_f	Characteristic time of the fluid motion	s
$\Delta P_{3-4} / P_3$	Combustor pressure drop	Percentage %

Acknowledgements

Many people have contributed to the achievement of this work. I would like to express my gratitude to all who helped me to complete my project.

I am indebted to my supervisor Professor Alain deChamplain for his guidance and continuous support.

I would like to thank our research associate Mr. Bernard Paquet, who always welcomed my questions and taught me several aspects related to the Gas Turbines.

I am grateful to the combustion research and technology team at Rolls–Royce Canada for allowing me to use their computational facilities and for providing me all the needed support and resources.

I am greatly thankful to all my colleagues at Université Laval for the pleasant and excellent atmosphere.

I owe a favour to McGill's University Professor Jeffrey Bergthorson and his team, for their contribution and assistance.

Many thanks to Professor Marcia L.Huber from NIST laboratory, for voluntarily developing biodiesel fuel liquid properties to the author of this thesis.

Financial support from Rolls-Royce Canada, NSERC, MITACS and CRIAQ was greatly appreciated with many thanks.

Finally, I extend my deepest gratitude to my family and friends for their encouragement and belief on me.

CHAPTER 1- INTRODUCTION

1.1. Biofuels at a glance

Fossil fuels have been the primary source of fuel ever since the pre-historical time, when caveman discovered how to burn coal to serve as heat and light sources. With the excessive usage of fossil fuel in form of coal, petroleum and natural gas as a source of energy, the amount of fossil fuel around the world is declining at a rapid rate. In fact, the global fuel crisis between the 1970s and 1980s triggered awareness amongst many countries regarding their vulnerability to oil embargoes, shortages and thus petroleum depletion. In addition, the continuous rise of the world crude oil prices has become a crucial factor and a primary concern for the energy market. The world is presently confronted with a triple crisis: fossil fuel depletion, their cost inflations, and their contribution to the environmental degradation. With increased interest to reduce emissions, and global warming from the greenhouse effect, considerable attention is now devoted to the development of alternative resources, in particularly biofuels.

The concept of biofuels is surprisingly old, during the Paris exposition in 1900, a small diesel engine was operated on peanut oil by the French Otto company. The term biofuel is referred to alternative fuels, which are produced from biomass. Such fuels include but are not limited to: Biodiesel, Bioethanol, Biomethanol, Pyrolysis oil, Biogas, Synthetic gas, and Synthetic fuels (Gupta, Rehman, & Sarviya, 2010) .One of the most important events that occurred in the 1970s, was the passage of the Clean Air Act by the Environmental Protection Agency (EPA), which can be considered as a decisive step towards controlling air pollution. It has allowed the EPA to closely regulate emission standards for pollutants like sulfur dioxide (SO_2), carbon monoxide (CO), ozone, and nitrogen oxides (NOx); and thus, to set the stage for developing cleaner-burning fuels as well as standards for fuel additives. The Clean Air Act amendments in 1990 and the Energy Policy Act in 1992; mandated the use of alternative or so called "clean" fuels in regulated truck and bus fleets. These amendments briefly introduced provisions for fuels with increased oxygen contents, to lower CO emissions. But the real turning point was through the amendments to the Energy Policy Act in 1998, which have provided credits for the biodiesel use; and hence, contributed to a significant increase in the use of such alternative fuels (Knothe, 2005). In the present study, we will address only the biodiesel fuels and their blends.

Biodiesel is an alternative fuel, composed of Fatty Acid Alkyl Esters (FAAE). Biodiesel is made through a chemical process called transesterification, wherein the glycerin is separated from the fat or the vegetable oil.

The process renders two commercial products: (1) Fatty Acid Methyl Esters (FAME), which is the chemical name for biodiesel if methanol is used as an alcohol during the process, and (2) Glycerin which is a valuable co-product usually sold for soaps, pharmaceuticals, and cosmetics applications. Among the biodiesel family, FAMEs are widely produced due to the low price of methanol (Board, 2013).Biodiesel is defined as mono-alkyl esters of long chain fatty acids derived from vegetable oils or animal fats, which conform to the ASTM D6751 specifications for use in diesel engines. Biodiesel refers to the pure fuel before being blended with conventional diesel fuel. Biodiesel blends are denoted as, "BXX" with "XX" representing the percentage of biodiesel contained in the blend (e.g. B20 is 20% biodiesel and 80% petroleum diesel on a volumetric basis) (ASTM 6751-11b, 2011). Biodiesel is one of the most diverse fuels on the planet, since it can be produced from agricultural co-products such as: soybean, cottonseed, rapeseed/canola, sunflower, shallower and coconut oils, as well as, animal fats usually tallows and recycled grease oils (e.g. frying oil) (Knothe, 2005). The next generation of biofuels (e.g. forest residues, micro algae, etc.) produced from cellulose, hemicellulose or lignin, will not be discussed in this study. It will be judicious to quickly review the transesterification process and cite the most influential parameters that contribute to the biodiesel quality.

Transesterification is a chemical reaction of triglycerides with alcohol in the presence of a catalyst to form esters and glycerol by modifying the molecular structure of the oil used. The triglycerides include the conversion step from di-glycerides to mono-glyceride and finally glycerol. The presence of a catalyst is to improve the reaction rate and yield. The level of Free Fatty Acids (FFAs) present in the lipid source will determine the type of catalyst to be used in the reaction. When catalysts such as Na-OH or K-OH are mixed with alcohol, an alkoxide group is formed. For alkali-catalyzed transesterification, alcohol must be substantially anhydrous, because water partially changes the reaction to saponification, which produces soap. For this type of process, low level FFAs is preferred. Lipid oil with high FFAs (e.g. trap grease, yellow grease, and tallow) cannot be etherified to biodiesel with a base catalyst; therefore, acid catalysts should be used (Knothe, 2005). Consequently, an esterification process in two stages is opted. First, an acid is used for the catalyzed esterification to convert FFAs into fatty acid methyl esters, and then a base transesterification will give the conversion a higher yield. Beside the FFA level and the catalyst type, other variables that are found influential to the transesterification process are: reaction temperature, alcohol to oil ratio, stirring RPM, and reactants (Sarviya & Rehman, 2010).

Biodiesel is renewable, biodegradable, and contains oxygen molecules within its structure. These are the reasons why it can be considered more environmental friendly, and cleaner than conventional diesel in emissions of unburnt hydrocarbons (UHCs), CO, and particulate matter (PM) (J.Haas, M.Scott, & L.Alleman, 2001), (Som, Longman, Ramirez, & Aggarwal, 2010), and (Hashimoto, Ozawa, Mori, & Yuri, 2008).

Additionally, biodiesel gives better lubrication to the engine components compared to conventional diesel (Steidley & Knothe, 2005). Also, (Waynick, 1997) showed in his study that castor oil esters offer better lubricity than lots of other vegetable oils derived biodiesels. This advantageous property can be exploited by mixing biodiesel to low sulfur content in petroleum-derived conventional diesel. This restores the lubricity of the conventional fuels, avoiding the addition of chemical additives. The advantage herewith, is that, biodiesel inherently possesses thermo-physical properties close to the conventional diesel. Contrary to these enhancing additives, as usually they do not share common properties with the fuel. However, along with all these advantages, comes the fact that pure biodiesel fuels and high concentration biodiesel blends, i.e. B50, B60, B80, have exhibited some atomization, evaporation, and flame stability problems. This can be mainly related to their high viscosity, their elevated surface tension, and their low volatility compared to conventional diesel fuels.

1.2. Objectives of the study

The current work is part of a large project, which started in 2010. This project involves eight Canadian universities, in partnership with Rolls-Royce Canada (RRC), Natural Science and Engineering Research Council of Canada (NSERC), MITACS Canada, and Consortium for Research and Innovation in Aerospace in Quebec (CRIAQ). The main goal of the project is to study the characteristics of novel fuels for gas turbines applications. The mandate for Université Laval is to characterize the combustion behaviour of selected biofuels at different engine operating conditions, for future applications in gas turbine engines. This mandate is realised following two main tasks. The first task is to measure experimentally smoke, and emissions (e.g. CO, CO_2, VOCs, NOx, H_2O, and O_2), using biofuels in a simple combustor equipped with a dual fuel air-blast injector, and to evaluate the exit and outer wall temperature profiles. These data will highlight potential combustion problems from the use of such alternative fuels, allowing the research team to better understand their behaviour.

The second task represents the core of this thesis, and its main objectives can be summarized as following:

- Create a robust model for the combustion of liquid fuels using diesel and biodiesel blends;
- Evaluate the computational code FLUENT™ v.14 in modeling multiphase flow combustion;
- Investigate the flow structure generated by a hybrid swirl injector with high turbulence intensity, and
- Validate emissions and temperature profiles with the available experimental measurements.

This study will lead to gain some insight into the development of biofuels for gas turbine applications, and will assist RRC in bringing greener, lighter and more cost effective engines to the market. Studying these alternative fuels will ultimately serve to improve emissions, combustor and turbine durability, and eventually less dependence on conventional hydrocarbon based fuels.

1.3. Numerical calculations outline

The numerical calculations are performed on five different liquid injection test cases, in correspondence to the operating conditions of the experimental test rig. The test matrix consists of four reacting flow cases, and one non-reacting liquid fuel injection case. Additionally, the reacting flow cases can be further divided into two sub-groups: the stoichiometric combustion class and the lean combustion class. The non-reacting flow injection was performed using only conventional diesel. This case allows development of the methodology the atomization technique, which will serve for the simulation of the reacting flow cases. The reacting flow cases address the conventional diesel, and the B20 blend, both at stoichiometry condition (ϕ = 1), and lean condition (ϕ = 0.8), respectively.

The geometry consists of a cylindrical combustor that represents only the primary zone of a Trent 60 engine, equipped with a dual fuel air-blast injector. The model is calculated using FLUENT™ v.14 code, in a 3D steady-state regime. The turbulent diffusion flame is modeled using the Laminar Flamelet approach. The RANS model is chosen for turbulence closure; the liquid fuel injection is achieved using the Lagrangian discrete phase technique, and heat transfer is considered through the P1 radiation approach.

1.4. Ambiguities and Known challenges

The combustion process in gas turbine combustors is very complex, and involves many variables acting simultaneously to process the fuel-air mixture in a limited space with very stringent emission standards. Reasonably accurate CFD tools for liquid-phase combustion should be able to account for parameters such as: atomization, evaporation and diffusion of the fuel droplets, turbulence aerodynamics, mixing, and turbulence–chemistry interaction. This process is further complicated with biodiesel, due to their long hydrocarbon chains (C_{12}-C_{19}), their complex thermo-physical properties, and their large chemical kinetic mechanisms (can reach up to 3 000 species and 10 000 chemical reactions). This contributes to an inefficient computational simulation, resulting in a serious drawback for the studies of such fuels.

The methodology for the numerical calculations was established between the project partners in 2010, rendering outline of the CFD part. It was agreed to complete the simulation work using the FLUENT™, for its large usage by several industrial/engineering firms, also to incorporate the laminar flamelet approach for the non-premixed combustion, to integrate the atomization technique with the primary and secondary breakup regimes for the discrete phase sub-model, and finally to include the multicomponent fuel droplet type for the injection sub-model of biodiesel blends. To fulfil these tasks, particular attention was paid to the following:

- The development of the liquid fuel spray model, and the choice of the secondary breakup sub-model;
- Acquiring a comprehensive chemical kinetic mechanism for the flamelet and tabulated chemistry generation;
- Accurately defining liquid fuels thermo-physical properties, this is a crucial step to correctly predict the atomization and the evaporation process, and
- Stabilizing the numerical solution, and obtain a good convergence behaviour with minimum residuals for the solved equations.

1.5. Thesis layout

This thesis is divided into six chapters. After this brief introduction in chapter (1), chapter (2) offers a literature review, related to the different technical aspects of combustion and numerical modeling. It covers turbulence sub-models, discrete phase flow approach, atomization techniques, evaporation theories, and combustion models with a focus on the theory of diffusion flames. Next, chapter (3) highlights the main fuel properties needed for the simulations, it also shows how the thermo-physical properties where acquired and integrated into the solver. Chapter (4) details the description of the numerical model, the discussion starts with the geometry and its mesh; followed by, an explanation of the different sub-models used and the implemented boundary conditions, as well as, justifications for the choices made. In chapter (5), the obtained results are reported from both the numerical models and the experimental test. It begins with the non-reacting cold flow case, moving to the flow velocity profiles, temperature profiles, and then emissions with their major trends. Validation is achieved by comparing available experimental measurements with the obtained CFD results. Also, a discussion on the suitability of FLUENT™ sub-models and a set of recommendations are presented. Finally, chapter (6) concludes the work by summarizing the main features of the model and shows the lessons learned, with an emphasis on the overall model performance in terms of advantages and disadvantages.

CHAPTER 2- LITERATURE REVIEW

2.1. Gas turbine combustion chambers

Broadly speaking, gas turbine engines are essentially heat engines using air as the working fluid to provide thrust for aero-engines or shaft power for industrial engines. To achieve this, the air passing through the engine has to be accelerated; which means that the velocity or the kinetic energy of the air is increased. In order for this increment to take place, heat addition is required, followed by a conversion to kinetic energy in the form of a high velocity jet efflux, or to shaft power by fully expanding the hot gases in a multistage turbine. This heat addition is achieved through the combustion chamber. The working cycle of a gas turbine is similar to a piston engine. However, in gas turbine engines, combustion occurs at constant pressure, whereas for many piston engines it occurs at constant volume. The second difference is, in piston engines the processes are intermittent, whilst they occur continuously in gas turbines. Due to the continuous action of combustion in gas turbine engines and the fact that the combustion chamber is not an enclosed space, the pressure of the air does not rise, but its specific volume does increase to deliver a flow with high enthalpy to the turbine section. This process is known as heating at constant pressure (Rolls-Royce ©, 1996).

Combustion chambers in gas turbine engines represent a wide topic, they exist under different types, and use different varieties of formation control technologies. In this section, we will recall some of the common fundamental aspects for all combustors. Regardless of the type, size, and geometry of the combustor; they all share the same basic requirements (Lefebvre, 1998):

- High combustion efficiency, i.e. the fuel should be completely burned so that all its chemical energy is liberated as heat;
- Wide stability limits, i.e. the flame should stay ignite over a wide range of operating conditions;
- Low pressure loss;
- Low emissions and pollutants species;
- Durability, and
- Multi-fuel capacity or the so called fuel flexibility.

To accomplish such requirements, it is necessary to divide the combustion process inside the combustor into either two or three zones. These zones are dictated by the geometry of the combustion chamber, as well as the aerodynamic of the air inside the chamber. Their presence allows the control of the combustion process throughout the combustor. ***Figure 1*** shows a typical arrangement inside a combustion chamber. In the context of the present thesis we will focus only on the primary zone, since it represents solely our area of study.

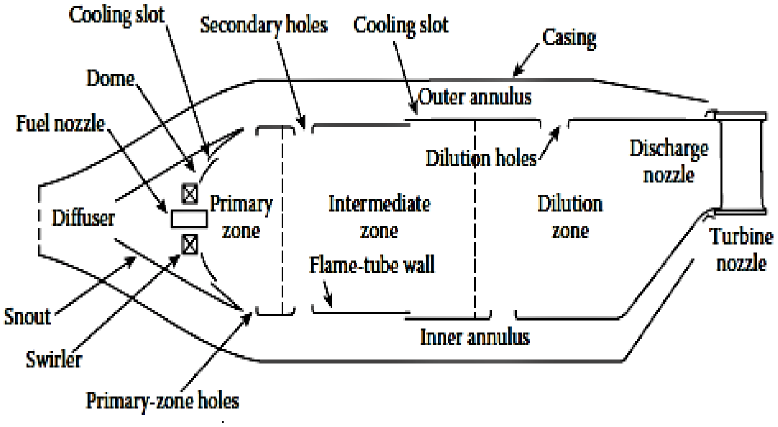

Figure 1 Conventional combustion chamber arrangement for gas turbines **(Lefebvre & Ballal, 2010)**

The main function of the primary zone is to anchor the flame, and to provide sufficient time, temperature and turbulence to ultimately achieve a complete combustion. The importance of the primary zone airflow pattern for the attainment of these goals cannot be overstated. Many different types of flow patterns can be employed, depending on the technique used inside the gas turbines. Nevertheless, the common feature to all is the generation of a toroidal flow, which entrains and recirculates a portion of the hot combustion gases. In return, these hot gases will ensure continuous ignition of the incoming air-fuel mixture (Lefebvre, 1998). Some combustors use air swirlers with the fuel injector to create the toroidal flow pattern, while others rely on holes formed or drilled in the liner wall as shown in ***Figure 1***, the rest use both techniques. ***Figure 2*** illustrates the results of a strong and stable air flow pattern, made by Joseph Lucas combustion group during their designs of the Whittle W2B/Welland engines for Rolls-Royce. This aerodynamic action and turbulent pattern greatly assist in breaking up the fuel, especially when it is in the liquid phase. Moreover, this action yields stronger mixing rate between the fuel and the incoming air, whether it is in the gaseous or liquid phase.

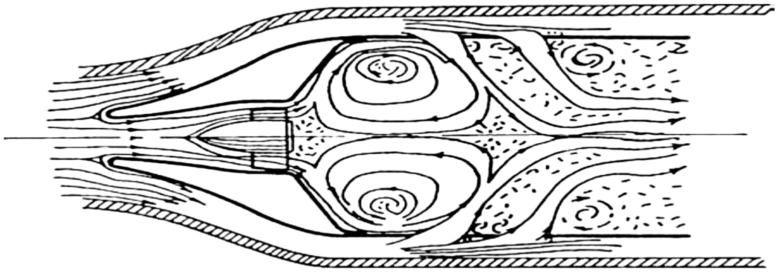

Figure 2 Lucas primary zone airflow pattern **(Lefebvre & Ballal, 2010)**

2.2. Turbulence modeling

The essential dilemma of solving turbulent flow problems is that, if all the information necessary for describing the flow is tracked, there will not be a computer in the world large enough to tackle the job. On the other hand, if the problem is simplified to be tractable, large errors may result. Therefore, turbulent flows continue to provide a challenge to engineers, mathematicians, and physicists. In practical industrial systems, turbulent flows are more frequently encountered than laminar flows. In such systems (e.g. rockets, aircraft engines, stationary gas turbines, furnaces etc.) combustion is strongly coupled to the aerodynamic, that is, if the flow is laminar, the flame will be laminar; similarly, if the flow is turbulent, the flame will be turbulent. Poinsot (Poinsot & Veynante, 2005) defined the turbulent combustion as being the result of the two-way interaction between chemistry and turbulence. He further clarified that when a flame interacts with a turbulent flow, turbulence is modified by combustion, due to the strong flow accelerations through the flame front. This acceleration is induced by both the heat release, and the large changes in kinetic viscosity associated with high temperature changes. This acceleration mechanism may generate turbulence, and is called «flame-generated turbulence». Or it can simply damp it, creating what we call « relaminarization due to combustion». Mutually, turbulence can alter the flame structure, which may enhance the chemical reaction, and yield the mixing between the reactants. But in the extreme cases, turbulence can completely inhibit it, leading to flame quenching /extinction.

In turbulent flows, a fluid particle can have velocity and momentum in any direction, which is described as nearly random or chaotic motion, since it does not have unique values in every repetition. Yet, this near randomness behaviour characterizes turbulent flows by their ability to transport and mix the fluid more effectively than laminar flows. In a turbulent flow field, at any point of time and space, flow field variables (e.g. the velocity field), will show fluctuations, i.e. deviations from a local mean value. Thus, one particularly useful method to characterize a turbulent flow field is to decompose its major field variables into fluctuating and averaged components. In order to obtain spatial profiles for the averaged physical properties, an averaging procedure is performed for the Navier-Stokes (N-S) equations governing the turbulent flow. Once the N-S equations are being averaged, new equations are formed, having a statistical nature (e.g. mean velocity components). However, this statistical averaging procedure generates new unknown terms. For example after the averaging of the momentum equation, the famous unknown term, namely the «Reynolds stress» appears. Thus, statistical equations cannot be considered as closed, and they require a closure model to handle these new unknowns.

Two different averaging procedures are commonly used: (1) Conventional time averaging, also known as Reynolds averaging, and (2) Mass-weighted time averaging, known as Favre averaging. Both techniques have been successfully used together in the combustion field. In order to give an overview on the process, let us consider the conventional time averaging procedure. The mean of a quantity $\Theta\left(x,t\right)$ in a turbulent flow field can be defined as:

$$\overline{\Theta}\left(x\right)=\lim_{\Delta t\to\infty}\frac{1}{\Delta t}\int_{t}^{t+\Delta t}\Theta\left(x,t\right)dt \tag{2.1}$$

Physical quantities such as velocity, temperature etc., can be decomposed into mean and fluctuation:

$$\Theta_i\left(x_j,t\right)=\overline{\Theta_i}\left(x_j\right)+\Theta_i^{'}\left(x_j,t\right) \tag{2.2}$$

Let us take any field variable, like the mean velocity denoted as ($\overline{u}$), drop the over-bar, substitute the expression of equation (2.2) into the instantaneous N-S equations for continuity and momentum, take the time average, and eventually write it in the Cartesian form:

$$\frac{\partial\rho}{\partial t}+\frac{\partial}{\partial x_i}\left(\rho u_i\right)=0 \tag{2.3}$$

$$\frac{\partial}{\partial t}\left(\rho u_i\right)+\frac{\partial}{\partial x_i}\left(\rho u_i u_j\right)=-\underbrace{\frac{\partial p}{\partial x_i}}_{\text{Mean pressure stress tensor}}+\underbrace{\frac{\partial}{\partial x_i}\left[\mu\left(\frac{\partial u_i}{\partial x_j}+\frac{\partial u_j}{\partial x_i}-\frac{2}{3}\delta_{ij}\frac{\partial u_k}{\partial x_k}\right)\right]}_{\text{Mean viscous stress tensor}}+\underbrace{\frac{\partial}{\partial x_i}\left(-\rho\overline{u_i^{'}u_j^{'}}\right)}_{\text{Reynolds stress tensor}} \tag{2.4}$$

Equations (2.3) & (2.4) are called Reynolds-averaged Navier-Stokes equations (RANS), and they are valid for incompressible, Newtonian fluid flows. As stated above, the problem relies in the new unknown term (Reynolds stress tensor), and it represents the first closure problem of the turbulent modeling. Presently, there are many techniques used to close the system of the governing equations. One of the simplest and widely used is centred on an analogy between the Reynolds stress tensor and the viscous stress tensor. This technique is based on the theory from Boussinesq (Boussinesq, 1877), under which an analogy between the

Reynolds stress tensor and the viscous stress tensor is drawn; introducing a new fiction term to represent turbulence called «Turbulent eddy viscosity (μ_t) ». The introduction of this term does not achieve the closure; but rather transform the problem into how to determine the turbulent eddy viscosity μ_t. Unlike the thermo-physical viscosity of the fluid itself, the eddy viscosity depends on the flow. For example, a swirling confined flow with recirculation is not likely to have the same value of μ_t as a free jet flow. Moreover, μ_t depends on the local flow thermo-physical properties; hence, it will take different values at different locations within the flow. The eddy viscosity analogy assumes that the turbulence is isotropic, which works well at smaller turbulent scales, like in shear flows dominated with only one of the turbulent shear stress tensors. Currently, there are several methods to model the eddy viscosity like: Prandtl mixing length model or so the called Zero-equation model (L.Prandtl, 1925), the Spalart-Allmaras model, known as the one equation model (Spalart & Allmaras, 1992), and the two-equation model, which represents the core of the chosen turbulence model in our study.

The two-equation turbulence model comprises the Reynolds averaged equations of motion for the mean flow variables, with the coupled partial differential equations of two turbulence variables. The overwhelming choice of the first variable is the «Turbulence kinetic energy » denoted by (*k*), the second variable is generally less agreed upon. One of the commonly used choices for the second variable is the «Eddy dissipation rate» denoted by (*ε*). Together, they generate the so called (*k*-*ε*) model (R.Turns, 2000). These two equations allow the determination of both, a turbulent length scale, and the energy of turbulence. Accordingly, two separate transport equations, one for the eddy dissipation rate and the other for turbulence kinetic energy, are to be solved (ANSYS, 2011). The equations for these two variables once solved will lead to the determination of the μ_t through the following relation:

$$\mu_t = \rho C_\mu \frac{K^2}{\varepsilon} \tag{2.5}$$

where C_μ can have the form of a constant value or of a function of the flow field variables, depending on the type of two-equation model used. Consequently, the Reynolds stress tensor can now be expressed as:

$$\left(-\rho\overline{u_i^{'}u_j^{'}}\right) = \mu_t\left[\left(\frac{\partial u_i}{\partial x_j}+\frac{\partial u_j}{\partial x_i}\right)-\frac{2}{3}\delta_{ij}\frac{\partial u_k}{\partial x_k}\right]-\frac{2}{3}\rho\delta_{ij}\tilde{k} \tag{2.6}$$

Equation (2.6) shows that the Reynolds stress tensor is related to the mean velocity gradients and to the turbulent eddy viscosity. The *k-ε* family contains three distinct formulations: (1) the Standard *k-ε* model*,* (2) the *RNG k-ε* model, and (3) the Realizable *k-ε* model. The major differences between the three models are in the method of calculating the turbulent viscosity, the turbulent Prandt number that governs the turbulent diffusion of the *k* and *ε* equations, and the generation/destruction terms of the *ε* equations (ANSYS, 2011). Jones and Lauder (Launder & Jones, 1972) were the first to develop the classical *k-ε* model, which is a semi-empirical model. Sharma and Launder (Launder & Sharma, 1974) retuned the model closure coefficients, nowadays most researchers use the form of the model presented in their 1974 paper. The standard *k-ε* model has attracted criticism in regard to the lack of strategy, and the rigorousness of modeling the source/sink terms in the *k* and *ε* (Stan, 2000). In order to improve the standard *k-ε* model, Yakhot and Orszag (Yakhot, 1986) have developed the RNG *k-ε* model, and later Shih and Zhu (Shih, Liou, Shabbir, & Zhu, 1995) developed the realizable *k-ε* model. Wilcox in this book (Wilcox, 1998), has fairly detailed all the deficiencies of the *k-ε* models, which can be roughly summarized in the failure of the *k-ε* model to predict moderate to strong adverse pressure gradients in reverse flows. Moreover, he commented the weakness of the viscous damping correlations used to accurately predict the low Reynolds number effects, typically found close to the wall. To this end, Wilcox has proposed the standard *K-ω* model, which can be considered more accurate and much more numerically stable, especially in near the wall regions.

The realizable *k-ε* model is chosen to model the turbulence in this study. Initial studies have shown that this model provides the best performance among all the *k-ε* family (ANSYS, 2011). Zuckerman and Lior have validated this point; they even extended their study to include almost all the available CFD techniques for turbulence (Zuckerman & Lior, 2006). Based on their comparison, they have concluded that the RANS modeling approach shows non-negligible amount of errors compared to experimental data sets, even with high–grid resolution. However, they stated that the RANS family represents the best compromise between solution speed and accuracy, which is typically required in the industrial field. Generally speaking, *k-ε* models can give sufficiently accurate results for engineering purposes, if a qualitative trend is needed rather than an accurately quantitative one (Rochaya, 2007).

The literature of turbulence modeling is very rich and goes far beyond the above stated two-equation approach. Alternatively, it includes the Reynolds stress model (RSM), the large eddy simulation model (LES), and lastly the direct numerical simulation (DNS) approach.

The DNS technique solves completely the flow dynamics up to the smallest scales requiring no modeling, i.e. all turbulence scales are explicitly determined, but is computationally very expensive. Furthermore, when including two-phase flows, it can quickly become very prohibitive. For this reason, its usage is limited to canonical test cases, where it greatly contributes to the fundamental understanding of many different types of flows.

The LES approach solves the largest scales of the flow up to a certain length-scale, i.e. threshold. As for scales below this length-scale, they will be modeled by means of sub-grid models. Hence, this technique can be considered in the middle between the DNS and the RANS. The balance equations are obtained by spatially filtering the instantaneous equations. The size of this filter determines the size of the scales to be solved from those to be modeled. This approach provides information about transient phenomena, and it is very suitable to perform unsteady flow simulations. The computational cost of LES is higher than that of RANS, but still moderate compared to DNS. Indeed, this is valid depending on the size of the scales that are solved, but affordable in most cases. It is in fact, a very good compromise between accuracy and computational time resources, when a decent degree of exactitude is required.

Lastly, the Reynolds averaging procedure detailed above is practical and widely used for incompressible flows. However, in situations where strong density variations are present like in compressible or reacting flows due to the high heat release, the Reynolds averaging procedure leads to many unclosed correlations, which include density fluctuations. Therefore, in combustion, the mass-weighted averages (Favre averages) are usually preferred (Veynante & Vervisch, 2001). This procedure will be reviewed in details in the subsequent section.

It should be also noted that this text is not intended to catalog all turbulence models. However, the author found it judicious to define the generic sense of the turbulence CFD modeling strategies.

2.3. Multiphase flows

Multiphase flows can be defined as any fluid flow system consisting of two or more distinct phases, flowing simultaneously in as a mixture, and having some level of phase separation at a scale much larger than the molecular level. Two-phase flow is the most reputed amongst the multiphase flow family. They can be classified according to the state of the different phases, that is, gas–solid flow, liquid-solid flow, or gas-liquid flow. Gas-liquid flow contains several configurations; one example is the motion of gas bubbles in a liquid flow, while another, is the motion of liquid droplets in a gas stream. These two examples are often recognised as dispersed flow. Liquid fuel sprays represent a classical application of the second example; it involves the liquid as the dispersed phase in the form of droplets, and the surrounding gas as the continuous phase. Liquid fuel sprays can be found in most combustion applications: internal combustion engines, aircraft engines, liquid propellant rockets, etc., and thus, it's of a great interest to our study.

In the context of gas-liquid multiphase flow, fluid particle flow can be further classified as being either dilute or dense. A dilute dispersed phase is the one in which particle motion is controlled by the surface, and body forces exerted by the carrier fluid on the particle, i.e. drag and lift forces. Alternatively, in the dense configuration, the particle motion is controlled primarily by particle-particle collisions and/or interactions (Crowe, Troutt, & Chung, 1996). Indeed, no flow is completely diluted or dense, but one regime or the other may be considered more descriptive to the physical phenomena. There is no definitive scaling parameter to define the boundary between dilute and dense flows. However, some primitive scaling parameters can be used to identify the regime, among them two can be identified: (1) the Stoke number (*St*), and (2) the ratio of the momentum response time (t_m) of a particle to the time between collisions (t_c). The Stoke number represents the ratio of the particle response time (t_r) to a characteristic time of the fluid motion (t_f) defined as:

$$St = \frac{t_r}{t_f} = \frac{\rho_p d^2 U}{18 \mu L} \tag{2.7}$$

where (U) is the characteristic fluid velocity, and (L) is a characteristic length scale. This implies that for a small *St* number (*St*<1) the response time of the particle is less than the time associated to the fluid motion. Thus, the particle will have an ample time to respond to changes in flow velocity; leading the particle to exhibit a state of near velocity equilibrium with the carrier fluid. Similar to the methodology of the Stoke number, the second scaling parameter suggests that, if the momentum response time is smaller than the collision time, i.e.

$t_f < t_c$, the regime can be considered dilute, because the particles will have sufficient time to respond to the local fluid forces before the next collision (Crowe, Schwarzkopf, Sommerfeld, & Tsuji, 2012).

Another essential notion in the numerical analysis of multiphase flows is the 'Coupling between phases'. When the gas-particle flow is dilute, the particle volume loading is assumed to be small enough, so that any effects due to the presence of the dispersed phase on the continuous phase can be neglected. This is called the 'One Way Coupling Technique', because the local velocity of the continuous phase has a direct impact on the particle while the reverse is not true. For slightly denser systems, the effects of the particles on the carrier fluid cannot be neglected, and the so called 'Two Way Coupling Technique' is required. For highly dense systems, the 'Four Way Coupling Technique' is necessary, in order to take into account the particle-particle collision effects, as well as, any turbulence modification in the continuous phase caused by the dispersed phase.

With the one way coupling, the velocity field is computed independently of the particle tracking by a standard single–phase simulation, thereafter, the trajectories of the individual particles are computed separately from one another. Oppositely, a two way coupled technique solves the full time dependent dispersed and continuous phase equations in an iterative manner. In a four way coupled system, there is a mutual (binary) interaction between the individual particles, along with a two way coupling between the dispersed phase and the carrier phase. This makes the phases dynamic equations strongly coupled, and leads to a more complex iterative process. On the other hand, this latter raises the computational time, and the difficulties to stabilise the solution (Jakobsen, 2008) .

Basically, there are two approaches in modeling two-phase flows: (1) Eulerian-Eulerian approach, and (2) Eulerian-Lagrangian approach. In both techniques, the continuous phase is treated with the Eulerian method, whereas, the dispersed phase can be treated either with the Eulerian, or the Lagrangian approach. The Eulerian-Eulerian technique simulates the particle phases as a continuous phase. Herewith, particle motions are predicted by solving a set of continuum equations, representing the carrier fluid and the dispersed phase. In contrast, the Eulerian-Lagrangian approach solves particle motions in a Lagrangian reference frame, such that, they are tracked individually through the flow field. It provides a detailed description of particle motions by integrating all the forces acting on the particle. Extensive comparisons between both approaches can be found in the literature, Subramaniam stated that the Eulerian-Eulerian formulation approaches are unable of representing the fluxes, and the resulting physical phenomena associated with the motion of two streams of particles with different velocities at the same physical location (Subramaniam, 2013). Tu et al. mentioned that the current Eulerian-Eulerian formulation is still far from being able to adequately quantify the incident and reflected particles during the process of particles-wall interaction (Tu, Yeoh, & Morsi, 2010). Both models have advantages and disadvantages; however, focus will be directed to the Eulerian-Lagrangian approach.

Commonly, the Lagrangian formulation is usually applied to describe a dilute flow, which has a small dispersed phase volume fraction (<10-12%), and where particle-particle interaction is not significant. This allows droplet trajectories to be tracked smoothly, without exacerbating the computational time. Equations for particle trajectories and any auxiliary equations, describing particles properties such as velocity, size, mass, and heat transfer from and to the particle, are solved by a set of Lagrangian ordinary differential equations (ODE). Simultaneously, the continuous phase is solved by a set of partial differential equations (PDE). The solver predicts particle trajectories, by integrating the force balance on the particle resulted from the solution of the carrier fluid field. As the trajectory of the particle is computed, the mass, the heat, and the momentum gained or lost by the particle stream, are incorporated in the subsequent continuous phase calculations. This two way coupling technique allows the interphase exchange of heat, mass and momentum, between the droplets and the carrier flow, as sketched in ***Figure 3***.

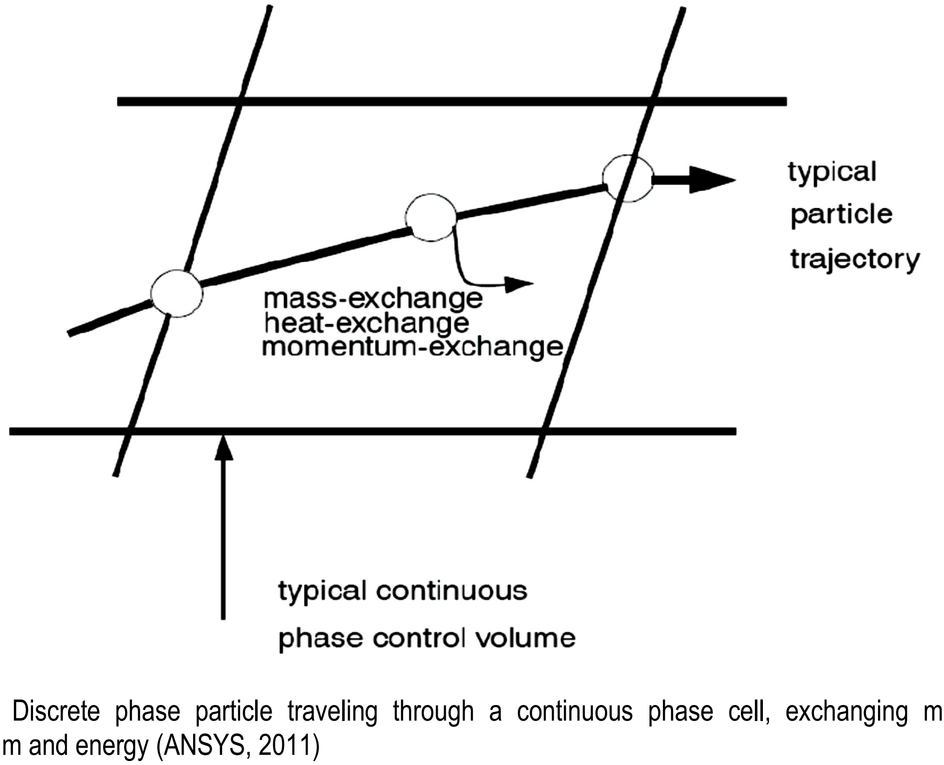

Figure 3 Discrete phase particle traveling through a continuous phase cell, exchanging mass, momentum and energy (ANSYS, 2011)

In the presence of turbulence, spray analysis should be able to account for droplet-turbulence interactions, which can be seen as the disperse effect on the droplet due to the turbulent fluctuations of the fluid phase. Faeth et al. classified the Lagrangian spray models as being either locally-homogenous flow (LHF), or deterministic separate flows (DSF). LHF implies infinitely fast interphase transport rate, while the DSF assumes finite interphase transport rates; yet, both techniques ignore the interaction between the dispersed phase elements and the turbulence. As a result, two main methods have been developed: (1) stochastic separated flow (SSF) which treats both finite interphase transport rates and dispersed phase droplet-turbulence interactions (Faeth, 1987), and (2) the particle cloud tracking model (Baxter & Smith, 1993).

Among these models, the separate flow family, either the DSF or the SSF, have been widely used in predicting particle dispersion in turbulent flows. They have the advantage of being easy to implement, and able to take into consideration the complexities related to particles in a turbulent regime (Zhang, Yang, Chan, & Lau, 2002).

In the DSF model, the influence of gas phase turbulence on the particle phase is neglected; since it uses the time-averaged fluid velocity at the particle location as the instantaneous fluid velocity, to calculate the particle trajectory. The name deterministic comes from the fact that, once the average Eulerian fluid velocity is known, the particle trajectories can be directly determined (Shirolkar, Coimbra, & McQuay, 1996).

Contrary to the stochastic method, in which a large number of particles is introduced into the flow of interest. This generates a 'synthetic' turbulence with some known statistical properties, such as the mean and variance of the fluid fluctuating velocity. These known properties can, in general, be obtained by solving any single-point closure scheme, such as those developed in the RANS equations for the carrier fluid. The large number of particles is then introduced into the flow, and their trajectories are simulated while updating temporally the various particle properties (e.g. velocity, and temperature). The statistical analyses on the particles are performed by collecting samples from a small control volume within the flow field. This procedure is similar to the protocols used in laboratory experiments, where particles crossing a small volume (e.g. probe) are sampled in time (Mashayek & Pandya, 2003). In a statistical sense, it is important to realize that the data generated using the synthetic turbulence approach, may represent the physics of real turbulence only after averaging over a large number of particles, i.e. samples.

The stochastic methods enclose two main formulations: (1) the random walk model (RWM), and (2) the Langevin stochastic differential equations (SDE). These two approaches approximate the flow-field velocity experienced by the particle Lagrangian velocity. The RWM specifies the velocity as the sum of the local mean fluid velocity, and a random fluctuation velocity. This random fluctuation velocity is selected from a Gaussian distribution, having a zero mean and a variance related to the turbulent velocity scale, coming from the turbulence model used in the mean field solution. The RWM model may be either continuous and thus the model will be named continuous random walk (CRW), or discontinuous leading to the so called discontinuous random walk (DRW), or sometimes referred to as discrete random walk (MacInnes & Bracco, 1992). Shirolkar et al. stated that the formulation of the SDE approach requires the Reynolds-stress transport description of turbulence, which typically includes the modeling of the triple-moments. This has not been tested extensively in particle-laden flows; hence, it cannot yet be generally recommended for engineering flows and applications. Furthermore, the SDE becomes complicated for wall interactions, since it requires Eulerian-type boundary conditions, which cannot robustly handle the wall reflection. Therefore, we will focus our attention on the more commonly used DRW and CRW models, and more precisely the DRW model which is available in the computational code FLUENT™ v.14.

The DRW typically assumes that the board spectrum of turbulent eddies can be simplified by local mean eddies. These latter are characterized by a single eddy strength (based on turbulence intensity), a size (based on an integral length, ℓ_e), and an eddy lifetime (τ_e) which is based on the size, strength and the time-averaged velocity. The integral length and time scales will be obtained from the Eulerian gas-phase solution (which in our model will be based on the RANS solution). The primary goal of this procedure is to determine the instantaneous fluid velocity as seen locally by the particle (recall the $\Theta_i^{'}$ term in equation (2.2) which represents the instantaneous value of the fluctuating scalar of interest).

The idea is simple, each eddy is assumed to have a constant velocity perturbation for as long as the particle is interacting with it. This perturbation is formed by choosing a random velocity perturbation, which has to satisfy a predefined probability density function, usually, a Gaussian distribution type (Loth, 2000). When a particle enters the eddy, the fluctuating fluid velocity for that eddy is added to the local mean fluid velocity, to obtain the instantaneous fluid velocity. This fluctuating fluid velocity is assumed to prevail as long as the particle-eddy interaction time is less than the eddy lifetime, and also, the displacement of the particle relative to the eddy is less than the eddy length. If either of these two conditions is exceeded, the particle is assumed to be entering a new eddy, and a new iteration starts. Gosman et al. have proposed the early formulation of the DRW model (Gosman & Ioannides, 1983), which is based on isotropic turbulence. The formulation of the fluctuating velocity components that obeys the Gaussian PDF distribution is as follows:

$$u' = \Gamma\sqrt{\overline{u'^2}} \tag{2.8}$$

$$\sqrt{\overline{u'^2}} = \sqrt{\overline{v'^2}} = \sqrt{\overline{w'^2}} = \sqrt{\frac{2k}{3}} \tag{2.9}$$

$$\ell_e = \frac{c_\mu{}^{3/4} k^{2/3}}{\varepsilon} \tag{2.10}$$

$$\tau_e = \frac{\ell_e}{u'} = \frac{\ell_e}{\sqrt{\frac{2k}{3}}} \tag{2.11}$$

$$\tau_{cros\sin g} = -\tau_{particle} \ln\left[1 - \left(\frac{\ell_e}{\tau_{particle}\left|u - u_{particle}\right|}\right)\right] \tag{2.12}$$

where (Γ) is a normally distributed random number to account for the randomness of turbulence around the mean value, ($\sqrt{\overline{u'^2}}$) is the local RMS value of the fluctuating velocity, (*k*) and (*ε*) are the local turbulent kinetic energy and dissipation respectively (calculated as explained above in the turbulence section), the (c_μ) is a factor used to relate the characteristic length to the eddy dissipation length scale, and both the ($\tau_{cros\sin g}$), ($\tau_{particle}$) are the particle crossing time and relaxation time, respectively. These two time scales are used to account for the effect of the eddy-particle interaction time, such that, the ($\tau_{\mathrm{int}eraction}$) will consider the smallest value of the ($\tau_{cros\sin g}$), or the (τ_e). Gosman model is far from being perfect (Tian, 2006); yet, it is still one of the most used in the sprays dispersion domain, due to its simplicity, as well as computational efficiency (Loth, 2000).

2.4. Atomization and Spray breakup

Gas turbines are distinguished by their high flexibility to burn wide range of fuels; the most common way to classify fuels is by splitting them into gaseous and liquid fuels. In this section we will focus on liquid fuels, which can be employed in almost all gas turbine engines. Liquid fuels must be atomized before being injected into the combustion chamber. Atomization is the process whereby a volume of liquid is converted into a multiplicity of small drops. Principally, it aims to create a high ratio of surface to mass in the liquid phase, which will increase the evaporation rate of the cloud of droplets. In a general way, atomization is fairly simple to accomplish, it needs a high relative velocity between the liquid to be atomized and the surrounding media (e.g. air or gas). Some atomizers achieve it, by discharging the fuel at high velocity into a relatively slow moving stream of air. Notable examples of this type of atomizer are the pressure, and the rotary atomizers. An alternative approach for the atomization is to expose a relatively slow moving fuel to a high-velocity air steam; this latter method is generally applied in the twin-fluid, the air-assist, and the air blast atomizers (Lefebvre, 1983).

In gas turbine combustion chambers, the atomization process represents a disruption of the consolidating influence of the surface tension, through the action of internal and external forces. In the absence of such disruptive forces, surface tension tends to pull the liquid to form a sphere; contrary, to the liquid viscosity, which has an adverse effect on the atomization because it opposes any change of the system geometry. On the other hand, aerodynamic forces will act on the liquid surface, promoting the disruption process, by applying external distorting forces to the bulk liquid. The outcome from the interaction of these forces, results in the breakup process, which occurs when the magnitude of the disruptive force just exceeds the consolidating surface tension force (Lefebvre, 1998). The atomization process involves complicated processes, such as the primary breakup of jet or sheet stream, the secondary breakup of droplets, and the collisions and coalescences between drops. These processes together will determine the detailed characteristics of the fuel spray in regard to the droplet velocities, and the drop-size distribution.

Lefebvre (Lefebvre & Ballal, 2010) stated that the primary & secondary breakup processes are affected by the internal geometry of the atomizer, the properties of the gaseous medium into which the fuel stream is discharged, and the physical properties of the liquid fuel itself. For example, the breakup mechanism of jet disintegration is of a great importance in the design of the plain-orifice pressure nozzles, and the plain-jet air blast atomizers; whereas, the breakup mechanism of sheet disintegration has a direct relevance to the performance of pressure-swirl, and pre-filming air blast atomizers. Both, jet and sheet disintegrations resulted from the primary and the secondary breakup mechanisms are represented in ***Figure 4***.

In the following sub-sections, we will explain separately the basic formation of the primary breakup regime for both jet and sheet streams; and then, we will discuss the secondary breakup mechanisms of drops, which are a common subject between both configurations, i.e. jets and sheets.

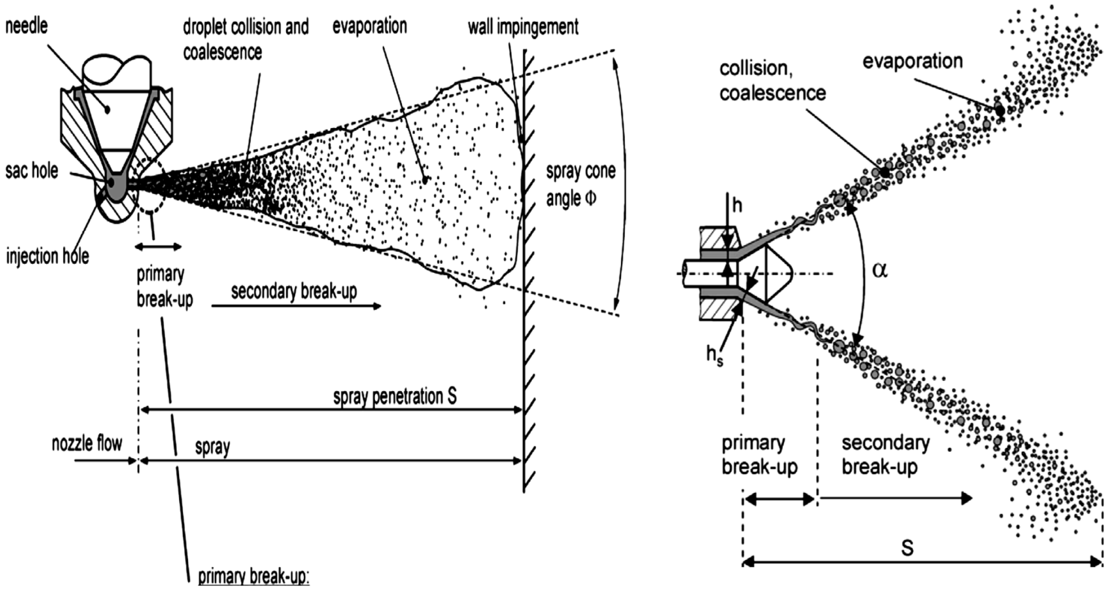

(a) (b)

Figure 4 (a): breakup mechanisms for a jet of fuel (full cone type), and (b) breakup mechanisms for a sheet of fuel (hollow cone type). **(Baumgarten, 2006)**

2.4.1. Breakup mechanisms with jet disintegration

Rayleigh was among the first to theoretically study the breakup of liquid jets (Lefebvre & Ballal, 2010), he considered the simple situation of a laminar jet issuing from a circular orifice. According to Rayleigh, breakup occurs when the fastest growing disturbance attains a wavelength of ($\lambda_{opt} = 4.51 D_{jet}$), where, ($D_{jet}$) is the initial jet diameter. Later, Weber extended Rayleigh's work to include the viscous effect on the liquid; he assumed that any disturbance causes rotationally symmetrical oscillations of the jet. If the wavelength of the initial disturbance is less than ($\lambda_{\min}$), the surface forces tend to damp out the disturbance. If on the other hand, the wavelength is greater than ($\lambda_{\min}$), the surface tension forces will tend to increase the disturbance, leading to the disintegration of the jet. There is however, one particular wavelength (λ_{opt}), which is the most favorable for the breakup process (Lefebvre, 1989), and can be calculated through the equation below:

$$\lambda_{opt} = 4.44 D_{jet} (1 + 3Oh)^{0.5} \tag{2.13}$$

where (*Oh*) is the Ohnesorge number defined in the next section. The disintegration of liquid jets is described by two main mechanisms. The first mechanism is the breakup of the intact liquid core into ligaments, and then into droplets; this is called the primary breakup. This mechanism is characterized by the breakup length (which provides a measure of the growth rate of disturbance), and by the droplet size. The second mechanism is the further disintegration of the formed droplet into smaller droplets; here, the size of the droplets is a characteristic parameter (Lefebvre, 1989).

In order to give a quantitative description to the jet breakup process, Ohnesorge performed measurements on the intact jet length. He showed that the disintegration process of a jet can be described by the liquid Weber number, and the Reynolds number (Baumgarten, 2006). His method became the most commonly quoted criteria in the classification of the jet disintegration mechanisms. Ohnesorge classified the data according to the relative importance of gravitational, inertial, surface tension, and viscous forces, through the introduction of a dimensionless number; referred to as the stability number, the viscous group number, or the Ohnesorge (*Oh*) number, obtained as following:

$$We_l = \frac{u^2 D \rho_l}{\sigma} \tag{2.14}$$

$$\mathrm{Re} = \frac{u D \rho_l}{\mu_l} \tag{2.15}$$

$$Z = Oh = \frac{\sqrt{We_l}}{\mathrm{Re}} = \frac{\mu_l}{\sqrt{\sigma \rho_l} D} \tag{2.16}$$

Ohnesorge showed that the various mechanisms for the jet breakup can be divided into three regions on a graph named, the Ohnesorge’s chart. Reitz et al. in a more recent study, attempted to resolve some of the uncertainties surrounding Ohnesorge’s chart. According to Reitz, there are four regimes of breakup, instead of three. These regimes are encountered, when the liquid injection velocity is progressively increased (Lefebvre, 1989). ***Figure 5*** shows the four main regimes of liquid jet, done by Reitz and Chigier (Kuo & Acharya, 2012).

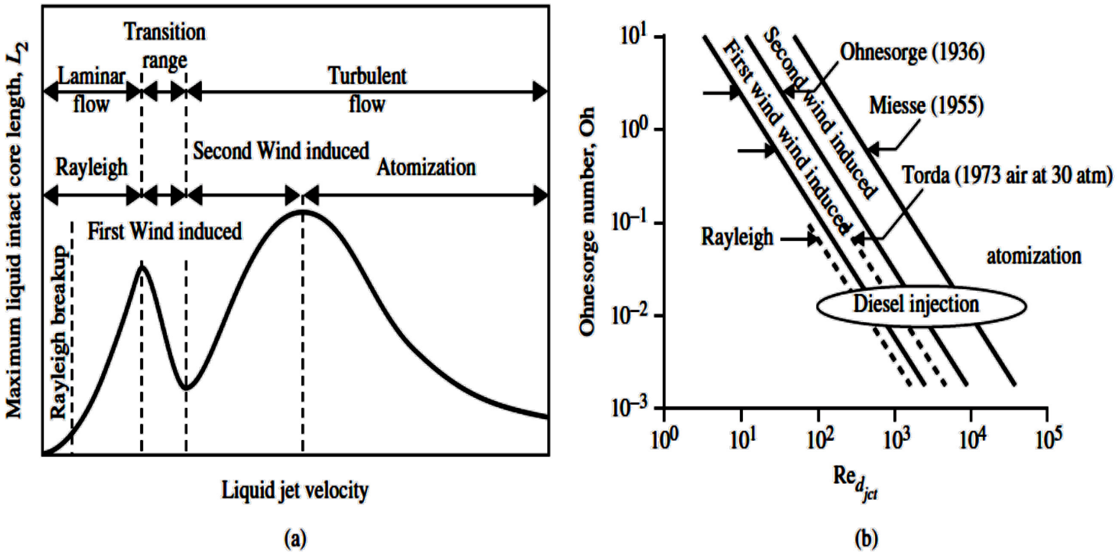

Figure 5 (a) Relationship of maximum liquid intact-core length with the injection velocity (b) breakup regimes on an Oh-Red map for a steady injection of liquid jet into stagnant air (modified from Fath, Munch, & Leipertz 1997). **(Lefebvre & Ballal, 2010)**

These regimes include: (a) The Rayleigh breakup regime, (b) the first wind-induced breakup, (c) the second wind-induced breakup, and (d) the atomization breakup regime.

(a) The Rayleigh jet breakup: In this regime, breakup occurs due to the growth of the axis-symmetric oscillations of the complete jet volume. This is initiated by liquid inertia, and surface tension forces. The droplets are pinched off the jet, and their size is greater than the nozzle hole diameter (Baumgarten, 2006).In terms of velocity, at very low liquid velocities, drip flow occurs and no jet is formed. An increase of the velocity of the liquid, will result in the formation of an unbroken jet, with a length that increases with the increasing liquid velocity (***Figure 5*** a) and ***Figure 7***.

(b) The First wind-induced breakup: The surface tension effect is now amplified by the aerodynamic force, due to the relative velocity between the jet, and the ambient gas. This will produce a static pressure distribution across the jet, causing an acceleration of the breakup process. In this regime, drops diameter are about the same order of magnitude as the nozzle diameter (Lefebvre, 1989). (***Figure 5*** a*)* shows that in this regime, a further increase in the liquid velocity will result in a decrease of the breakup length.

(c) The second wind-induced breakup: In the second wind-induced breakup regime, the flow inside the nozzle becomes turbulent. Jet breakup now occurs due to the instable growth of the short wavelength surface waves, which are initiated by jet turbulence, and amplified by aerodynamic forces arisen from the relative velocity between the gas and the jet. The diameter of the resulting droplets is smaller than the nozzle diameter. The jet shall no longer break as a whole. Due to the separation of small droplets from the jet surface, the disintegration process begins at the surface, and then gradually erodes the jet until it is completely broken up. Now two breakup lengths should be accounted for: (1) the length describing the beginning of surface breakup (intact surface length), and (2) the length describing the end of jet breakup (intact core length). While the intact surface length decreases with increasing the jet velocity as illustrated in ***Figure 7*** , the core length may increases, as shown in (***Figure 5*** a) (Baumgarten, 2006).

(d) Atomization regime: The atomization regime is characterized by jet breakup immediately at the jet exit. Flow in the atomization regime yields drops whose average diameter is much smaller than the jet diameter (Kuo & Acharya, 2012).

It was observed that including only the liquid phase for the description of the regimes is not sufficient, because atomization can be enhanced by increasing the gas density (Baumgarten, 2006). Thus, Reitz suggested to include the gas-to-liquid density ratio, and to extend the two dimensional Ohnesorge's chart into a three dimensional one as shown in ***Figure 6***. Also a schematic diagram describing the characteristic behavior of the four breakup regimes is presented in ***Figure 7***.

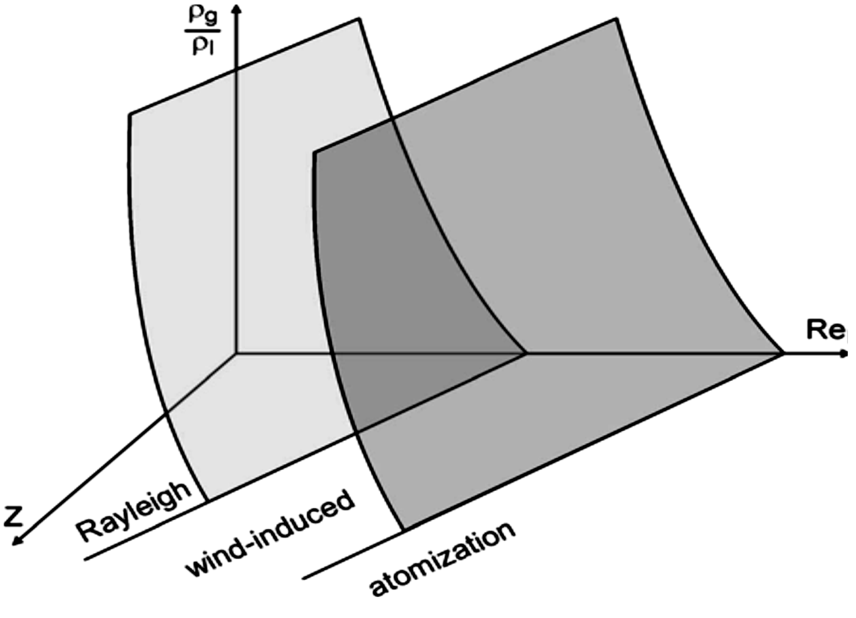

Figure 6 Schematic diagram including the effect of gas density on jet breakup **(Baumgarten, 2006)**

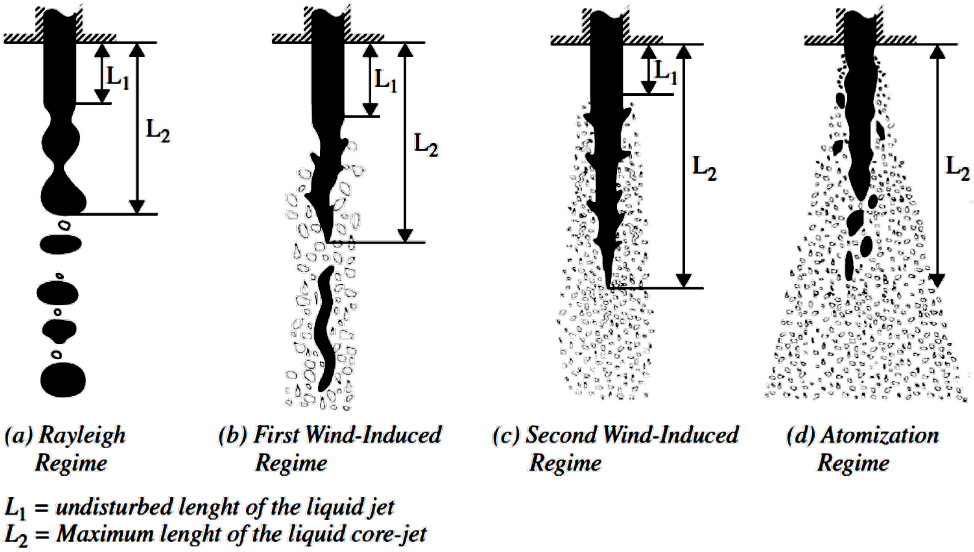

(a) Rayleigh Regime *(b) First Wind-Induced Regime* *(c) Second Wind-Induced Regime* *(d) Atomization Regime*

L_1 = undisturbed lenght of the liquid jet
L_2 = Maximum lenght of the liquid core-jet

Figure 7 Schematic diagrams for describing the characteristics behavior of the different regimes of the jet breakup mechanisms **(Lefebvre & Ballal, 2010)**

2.4.2. Breakup mechanisms of sheet disintegration

The information in this sub-section is mostly based on the book of Arthur Lefebvre chapter II (Basic process in Atomization) (Lefebvre, 1989)

Many atomizers do not form jets of liquid; but rather form flat or conical sheets sometimes also known as hollow cone sprays. Conical sheets can be formed if a liquid flowing in a pipe is deflected through an annular orifice, the form of the sheet being governed by the angle of deflection. Pressure-swirl atomizers and pre-filming air-blast nozzles are known by their capacity of producing such conical sheets; where the liquid will exit the orifice with a tangential velocity component resulting from its passage through tangential or helical slots. Flat sheets, can be produced by the impingements of two liquid streams, or by feeding the liquid to the center of a rotating disk or a cup.

When a sheet of liquid emerges from a nozzle, its subsequent development is influenced mainly by the liquid physical properties, the ambient surrounding, and its initial velocity. To expand the sheet against the contracting surface tension force, a minimum sheet velocity is required, which can be achieved depending on the atomizer type. For example, in the case of the pressure swirl type, this velocity is maintained through the high pressure injection force, whereas; in the air-blast type it is achieved through the aerodynamic drag force. Increasing the initial velocity lengthens, and expands the sheet until a leading edge is formed, where equilibrium between the surface tension and the inertia forces is satisfied.

Fraser and Eisenklam defined three modes for the sheet disintegration: (a) the rim, (b) the wave, and (c) the perforated-sheet. Photographs of these three regimes are shown in ***Figure 8***.

(a) The rim mode: In this mode, forces created by the surface tension cause the free edge of the liquid sheet to contract into a thick rim, which then breaks up by a mechanism similar to the jet disintegration mechanism. In the rim regime, the resulting drops continue to move in the original flow direction, and they remain attached to the receding surface by thin threads, which in their turn will rapidly break up into rows of drops. This mode of disintegration is mostly prominent when both the viscosity and the surface tension of the liquid are high.

(b) The wave mode: Here the disintegration is created through the generation of a wave motion on the sheet; whereby areas of the sheet, corresponding to a half or a full wavelength of the oscillation, are torn away before the leading edge is reached. These areas rapidly contract under the action of surface tension, but they suffer disintegration by the action of the air, or the liquid turbulence before a regular network of threads can be formed.

(c) The perforated sheet mode: this regime is distinguished by the presence of holes in the sheet. These holes grow rapidly in size until it coalesces with one another, producing ligaments of irregular shape that finally break up into drops of varying sizes.

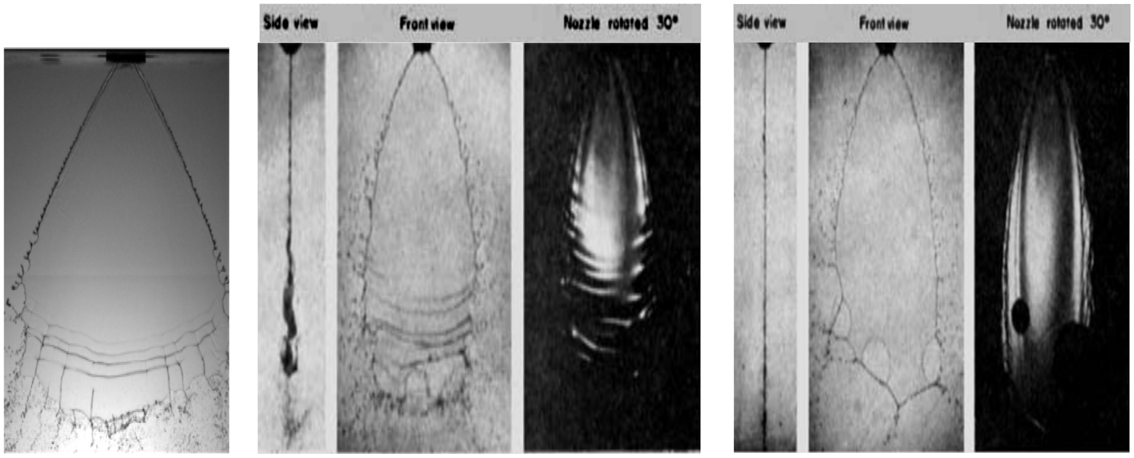

(a) (b) (c)

Figure 8 (a) the rim disintegration regime, (b) the wave mode in three views and (c) the perforated sheet mode in three views (photographs to illustarte the sheet atomization mechanism **(Lefebvre, 1989)** & **(Altimira, Rivas, & Ramos, 2011)**)

Atomizers that discharge the liquid in the form of a sheet are usually capable of displaying all the three modes detailed above. Sometimes, two different modes occur simultaneously, depending on the operation condition of the atomizer. Dombrowski, Fraser, Eisenklam and co-workers made numerous studies on the mechanisms of sheet disintegration, and they established that ligament formation is caused principally by perforations effects in the liquid sheet. They also observed that if holes are generated by air friction means, breakup of ligaments into drops will occur very rapidly, but if they are created by other means such as turbulence in the nozzle, the ligaments breakup will occur more slowly. They have concluded that the effect of liquid density on sheet disintegration is negligibly small.

To simplify the explanation of the sheet disintegration process, let us recall (***Figure 4*** b). First, a liquid film with an initial thickness (h_s) and a spray angle (α) becomes thinner, because of the conservation of mass as it departs from the nozzle. The instabilities produced inside the nozzle causes the formation of initial perturbations on the liquid surface. The frequency, and amplitude of such perturbations depend on the internal nozzle hole flow. These waves grow instable due to the aerodynamic interaction with the surrounding gas. At critical wave amplitudes, the liquid film breaks up into ligaments, which, under the influence of surface tension and gas forces, rapidly disintegrate into drops. Besides these oscillations phenomena, a spontaneous separation of small satellite droplets directly at the nozzle may exit, if sufficient turbulent kinetic energy is presented. This phenomenon mainly occurs at high injection pressures, typically found in the pressure swirl atomizers (Baumgarten, 2006).

As stated by Fraser et al. (Lefebvre & Ballal, 2010), for low relative velocity between the fuel sheet and the surrounding air, a wave motion is generated on the sheet causing rings of fuel to break away from its leading edge. The volume of fuel contained in the rings can be estimated as the volume of a ribbon cut out of the sheet, having a thickness equal to that of the sheet at the breakup distance, and a width equal to one-half wavelength of the oscillation ($^{\lambda_{opt}}\!/_{2}$). These cylindrical ligaments then disintegrate into drops of uniform size according to the Rayleigh mechanism as illustrated in ***Figure 9***. With the continuous increment of the relative velocity, sheet breakup occurs closer to the nozzle. Also, the optimum wavelength for the breakup becomes smaller, and ligaments, as well as, drop diameters are reduced, accordingly. Finally, at very high relative velocities, atomization starts at the nozzle exit. Under this later condition, the fuel sheet will not have the time to develop a wavy structure; instead it will immediately tear up into fragments by its vigorous interaction with the surrounding air.

The essential feature of this mode of atomization lays in the rapid and violent disruption of the fuel to ensure that the ensuing drop sizes are largely independent of the initial fuel nozzle dimension, i.e. sheet thickness.

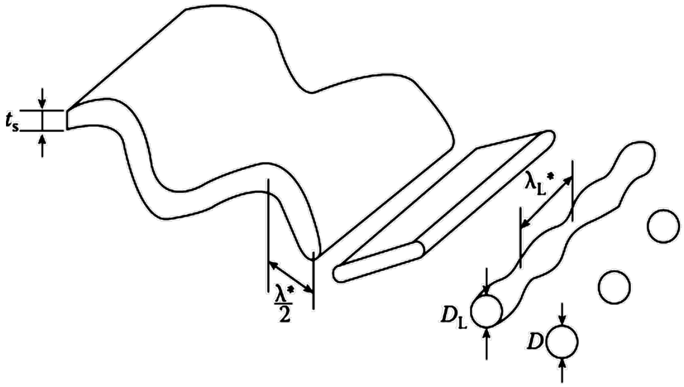

Figure 9 Successive stages in the idealized breakup of a fuel sheet **(Lefebvre & Ballal, 2010)**

2.4.3. Secondary breakup mechanism

The breakup of drops in a spray is caused by the aerodynamic forces; these include both friction and pressure forces, which are induced by the relative velocity between the droplet and the surrounding media (gas or air). The aerodynamic forces result in an instable growing of waves on the air-liquid interface of the whole droplet itself, which finally leads to disintegration and formation of smaller droplets (Lefebvre & Ballal, 2010). The newly formed droplets are again subject to further aerodynamically induced breakup, based on the state of equilibrium between the external aerodynamic forces, and the internal forces (e.g. the surface tension and the viscosity). Klüsener et al. explained this equilibrium condition through the following relation:

$$p_i = p_A + p_\sigma = cons. \tag{2.17}$$

Note that for a spherical droplet:

$$p_\sigma = \frac{4\sigma_s}{d_{droplet}} \tag{2.18}$$

where (p_i) represents the internal pressure at any point on the droplet surface, (p_A) the external aerodynamic pressure, and (p_σ) the surface tension pressure.

Equation (2.17) shows that a droplet can remain stable, as long as, the changes in the aerodynamic pressure at any point on its surface can be compensated by a corresponding a change in (p_σ); such that, (p_i) remains constant (Lefebvre, 1989). Clearly, the surface tension forces try to keep the droplet spherical, hence counteract the deformation forces. The surface tension force depends on the curvature of the surface; that is, the smaller the droplet, the bigger the surface tension force, and the bigger the critical relative velocity needed to destabilize the droplet (Baumgarten, 2006).

This behavior is expressed by the gas phase Weber number as following:

$$We_g = \frac{\rho_g \left|U_{rel}\right|^2 D_{droplet}}{2\sigma_s} = \frac{\text{Aerodynamic pressure}}{\text{Surface tension pressure}} \tag{2.19}$$

Note that in the definition of the gas We_g number there is a factor of two in the denominator, which is different from the We_g used in many other studies. However, this definition is physically more meaningful, since the dynamic pressure is represented by ($\rho\left|U_{rel}\right|^2 \big/ 2$), and the surface tension pressure as shown in equation (2.18) contains the factor of four.

Borisov et al. compiled regimes reported by various researches, and they reported mainly three droplet breakup regimes as shown in ***Table 1***: (a) the parachute type, also known as the bag type, the umbrella shape body, or the bag and stamen shape body type, (b) the stripping type, and (c) the explosion type. Note that the term 'stamen' comes from the observation of Theofanous et al., since they observed that the spherical droplet is deformed into parachute-shape bodies with a short cylindrical liquid zone near the center as illustrated in ***Figure 10***. Pilch and Erdman made an extensive study on the acceleration induced droplet breakup processes. They further extended the original definition of Borisov, concluding the presence of five distinct mechanisms as illustrated in ***Figure 10*** (Kuo & Acharya, 2012).

Table 1 The Three Droplet breakup regimes

Drop Breakup Type	Range of governing gas We number	Physical process

Parachute type	$4 \leq We_g \leq 20$	Droplet flattens perpendicularly to the flow, and forms a bag. Liquid around the forward stagnation point of the drop is deflected by the flow piercing effect. The bag expands, and eventually shatters into a small drops, due to the bag shape instability
Stripping type	$10 \leq We_g \leq 10\,000$	The surface layer is torn off the droplets due to the high stripping, and the shearing forces, resulting in a significant fraction of very fine droplets
Explosion type	$1\,000 \leq We_g \leq 100\,000$	The newly formed droplets are significantly smaller than the original drops.

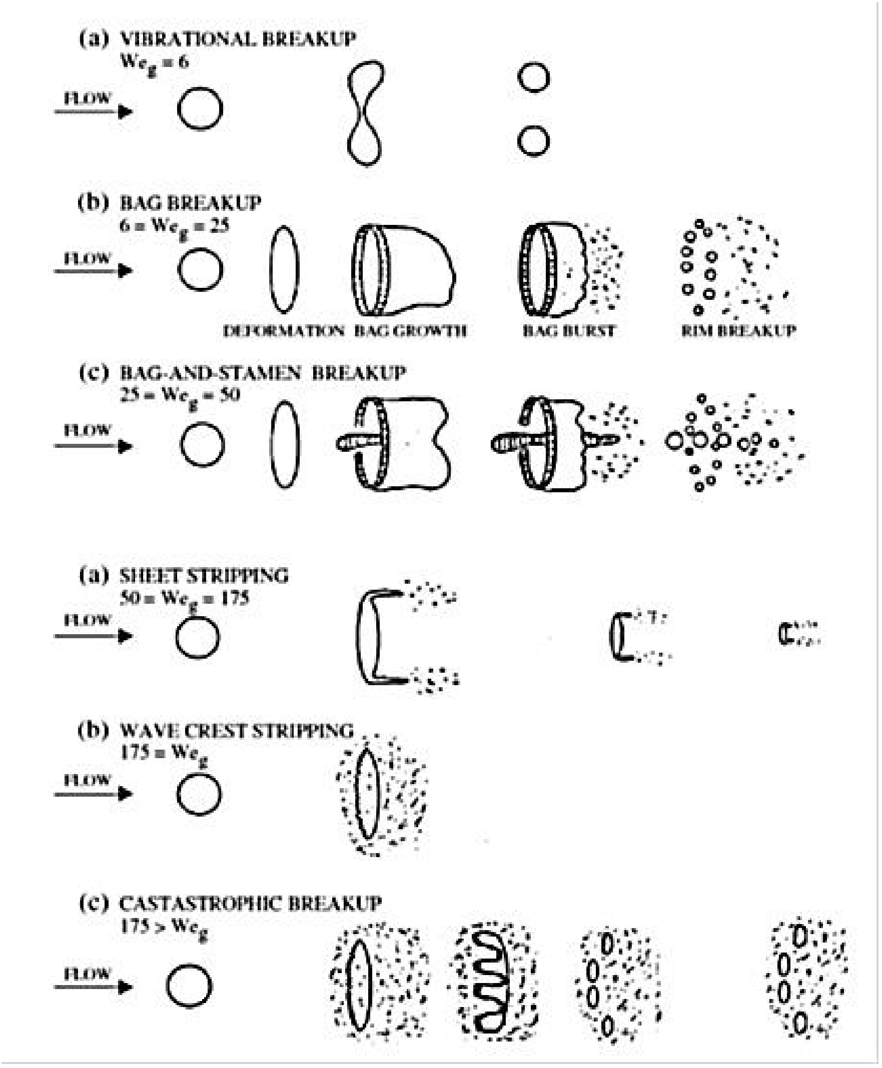

Figure 10 Droplet acceleration-induced breakup mechanisms (modified from Pilch and Erdman, 1987) **(Kuo & Acharya, 2012)**

The distinct five breakup mechanisms are summarized as follow (Pilch & Erdman, 1987):

(a) Vibration breakup regime: This mechanism occurs at small We_g, where oscillations may develop at natural frequency of drop. When oscillation amplitude increases, the drop may decompose into a few large fragments. Breakup time is longer than that of other mechanisms; thus, this mechanism is not usually considered in drop breakup studies.

(b) Bag breakup regime: The Breakup process is analogous to the bursting of soap bubbles, blown from a soap film attached to a ring. Eventually, the thin hollow bag bursts, forming a large number of small fragments, as well as, rims that disintegrate into a small number of large fragments.

(c) Bag and Stamen breakup regime: Breakup mechanism has features similar to bag breakup; however, a column of liquid (stamen) is formed along the drop axis parallel to the approaching flow. First, the bag bursts, followed by the disintegration of the rim and the stamen.

(d) Sheet stripping breakup regime: This breakup mechanism is distinctly different from the above breakup mechanisms. No bags are formed; instead, a thin sheet is continuously being stripped from its periphery to form small drops. A coherent residual drop exists during the entire breakup process.

(e) Wave Crest stripping regime: At higher We_g, large-amplitude having small-wavelength waves are formed on the windward surface of the deformed drop. The wave crests are continuously eroded by the action of the flow field over the surface of the drop.

(f) Catastrophic breakup regime: In this regime long-wavelength waves will finally penetrate the drop, creating several large fragments, before the wave crest stripping can significantly reduce the mass of the droplet. Catastrophic breakup leads to a multistage process, in which fragments and fragments of fragments are subject to further breakup.

Note that the above classification has included six different categories not five as mentioned above, this is due to the fact that at elevated We_g ranges, the wave crest stripping regime will be followed by the catastrophic breakup regime systematically; hence they can be grouped in a single category (Pilch & Erdman, 1987). The critical condition of droplet breakup is a subject of prime importance, since it addresses the beginning of the secondary breakup process. This critical condition is achieved when the aerodynamic drag force is just equal to the surface tension force (Lefebvre & Ballal, 2010), mathematically expressed as following:

$$C_D\left(\frac{\pi D^2}{4}\right)\frac{1}{2}\rho U^2_{relative} = \pi D\sigma \tag{2.20}$$

where C_D is the drag coefficient of the drop. Rearranging these terms provides the dimensionless group:

$$\left(\frac{\rho D U^2_{relative}}{\sigma}\right) = \frac{8}{C_D} \tag{2.21}$$

The first term in equation (2.21) represents the We number; and thus, may be written as:

$$We_{critical} = \frac{8}{C_D} \tag{2.22}$$

The subscript 'critical' denotes that a critical condition has been reached. When the effect of viscosity is negligible (low viscous fluids), experimental data on C_D indicate an average value around 12 for the R.H.S term in equation(2.22); and thus, the $We_{critical}$ can have the value of 12 (Lefebvre & Ballal, 2010). According to Brodkey (1969), for gas-liquid systems, the effect of viscosity on the $We_{critical}$ can be expressed by the following useful empirical correlation:

$$\begin{aligned} We_{critical} &= We'_{critical} + 12.964 Oh^{1.6} \\ We_{critical} &= 12(1 + 1.077 Oh^{1.6}) \end{aligned} \tag{2.23}$$

where $We'_{critical}$ is the $We_{critical}$ as defined in equation (2.22) for zero viscosity fluids. Readers can recognize that $We_{critical}$ defined in (2.23), and used by Pilch and Brodkey, differs from that offered in equation (2.19), ***Table 1***, and ***Figure 10*** by a factor of two. Therefore, the onset of the vibration breakup regime with the value of six shown in ***Figure 10***, should be multiplied by two to correspond to the original correlations (Kuo & Acharya, 2012) , which is 12.

The above mentioned literature review and correlations for the primary and secondary breakup mechanisms of both jet and sheet disintegrations are deemed valid and true for almost all conventional fuels, however, different trends, breakup regime maps and correlations were observed for non-conventional fuels. To the best of our knowledge, no specific research was found for correlating the spray behavior of biodiesel and its blends in cross flows, which is fundamental to study spray characteristics, such as penetration depth, droplet diameter, velocity, and volume flux. However, a recent study achieved by a group of researchers from Concordia University revealed outstanding results related to this matter.

Farvardin et al (E.Farvardin, M.Johson, H.Alaee, A.Martinez, & A.Dolatabati, 2013) performed an experimental study on biodiesel and diesel jet in a gaseous cross flow using the shadowgraph method and the PDPA analyser, to capture the penetration depth, and to investigate the different regimes of breakup generated from biodiesels and their blends. They found that the previously developed correlations used to determine fuels breakup regimes are not fully adequate for biodiesel, and thus, an improved correlation was required. They also concluded that the effect of the high viscosity and surface tension associated to these non-conventional fuels was behind several discrepancies between both fuels, such as lower penetration depth of the biodiesel jet, and higher drag coefficient with biodiesel jet resulting in a blunt jet.

2.4.3.1. Modeling of spray breakup

Information in this sub-section is mostly based on the book of Carsten Baumgarten chapter IV (Baumgarten, 2006).

Currently, multiple atomization models exist to simulate the breakup mechanism. As the phenomenological breakup mechanisms involve primary and secondary processes, the breakup models can be divided into two groups: (a) the primary breakup models, and (b) the secondary breakup models.

The primary breakup process provides the starting conditions for the calculation of the subsequent spray formation inside the domain. The fact that the Lagrangian description of the liquid phase requires the existence of the drops, the simulation of the spray formation always begins with drops penetrating into the combustion chamber. The main task of a primary breakup model is to determine the starting conditions of these drops, such as but not limited to, initial radius, velocities, and spray angle. There are only very few detailed models for the simulation of the primary breakup mechanism. One reason is that, the experimental investigations are extremely complicated, since the spray is dense. The high spray density exacerbates the understanding of the relevant processes involved; and hence, the development of primary breakup models is limited. Moreover, from a numerical point of view, the simulation of the flow inside the injector requires different mathematical descriptions of the liquid phase; that is, the use of the Eulerian scheme inside the nozzle, and the Lagrangian description outside the nozzle. Thus, the practical solution is to avoid direct calculations of the primary breakup mechanisms, and to rely on modeling them.

Among models created to simulate the primary breakup mechanism, there is: (a) the blob method, (b) the turbulence induced breakup model, (c) the cavitation-turbulence breakup model, and (d) the sheet atomization model for hollow cone sprays.

(a) The blob method: this is the simplest and most popular way of defining the starting condition of the first droplets at the nozzle exit. This method is based on the assumption that the atomization, and droplet breakup within the dense spray near the nozzle, is an indistinguishable processes (e.g. no difference between the primary and the secondary breakup mechanisms in the dense area near the nozzle exit). By assuming that the detailed simulation can be replaced by the injection of big spherical droplets called 'Blobs', having uniform size. Blobs are then subject to secondary aerodynamic induced breakup see ***Figure 11***. The diameter of these blobs equals the nozzle hole diameter, and their injected numbers per unit time is determined from the mass flow rate.

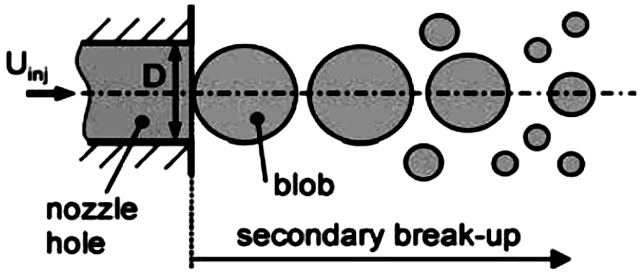

Figure 11 Blob analogy **(Baumgarten, 2006)**

(b) The turbulence induced breakup model : Huh and Gosman assumed that the turbulent forces within the liquid emerging from the nozzle are the producers of the initial surface perturbations, which grow exponentially due to aerodynamic forces, and form new droplets. The wavelength of the most unstable surface wave is determined by the turbulent length scale. The turbulent kinetic energy at the nozzle exit is estimated, using simple overall mass, momentum, and energy balances. The atomization model starts with the injection of spherical blobs, with a diameter equals to the nozzle hole diameter. Initial surface waves grow due to relative velocity between the gas and the drops (the Kelvin-Helmholtz instability theory). The breakup rate of a primary blob is set proportional to the atomization length, and the time scale, using an arbitrary constant. The values of the atomization length, and time scales, are time dependent because outside the nozzle the internal turbulence of the parent drops decays with time as they travel downstream. The effects of cavitation are not included in Huh & Gosman model; instead, it is assumed that the turbulence at the nozzle hole exit, can be sufficient to represent the influence of the nozzle characteristics on the primary spray breakup. The use of this model is limited to sprays from non cavitating turbulent nozzle hole flows.

(c) Cavitation and turbulence induced breakup model: Cavitation is the transition from the liquid phase to the gas phase due to a decrease of the static pressure below the vapor pressure. At the upstream edge of the injector nozzle, the curved stream lines result in a high radial pressure gradient, causing a reduction of the pressure below the vapor pressure of the liquid; and thus, forming the cavitation bubbles (Bekdemir, 2008). These bubbles contribute to the primary breakup mechanism, since they will burst on the surface of the liquid. Therefore, the cavitation effects cannot be neglected. Nishimura and Assanis have presented a cavitation and turbulence induced primary breakup model for the full cone spray types, their model takes cavitation, turbulence, and aerodynamic effects into account. They have assumed that the injected liquid is on a form of discrete cylindrical ligaments, with a diameter and volume equal to that of a blob see ***Figure 12***. Each cylinder contains bubbles according to the volume fraction and size distribution at the hole exit. These bubbles are computed from a phenomenological cavitation model inside the injector. Several authors have successfully validated their model against experimental data, and the model is found well suited for the simulation of cavitation and turbulence induced primary breakup. However, it assumes axis-symmetry, and therefore, will not be capable to predict the influence of 3D flow for a nozzle with an asymmetric hole. Later, other authors have solved this problem. Von Berg et al., and Baumgarten et al. have introduced an advanced version of the cavitation and turbulence induced model. The most important features of their primary breakup models are, the detailed modeling of the effect of the bubbles collapsing outside the nozzle, and the ability to simulate the influence of asymmetric nozzle flow on the 3D spray structure, see ***Figure 13***. Their model is well suited for the simulation of high-pressure diesel injection. However, a complete CFD simulation of the nozzle flow is required as an input data.

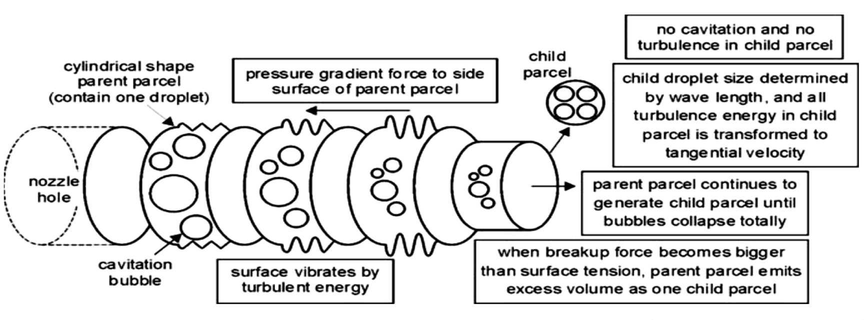

Figure 12 Primary breakup model of Nishimura and Assanis **(Baumgarten, 2006)**

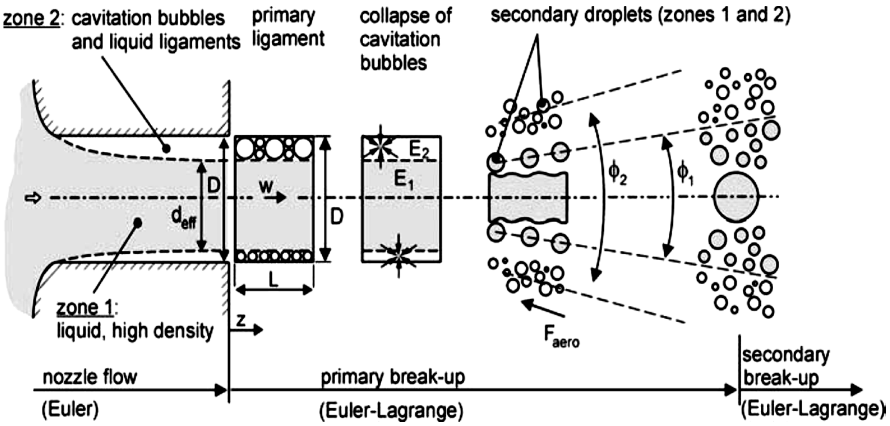

Figure 13 Primary breakup model of Baumgarten et al. **(Baumgarten, 2006)**

(d) Sheet atomization model for hollow cone sprays: Hollow cone sprays are typically characterized by their ability to form small droplets with, elevated droplet dispersion, effective fuel-air mixing, and thus, high atomization efficiency. But, on the other hand, relatively reduced droplet penetration. ***Figure 14*** shows two typical nozzle concepts for the production of hollow cone sprays: (a) an inwardly opening nozzle, and (b) an outwardly opening nozzle. The hollow cone sprays category is of a great interest to our project, since it represents the type of configuration chosen in our numerical model. Schmidt et al. have developed a well suited model to describe the primary breakup mechanism of hollow cone sprays, called the linearized instability sheet atomization (LISA).

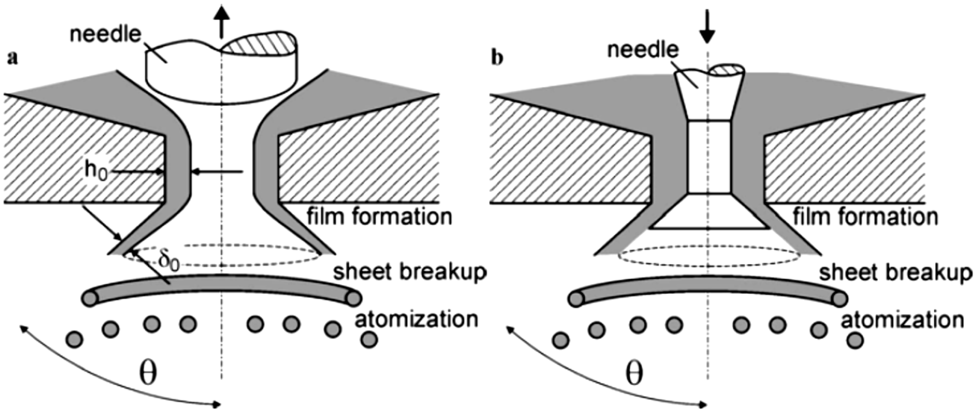

Figure 14 (a) Inwardly opening pressure-swirl atomizer, (b) outwardly opening nozzle **(Baumgarten, 2006)**

In their model, a zero dimensional approach is used to represent the internal injector flow, and to determine the total velocity at the nozzle hole exit (U_{inj}). The rotational motion of the fuel inside the swirl chamber will create an air core, surrounded by a liquid film as shown in (***Figure 14*** *a*). The thickness of the film (δ_0) is related to the mass flow rate through the following relation:

$$\dot{m} = \pi \rho_l u (D_{hole} - \delta_0) \tag{2.24}$$

where (D_{hole}) is the hole diameter at the exit, (ρ_l) is the liquid density of the fluid, and ($\dot{m}$) is the mass flow rate. These three parameters must be measured experimentally. The problem lies in the determination of the axial velocity component (u), which is related to the total velocity (U_{inj}) by:

$$u = U_{inj} \cos\theta \tag{2.25}$$

where (θ) is the spray angle, and must be assumed to initiate the calculation. To calculate the total velocity (U_{inj}), the approach of Han el al. is used; so that, the (U_{inj}) can be related to the injection pressure through:

$$U_{inj} = C_D \sqrt{\frac{2\Delta p_{inj}}{\rho_l}} \tag{2.26}$$

where (C_D) is the discharge coefficient. Physical limitations on the value of the (C_D) are required; such that, the (C_D) must be less than unity to conserve the energy. On the other hand, it must be large enough to conserve the mass, and to avoid the prediction of negative air core sizes. These restrictions are satisfied using the following expression:

$$C_D = \max\left(0.7, \frac{4\dot{m}}{\pi D^2 \rho_l u} \right) \tag{2.27}$$

Once the (U_{inj}) is calculated, the axial velocity component (u) can be determined, as well as, the film thickness. The transition from the injector flow to the fully developed spray is modeled over a three steps mechanism consisting of, film formation, sheet breakup, and finally disintegration into droplets (the secondary breakup). First, a liquid film with an initial thickness (δ_0), a spray angle (θ), an axial velocity (u), and a total velocity (U_{inj}) is formed as explained above. This film penetrates into the combustion chamber. The liquid sheet becomes thinner because of the conservation of mass as it departs from the nozzle. Further downstream, Kelvin-Helmholtz instabilities are assumed to develop and grow on the film surface, resulting in a first breakup, and in the formation of ring shaped ligaments. Lastly, these ligaments will breakup into droplets.

Schmidt et al. have shown that when the film exits the injector as a free liquid sheet, its tangential velocity is completely transformed into radial velocity, and the trajectory approaches a straight line. The angle (θ) measured from the centerline, is determined by the ratio of radial to axial velocities. Hence, at the point of film breakup and drop formation, the swirl velocity of the drops can be neglected. This is a very convenient approach, because the swirl velocity at the nozzle orifice is usually unknown.

As briefly stated, the disintegration of the liquid film is modeled in direct analogy to the Kelvin-Helmholtz model (same analogy will be used in the definition of the secondary breakup models). The model as detailed by Senecal et al., assumes that a 2D, viscous, and incompressible liquid sheet with thickness ($2h$) moves with a relative velocity (U_{rel}) through a quiescent, in-viscid, and incompressible gas. The spectrum of the infinitesimal disturbances can be expressed by:

$$\eta(t) = \eta_0 \exp\left[ikx + \omega t\right] \tag{2.28}$$

where (η_0) is the initial wave amplitude, ($k = 2\pi.\lambda^{-1}$) is the wave number, and (ω) is the complex wave growth rate; such that, ($\omega = \omega_r + i\omega_i$). It is assumed that the most unstable disturbance, i.e. the wave with the highest growth rate, with a growth rate (ω_r) equals to (Ω) causes the sheet breakup. The disturbance in equation (2.28) is imposed on the sheet surface producing pressure, and velocity fluctuations for both the liquid and the gas phases. The amplitudes of these disturbances increase due to the liquid-gas interaction.

It is desired to obtain a relation for dispersion from which the most unstable disturbance can be calculated as a function of the wave number ($\omega = \omega(k)$). Squire et al., Li & Tankin, and Hagerty & Shea have shown that there are two modes which can satisfy the liquid governing equations, subject to the boundary conditions at the upper and lower interfaces. The first mode, called the sinuous mode, in which the waves at both surfaces are exactly in phase. While for the second mode, namely the varicose mode, the waves are 180 degrees out of phase. Senecal et al. observed that the sinuous mode dominates the growth over the varicose waves at low velocities, and that, both modes become indistinguishable at high flow relative velocities (U_{rel}). Furthermore, they deduced the simplified relation for dispersion based on the sinuous mode as following:

$$\omega_r = \Omega = -2\nu_l k^2 + \sqrt{4\nu_l^2 k^4 + \frac{\rho_l}{\rho_g} U^2 k^2 - \frac{\sigma k^3}{\rho_l}} \qquad (2.29)$$

where (ν_l) is the liquid kinematic viscosity, (σ) is the surface tension, and (ρ_g) is the gas density. If the unstable waves on the sheet surface have reached critical amplitude, the sheet is assumed to break up into primary ligaments.

Because the wave growth is independent of the sheet thickness, the breakup time (t_b), and the corresponding breakup length (L_b) can be formulated based on an analogy with the breakup of a cylindrical liquid jets, made by Reitz et al. as following:

$$\eta_b = \eta_0 \exp(\Omega t_b) \text{, and thus } t_b = \frac{1}{\Omega} \ln\left(\frac{\eta_b}{\eta_0}\right) \qquad (2.30)$$

where (Ω) can be obtained from equation (2.29). Assuming that the velocity (U_{inj}) of the liquid sheet is not reduced until breakup occurs, and also that (U_{inj}) equals to the relative velocity (U_{rel}) since the liquid is initially assumed to be injected into a quiescent gas, the breakup length (L_b) can be calculated through:

$$L_b = U_{rel} t_b = \frac{U_{inj}}{\Omega} \ln\left(\frac{\eta_b}{\eta_0}\right) \tag{2.31}$$

The ratio $\ln(\eta_b . \eta_0^{-1})$ can have the value of 12 as suggested by Dombrowski & Hoper, which agreed favorably with experimental data of the sheet breakup lengths over a range of Weber numbers from 2 to 200. The diameter of the primary ligaments is obtained from the mass balance as follows:

$$d_{ligament} = \sqrt{\frac{16 h_b}{k_s}} \tag{2.32}$$

where (k_s) is the wave number of the fastest growing surface wave, and (h_b) is the sheet half thickness at the point of breakup, calculated from:

$$h_b = \frac{h_0 (D_{hole} - t_b)}{2 L_b \sin(\theta) + D_{hole} - t_b} \tag{2.33}$$

The (h_0) is the initial half sheet thickness at the nozzle orifice, and can be approximated as:

$$h_0 \approx 0.5 \delta_0 \cos(\theta) \tag{2.34}$$

The (δ_0) is obtained from equation (2.24).The subsequent disintegration of the ligaments into drops is calculated using another stability analysis, based on an analogy to Weber's result for the growth of waves on cylindrical viscous liquid columns. The wave number of the fastest growing wave on the ligament becomes:

$$k_{ligament} = \frac{1}{d_{ligament}} \left(0.5 + \frac{3 \mu_l}{2 \sqrt{\rho_l \sigma d_{ligament}}} \right)^{-0.5} \tag{2.35}$$

As proposed by Dombrowski and Johns, it is assumed that breakup occurs if the amplitude of the wave is equal to the radius of the ligament, and that one drop is formed per wavelength. A mass balance gives the droplet diameter:

$$d_{drop}^{initial} = \sqrt[3]{\frac{3\pi d_{ligament}^{2}}{k_{ligament}}} \tag{2.36}$$

In the numerical implementation, it is assumed that the sheet does not interact with the gas phase. That is, the sheet does not experience any drag, nor undergo any breakup, collision, and/or evaporation, until its distance from the nozzle orifice is equal or greater than the breakup length as given by equation(2.31).

The above explicitly detailed starting conditions of the drops formed at the point of breakup, are used as input for the CFD calculation for the spray formation. In other words, once the drop initial diameter has been determined from equation (2.36) it is assumed that this drop is the most probable drop size, i.e. SMD, of a Rosin-Rammler distribution with a default spread parameter of 3.5 and a default dispersion angle of 6° (an assumption based on past modeling experience and used by default in ANSYS FLUENT™, but it can be modified if required). The parcels are injected as a hollow cone with a mean spay angle (θ) from the spray axis. The exact trajectory of each discrete parcel is determined by randomly distributing the spray angle over a range of ($\theta + \Delta\theta$); where ($\Delta\theta$) is the dispersion angle. From now on, the parcels will be treated subject to the aerodynamic forces, the drag forces, and the so called secondary breakup mechanism (as detailed below). Also, if applicable the collision processes/forces can be applied.

The LISA model has been successfully validated over a wide range of applications, and has proven its capability in predicting the spray behavior during the steady state phase.

As explained above, the secondary breakup mechanism is the disintegration of the already existing droplets into smaller ones, due to the aerodynamic forces that are induced by the relative velocity between the droplets and the surrounding media. The surface tension on the other hand, will try to keep the droplet spherical and counteracts the deformation forces. There are mainly four formulations used in the CFD codes to model the secondary breakup mechanisms: (a) Taylor-Analogy breakup model, known as (TAB), (b) Kelvin-Helmholtz (KH) breakup model, sometimes called the Wave model, or the Reitz & Diwakar (RD) model, (c) Rayleigh-Taylor (RT) breakup model, and (d) Combined Rayleigh-Taylor/Kelvin-Helmholtz breakup model (RT-KH).

(a) Taylor-Analogy breakup model: The TAB model was proposed by O'Rourke and Amsden, and it's based on an analogy between a forced oscillating spring mass system and an oscillating drop penetrating a gaseous media with a relative velocity (U_{rel}) see ***Figure 15***. The force (F) initiating the oscillation of the mass (m), corresponds to the aerodynamic forces deforming the droplet; and thus, making its mass oscillates. On the other hand, the restoring force of the spring $(F_{spring} = K.x)$ is analogous to the surface tension forces, which tries to keep the drop spherical and minimize its deformation. The damping force $(F_{damping} = d.\dot{x})$ corresponds to the friction forces inside the droplet, caused by its dynamic viscosity (μ_l). The governing equation of motion for a damped spring mass system is expressed as following:

$$\ddot{x} = \frac{F}{m} - \frac{k}{m}x - \frac{d}{m}\dot{x} \tag{2.37}$$

where (x) is the displacement of the mass from the idle state, and it is equivalent to displacement of the droplet's equator from its equilibrium position, as illustrated in ***Figure 15***. According to the analogy, the coefficients in equation (2.37) are to be replaced by:

$$\frac{F}{m} = c_F \frac{\rho_g U_{rel.}^2}{\rho_l r}, \frac{k}{m} = c_k \frac{\sigma}{\rho_l r^3}, \frac{d}{m} = c_d \frac{\mu_l}{\rho_l r^2} \tag{2.38}$$

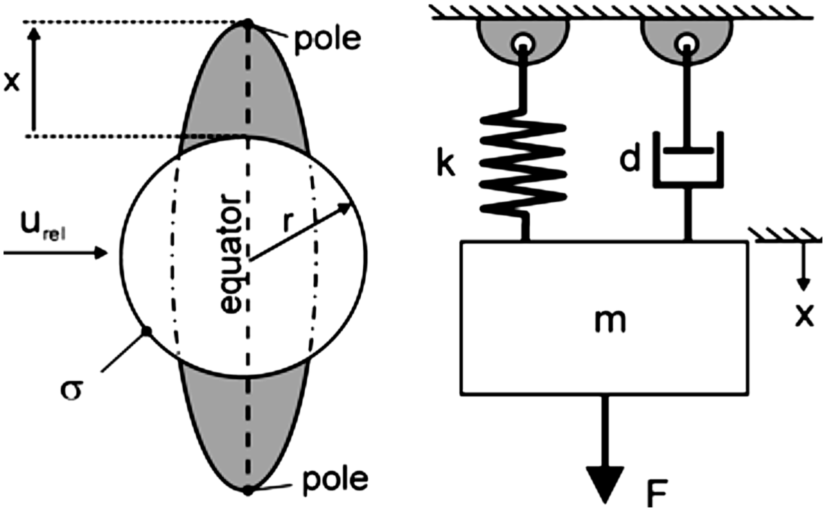

Figure 15 Taylor analogy breakup model **(Baumgarten, 2006)**

where (c_F, c_k, c_d) are the model constants. There is another parameter called the distortion parameter (y), which represents the departure of the drop from its spherical shape divided by its radius $\left(y = x.(c_b.r)^{-1} \right)$, where (c_b) is also a constant. Substituting the distortion parameter (y) and the coefficients of equation(2.38) into equation(2.37), the equation of motion becomes:

$$\ddot{y} = \frac{c_F \rho_g U_{rel.}^2}{c_d \rho_l r^2} - c_k \frac{\sigma}{\rho_l r^3} y - c_d \frac{\mu_l}{\rho_l r^2} \dot{y} \tag{2.39}$$

Assuming a constant relative velocity, which is numerically satisfied for a given time, and interval, equation(2.39) can be solved analytically:

$$\begin{aligned}
& y(t) = \frac{c_F}{c_k c_b} We_g + e^{-\frac{t}{t_d}} . \left[A \cos \omega t + \frac{1}{\omega t_d} B \sin \omega t \right] \\
& \text{where,} \\
& A = \left(y_0 - \frac{c_F}{c_k c_b} We_g \right), B = \left(y_0 t_d + \dot{y} - \frac{c_F}{c_k c_b} We_g \right) \\
& We_g = \frac{\rho_g U_{rel}^2 r}{\sigma}, \frac{1}{t_d} = \frac{c_d \mu_l}{2 \rho_l r^2}, \omega^2 = c_k \frac{\sigma}{\rho_l r^3} - \frac{1}{t_d^2} \\
& for, \\
& y_0 = y_{t=0}, \dot{y} = \left(\frac{dy}{dt} \right) \Bigg|_{t=0}
\end{aligned} \tag{2.40}$$

It's assumed that the breakup occurs if ($x \geq 0.5r$) resulting in (c_b) of 0.5 and ($y \geq 1$), also the breakup time can be determined from equation(2.40).

The Taylor-Analogy breakup provides a complete disintegration of the old drop into a number of smaller new droplets. However, this model gives no information about their numbers, and sizes. Thus, the determination of these values is estimated using the energy balance equation (kinetic energy due to the oscillation and the surface energy), that is:

$$E_{old} = \underbrace{K\frac{\pi}{5}\rho_l r^5\left(\dot{y}^2 + \omega^2 y^2\right)}_{\mathrm{I}} + \underbrace{4\pi r^2\sigma}_{\mathrm{II}} \tag{2.41}$$

where the term (I) represents the energy of oscillation (kinetic energy) and the distortion energy of the droplet before the breakup, the term (II) represents the sum of the drop minimum surface energy before breakup,($K = 3.33$) is a constant, and $(\omega^2 = 8\sigma / r_3\rho_l)$. After breakup, it is assumed that the new droplets are spherical, and will not oscillate; that is, ($y_0 = \dot{y} = 0$). This will lead to the energy balance equation of the new formed droplet:

$$E_{new} = \underbrace{4\pi r^2\sigma\frac{r}{SMR}}_{\text{New surface energy}} + \underbrace{\frac{\pi}{6}r^5\rho_l\dot{y}}_{\text{New kinetic energy}} \tag{2.42}$$

where (SMR) is the Sauter mean radius obtained from:

$$\frac{r}{SMR} = 1 + \frac{8K}{20} + \frac{\rho_l r^3}{\sigma}\dot{y}^2\left(\frac{6K-5}{120}\right) \tag{2.43}$$

Regarding the number of the product droplets, this can be obtained from the mass conservation constraint as follows:

$$N^{n+1} = N^n\left(\frac{r^n}{r^{n+1}}\right)^3 \tag{2.44}$$

The TAB model is generally known to under-predict the droplet sizes, and to underestimate the penetration, especially if combined with the Blob-method for the primary breakup modeling (Tanner et al. and Liu et al.). Moreover, one of its disadvantages is that, only one oscillation mode can be tracked; while in reality many modes exist. However, this model is simple, and does not require many inputs from the user.

(b) The wave, the RD or the KH model: The wave breakup model takes in account the unstable growth of the Kelvin-Helmholtz (KH) waves at the liquid-gas interface due to the so called KH instabilities. It is well known that the KH instability occurs when there is an intense shear motion of two fluids flowing alongside each other. Significant contributions for the development of this model have been made by Reitz and Diwakar. Their model is based on a first order linear analysis of KH instability, growing on the surface of a cylindrical liquid jet with an initial diameter ($2a$) that is penetrating into a stationary incompressible, in-viscid gas, with a relative velocity (U_{rel}). Furthermore, it assumes that due to the turbulence generated inside the nozzle hole, the jet surface is covered with a spectrum of sinusoidal surface waves with an infinitesimal axisymmetric displacement ($\eta = \eta_0 \exp(\Omega t)$). These waves will cause small axisymmetric fluctuating pressures, as well as, axial and radial velocities components in both liquid and gas phases, as shown in ***Figure 16***.

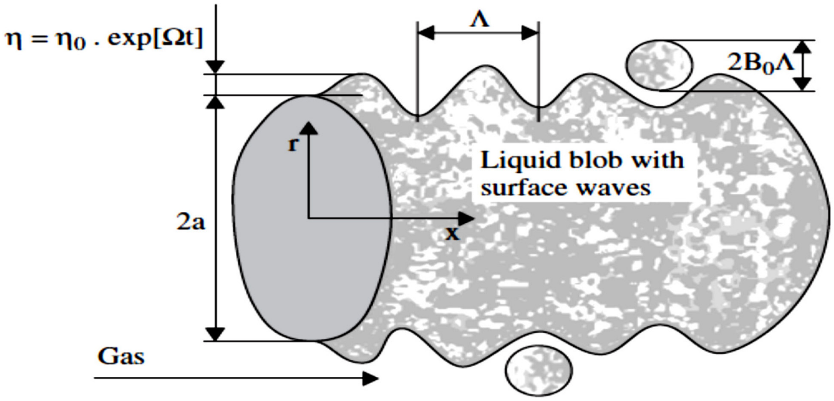

Figure 16 Schematic growth of surface perturbations in the wave breakup model (modified from Rietz and Diwakar, 1987). (Kuo & Acharya, 2012)

Their analysis yields an equation for the dispersion, relating the growth rate of the perturbation (ω) (can be seen as the increase of the amplitude per unit time) to its wavelength ($\lambda = 2\pi . k^{-1}$). The numerical solution of the function for dispersion shows the growth rate (Ω) of the fastest growing (the most unstable surface wave) as following:

$$\Omega\left[\frac{\rho_l a^3}{\sigma}\right]=\frac{0.34+0.38We_g^{1.5}}{(1+Z)+(1+1.4T_{Taylor}^{0.6})},$$

where, (2.45)

$$Z=\frac{\sqrt{We_l}}{\mathrm{Re}_l},We_g=\frac{\rho_g aU_{rel}^2}{\sigma},We_l=\frac{\rho_l aU_{rel}^2}{\sigma},\mathrm{T}_{Taylor}=Z\sqrt{We_g}$$

and (T_{Taylor}) is called the Taylor parameter .The corresponding wavelength (Λ) to this fastest growth rate is expressed as :

$$\frac{\Lambda}{a}=9.02\frac{(1+0.45Z^{0.5})(1+0.4T_{Taylor}^{0.7})}{(1+0.865We_g^{1.67})^{0.6}} \tag{2.46}$$

Reitz applied this theory to the breakup modeling of liquid droplets with a radius (r). Again, waves grow on the droplet surface with a growth rate and a wavelength (Ω), (Λ), respectively. Because the new child drops are formed from the surface waves that are sheared off the parent drops, it is assumed that the size of the new droplets is proportional to the wavelength (Λ) as shown in ***Figure 16***. The (r_{new}) can be expressed as:

$$r_{new}=B_0\Lambda \tag{2.47}$$

where (B_0 = 0.61) is a constant. A new parcel containing newly produced drops with the size (r_{new}) is created and added to the calculations. In contrast to the TAB model, the parent drop does not perform a complete breakup, but continuously loses mass while penetrating into the gas. This result in a shrinking radius, whose rate of reduction at a certain time will depend on, the difference between the actual value of the parent droplet radius (r), the child droplet radius (r_{new}), and a characteristic time span, usually the breakup time (τ_{bu}), calculated as following:

$$\frac{dr}{dt}=-\frac{r-r_{new}}{\tau_{bu}},$$

$$\tau_{bu}=3.788.B_1\frac{r}{\Lambda\Omega} \tag{2.48}$$

(B_1) is an adjustable model constant, it accounts for the influence of the nozzle hole flow effects such as turbulence level, and nozzle design. (B_1) can take any value between 1.73 and 60. A higher value of (B_1) leads to a longer (τ_{bu}), which means reduction of the breakup process, because the parent droplet will require more time to lose a certain amount of mass. However, it also means an increment in the penetration of the droplets. On the other hand, smaller values of (B_1) will results in an increment of the spray disintegration, leading to a faster fuel-to air mixing, and certainly reduction in the penetration. Liu et al. have recommended a value of 1.73 for the (B_1).The number and the size of the new child droplet per time step, can be calculated from the decrease in the parent drop radius using equation(2.48). The new child droplets become parent drops in a new parcel, and are subject to further breakup. The KH model predicts a bimodal size distribution, consisting of a small number of big parent drops having the radius which is slowly shrinking, and an increasing number of small child droplets. This procedure can be unrealistic in the presence of a sudden disintegration, commonly seen in the vicinity of the injector nozzle. During a sudden disintegration the complete drop is shredded into droplets with diameter much bigger than the child droplets predicted by the KH model. For this reason, the KH model is usually combined with the Rayleigh-Taylor.

(c) The Rayleigh-Taylor (RT) model: This model is based on the theoretical work of Taylor, who investigated the instability at the interface between two fluids of different densities, under both acceleration and deceleration cases. If the two fluids are liquid and gas, the interface is stable when the acceleration is directed into the liquid. The instable disturbances can grow, if the acceleration is directed into the gas. Regarding the situation where the droplet and the gas are moving with a relative velocity (U_{rel}), the deceleration of the drop (in the forward direction) caused by the drag forces can also be treated as an acceleration of the drop in the direction of the airflow (backward direction). Thus, instable waves can grow on the back side of the drop, see ***Figure 17***.

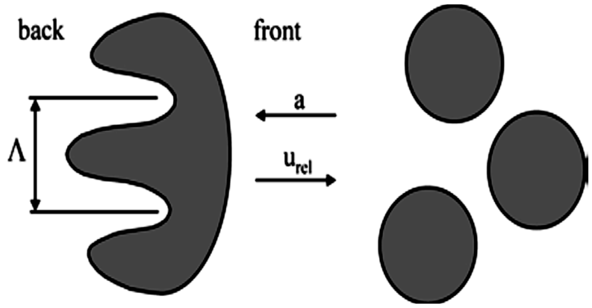

Figure 17 Schematic of the Rayleigh-Taylor instability on a liquid drop **(Baumgarten, 2006)**

At very high air velocities, the drop undergoes intense deceleration due to the drag forces, these conditions favor the development of RT instabilities, leading to the drop disintegration, which can arise if the fluid acceleration has an opposite direction to the density gradient (Kuo & Acharya, 2012). The aerodynamic drag force is given by,

$$F_{drag} = \pi r^2 C_D \frac{\rho_g U_{rel.}^2}{2} \tag{2.49}$$

Dividing the drag force by the mass of the drop, the acceleration of the drop can be found as,

$$a_{cc} = \frac{3}{8} C_D \frac{\rho_g U_{rel.}^2}{\rho_l r} \tag{2.50}$$

Using a linear stability analysis, growth rate and wavelength (Ω), (Λ), respectively of the fastest growing wave are:

$$\begin{aligned} \Omega &= \sqrt{\frac{2\left[a_{cc}(\rho_l - \rho_g\right]^{3/2}}{3\sqrt{3\sigma}(\rho_l + \rho)}}, \\ \Lambda &= C_{RT} 2\pi \sqrt{\frac{3\sigma}{a_{cc}(\rho_l - \rho_g)}} \end{aligned} \tag{2.51}$$

where the (C_{RT}) is an adjustable constant, introduced to allow the modification, if necessary, of the effective wavelength. Similar to the constant (B_1) in the (KH) model, the (C_{RT}) includes the unknown effects, of the initial conditions on the secondary breakup model. These effects arise from turbulence, and/or cavitation inside the nozzle hole. (C_{RT}) can have a value between 1 and 5.33, and it affects both the size of the new produced droplets, and the likelihood of breakup events. By increasing the (C_{RT}), the breakup is reduced and the size of the new droplets is increased, since it is related to the (C_{RT}) through the following equation:

$$r_{new,child} = \pi C_{RT} \left(\frac{a_{cc}(\rho_l - \rho_g)}{3\sigma} \right)^{-0.5} \qquad (2.52)$$

The breakup time is assumed to be reciprocal to the frequency of the fastest growing wave, i.e. $\tau_{bu} = \Omega^{-1}$. At a time = τ_{bu}, the drop disintegrates completely into small droplets, whose radius can be obtained from equation(2.52), and is assumed to be proportional to the wavelength. The drop is only allowed to break up if (Λ) is smaller than its diameter.

The drag-deceleration induced RT breakup provides an effective and rapid disintegration, only near the nozzle, where the very high relative velocities between drop and gas result in a strong deceleration. Further downstream, the shear flow induced KH breakup becomes the dominant process. For that, the RT model is always used in combination with a second breakup model, usually the KH model.

(d) Combined RT-KH model: As detailed above, neither the RT nor the KH alone are capable of modeling the secondary breakup mechanism. The experimental investigations of Hwang et al. revealed that the breakup mechanism in the catastrophic breakup regime consists of a series of characteristic processes. The aerodynamic force on the drop flattens its surface to the shape of a liquid sheet, causing the decelerating sheet to breakup into large-scale fragments by means of RT instability. This process is followed by the KH waves with a much shorter wavelength originated at the edges of the fragments, which will breakup these fragments to micrometer-size drops as illustrated in ***Figure 18***.

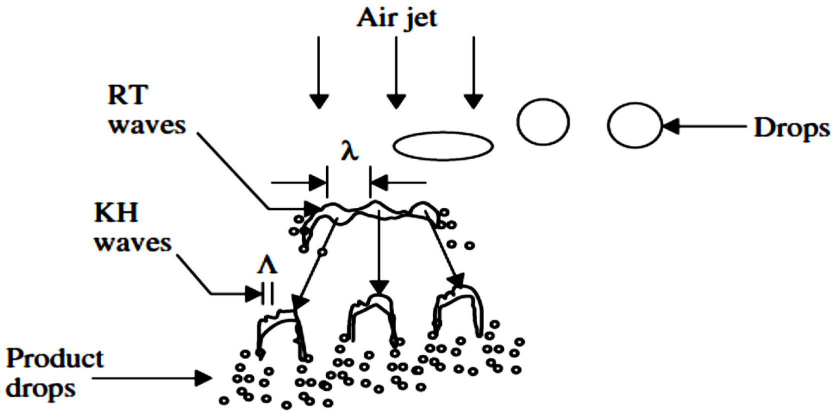

Figure 18 Schematic diagram of breakup mechanism in catastrophic breakup regime involving both (RT) and (KH) waves (modified from Hwang, Liu, and Reitz, 1996) (Kuo & Acharya, 2012)

Because a single breakup model usually will not able to describe all relevant classes of the breakup processes, i.e. from primary to secondary breakup, the use of combined models is necessary. This combination contains of at least two different breakup models, and it is becoming more and more popular; since this approach improve the accuracy of the prediction. The most popular combinations of models found are: (a) The Blob-RT/KH model, (b) The LISA-TAB model, (c) LISA-DDB, and many other different hybrid models, a detailed review on these models can be found in (Baumgarten, 2006). However, the following sub-section will address the hybrid Blob-RT/KH model only, because it is the most popular among the hybrid models family, and it has been successfully validated against experimental data.

When the blob-method is integrated to inject initial drops into the numerical grid, two secondary breakup models are required. The first one, describes the relevant processes of the spray disintegration near the nozzle (part of the primary breakup mechanism that is not been correctly described by the blob-method), and the second one is responsible for the remaining spray region. Both models are allowed to produce unstable waves simultaneously. They are activated once a certain distance from the nozzle is being reached, called the breakup length (L_b). In the dense fragmented core region, typically observed near the nozzle, only the (KH) stripping breakup is allowed to occur. The introduction of such parameters as L_b, along with B_1, and C_{RT}, allow a high flexibility and control on the overall breakup process; since they can be adjusted to reflect the physical model requirements. The breakup length is calculated through the following relation:

$$L_b = C.D_{nozzle}\sqrt{\frac{\rho_l}{\rho_g}} \tag{2.53}$$

where (C) is a constant representing the influence of the nozzle, and can have a value between 3.3 to 15.8. Outside the dense liquid core, both KH and RT effects are calculated, and both are considered for breakup. Typically, the RT instability grows faster when droplet acceleration is high, and its effect dominates for high Weber number sprays (ANSYS, 2011). Compared to the use of a single the KH model, the combined model offers a faster disintegration of big drops, an increment in the evaporation, and a reduction of the spray penetration. Another advantage of the combined RT-KH model is that, the RT model damps the formation of the strong bimodal droplet size distribution, since the RT breakup gives a reasonable number of equally sized droplets. A combined model is thus beneficial, because it can cover a wide range of spray operation, compared to a single model. For example, the TAB breakup model is limited to the low Weber number regimes; whereas, the Wave to the high ones. Using a combined model such as the RT-KH can thus give the opportunity to deal with the moderate to high Weber numbers.

2.5. Spray evaporation modeling

Many numerical models exist for the vaporization process, as well as, the burning process of the droplet. These models are mainly based on empirical results from single isolated droplets, which can be modified to include the effects of neighbouring droplets, convection, radiation, and multicomponent fuels. An exhaustive review for the theoretical models of droplet evaporation can be found in (Sazhin, 2006), and in classical textbooks such as (Sirignano, 1999), and (Kuo, 2005).

As a first step towards the understanding of the evaporation process in a spray, the isolated droplet approach represents the ideal model of the physical phenomena. From there the effects of convection, high pressure and temperature, as well as radiation can be included. Studies on droplet evaporation in convective streams can be found in (Marshall, 1952), (Maqua, Castanet, & Grish, 2008), (Wong & Yang, 2002), and (Kristyadi & Lemoine, 2010)), effects of the multicomponent nature of the fuel is reported by (Ghassemi & Khan, 2006), and extensive studies for high pressure and temperature effects can be found in (Morin & Dagat, 2004), (Latlosz & Leipziger, 1972), (Kadota & Hiroyasu, 1976)).

Following (Sirignano, 1999), models of droplet-vaporization can be classified into the following six groups, with increasing complexity:

- Constant-droplet temperature model: The droplet surface temperature is uniform, i.e. no temperature gradient inside the droplet, and does not change with time. This theory yields the famous d^2-law, which is implemented in FLUENT code.
- Infinite liquid conductivity model: The droplet surface temperature is uniform, but time-varying droplet temperature is considered.
- Spherically symmetric transient droplet heating model: This model takes into account finite liquid thermal conductivity, but not the recirculation inside the droplets. It is a conduction limit model.
- Effective-conductivity model: This model takes into account both the finite liquid thermal conductivity and the recirculation inside the droplet.
- Vortex model for droplet heating model: This model describes the recirculation inside the droplet in terms of vortex dynamic.

- Navier-Stokes solution model: This model provides full exact solution of the Navier-Stokes equations inside the droplet and in the gaseous flow, and can be considered as the most sophisticated.

Most models assume the diffusion in the gas phase from and to the droplet to be spherically symmetric. This assumption takes root from the Spalding model, which can be considered as the first, and the simplest theoretical model for problems with droplet evaporation. The spherically symmetric assumption, can take into account the convection effect through the Frössling correlations based on Sherwood and Nusselt numbers. Other assumptions, include the effect of convection taking into account the presence of a film around the droplet, introducing correction factors to the spherically symmetric model like the Abramzon & Sirignano model, while a third group proposed a model which solves the flow completely around the droplet (Sirignano, 1999). This last option is computationally very expensive.

In addition, transport properties are often considered constant between the droplet surface and the infinity. Miller et al. showed that the heat and mass fluxes to the droplet strongly depend on the evaluation of the transport, and thermodynamic properties of both the gas and the liquid phases (Sanchez, 2012).

To model the temperature distribution inside the droplet; and thus, the diffusion in the liquid phase, multiple options exist. The simplest models neglect the heat diffusion inside the droplet, and suppose constant droplet temperature, assuming that all the heat arriving to the surface is employed for the vaporization process. Other models, have considered constant droplet temperature but varying with time like Sazhin el al. model. Sazhin's model supposed that the droplet temperature follows a polynomial profile. More complex models solve the heat equation inside the droplet, and suppose a Hill's vortex flow type inside the droplet. These fully developed models are capable of solving the complete set of equations inside the droplet, like Rangel & Sirignano model. A comparison of the effects of each of these models can be found in (Abramzon & Sirignano, 1989).

In the following section, we will recall the equation used in the evaporation model from Spalding, with modification implemented by Ranz and Marshall to account for the convection effects, and introduce the adjustments proposed by Abramzon and Sirignano into this evaporation model (Sanchez, 2012). The purpose of this practice is thus to give a global idea about the procedure for calculating the droplet evaporation problem.

Spalding initial classical approach treated a single fuel droplet in a quiescent (non-convective) atmosphere, at a given pressure and temperature. A quasi-steady assumption is utilized to determine the distributions of fuel vapor mass fraction, and temperature around the evaporating spherical droplet. The main advantage of this assumption is to temporarily avoid the consideration of time variations associated with the droplet regression process (Kuo, 2005).

With the assumption of quasi-steady burning, the mass exchange through the droplet surface may be represented by the fuel mass flux leaving the droplet surface. This also follows that the mass flow rate can be considered constant:

$$\dot{m} = \dot{m}_f = 4\pi\rho_g u r_p^2\Big|_s = const. \tag{2.54}$$

where the subscript (*s*) is used to designate the position just above the droplet surface, and (r_p) is the droplet radius at the surface. We obtain the droplet radius history, by writing the temporal evolution of the total mass of the droplet ($\dot{m}_d$); which states that the rate at which the mass of the droplet decreases is equal to the rate at which the liquid is vaporized as following:

$$\frac{dm_d}{dt} = -\dot{m}_p \tag{2.55}$$

As the mass released from the droplet due to the evaporation is totally converted into the gaseous phase, a simple relationship between ($\dot{m}_p$) and ($\dot{m}_f$) can be formulated as:

$$\dot{m}_f = -\dot{m}_p \tag{2.56}$$

Spalding proposed the following expression for the calculation of the droplet mass released (as stated above details of his classical model, assumption, derivations can be found in (Kuo, 2005), and (Sirignano, 1999):

$$\dot{m}_p = -\pi d_p Sh \rho_g D_s \ln(1 + B_M) \tag{2.57}$$

where (D_s) is the diffusion coefficient of the fuel species in the mixture, (Sh) is the Sherwood number which is a dimensionless number that represents the ratio of convective to diffusive mass transport, and (B_M) is the so-called Spalding number, given by :

$$B_M = \frac{Y_{F,S} - Y_{F,\infty}}{1 - Y_{F,S}} \qquad (2.58)$$

where ($Y_{F,S}$) and ($Y_{F,\infty}$) are the mass fractions of the evaporated fuel in the film surrounding the droplet surface and at the far field, respectively. In order to calculate the mass flow rate from equation(2.57) , the value of (B_M) must be evaluated, but before that, the mass fractions must be determined. Fuel vapor mass fraction at the droplet surface is deduced from the Clausius-Clapeyron law:

$$p_{F,s} = p_{F,ref} \exp\left(\frac{\triangle h_v}{R} \left(\frac{1}{T_{s,ref}} - \frac{1}{T_s} \right) \right) \qquad (2.59)$$

where the subscript (*ref.*) designates an arbitrary reference point/state at the saturation curve of the fuel, (R) is the universal gas constant, and ($\triangle h_v$) is the latent heat of vaporization of the liquid fuel. The partial vapor pressure ($p_{F,s}$) is related to the molar fraction through Dalton’s law, which in return, is related to the mass fraction. The Sherwood number is set to two under the assumption of evaporation in quiescent media for the non-convective case.

When the convective effects are to be taken into account, Ranz & Marshall proposed a modification on the originally derived correlation of Frössling. Their correlation is based on the particle Reynolds number, Schmidt number, and the Nusselt number, which represents the ratio between convective to conductive heat transfer normal to the boundary. Moreover, in consistence with the assumption of the unity Lewis number, the Sherwood number is to be assumed equal to the Nusselt number (R.Turns, 2000) :

$$Le = Sc = \mathrm{Pr} = 1 \text{, leading to } Sh = Nu = 2 + 0.55\,\mathrm{Re}_p^{1/2}\,\mathrm{Pr}^{1/3} \qquad (2.60)$$

The Spalding model for evaporation does not take into account the existence of a vapor film surrounding the droplet. In other words, it does not consider the finite thickness of the thermal and mass boundary layers around the droplet (Sanchez, 2012).

To solve this problem, Abramzon & Sirignano have modified the Sherwood and Nusselt numbers as follows:

$$\begin{aligned} Sh &= 2 + 0.55\frac{\mathrm{Re}_p^{1/2}\,Sc_F^{1/3}}{F(B_M)} \\ Nu &= 2 + 0.55\frac{\mathrm{Re}_p^{1/2}\,\mathrm{Pr}_F^{1/3}}{F(B_T)} \\ &where, \\ F(B) &= (1+B)^{0.7}\,\frac{\ln(1+B)}{B} \end{aligned} \tag{2.61}$$

Note that the parameter (B) refers to (B_M) when assigned to the Sherwood number, and to (B_T) for the Nusselt number. The relation between (B_M) and (B_T) can be expressed as follows:

$$B_T = (1 + B_M)^{\beta} - 1 \tag{2.62}$$

where (β) is a dimensionless parameter expressed as:

$$\beta = \frac{C_{p_{F,ref}}}{C_{p_{g,ref}}}\frac{Sh}{Nu}\frac{\mathrm{Pr}}{Sc} \tag{2.63}$$

where ($C_{p_{F,ref}}$) and ($C_{p_{F,ref}}$) are the heat capacities at constant pressure of the gaseous fuel and the gaseous mixture in the film around the droplet, respectively. They are evaluated at the reference state (explained above).

The composition and the temperature of the mixture film are evaluated by interpolating their values between the droplet surface and the far field denoted by the subscripts (s and ∞, respectively). This is performed using the so-called third law (Sanchez, 2012). This law assumes that the properties of the gaseous mixture in the film around the droplet are in a quasi-stationary evolution, and can be expressed as following:

$$T_{ref} = T_s + \frac{1}{3}(T_\infty - T_s)\text{, and } Y_{i,ref} = Y_{i,s} + \frac{1}{3}(Y_{i,\infty} - Y_{i,s}) \tag{2.64}$$

Sazhin et al. (Sazhin, 2006) showed that the Abramzon-Sirignano model (AS) can predict larger evaporation times compared to the classical Spalding model under the same operating conditions. They have demonstrated that, the evaporation rate decreases when considering a finite thickness of thermal and mass boundary layers surrounding the droplet, instead of considering it as infinitely thin, i.e. the Spalding assumption.

2.6. Drag Coefficient modeling (C_D)

Droplet drag coefficient is a crucial parameter for the equation of the droplet dynamic motions, since the momentum exchange between the droplet and the gaseous phase is governed by the drag law. Spalding remarked that the existence of the flame around and in the wake of the droplet tends to decrease the drag force (Rochaya, 2007). Yuen and Chen (1976) found that the droplet drag coefficient is close to that of a solid sphere, if the same diameter is used. Renksizbulut and Yuen (1983) concluded that the Stefan convective effects manifested in the presence of evaporation reduces the drag coefficient by a factor of $(1+B_M)$. Dwyer et al. showed clearly the effect of the vaporization on the droplet, and the concluded that the vaporization reduces the drag coefficient as shown in ***Figure 19*** (Dwyer & Sanders, 1984).

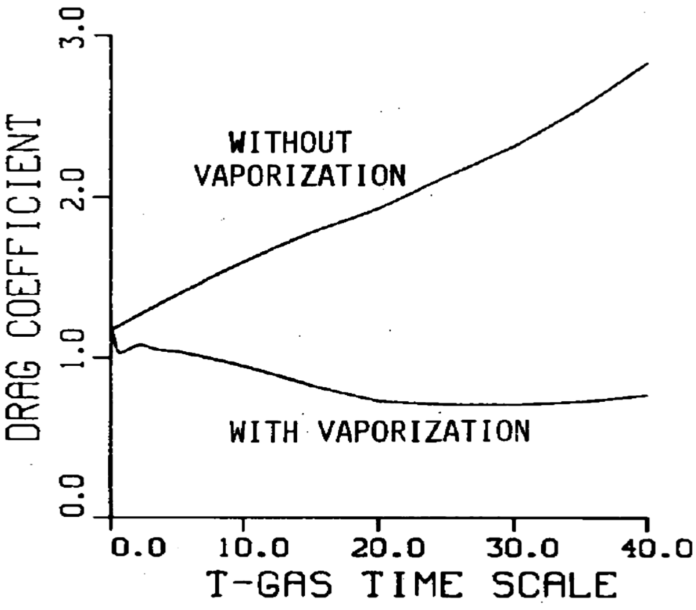

Figure 19 Drag coef. variation **(Dwyer & Sanders, 1984)**

In general, the drag coefficient of a flow around an accelerating particle is expressed as a function of Reynolds number. For low Reynolds numbers, it follows:

$$C_D = \frac{24}{\mathrm{Re}_{dp}} \text{ , and } \mathrm{Re}_{dp} = \frac{\rho v_{rel} d_p}{\mu} \tag{2.65}$$

The standard drag coefficient for solid spheres is usually employed in the calculations of diluted spays (Kuo & Acharya, 2012). Amelioration to the above C_D relation is proposed by Putnam (1961), which covers both low and high Reynolds regimes, as following:

$$C_D = \begin{cases} \dfrac{24}{\mathrm{Re}_{dp}}\left[1 + \dfrac{\mathrm{Re}_{dp}^{2/3}}{6}\right] & for\,\mathrm{Re}_{dp} \leq 1000 \\ 0.44\, for\,\mathrm{Re}_{dp} \geq 1000 \end{cases} \tag{2.66}$$

Liu et al. (1993) modified the above expression to yield very similar results, except for a slight change for the C_D, that is: ($C_D = 0.424\, for\, \mathrm{Re}_{dp} \geq 1000$). Their expression is the most used in the current CFD codes (Rochaya, 2007). The above assumption states that the droplet will remain spherical throughout its trajectory in the domain. However, for an initially spherical droplet that moves across a gas stream, the droplet shape is significantly distorted, especially at high Weber number. In the extreme case, the droplet shape deforms, and approaches to that of a disk. The drag of a disk is significantly higher than that of a sphere. Consequently, the drag coefficient should not be only a function of its Reynolds number as accounted for in equation(2.66), but also to its oscillation amplitude. Based on these observations, Liu et al. use the TAB model ***Figure 20***, in order to predict the droplet distortion (y), and then, they modified the drag coefficient by relating it empirically to the magnitude of the drop deformation. Since the drag coefficient of a distorting drop should lie between that of a solid sphere, equation (2.66) (lower limit), and that of a disk, which is about 3.6 times higher (upper limit), a simple linear expression is used for the dynamic drag coefficient (Baumgarten, 2006):

$$C_D = C_{D,sphere}(1 + 2.632y) \tag{2.67}$$

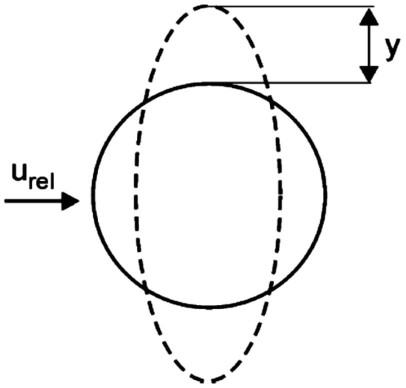

Figure 20 schematic of drop distortion **(Baumgarten, 2006)**

The above equation(2.67) is known as the dynamic drag formulation, it satisfies the drag coefficient of a spherical and a disk droplet from the un-deformed ($y = 0$) to the fully deformed limits ($y = 1$).

The consideration of dynamic drag results in an increase of the overall drag coefficients for large Weber regimes, since the effects of the droplet distortion are integrated into the drag coefficient equation. Also, the dynamic drag formulation leads to a more realistic calculation for the droplet deceleration, since the increment in the droplet deceleration yields a reduction of the penetration of larger droplets. Physically this is true, and it is due to the shorter time span between the gas and the liquid at high relative velocity. The dynamic drag law is thus, more representative to the physical aspect, as it accounts for the variation of the drag coefficient due to the droplet shape changes.

It must be pointed out that the TAB model will be used for the calculation of drop distortion (y) as shown in equation(2.39), regardless of the choice of the breakup model, and it does not influence the breakup modeling process. If, for example, the Wave model or the combined KH-RT is used in order to predict the droplet breakup, the value of (y) will be obtained from the formulation of the TAB model only during the calculation of the (C_D), and will not interfere with the calculations of the droplet breakup.

2.7. Combustion and Turbulent reacting flows

Flames can be classified in different ways, but probably the most common classification is the one based on how the reactants are supplied to the reaction zone. Depending on how fuel and oxidizer are brought into contact in the combustion system, different combustion modes or regimes can be identified. Traditionally, three regimes have been recognized: (a) Non-premixed, (b) Premixed, and (c) Partially-premixed combustion. These regimes exist either in the laminar or the turbulent form, depending on the flow configuration, and the area of application.

(a) Non-premixed combustion: Whether the flow is laminar or turbulent, in this regime the fuel and oxidizer enter the reaction zone separately. Reacting species have to reach, by molecular diffusion, the flame front before reaction. Hence, non-premixed flames are also called diffusion flames (Poinsot & Veynante, 2005). This type of combustion is also called diffusion, because the characteristic timescales of the diffusion processes are usually larger than those of the chemical processes, and thus, the velocity of the overall phenomena is mainly controlled by the species diffusion. The fact that the characteristic chemical time is smaller than the characteristic diffusion time makes the chemical reaction occur in a very narrow region between the fuel and the oxidizer (Peters, 2000). This kind of combustion is relatively stable, and safe, because the contact between the fuel and oxidizer can be controlled; hence, these flames do not strictly exhibit propagation speeds like premixed flames and can rarely flashback or auto-ignite in undesired locations. For these reasons non-premixed combustion is still applied widely in several of combustion devices.

(b) Premixed combustion: Opposite to the non-premixed flames, in the premixed combustion, fuel and oxidizer are already mixed, and are inside the flammability limits, before they reach to the flame front. Here the determining step becomes the rate of chemical reactions that is characterised by measuring the flame propagation speed, which spreads through heat and radical diffusion in the unburned mixture.

(c) Partially-premixed combustion: Partial premixed combustion occurs when fuel and oxidizer are mixed together outside the flammability limits, before entering the reaction zone. Partial premixing may occur, voluntarily or involuntarily, from the fresh flow mixing before ignition. It can also occur from the local quenching of highly turbulent flames, or in the recirculation zones of non-premixed combustors. In combustion applications, partial premixing can be used as a strategy to avoid the drawbacks, and retain the advantages, of the two combustion modes mentioned above.

Turbulent non-premixed combustion is an important theme, and the literature in this area is huge. Here, the focus is on the modeling approaches of turbulent diffusion flames, precisely the flamelet modeling technique. An explanation of other theoretical models is also offered in a summarily fashion. Turbulent reacting flows involve a wide range of different processes, which can be grouped in four categories: thermodynamics, chemical kinetics, fluid mechanics, and transport processes (Poinsot & Veynante, 2005). The laws, and equations, governing these phenomena in the turbulent combustion regime will be reviewed briefly in the coming sub-sections. In this way, the instantaneous set of Navier-Stokes equations for reacting flows is presented, along with, a review of the common turbulent combustion models used in the CFD codes.

2.7.1. Fundamental variables for reacting flows

To begin, some useful concepts used to characterize the composition of the mixture in reacting flows must be introduced, for the clarity of the offered material. These are: the mass fraction, the mole fraction, the equivalence ratio, and the mixture fraction.

(a) The mass fraction (Y_k) of the (k^{th}) species is defined as :

$$Y_k = \frac{m_k}{m_{total}} \text{ , and } \Sigma_{k=1}^{N} Y_k = 1 \tag{2.68}$$

where (m_k) is the mass of the (k^{th}) species , (m_{total}) is the total mass of species in the mixture, and (N) is the number of the different species in the mixture.

(b) The mole fraction (X_k) is defined as :

$$X_k = \frac{n_k}{n_{total}} \text{, and } \Sigma_{k=1}^{N} X_k = 1 \tag{2.69}$$

where (n_k) is the number of moles of the (k^{th}) species.

(c) In combustion, it is very useful to define the so-called stoichiometric ratio, which is the amount of oxidizer just needed to completely burn a defined quantity of fuel. If for example more than the stoichiometric quantity of oxidizer is supplied, the mixture is said to be lean, while the opposite indicates a rich mixture. For a hydrocarbon fuel given by (C_xH_y) without dissociation, the stoichiometric relation can be expressed as:

$$\begin{aligned}&C_xH_y + a(O_2 + 3.76N_2) \rightarrow xCO_2 + (y/2)H_2O + 3.76aN_2\\ &where,\\ &a = x + \frac{y}{4}\end{aligned} \tag{2.70}$$

The stoichiometric air-fuel ratio can be written as:

$$({}^{A}\!/\!{}_{F})_{stoic} = \left(\frac{m_{air}}{m_{fuel}}\right) = \left(\frac{4.76aMw_{air}}{1.Mw_{fuel}}\right) \tag{2.71}$$

where (Mw_{air}) and (Mw_{fuel}) are the molecular weights of the air and the fuel, respectively. This brings us to introduce the equivalence ratio, which relates the mass fraction of reactants to their mass fraction at the stoichiometric conditions. Through this ratio, the fuel-oxidizer mixture can be quantitatively classified as rich, lean, or stoichiometric. The equivalence ratio is defined as:

$$\phi = \frac{(Y_{air}/Y_F)_{stoi}}{(Y_{air}/Y_F)_{real}} = \frac{(A/F)_{stoi}}{(A/F)_{real}} = \frac{(m_{air}/m_{fuel})_{stoi}}{(m_{air}/m_{fuel})_{operating,condition}} \tag{2.72}$$

And thus, the mixture is called lean, if (0< ϕ <1), rich if (1< ϕ <∞), and stoichiometric if (ϕ =1).

(d) The mixture fraction (*Z*): Diffusion flames constitute a specific class of combustion problems, where fuel and oxidizer are not mixed before they enter the combustion chamber. For these flames, mixing must bring reactants into the reaction zone fast enough for combustion to proceed (Poinsot & Veynante, 2005). Thus, the proper description of the mixing process is a key aspect in non-premixed combustion. (*Z*) is a conserved scalar that accounts for the level of mixing between the oxidizer and the fuel, and changes because of diffusion and convection, but not reaction. It can be thought of as an equivalent to the equivalence ratio. Introducing this parameter will save us from solving transport equations for individual species; instead, species concentrations are derived from the predicted mixture fraction distribution in the domain. This is achieved through the solution of a conservative equation for the mean mixture fraction, and its variance. This is called the conserved scalar approach, various definitions of this approach, and method to calculate it can be found in (R.W.Bilger, 1980). Here, we will follow the definition according to Poinsot (Poinsot & Veynante, 2005).

Consider a global reaction that involves fuel (F), oxidizer (O) and products (P):

$$\nu_F F + \nu_O O \rightleftharpoons \nu_P P \tag{2.73}$$

where (ν_F, ν_O, ν_P) are called the stoichiometric coefficients, the mass fraction (Y_k) of each species in (F , O and P) follows a balance equation given by:

$$\frac{\partial \rho Y_k}{\partial t} + \frac{\partial}{\partial x_i}(\rho u_i Y_k) = \frac{\partial}{\partial x_i}\left(\rho D_k \frac{\partial Y_k}{\partial x_i}\right) + \dot{\omega}_k \tag{2.74}$$

where ($\dot{\omega}_k$) is the species reaction rate, (D_k) is the diffusion coefficient of each species. The reaction rate is related to a single step reaction rate (RR) through:

$$\dot{\omega}_F = Mw_k \nu_k RR \tag{2.75}$$

where ($\dot{\omega}_F$) is the fuel reaction rate. Also, the oxidizer reaction rate is linked to the fuel reaction rate through:

$$\begin{aligned} &\dot{\omega}_O = s\dot{\omega}_F \\ &with, \\ &s = \frac{\nu_O Mw_O}{\nu_F Mw_F} = \left(\frac{Y_O}{Y_F}\right)_{stoi.} \end{aligned} \tag{2.76}$$

where (s) is the mass stoichiometric ratio. The adiabatic flame temperature is also linked the fuel reaction rate through:

$$\dot{\omega}_T = -Q\dot{\omega}_F \tag{2.77}$$

where (Q) is the heat release per unit mass from the complete combustion of 1 kg of fuel. Using these relations, i.e. equations (2.75), (2.76) and (2.77), the equations of conservation for fuel, oxidizer, and temperature under the assumption of unity Lewis number ($Le = \lambda/\rho C_p D = 1$) become:

$$\begin{aligned}
\frac{\partial \rho Y_F}{\partial t} + \frac{\partial}{\partial x_i}(\rho u_i Y_F) &= \frac{\partial}{\partial x_i}\left(\rho D \frac{\partial Y_F}{\partial x_i}\right) + \dot{\omega}_F \\
\frac{\partial \rho Y_O}{\partial t} + \frac{\partial}{\partial x_i}(\rho u_i Y_O) &= \frac{\partial}{\partial x_i}\left(\rho D \frac{\partial Y_O}{\partial x_i}\right) + s\dot{\omega}_F \\
\frac{\partial \rho T}{\partial t} + \frac{\partial}{\partial x_i}(\rho u_i T) &= \frac{\partial}{\partial x_i}\left(\frac{\lambda}{C_p}\frac{\partial T}{\partial x_i}\right) - \frac{\dot{Q}}{C_p}\dot{\omega}_F
\end{aligned} \tag{2.78}$$

Combining these conservative equations two by two is then possible to get the three following quantities:

$$Z_1 = sY_F - Y_O, Z_2 = \frac{C_p T}{Q} + Y_F \text{, and } Z_3 = s\frac{C_p T}{Q} + Y_O \tag{2.79}$$

These quantities follow the same balanced equation(2.74), but without a source term, since (Z) as defined is a conserved scalar, i.e. passive scalar that changes because of diffusion and convection but not reaction, that can be summarized with:

$$\frac{\partial \rho Z}{\partial t} + \frac{\partial}{\partial x_i}(\rho u_i Z) = \frac{\partial}{\partial x_i}\left(\rho D \frac{\partial Z}{\partial x_i}\right) \tag{2.80}$$

The three passive variables (Z_1, Z_2, and Z_3) follow the same balanced equation, with boundary conditions summarized in ***Table 2*** as following:

Table 2 Boundary conditions for the passive scalars

Passive scalar (Z)	Fuel value Z_i^F	Oxidizer value Z_i^O
Z_1	sY_F^O	$-Y_O^O$
Z_2	$\frac{C_p T_F^O}{Q} + Y_F^O$	$\frac{C_p T_O^O}{Q}$
Z_3	$s\frac{C_p T_F^O}{Q}$	$\frac{C_p T_O^O}{Q} + Y_o^O$

where (Y_F^O) and (Y_O^O) are fuel and oxidizer mass fractions in pure fuel or oxidizers stream, respectively, and (T_F^O) and (T_O^O) denote the corresponding temperatures. The normalized passive variable (Z_i), which follows also the same convective/diffusion balanced equation is defined as:

$$Z_i = \frac{Z_i - Z_i^O}{Z_i^F - Z_i^O}, \text{ for i = } 1, 2, 3 \tag{2.81}$$

These equations are developed under the assumption of constant, equal (C_p), pressure is constant, and the heat transfer due to the radiation is neglected. Imposing the same boundary conditions for (Z_i), leads to: (Z_i) = 1 in the pure fuel stream side and (Z_i) = 0 in the pure oxidizer side. Moreover, because they all follow the same convection/diffusion balanced equation(2.80), all these variables are, therefore, equal ($Z = Z_1 = Z_2 = Z_3$). One can express the mixture fraction (*Z*) using the boundary conditions detailed above as following:

$$Z=\frac{sY_F-Y_O+Y_O^O}{sY_F^O+Y_O^O}=\frac{\frac{Cp}{Q}(T-T_O^O)+Y_F}{\frac{Cp}{Q}(T_F^O-T_O^O)+Y_F^O}=\frac{\frac{sCp}{Q}(T-T_O^O)+Y_O-Y_O^O}{\frac{sCp}{Q}(T_F^O-T_O^O)-Y_O^O} \tag{2.82}$$

Equation(2.82) shows clearly how the introduction of a chemistry-independent variable, such as, (*Z*) for the description of the mixing process, can link all species and temperatures to this single variable. Hence at stoichiometry ($sY_F=Y_O$) from equation(2.76), the stoichiometric mixture fraction denoted as (Z_{st}) can be easily deduced from equation(2.82) :

$$Z_{st}=\frac{1}{1+sY_F^O/Y_O^O} \tag{2.83}$$

The value of the mixture fraction may also be related to the equivalence ratio, by combining equations(2.72),(2.82), and(2.83) :

$$\phi=\frac{Z}{1-Z}\frac{(1-Z_{st})}{Z_{st}} \tag{2.84}$$

A more general way to describe the mixture fraction is to relate it to the chemical elements mass, rather than to the equivalence ratio and the species mass fractions. Details about this configuration can be found in (Peters, 2000), and (Kuo & Acharya, 2012) .Various ways can be chosen to define the mixture fraction, but the definition must be based on a conserved variable which usually is normalized between zero and one.

2.7.2. Conservative equations for turbulent reacting flows

The dynamic behaviour of reacting mixtures is represented in a mathematical language, by a set of conservative equations for mass, species, momentum, and energy. Since the mass is also conserved during the combustion processes, its conservative equation is unchanged for both non-reacting and reacting mixtures. The mass, momentum, and species equations of conservation were addressed previously in equations(2.3),(2.4), and (2.74). Concerning the energy conservative equation, multiple forms exist. In this sub-section, we will present it based on its enthalpy form.

The enthalpy of the (k^{th}) species can be defined as the sum of the heat of formation at a given temperature (T_0), and the sensible enthalpy, such that:

$$h_k = \Delta h^{o}_{f,k} + \int_{T_0}^{T} C_{p,k} dT \text{ and the total enthalpy is } h = \sum_{K=1}^{N} Y_k h_k \qquad (2.85)$$

where ($C_{p,k}$) is the species heat capacity at constant pressure, and under the ideal gas assumption the ($C_{p,k}$) is only function of temperature. The balanced equation for the total enthalpy is thus, expressed as:

$$\frac{\partial}{\partial t}(\rho h - p) + \frac{\partial}{\partial x_i}(\rho u_i h) = \underbrace{\frac{\partial}{\partial x_i}\left(\lambda \frac{\partial T}{\partial x_i} + \sum\nolimits_{k=1}^{N} \rho D_k h_k \frac{\partial Y_k}{\partial x_i}\right)}_{\mathrm{I}} + \underbrace{\dot{q}}_{\mathrm{II}} + \underbrace{\frac{\partial}{\partial x_i}(\tau_{ij} u_i)}_{\mathrm{III}} \qquad (2.86)$$

The term (I) takes into account the diffusion of enthalpy through conduction and mass transfer. The second term (II) represents the sources or sinks of enthalpy; thermal radiation is a typical example. This term is not to be confused with the heat released by combustion, which has been already taken into account in the definition of enthalpy. Finally, the third term (III) represents the work due to viscous stresses, and called the viscous dissipation term (Piffaretti, 2007). This term takes into accounts the internal heating by viscosity in the fluid, and it is negligible in most flow codes.

2.7.3. Averaging procedure

The Reynolds averaging or the conditional time averaging procedure was discussed earlier (see § 2.2), this approach is not suitable in situations with strong density variations, like in reacting flows. Therefore, in combustion, mass-weighted averages (e.g. Favre averages) are usually preferred. The Favre averaging procedure is defined as:

$$\tilde{\varphi} = \frac{\overline{\rho\varphi}}{\overline{\rho}} \qquad (2.87)$$

where the tilde denotes a mass averaged quantity. Similar to the Reynolds averaging approach, a local instantaneous variable (φ) may be divided into Favre averaged mean, and its fluctuation, as following:

$$\varphi = \tilde{\varphi} + \varphi'' \tag{2.88}$$

There is a link between the Favre averaging and the Reynolds averaging, as following:

$$\tilde{\varphi} = \bar{\varphi} + \frac{\overline{\rho'\varphi'}}{\bar{\rho}} \tag{2.89}$$

This relation requires the knowledge of correlations for density fluctuation denoted as ($\overline{\rho'\varphi'}$). Indeed if ($\rho'\varphi'$) is weak, or poorly correlated, the difference between Reynolds averaging and Favre averaging becomes negligible. This fact is particularly true in incompressible flows, where the two averaging procedures lead to equal results.

Measurements from experimental devices can be presented in either Favre or Reynolds averaged mode, a choice which strongly depends on the experimental technique used. For this reason, special attention must always be given when Favre averaged numerical results are compared with experimental data.

Using Favre strategy to average the flow variables, the instantaneous (N-S) balance equations for continuity, species, momentum, and energy become:

- Continuity :

$$\frac{\partial \bar{\rho}}{\partial t} + \frac{\partial \bar{\rho}\tilde{u}}{\partial x_i} = 0 \tag{2.90}$$

- Chemical species :

$$\frac{\partial \bar{\rho}\tilde{Y}_k}{\partial t} + \frac{\partial \bar{\rho}\tilde{Y}_k\tilde{u}_i}{\partial x_i} = \frac{\partial}{\partial x_i}\left(\overline{\rho D_k}\frac{\partial \tilde{Y}_k}{\partial x_i} - \bar{\rho}\widetilde{u_i''Y_k''} \right) + \overline{\dot{\omega}_K} \tag{2.91}$$

- Momentum:

$$\frac{\partial \overline{\rho}\widetilde{u}_i}{\partial t} + \frac{\partial \overline{\rho}\widetilde{u}_i \widetilde{u}_j}{\partial x_i} = \frac{\partial}{\partial x_i}\left(\overline{\tau_{ij}} - \overline{\rho}\widetilde{u''_i u''_j}\right) - \frac{\partial \overline{p}}{\partial x_i} \tag{2.92}$$

- Energy :

$$\frac{\partial}{\partial t}(\overline{\rho}\widetilde{h} - \overline{p}) + \frac{\partial}{\partial x_i}(\overline{\rho}\widetilde{u}_i \widetilde{h}) = \frac{\partial}{\partial x_i}\left(\overline{\lambda}\frac{\partial \widetilde{T}}{\partial x_i} + \sum_{k=1}^{N} \overline{\rho D_k}\,\widetilde{h}_k \frac{\partial \overline{Y_k}}{\partial x_i} - \overline{\rho}\widetilde{u''_i h''}\right) + \overline{\dot{q}} + \frac{\partial}{\partial x_i}(\overline{\tau_{ij} u_i}) \tag{2.93}$$

As mentioned in the turbulence section, the main challenge in the instantaneous (N-S) equations lays in the unclosed terms, which are generated from the averaging procedures. These unclosed terms may be interpreted as a loss of information, and thus, analogies, correlations, and models capable of providing closures for these quantities are indispensable. In particular, three to four unclosed terms are recognized (Poinsot & Veynante, 2005) depending on the assumptions used to build the numerical model:

a) Reynolds stresses ($\widetilde{u''_i u''_j}$): These terms are closed by a turbulence model as detailed (see § 2.2). The closure may be done directly, or by deriving balanced equations for the Reynolds stresses. In this study the combustion work is based on the classical turbulence model developed for non-reacting flows, i.e. the (*k-ε*) model in its Favre averaging form.

b) Turbulent fluxes for the species and the energy balanced equations ($\widetilde{u''_i Y''_k}$) , and ($\widetilde{u''_i h''}$), respectively : These fluxes are generally closed using a classical assumed gradient :

$$\overline{\rho}\widetilde{u''_i Y''_k} = -\overline{\rho}\frac{\mu_t}{Sc_{kt}}\frac{\partial \widetilde{Y}_k}{\partial x_i} \tag{2.94}$$

where (μ_t) is the turbulent kinetic viscosity, provided from the turbulent model like in equation (2.5), and (Sc_{kt}) is a turbulent Schmidt number, assumed to be constant. Equation(2.94) is directly inspired from the turbulent scalar transport model in non-reacting and constant density flows. Also, from a numerical point of view, this equation leads to a smooth integration, and increases the stability of CFD solution. The modeled term in equation(2.94), is a diffusive contributing term, and is simply added to the laminar diffusion term of the transport equation as following:

$$\frac{\partial \overline{\rho}\widetilde{Y_k}}{\partial t}+\frac{\partial \overline{\rho}\widetilde{Y_k}\widetilde{u_i}}{\partial x_i}=\frac{\partial}{\partial x_i}\left(\overline{\rho}\left(\overline{D_k}+\frac{\mu_t}{Sc_{kt}}\right)\frac{\partial \widetilde{Y_k}}{\partial x_i}\right)+\overline{\dot{\omega}_K} \tag{2.95}$$

Equation(2.95) vividly shows how the model used for molecular transport, has a limited impact in turbulent combustion codes: ($\overline{D_k}$) is usually much smaller than the turbulent diffusivity (μ_t/Sc_{kt}) in RANS codes, and can simply be neglected. Nevertheless, theory and experiments have shown that this assumed gradient, as well as, the ignorance of the ($\overline{D_k}$), are not appropriate for some turbulent premixed flames (Poinsot & Veynante, 2005).

c) Species chemical reaction rates ($\overline{\dot{\omega}_K}$): The main task of turbulent combustion modellers is to find approaches for a meaningful closure of the mean reaction rate term. A detailed discussion on how to model is detailed in the coming sub-section see (§ 2.7.4).

2.7.4. Modeling approaches for non-premixed combustion

This sub-section is dedicated to the description of the strategies developed to model the mean chemical reaction rate for turbulent non-premixed combustion. This term appears in the species conservative equation (2.91) after the averaging procedure. Since this work is centred on the steady flamelet modeling approach for non-premixed turbulent flows, more emphasis will be given to the description of the flamelet closures.

Tsuji (Tsuji, 1982) asserted that the diffusion flame differs from the premixed flame, in that, the combustion occurs at the interface between the fuel and the oxidizer; and the burning process depends more upon the rate of mixing rather than the rates of the chemical processes involved. First, a non-premixed flame is not able to propagate towards neither the rich nor the lean mixture, due to the lack of oxidizer or fuel. Hence, non-premixed combustion does not have any reference flame speed like in the premixed flame cases. This fact makes non-premixed combustion more sensible to turbulent perturbations. Secondly, a reference non-premixed flame thickness cannot be accurately defined, because it strongly depends on the local flow stretch; thus, it can take a wide range of values (Poinsot & Veynante, 2005). To investigate the diffusion flame structure, it is desirable to establish a simple configuration that can be studied in details. The counter-flow diffusion flame illustrated in ***Figure 21*** represents such configuration, as it leads to an essentially 1D diffusion flame structure (Peters, 2000).

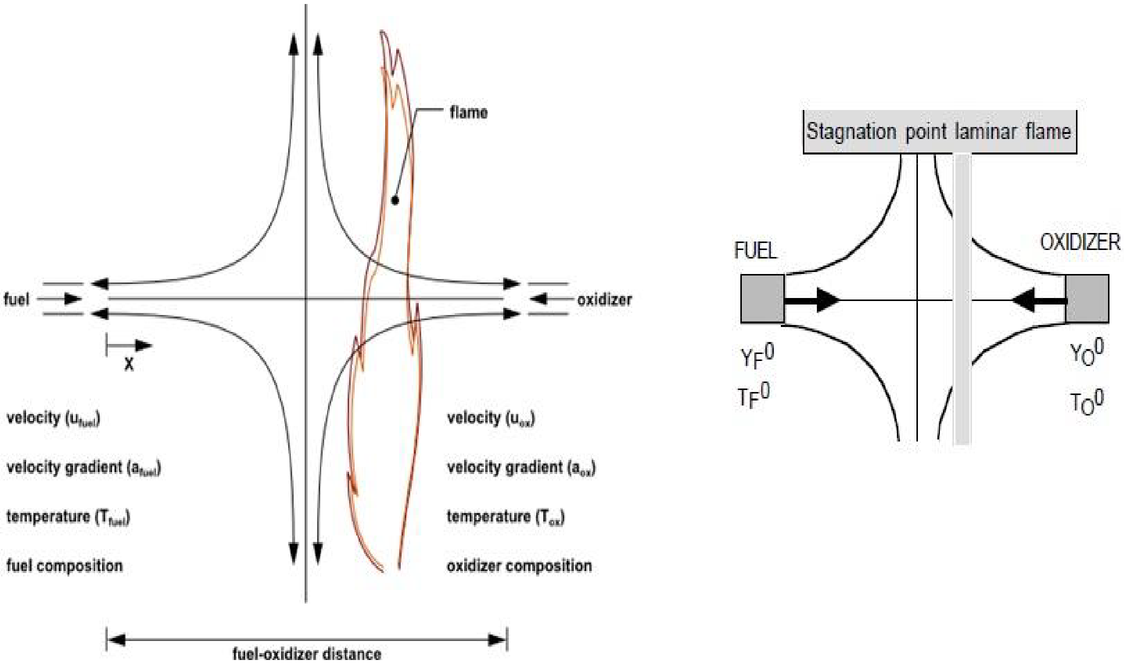

Figure 21 Opposing flow laminar diffusion flame configuration **(ANSYS, 2011)**, and **(Poinsot & Veynante, 2005)**

In this configuration, opposing jets of fuel and oxidizer are directed toward each other, and after ignition, a planar diffusion flame is established normal to the axis of the jets. Mainly, two parameters used to stabilize a counter-flow diffusion flame. The first is the mass fraction of the oxidizer in the oxidizer stream, and the second is the velocity of the oxidizer jet at the injection plane, which can be related to the strain rate and the extinction of the flame. Pioneering work on the extinction of the counter-flow diffusion flames was done by Norris and Pope (Rochaya, 2007), who conducted experimental tests on the maximum oxidizer velocity a flame can persists, using kerosene as the fuel. Tsuji (Tsuji, 1982) mentioned that in a diffusion flame, the combustion is controlled by the rate at which the fuel and the oxidizer diffuse to the reaction zone. This combustion rate is strongly dependent on the aerodynamics of the flow. By increasing the flow velocity the characteristic aerodynamic time, and consequently, the diffusion time become shorter. In this case, the chemical reaction will not be able to keep pace with the supply of the fuel and oxidizer and the reaction ceases. In fact, Tsuji stated that there is a critical stagnation velocity gradient, beyond which a flame can never be stabilized, and this is defined as the extinction mechanism.

Since mixing is the controlling physical phenomena in non-premixed flames, it is usually preferred to study the structure of these flames, not in the physical space, but in the mixture fraction space. In this way, the thermo-chemical variables of the flow will be considered as piecewise linear functions of the mixture fraction only.

This analysis was first proposed by Burke and Schumann in 1928 (Burke & Schumann, 1928), and the resulting analytical flame structure is usually known as the Burke-Schumann (B-S) limit or the Burke-Schumann solution. Such a solution for a methane flame is shown on the r.h.s. of ***Figure 22***.

From this graph one can immediately recognize the location of the stoichiometric mixture fraction value (Z_{st}), where the reactants are completely consumed, and products, as well as, temperatures reach their peak values. The fuel and oxygen mass fractions of any hydrocarbon fuel may be easily computed by re-arranging equation(2.82), in which the oxidizer and the fuel mass fractions become zero in the rich, and the lean side of the flame, respectively. The stoichiometric mass fractions for the two stable combustion products generated by hydrocarbon flames, namely CO_2 and H_2O, can be found by considering the element mass fraction balance of carbon and hydrogen. Last, the temperature at stoichiometric conditions for the Burke-Schumann limit is equal to the stoichiometric adiabatic flame temperature obtained from the equilibrium theory (e.g. Gibbs minimization approach). The B-S approach reduces the problem of reacting flows to a pure mixing problem, and its distributions give reasonable results when compared to the experimental data (Piffaretti, 2007). Although, the Burke-Schuman analysis is based on strong limiting assumptions, such that : (a) velocity of air and fuel are constant, equal, and uniform, (b) the chemistry is infinitely fast (can be considered at the equilibrium), (c) the chemistry is described by a single one-step reaction, (d) the chemistry is irreversible, i.e. no backward reaction, and (e) diffusion in the axial direction can be neglected compared to the diffusion in the radial direction (Kuo, 2005); it is very useful when rough picture of the structure of a diffusion flame is required.

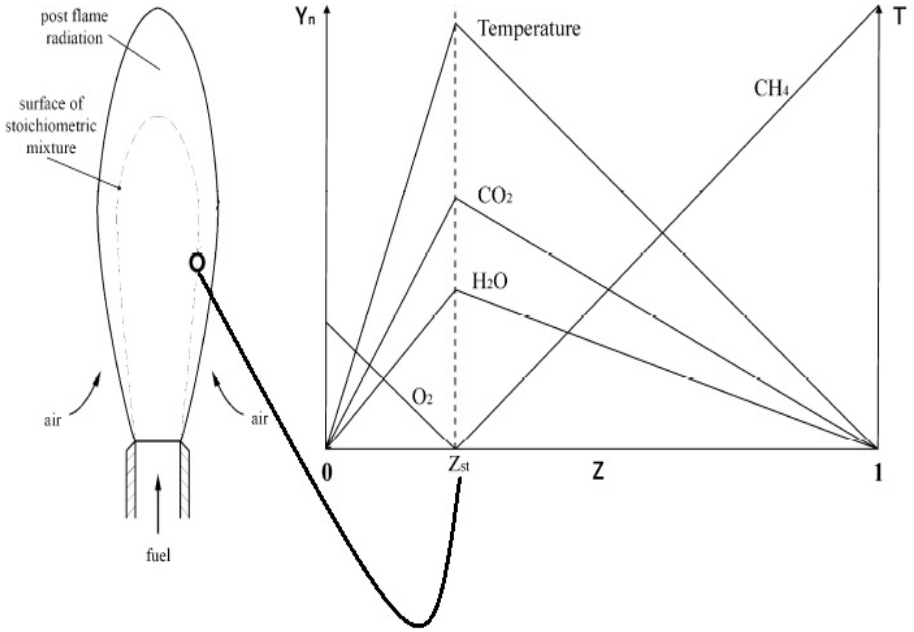

Figure 22 Non-premixed flame and its laminar structure **(Piffaretti, 2007)**

Under the assumption that a diffusion flame is a mixing-controlled phenomenon, the turbulent processes and the chemical reaction ones may be decoupled and studied separately. The outcome renders a split of two main computational problems:

(a) A mixing problem providing the average mixture fraction filed $\widetilde{Z}(x_i,t)$: To determine the average values that depends on (Z), the mean value of mixture fraction is not sufficient; and thus, its higher moments should be provided, i.e. the mixture fraction variances ($\widetilde{Z''^2}$). Moreover, if possible, a full probability density function (PDF) of (Z) is needed to forecast its statistical distribution. However, depending on the complexity of the numerical model, the probability density function may be extrapolated from a function that describes the presumed probability distribution, to a directly computed one from an exact transport equation. The last option is computationally more expensive.

(b) A flame structure problem: Species mass fractions (Y_k), temperatures (T), and reaction rates ($\dot{\omega}_k$) are expressed as functions of the mixture fraction. These functions are formulated as conditional expressions ($Y_k\big|_z , T\big|_z$). The word conditional is used, since (Y_k) and (T) may depend on multiple parameters in the turbulent flow; hence, their dependence to the mixture fraction field should be limited or conditioned.

When the (PDF) of (Z) also denoted by p(Z) is known, averaged species mass fraction ($\widetilde{Y_k}$), average temperature ($\overline{T}$), and averaged reaction rates ($\overline{\dot{\omega}_k}$) can be expressed as:

$$\overline{\rho T} = \int_0^1 \left(\overline{\rho T}\Big|_Z \right) p(Z)dZ \; ; \; \overline{\rho}\widetilde{Y_k} = \int_0^1 \left(\overline{\rho Y_k}\Big|_Z \right) p(Z)dZ \tag{2.96}$$

$$\overline{\dot{\omega}_k} = \int_0^1 \left(\overline{\dot{\omega}_k}\Big|_Z \right) p(Z)dZ \tag{2.97}$$

Poinsot (Poinsot & Veynante, 2005) further suggests two different levels to model turbulent non-premixed flames, based on the above mentioned two expressions:

- The primitive variable method which is based on equation(2.96) : Here, assumption is made on the flame structure to provide conditional quantities, i.e. ($Y_k\big|_z , T\big|_z$). Species mass fraction balanced equation(2.91) is no longer required, and the mean reaction rates ($\overline{\dot{\omega}_k}$) are not modeled. Examples of models using this technique are: (a) Infinitely fast chemistry assumption, solved by the equilibrium model, and (b) Finite rate chemistry assumption, solved using either the laminar steady flamelet model, or the conditional modeling closure approach (CMC).
- The reaction rate approach which is based on equation(2.97): Here, species mass fraction, and temperature balance equations are solved; accordingly, mean reaction rates ($\overline{\dot{\omega}_k}$) are modeled. Examples of models using this technique are: (a) Infinitely fast chemistry assumption, solved by the eddy dissipation (ED), and the eddy dissipation concept (EDC) models, (b) Finite rate chemistry assumption, solved by the PDF transport model.

These two approaches show clearly the link between the variables in turbulent reacting flows, which is achieved by integrating the product between conditional quantities found in the reactive layer, and statistical distribution of the variables that characterize the turbulent mixing. In a mathematical language, this process is expressed by equation (2.96) for the primitive approach and by equation (2.97) for the reaction rate approach. Nevertheless, one has to be aware that, even under the same assumptions, the two approaches (primitive and reaction rate) are not a priori equivalent, and may lead to quite different results (Poinsot & Veynante, 2005).

The probability density function (PDF), or $p(\theta;x,t)$, quantifies the probability to find a variable (θ) at a given location (x) for a given time (t), within a range of $\left(\theta - {}^{\Delta\theta}\!/_{2} ; \theta - {}^{\Delta\theta}\!/_{2}\right)$. This variable can be (temperature, mass fraction, velocity, mixture fraction etc.). The PDF has the properties that its integral over all possible states is unity, and its integral times a function of a variable (θ) gives the mean value of the function (Bray N. , 2011).

Following this definition, the probability density function is simply a statistical approach, describing the temporal fluctuation of a variable (θ), and can be used to compute the averaged values of any variable that depends on (θ). This is the key behind the coupling of the chemistry with the turbulence, also known as the turbulence-chemistry interaction. Sometimes, more than one variable is required to capture the flame structure. Thus, the so called joint probability density function is introduced, can be expressed as (Poinsot & Veynante, 2005):

$$\int_{\psi_1,\psi_2,...\psi_N} .....\int p(\psi_1,\psi_2,....\psi_N)d\psi_1 d\psi_2....d\psi_N = 1 \tag{2.98}$$

where ($\psi_1,\psi_2,....\psi_N$) are any variables such as mixture fraction, and strain rate. Any averaged quantity such as ($\overline{f}$) that is function of these variables can be determined as:

$$\overline{f} = \int_{\psi_1,\psi_2,...\psi_N} .....\int f(\psi_1,\psi_2,....\psi_N)p(\psi_1,\psi_2,....\psi_N)d\psi_1 d\psi_2....d\psi_N \tag{2.99}$$

The difficulty lays in the determination of the PDF which changes at every point in the flow field. In general, a PDF function can take any shape, and can exhibit multiple peaks. It contains information not only on the mean value of the variable, but also on its variance (first moment), and on all higher moments if included. Two main paths have been proposed by Pope, Dopazo & al. (Poinsot & Veynante, 2005): (1) to presume the PDF shape, rendering the so called presumed PDF family, and (2) to solve a balance equation for the PDF. The following section will present only the presumed approach, since it's the one used in our calculations.

Presumed PDF approach: this approach supposes that the PDF has a fixed shape, parameterized using, for example, only one or two parameters. The logical parameters to use are the moments of the variable: mean quantities, and/or first moment (variance). The most popular presumed PDF shape is the so called β- function shape (Poinsot & Veynante, 2005). To serve our course, the β- function of the mixture fraction shall be offered as example.

The β- function shape for the mixture fraction in the Favre form will depend on two parameters, ($\widetilde{Z}$) and ($\widetilde{Z''^2}$), and it has the form of:

$$p(Z) = Z^{(\alpha-1)}(1-Z)^{(\beta-1)}\frac{\Gamma(\gamma)}{\Gamma(\alpha)\Gamma(\beta)} \tag{2.100}$$

where,

$$\alpha = \widetilde{Z}\gamma \ , \ \beta = (1-\widetilde{Z})\gamma \text{ and } \gamma = \frac{\widetilde{Z}(1-\widetilde{Z})}{\widetilde{Z''^2}} - 1 \tag{2.101}$$

Here (Γ) is the gamma function, and (α), (β) are the two coefficients relating the Favre mean $\widetilde{Z}(x,t)$ to its variance $\widetilde{Z''^2}(x,t)$. Hence, this technique requires the solving of a balance equation of $\widetilde{Z}$ and $\widetilde{Z''^2}$ as presented in the coming sub-section (see § 2.7.4.1). The β - function is plotted for different combinations of the parameters ($\widetilde{Z}$) and (γ) in ***Figure 23*** (Peters, 2000). It can be observed that at small values of the mixture fraction variances, i.e. large values of (γ) the distributions are bell-shapes and approaching Gaussian distributions (Peters, 2000). This state is reached when the reactants are sufficiently mixed (Z~0.4-0.6) (Veynante & Vervisch, 2001) . When (α < 1) a singularity at Z = 0 is developed, also for (β < 1) a singularity at the other bound of the mixture fraction domain is seen. This will result in "*L*", "*J*" or "*U*" distribution shapes, these states domain when the oxidizer and the fuel are completely segregated. Other, presumed PDF functions exist, like the Dirac-delta function used for the scalar dissipation that will be introduced during the explanation of the flamelet approach.

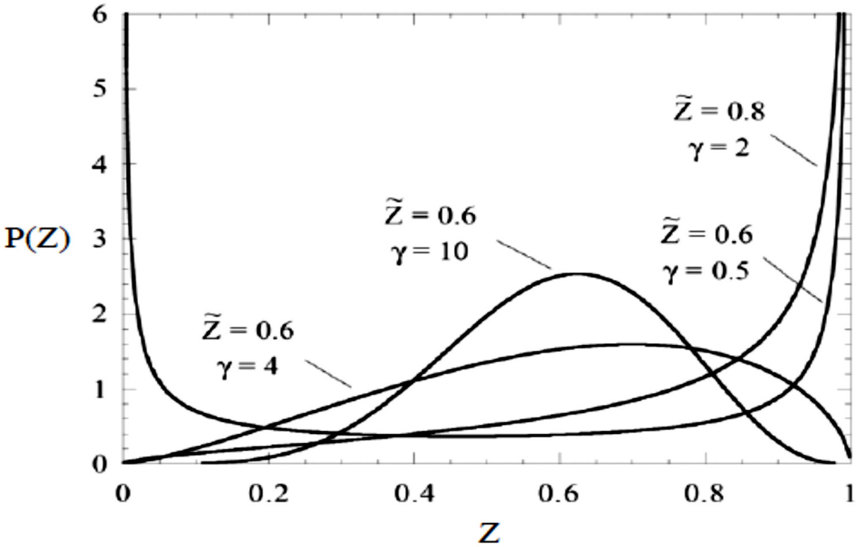

Figure 23 Shapes of the beta-function **(Peters, 2000)**

2.7.4.1. Models for turbulent combustion

Peters has classified the turbulent combustion models in terms of chemistry and mixing (Peters, 2000) as presented in ***Table 3*** below:

Table 3 Classification of turbulent combustion models

	Premixed combustion	Non-premixed combustion
Infinitely fast chemistry	Bray-Moss-Libby model (BML) Coherent flame model (CFM)	Conserved scalar equilibrium model
Finite rate chemistry	PDF transport equation model	PDF transport equation model
	Flamelet model based on the G-equation	Flamelet model based on the mixture fraction (ex. steady flamelet approach) Conditional moment closure (CMC).
	Linear Eddy model (LEM)	Linear Eddy model (LEM)

A comprehensive review on each model can be found in (Peters, 2000), (Poinsot & Veynante, 2005), and (Bray N. , 2011). In the present section, the focus will be accorded to the Flamelet approach based on the mixture fraction for finite rate chemistry assumption.

Assuming infinitely fast chemistry (chemical equilibrium) may not be sufficient in turbulent flows, where local diffusion timescales vary considerably and non-equilibrium effects must be taken into account. The non-equilibrium state includes NOx formation, low-temperature CO oxidation, and ignition. As shown above, assuming the equilibrium chemistry (for example Burke-Schuman model) can simplify the problem, and help to relate mass fractions, temperatures, and reaction rate to the mixture fraction (Z) only. However, when the chemical timescale is comparable to the fluid mixing timescale, the species can be considered to be in global chemical non-equilibrium because turbulence can penetrate into the reaction zone and alters the flame.

In order to introduce the departure from the equilibrium chemistry in turbulent combustion models, models such as the steady state laminar flamelet can be employed. In this approach, the turbulent non-premixed flame is viewed as an ensemble of thin, laminar, and locally one-dimensional flamelet structures, embedded within the turbulent flow field (ANSYS, 2011). Each element of the flame front can then be viewed as a small laminar flame, known as 'flamelet'. Physically, the flame structure is considered locally one-dimensional, and only depends on the time, and the coordinate normal to the flame front.

The flamelet equations can be derived using a coordinate system attached to the surface of the stoichiometric mixture (Z_{st}). A transformation is performed from the physical spatial–temporal space to a space, in which the mixture fraction is introduced as a new independent variable. Thus, a new coordinate is locally attached to the iso-surface of the stoichiometric mixture fraction (Z_{st}), and the other new coordinates (Z_2) and (Z_3) lay within this surface as graphically presented in ***Figure 24***. This is achieved through a Crocco-type coordinate transformation. The transformation rules are systematically applied to the governing equations of the species and energy (Claramunt, Cònsul, & Carbonell, 2006). Terms corresponding to gradients along the flame front (gradients along Z_2 and Z_3) are neglected in comparison to the terms normal to the flame (gradients along Z) (Peters, 2000) .

It should be also noted that, the justification for determining the flame surface location by the iso-surface of the stoichiometric mixture (Z_{st}) is an approximation made by Peters; since the temperature is the highest in the vicinity of this surface under the assumption of moderate non-equilibrium, i.e. fast chemistry but not infinitely fast. Moreover, Peters highlighted that in the flamelet formulation, all the scalars (e.g. Z, T, Y_k) are transported with the same convection speed; and thus, no convective term is needed in their transport equation (this will be explicitly shown in the flamelet equations) (Peters, Barths, Brehm, & Mack, 1998).

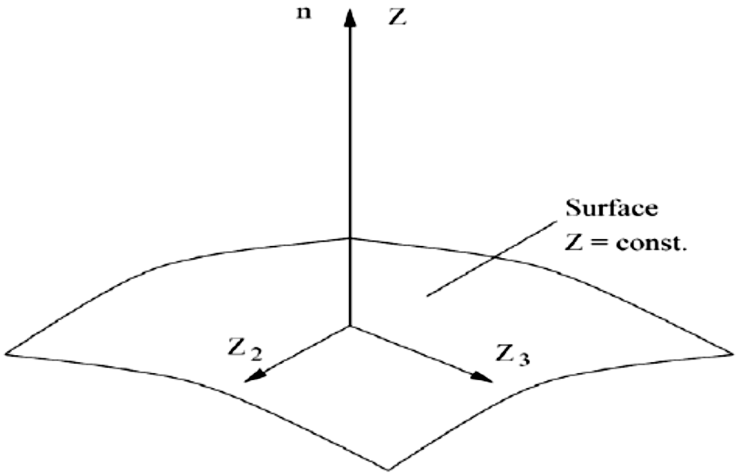

Figure 24 (Z) iso-surface and its orthogonal coordinate system **(Piffaretti, 2007)**

The flame structure in the (Z) space allows the reduction in the number of variables, like for example equation (2.82) which shows the link of the flame structure to the mixture fraction. Under these assumptions, and after the Crocco transformation, the species mass fraction balance equation(2.74) can be rewritten as:

$$\rho\frac{\partial Y_k}{\partial t}=\frac{\rho\chi}{2Le_k}\frac{\partial^2 Y_k}{\partial Z^2}+\dot{\omega}_k+\frac{1}{4}\left(\frac{1}{Le_k}-1\right)\left(\frac{\partial\rho\chi}{\partial Z}+\rho\chi\frac{C_p}{\lambda}\frac{\partial}{\partial Z}\left(\frac{\lambda}{C_p}\right)\right)\frac{\partial Y_k}{\partial Z} \quad (2.102)$$

and the energy equation:

$$\rho\frac{\partial T}{\partial t}=\frac{\rho\chi}{2}\frac{\partial^2 T}{\partial Z^2}-\frac{1}{C_p}\sum\nolimits_k h_k\dot{\omega}_k+\frac{Q_R}{C_p}+\frac{\rho\chi}{2C_p}\left[\frac{\partial Cp}{\partial Z}\frac{\partial T}{\partial Z}+\sum\nolimits_N\left(\frac{C_{pk}}{Le_k}\frac{\partial Y_k}{\partial Z}\right)\frac{\partial T}{\partial Z}\right] \quad (2.103)$$

These set of equations are called the complete flamelet equations (CE) (Claramunt, Cònsul, & Carbonell, 2006). (C_{pk}) is the specific heat of the (k^{th}) species, (h_k) the enthalpy of the (k^{th}) species, (Q_R) is the radiation heat loss, and (Le_k) is the Lewis number of the (k^{th}) species. The (χ) is the scalar dissipation, which is the only term that depends on the spatial variables (x_i) in the flamelet formulation. This parameter controls the mixing, because it controls the gradients of (Z). Once (χ) is specified, the flamelet equations can be entirely solved in the (Z) space to provide the flame structure. The scalar dissipation rate (χ) is defined as:

$$\chi=2D\left(\frac{\partial Z}{\partial x_i}\right)^2 \quad (2.104)$$

where (D) is the diffusion coefficient, and (χ) has the dimension of one over second (s^{-1} or Hz). This variable corresponds to a characteristic strain rate in the physical space, and may be interpreted as the inverse of a characteristic diffusion time. Note that, the scalar dissipation in general, is a function of the mixture fraction; hence, it may change within the flame structure. Arising from the flamelet formulation described above, a key difficulty in integrating the flamelet equations is to know a priori information of the scalar dissipation rate dependence on the mixture fraction, i.e. χ (Z).

In the flamelet calculations for turbulent flows, the use of flamelet libraries is often advocated. These libraries are computed in advance, and are assumed to be independent of the flow. Therefore, the scalar dissipation rate cannot be taken from the flow field calculation during the flamelets calculation, but, it has to be introduced as a scalar parameter. Then, the mixture fraction dependence of the scalar dissipation rate, which is required to complete the calculation of the flamelet libraries, has to be modeled (Pitsch & Peters, 1998). It was shown by Peters (Peters, 2000) from the analytic solutions of laminar counter-flow diffusion flames, that the scalar dissipation can be expressed as a function of the mixture fraction as following:

$$\chi(Z) = \frac{a_s}{\pi} \exp\left(-2\left[erfc^{-1}(2Z)\right]^2\right) \tag{2.105}$$

where (a_s) corresponds to the characteristic strain rate, and ($erfc^{-1}$) stands for the inverse of the complementary error function (not the reciprocal). Another improved formulation for scalar dissipation was derived by Kim and Williams (Pitsch & Peters, 1998), which takes into account the effect on the density variation as following:

$$\chi(Z) = \frac{a_s}{\pi} \frac{3\left(\sqrt{\rho_\infty / \rho} + 1\right)^2}{2.\sqrt{\rho_\infty / \rho} + 1} \exp\left(-2\left[erfc^{-1}(2Z)\right]^2\right) \tag{2.106}$$

The subscript (∞) means the oxidizer stream. Physically, as the flame is strained, the width of the reaction zone diminishes, and the gradient of the mixture fraction at the stoichiometric position ($Z = Z_{st}$) increases. The instantaneous stoichiometric scalar dissipation, denoted as (χ_{st}), is used as the essential non-equilibrium parameter. In the limit of (χ_{st} = 0), the chemistry tends to equilibrium, and as (χ_{st}) increases due to aerodynamic straining, the non-equilibrium increases. Local quenching of the flamelet occurs when (χ_{st}) exceeds a critical value, i.e. ($\chi_{st} = \chi_{quenching}$). Using this expression in the flamelet equations links the flamelet library to two input parameters: (Z) and (χ_{st}). The scalar dissipation rate at the stoichiometric conditions is evaluated at (Z_{st}), calculated according to the definition for mixture fraction definition in equation(2.83). The choice of equation(2.83) is justified, because the stoichiometric mixture fraction, if determined from the solution of the transport equation(2.80), will not be constant; and therefore, cannot be referenced as a constant value in the presented flamelet formulation (Pitsch & Peters, 1998). ***Figure 25*** shows a comparison of different approximations for the scalar dissipation rate at (Z_{st}) obtained from the solution of the transport equation and from the equation(2.83).

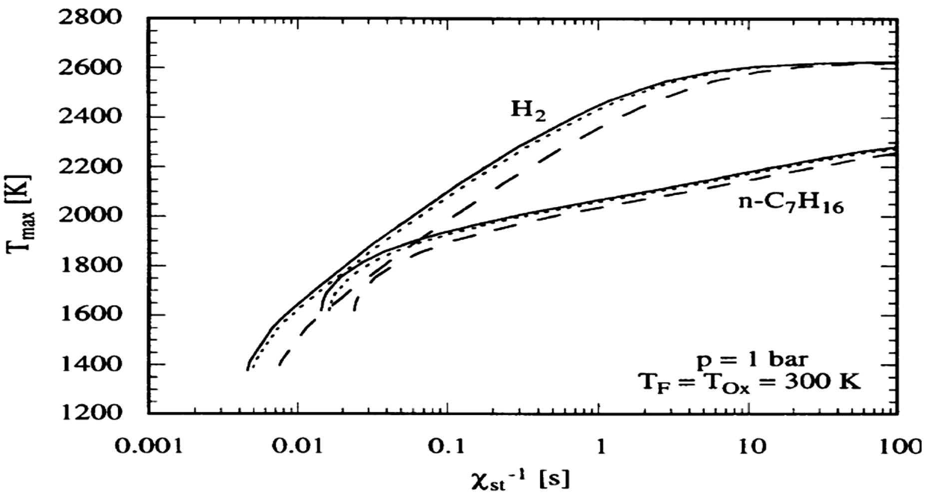

Figure 25 Comparison of different approximations for scalar dissipation rate at (Z_{st}). Solid lines represent (χ_{st}) calculated with transport equation (Eq. 2.80); dashed and dotted lines represent (χ_{st}) from Eqs. (2.105) and (2.106), respectively **(Pitsch & Peters, 1998)**.

Both formulas, i.e. equations(2.105) and(2.106), describe the trends quite well; while, equation (2.106) shows a superior accuracy and it is the one integrated in the FLUENT™. With this approach, the functional dependence of the scalar dissipation rate on the mixture fraction $\chi(Z)$ is parameterized by (χ_{st}). The (χ_{st}) acts as an external parameter that is imposed on the flamelet structure by the mixture fraction field. A set of discrete values of (χ_{st}) are usually used from a low value, i.e. starting value for the iteration (10^{-4} s^{-1}) to a quenching value ($\chi_{st} = \chi_{quenching}$). Other strategies to simulate the key aspect of the scalar dissipation dependence on the mixture fraction can be found in (Claramunt, Cònsul, & Carbonell, 2006).

As stated above, the non-premixed turbulent flame is viewed as an ensemble of thin, laminar flames. Computational codes can generate multiple steady diffusion flamelets over a range of strain rates to account for the varying strain field in the multi-dimensional simulation. In FLUENT™, diffusion flamelets are generated until either the maximum number of flamelets is reached (as requested by the user), or the flamelet is extinguished, whichever occurs first.

The flamelet structure obtained from equations (2.102) and (2.103) depends on both time (*t*) and mixture fraction (*Z*). It can be used in two ways:

- Unsteady laminar flamelets: The dependence of the (*T*) and (Y_k) functions versus time can be conserved, leading to a class called ‘unsteady flamelets’ approach.

- Steady laminar flamelets: The structure of the flamelet can be assumed to be steady, even though the flow itself (and especially the *Z* field) will depend on the time.

The steady laminar flamelet case will be further discussed, since it is relevant to the numerical model used in this project. By neglecting the unsteady term, the last term in the energy equation as being small compared to the source term (Peters, 1984), the radiation heat loss term, and assuming Lewis number of unity for the species (Le_k), the flamelet equations transform to its simplified form known as simplified equation (SE):

$$\begin{aligned}&\frac{\rho\chi}{2}\frac{\partial^2 Y_k}{\partial Z^2}+\dot{\omega}_k=0\\&\frac{\rho\chi}{2}\frac{\partial^2 T}{\partial Z^2}-\frac{1}{C_p}\sum_k h_k\dot{\omega}_k=0\end{aligned} \tag{2.107}$$

This hypothesis assumes that the flamelet lifetime is much longer than the characteristic time scale of the phenomena involved in the flamelet equations; and consequently, the transient terms can be neglected (Claramunt, Cònsul, & Carbonell, 2006). Equation(2.107) shows that the flame structure is given by a set of functions, i.e. *T*, (*Z*, χ_{st}), and Y_K (Z, χ_{st}), which can be computed independently from the turbulent formulation; then stored in the so called flamelet library. Embedding these local laminar flames in the turbulent flow, is performed through the probability density function as highlighted previously, and since the dependence is on more than one variable, i.e. (χ_{st} , *Z*) , this will be done through a presumed joint PDF. The created presumed joint PDF will allow the determination of the mean species mass fractions, and the mean temperatures (Favre averaging) as following:

$$\begin{aligned}&\overline{\rho}\widetilde{Y}_k=\int_0^{+\infty}\int_0^1\rho Y_k(Z,\chi_{st})p(Z,\chi_{st})dzd\chi_{st}\\&\overline{\rho}\widetilde{T}=\int_0^{+\infty}\int_0^1\rho T(Z,\chi_{st})p(Z,\chi_{st})dzd\chi_{st}\end{aligned} \tag{2.108}$$

It should be noted that, there is a statistical independence between the (Z) and (χ_{st}) leading to:

$$p(Z,\chi_{st})=p(Z)p(\chi_{st}) \tag{2.109}$$

Though that this assumption seems, a priori, very crude. In fact, this statistical independence is quite well verified in direct numerical simulations (DNS). The mixture fraction (*Z*) measures the mixing for the reactants, and is mainly related to large scale flow motions. On the other hand, (χ_{st}) is linked to the local flame structure (χ_{st} corresponds to a local Z-gradient and measures the local diffusion zone thickness), and is governed by small scale features (Poinsot & Veynante, 2005).Thus, this statistical independence may be justified.

As already mentioned (see § 2.7.4), the mixture fraction PDF is generally presumed using a β-function based on the solution of two transport equations, i.e. $\widetilde{Z}$ and $\widetilde{Z''^2}$; additionally, another presumed distribution will be required for the ($\widetilde{\chi_{st}}$). For simplification a single Dirac-delta function will be presented, note that, FLUENT™ uses the Dirac function for the scalar dissipation. The Favre averaged transport equation of these quantities can be expressed as (it should be reminded that the unclosed terms are modeled using the classical gradient assumption as seen in equation(2.94)):

$$\frac{\partial \overline{\rho}\widetilde{Z}}{\partial t}+\frac{\partial \overline{\rho}\widetilde{u_i Z}}{\partial x_i}=\frac{\partial}{\partial x_i}\left(\overline{\rho}\left(\overline{D_k}+\frac{\mu_t}{Sc_{kt}}\right)\frac{\partial \widetilde{Z}}{\partial x_i}\right) \tag{2.110}$$

$$\frac{\partial \overline{\rho}\widetilde{Z''^2}}{\partial t}+\frac{\partial \overline{\rho}\widetilde{u_i Z''^2}}{\partial x_i}=\frac{\partial}{\partial x_i}\left(\overline{\rho}\left(\overline{D_k}+\frac{\mu_t}{Sc_{kt}}\right)\frac{\partial \widetilde{Z''^2}}{\partial x_i}\right)+\underbrace{2\frac{\mu_t}{Sc_{kt}}\left(\frac{\partial \widetilde{Z''^2}}{\partial x_i}\right)^2}_{\text{Production}}\underbrace{-\overline{\rho}\widetilde{\chi_p}\widetilde{Z''^2}}_{\text{Dissipation}} \tag{2.111}$$

where the last two terms on the r.h.s correspond to the production and the dissipation of the variance, respectively. The ($\widetilde{\chi_p}$) is also called the scalar dissipation, and it measures the decay of ($\widetilde{Z''^2}$) in the flow field. In fact, the scalar dissipation rate plays for the mixture fraction the same role as the dissipation rate (ε) for the turbulent kinetic energy in the velocity field (Poinsot & Veynante, 2005) and it's modeled by:

$$\widetilde{\chi_p}=C_\chi\frac{\widetilde{\varepsilon}}{\widetilde{k}}\widetilde{Z''^2}\text{, and } C_\chi=2 \text{ which is a constant} \tag{2.112}$$

Concerning the presumed probability density function of the scalar dissipation, the single Dirac-delta function is used, such that, the fluctuations will be neglected, leading to:

$$p(\chi_{st}) = \delta(\chi_{st} - \widetilde{\chi_{st}}) \qquad (2.113)$$

and ($\widetilde{\chi_{st}}$) will be modeled using the same equation as in(2.112), the only difference is the subscript 'st' instead of 'p'.

Regarding the diffusion coefficients (D_k), and ($D_t = \mu_t / Sc_{kt}$) in equations(2.110) and(2.111), the diffusion coefficient (D_k) can have an arbitrary value under the assumption that all the chemical species have the same molecular diffusivity. Peters (Peters, 2000) argues that since the maximum temperature locates the position of the reaction zone, and thus, the diffusion of enthalpy becomes the most important factor in mixture fraction space. As a conclusion, the thermal diffusivity may be chosen as the diffusion coefficient. However, the introduction of the classical gradient assumption (for the unclosed terms) produces the turbulent diffusion coefficient (D_t), and can allow the omission of the (D_k) since ($D_k <<< D_t$) (Poinsot & Veynante, 2005). To calculate the (D_t), equation(2.5) is used to acquire the turbulent eddy viscosity (μ_t if the *k-ε* model is chosen), along with a constant value for the turbulent Schmidt number. In FLUENT™ the (Sc_{kt}) is referred to as the PDF Schmidt number, written as (σ_t), and has the value of (0.85). Defining the diffusion coefficient as such, i.e. arbitrary value, emphasises the independence of the conserved scalar (*Z*) from any combination of the reactive scalars, and thus, allowing the derivation of the (*Z*) without any assumption of Lewis numbers for the chemical species (Claramunt, Cònsul, & Carbonell, 2006).

The determination of the mean mass fractions, and temperature from the presumed joint PDF of (χ_{st} , *Z*) is true for adiabatic systems. Nevertheless, many reacting systems involve heat transfer through wall boundaries, heat transfer to/from discrete phase droplets, and/or multiple inlets at different temperatures. In such flows, the local thermochemical state is no longer related only to the mixture fraction, but, also to the enthalpy. Consequently, changes in enthalpy due to heat losses must be considered when computing the scalars from the mixture fraction. For non-adiabatic systems, turbulent fluctuations should be accounted for by means of a joint PDF that takes into account the enthalpy, i.e. $p(Z, H)$. However, the computational cost of modeling steady diffusion flamelets over a range of enthalpies is prohibitive; accordingly some approximations are made. Heat gain/loss to the system is assumed to have a negligible effect on the species mass fractions, also, the effect of the heat loss on the extinction limits is not taken into account. Heat gain/loss will be only reverted on the temperature calculations, which will not only be a function of the mixture fraction, and the scalar dissipation as shown previously, but also, on the mean enthalpy calculated from equation(2.85), (2.93) :

$$\tilde{h} = \sum_{k=1}^{n} \widetilde{Y_k} h_k(\tilde{T}) \tag{2.114}$$

By doing so, no additional equation for the enthalpy is required. Moreover, it should be noted that, enthalpy fluctuations are not considered, because in the non-premixed turbulent combustion, it is often assumed that the fluctuations of the enthalpy are mainly due to the mixture fraction fluctuations, and thus can be described by ($\widetilde{Z''^2}$) (Peters, 2000). As a result, in FLUENT™ the non-adiabatic PDF will have the following characteristics: mean temperature $\widetilde{T}(\widetilde{Z}, \widetilde{Z''^2}, \widetilde{H}, \widetilde{\chi_{st}})$, mean species mass fractions $\widetilde{Y_k}(\widetilde{Z}, \widetilde{Z''^2}, \widetilde{\chi_{st}})$, and mean density $\overline{\rho}(\widetilde{Z}, \widetilde{Z''^2}, \widetilde{H}, \widetilde{\chi_{st}})$. Accordingly, PDF tables for the mean temperature, and density, will have an extra dimension to accommodate the mean enthalpy.

To summarize a simulation with FLUENT™, the flamelet equations are calculated in the pre-processing solver independently of the flow field variables. Then, equations for the mean mixture fraction, mixture fraction variance, and mean enthalpy are solved in the main solver. The scalar dissipation field is calculated from the turbulence field, and the mixture fraction variance. The mean values of cell temperature, density, and species mass fractions, are obtained from the PDF look-up table.

2.7.5. Two way coupling influence on the flow field equations

The effect of drops on the gas phase is considered by introducing appropriate source terms in the gas phase equations of motion. The source terms, due to drops in the Eulerian gas-phase solution, are determined by computing changes in droplet properties as they traverse each computational cell. Generally, drop source terms are provided, or better said, added to the equations for mass conservation (continuity equation), momentum, energy, and injected species (species transport equation Y_K or the mixture fraction equation (Z), depending on the combustion model used), they are summarized as following:

$$
\begin{aligned}
&\frac{\partial\overline{\rho}}{\partial t}+\frac{\partial\overline{\rho}\tilde{u}}{\partial x_i}=\widetilde{\dot{S}}_m \\
&\frac{\partial\overline{\rho}\widetilde{u_i}}{\partial t}+\frac{\partial\overline{\rho}\widetilde{u_i}\widetilde{u_j}}{\partial x_i}=\frac{\partial}{\partial x_i}\left(\overline{\tau_{ij}}-\overline{\rho}\widetilde{u_i''u_j''}\right)-\frac{\partial\overline{p}}{\partial x_i}+\widetilde{\dot{S}}_u \\
&\frac{\partial\overline{\rho}\widetilde{Z}}{\partial t}+\frac{\partial\overline{\rho}\widetilde{u_iZ}}{\partial x_i}=\frac{\partial}{\partial x_i}\left(\overline{\rho}\left(\overline{D_k}+\frac{\mu_t}{Sc_{kt}}\right)\frac{\partial\widetilde{Z}}{\partial x_i}\right)+\widetilde{\dot{S}}_m \\
&\frac{\partial}{\partial t}(\overline{\rho}\tilde{h}-\overline{p})+\frac{\partial}{\partial x_i}(\overline{\rho}\widetilde{u_i}\tilde{h})=\frac{\partial}{\partial x_i}\left(\overline{\lambda}\frac{\partial\tilde{T}}{\partial x_i}+\sum_{k=1}^{N}\overline{\rho D_k}\widetilde{h_k}\frac{\partial\overline{Y_k}}{\partial x_i}-\overline{\rho}\widetilde{u_i''h''}\right)+\overline{\dot{q}}+\frac{\partial}{\partial x_i}(\overline{\tau_{ij}u_i})+\widetilde{\dot{S}}_h
\end{aligned}
\tag{2.115}
$$

It should be noted that, the source term added to the mixture fraction equation, is solely due to the mass transfer from liquid fuel droplets to the gas phase, i.e. it is the same source term used for the continuity equation. If the *k*-*ε* model is used for turbulence closure, than source terms for the *k*–*ε* equations are neglected. This assumption is made mainly, because models for predicting turbulence production and dissipation due to particle motions are not well developed. This implies that, if a higher-order turbulence model is used, drop source terms should appear in the governing equations for turbulence. Widely, the omitting procedure is acceptable at the limit of dilute sprays, where such effects should be small due to low particle densities. Combusting sprays are generally modeled by assuming that drops simply evaporate without the presence of envelope flames, which is contrary to the real liquid combustion. Subsequently, the fuel vapor is assumed to react in the gas phase with rates determined in the same manner as for the gas flames. To this end, drops within the spray are assumed to act as distributed sources for the fuel vapor (Kuo & Acharya, 2012).

The liquid phase is treated by assuming a uniform liquid temperature at each instant of time. The rate of mass transfer, which is the driving potential, is then, determined using the difference in fuel vapor concentration between the surface of the drop, and its local surroundings. This procedure correctly represents the fact that, a drop within a spray has no fixed wet-bulb temperature, due to the continuous change of its surroundings properties. The presence of envelope flames is generally ignored and empirical expressions developed for single drops; are thus, used to represent the drop drag, and the effect of forced convection on the drop heat and mass transfer rates. This procedure is called the two-stage method, in which, the first stage consists of drop heat-up to a fixed wet-bulb temperature without any evaporation. In the second stage, the evaporation is activated, and the process is driven by the temperature difference between the drop and its surroundings. The wet-bulb temperature is to be taken as the boiling temperature of fuel at the chamber pressure where the spray emerges. Two-stage drop models simplify the computations, but their ability to represent accurately the real drop processes within a spray, is questionable (Kuo & Acharya, 2012).

The present section will treat the procedure for calculation of the source terms as implemented in the computational code FLUENT™. To study the dynamics of the particle motion or their momentum, and to determine particle trajectories, the general equation of particle motion for a spherical particle is considered, which can be written as:

$$m_p \frac{DU_p}{Dt} = \sum Forces \qquad (2.116)$$

This equation is also called the (B-B-O) equation, as it includes effects studied by Basset, Boussinesq, and Oseen (Kuo & Acharya, 2012). $\sum Forces$ are the forces acting on the particle, and affect the particle acceleration, due to the differences in velocity between the particle and fluid, as well as, the displacement of the fluid by the particle. Such forces are, but not limited to: the drag force, the buoyancy force, the centripetal, and Coriolis forces, the added mass forces, namely virtual forces, i.e. the force that accelerates the virtual mass of the fluid in the volume occupied by the particle, the pressure gradient forces, the Basset force, and lastly the external or body-forces (e.g. gravity). FLUENT™, as well as, the majority of computational codes, integrate the simplified form of the (B-B-O) equation , by considering mainly, the drag and the gravity forces, keeping the other forces (stated above) as an additional option subject to the user choice. Equation (2.116) becomes:

$$\begin{aligned} & m_p \frac{DU_p}{Dt} = \frac{\pi}{8} d_p^2 \rho C_D \left| U_p - U \right| (\overrightarrow{U_p} - \vec{U}) + F_{gravity}, \\ & where, \qquad (2.117) \\ & m_p = \frac{\pi}{6} d_p^3 \rho \end{aligned}$$

The momentum exchange is computed by examining the change in momentum of a particle, as it passes through each control volume. This momentum exchange appears as a momentum source term ($\widetilde{\dot{S}_u}$) in the continuous phase momentum balance equation, and in any subsequent calculations of the continuous phase flow field:

$$\frac{DS}{Dt} = -\sum F = -\left(F_{Drag} + F_{others}\right)\dot{m}_p \Delta t \qquad (2.118)$$

where ($\dot{m}_p$) is the mass flow rate, and (Δt) is the integration time step, since as mentioned previously, it is a Lagrangian approach; and thus, the trajectory equations, and any auxiliary equations describing heat or mass transfer to/from the particle, are solved by stepwise integration over discrete time steps, i.e. the integration of time of equation (2.116) (ANSYS, 2011).

Regarding the mass and heat transfer, as explained in the two-stage approach, during the first stage the droplet will heat-up without evaporation till it reaches a fix/pre-set temperature; this temperature is the vaporization temperature, and can be chosen as the flash point. Accordingly, there will not be a mass transfer/exchange, and only the heat transfer/exchange will be considered. During this stage, the rate of change in the temperature is governed by the convective heat transfer (Q_C), and the radiative heat transfer (Q_R) as following:

$$m_p c_p \frac{DT_p}{Dt} = \underbrace{hA_p(T_\infty - T_p)}_{Q_C} + \underbrace{\varepsilon_p A_p \sigma (T_R^4 - T_p^4)}_{Q_R} \qquad (2.119)$$

where (h) is the heat transfer coefficient evaluated from the Nusselt number(2.60), (ε_p) is the particle emissivity, (σ) is Stefan-Boltzman constant, (T_∞) is the temperature of the surrounding continuous phase, (A_p) is the area of the particle, (T_R) is the radiation temperature, and ($T_p = G/4\sigma$) where (G) is the incident radiation coefficient. It should be reminded that, equation (2.119) assumes that the particle is at uniform temperature throughout (no internal resistance, see § 2.5). The heat lost or gained by the particle, as it traverses each computational cell, appears as a source or sink of heat term ($\widetilde{\dot{S}_h}$) in subsequent calculations of the continuous phase energy equation:

$$\frac{DS}{Dt} = \sum m_p c_p \frac{DT_p}{Dt} = -(Q_C + Q_R) \qquad (2.120)$$

When the temperature of the droplet exceeds the vaporization temperature, but still below the boiling point, the evaporation starts (second stage), and the mass exchange becomes important. This mass exchange will be determined as detailed in equations(2.55), (2.56), (2.57), and (2.58) yielding to (after substitution) :

$$\frac{Dm_p}{Dt} = K_c A_p \rho_{gas} \ln(1 + B_M) \tag{2.121}$$

where (K_c) is the mass coefficient determined from the Sherwood number. The mass source term ($\widetilde{\dot{S}_m}$) that will be added to the continuity, the mixture fraction or the species transport equation will be:

$$\frac{DS}{Dt} = -\frac{Dm_p}{Dt} \tag{2.122}$$

In the second stage, the heat exchange is calculated using the same formulation as in equation(2.119), except for the addition of the latent heat transfer term associated with the mass transfer (-Q_M), the rate of temperature change; thus, becomes:

$$m_p c_p \frac{DT_p}{Dt} = hA_p (T_\infty - T_p) + \varepsilon_p A_p \sigma (T_R^4 - T_p^4) - \frac{Dm_p}{Dt} h_{fg} \tag{2.123}$$

where (h_{fg}) is the latent heat of vaporization. During the evaporation process, as the particle changes its temperature, the latent heat varies according to:

$$h_{fg} = h_{fg,bp} + \int_{T_p}^{T_{bp}} C_{p,fuel} dT - \int_{T_p}^{T_{bp}} C_{p,gas} dT \tag{2.124}$$

When the droplet temperature exceeds the boiling point, i.e. $T_p \geq T_{bp}$, the mass exchange determination through equation(2.121) is superseded by the following:

$$\frac{Dm_p}{Dt} = \frac{Q_c + Q_R}{h_{fg}} = \frac{hA_p (T_\infty - T_p) + \varepsilon_p A_p \sigma (T_R^4 - T_p^4)}{h_{fg}} \tag{2.125}$$

After rearranging, introducing the Nusselt number correlation, and replacing the Prandtl number term with an empirical constant (Kuo, 2005), equation(2.125) becomes:

$$\frac{D(d_p)}{Dt} = \frac{2}{\rho_f h_{fg}}\left[\frac{2k_g\left[1+0.23\,\mathrm{Re}^{1/2}\right]}{d_p}\left(T_\infty - T_p\right) + \varepsilon_p \sigma (T_R^4 - T_p^4)\right] \qquad (2.126)$$

To summarize the process in the limit of the second stage, equation(2.126) is used for the mass transfer/exchange, and consequently, for the mass source term. The droplet is assumed to stay at constant temperature (T_{bp}), once the boiling rate is applied. As for the heat exchange, the definition introduced in equation(2.123) is used. Hence, the difference will be in the calculation of the evaporation rate (${}^{Dm_p}\!/_{Dt}$) between equations(2.121), and(2.126).

Before ending this section, it should be highlighted that, the vaporization temperature is of course an artificial and arbitrary parameter used to differentiate between heating only and vaporization. In reality, liquid can vaporize at any temperature depending of the pressure; hence, the concept of vapor pressure. However, in this way, i.e. the two stage method, the mass exchange calculation due to vaporization at low temperatures can be neglected; this is cast to save in computational time. Also note that, when the boiling temperature is reached, all the added heat to the particles will be directed to the vaporization, so the droplet temperature does not change any more.

When two-way coupling is applied, an iterative procedure is followed; that is, after the particle trajectory calculation, the continuous flow field is solved again with updated source terms until convergence is reached as graphically shown in ***Figure 26***.

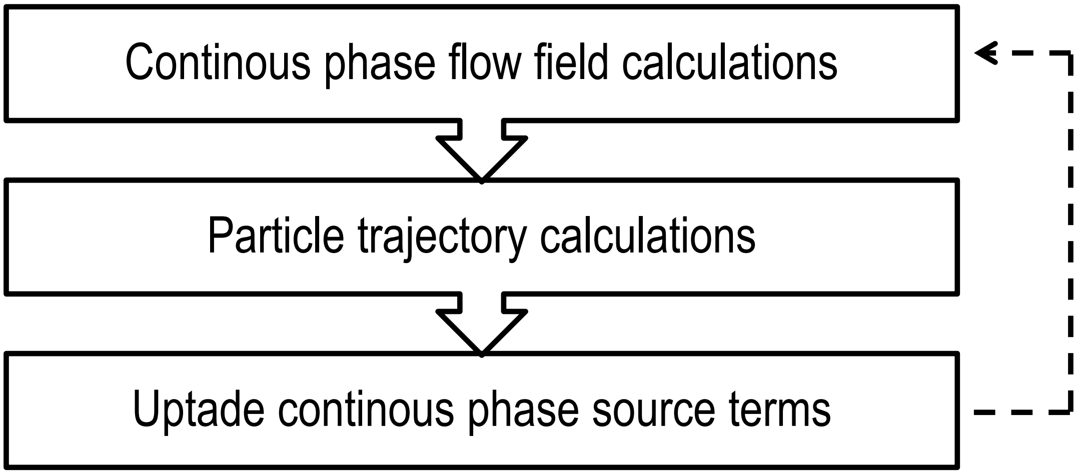

Figure 26 Solution procedure for two-way coupling

CHAPTER 3- FUEL PROPERTIES

In a combustion chamber, the liquid fuel must be injected, vaporized, and mixed with air before combustion can occur. The extent, to which these processes are limiting to combustion, depends highly on the thermo-physical properties of the fuel. Whether, the fuel is liquid or gaseous, conventional or synthetic; the dependence of these processes on the thermo-physical fuel properties stands true and valid. Lefebvre (Lefebvre, 1985) performed a pioneering study on the influence of fuel properties on combustion performance in gas turbines. The main outcome of the study indicates that fuel physical properties, which govern atomization quality and evaporation rates, strongly affect combustion efficiency, weak extinction limits, lean light-off limits, and pollutant emissions. Kretschmer and Odgers (Kretschmer & Odgers, 1986) conducted a study on the influence of low calorific values gaseous fuels in gas turbine combustion chambers. They have concluded that light-up, flame stability, and combustion efficiency, are not only dependent upon the calorific values of the fuel, but also, on the gas composition, i.e. fuel structure.

While the effects of physical and chemical properties of the fuel on combustion can be investigated experimentally, in computational studies, a precise representation of such properties is an essential step for an accurate simulation of spray atomization, and combustion. Despite the fact that, the combustion process in FLUENT™ is solely a gaseous combustion solver (as shown in the flamelet equations, the code considers only the gaseous state of the fuel), the characteristics of fuel spray, and vapor structures, are deemed important, as they dictate the fuel vaporization rate. Consequently, it affects the source terms considered in the continuity, the momentum, the mixture fraction, and the energy balance equations. Fuel spray and vapor structures are predominantly governed by the thermo-physical and the transport properties of the fuel. Therefore, it is imperative to understand the impact of these properties, as well as, the way by which they are interconnected to the different combustion processes.

Generally, fuel spray and vapor structures are typically influenced by 12 thermo-physical and transport properties (Harun, et al., 2012). These proprieties are: liquid density, vapor pressure, heat of vaporization also known as latent heat of vaporization, liquid heat capacity, vapor heat capacity, second-virial coefficient, liquid viscosity, vapor viscosity, liquid thermal conductivity, vapor thermal conductivity, surface tension, and vapor diffusivity. From these 12 properties, they have concluded that only five have significant effects on fuel spray structure, combustion, and emission characteristics, such properties are: vapor pressure, vapor diffusivity, surface tension, liquid density, and liquid viscosity. Moreover, they found that vapor pressure and surface tension have the strongest influence on the mixture preparation process. Similarly, another study performed by

Reitz & Stuart (Reitz, Youngchul, Stuart, & McFarlane, 2008) highlighted the same thermo-physical and transport properties, except for the second-virial coefficient, which is usually used as a correlation in the ideal-gas equation of state, to account for the gas expansion effects. Among their 11 properties, they found that liquid fuel density, vapor pressure and surface tension are the most critical factor for the mixture preparation process.

The aim is thus, to acquire all the properties of interest over a wide range of temperature; so that, they can be used in the combustion modeling. The need to define them as a function of temperature arises from the fact that, a liquid fuel droplet traveling the combustion chamber will be facing a wide range of temperature from its defined inlet temperature to its critical point (point at which the liquid and vapor states merge together, and all their thermodynamic properties become the same). There are however, limitations associated to the solver used during the integration of the liquid fuel properties. FLUENT™, does not account for all of the above mentioned properties, since some are not integrated in its formulation, however, it considers the most critical ones. Moreover, not all the considered properties can be defined as a function of the temperature. Liquid fuel properties considered in FLUENT™ are summarized in ***Figure 27*** to highlight the role of the thermo-physical properties during the combustion process.

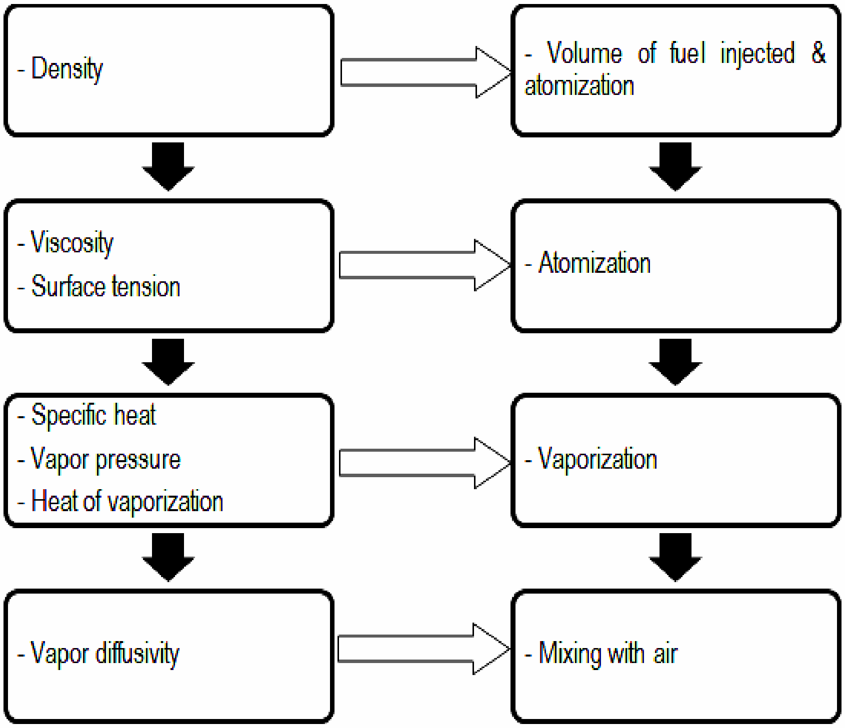

Figure 27 Role of the thermo-physical properties during the combustion process.

The idea is simple; during the definition of the numerical model, these properties should be acquired and introduced in the solver as a function of the temperature. In FLUENT™, the temperature dependence for each property can be accounted for with piecewise linear functions or polynomial functions; however, it is not available for all seven properties. For this reason, density, latent heat of vaporization (can be seen as, the difference between the enthalpy of the saturated vapour and the enthalpy of saturated liquid), and vapor diffusivity (also known as, the binary diffusivity), will be introduced as constant. As for, viscosity, surface tension, vapor pressure, and specific heat, these properties will be introduced as a function of the temperature.

3.1. Conventional diesel fuel properties

Conventional diesel fuels are complex, and in real life they are composed of hundreds to thousands of hydrocarbons compounds. Development of numerical models that can account for all these components is prohibitive, because the model would be too large for the current computational resources. This situation suggests the use of a diesel fuel surrogate. A fuel surrogate is composed of small number of pure compounds, and its behavior matches certain characteristics of the conventional fuel. These characteristics include, both combustion properties (ignition behavior, molecular weight, calorific value, flame temperature, etc.), and thermo-physical properties as detailed in the intro of this chapter. Ultimately, a properly produced diesel surrogate should share nearly the same chemical kinetics, as well as the thermo-physical properties of real diesel. N-Heptane has been widely used as a single component diesel fuel surrogate, because, it has a similar cetane number as the diesel fuel; moreover, its kinetic model is well established (Lin & Tavlarides, 2012).

The main properties of interest for the N-heptane were acquired from NIST online webBook (NIST, 2011). The N-heptane properties were then implemented in FLUENT™ as a piecewise function of temperature from its melting point to its critical point, i.e. temperature range (182 ~ 540 K). ***Table 4*** below shows the properties that were introduced as constants for the N-heptane.

Table 4 N-heptane fuel properties

N-heptane liquid properties $n\text{-}C_7H_{16}$	Boiling temp.(K)	Density (kg/m^3) @ 300 K	Latent heat of vaporization @ boiling point (J/kg)	Binary diffusivity @ ambient conditions (m^2/s)	Molecular weight	Vaporization temp.(K)
Value	371	684	317 000	6.56e-6	100.4	262

Regarding specific heat, viscosity, surface tension and vapor pressure, ***Figure 28*** summarizes them graphically as a function of temperature.

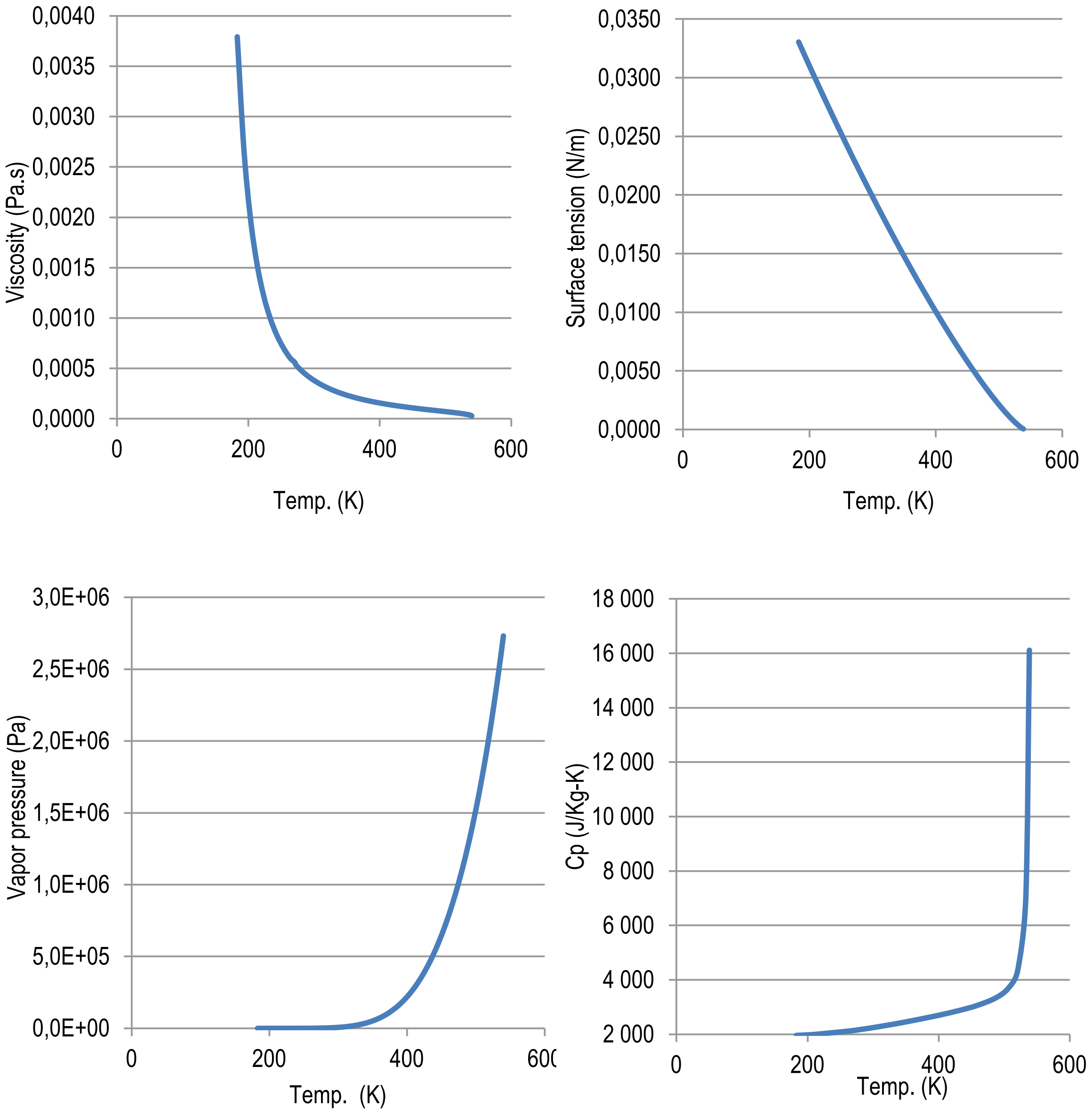

Figure 28 N-heptane fuel properties as a function of temperature viscosity, surface tension, specific heat, and vapor pressure (from left to right in a clock wise fashion)

It should be noted that N-heptane binary diffusion coefficient, was acquired from Yaws' Handbook (L.Yaws, 2013) .

3.2. Biodiesel fuel properties

Concerning the biodiesel case, the property issue is further complicated, due to the lack of studies in this domain. As defined previously, biodiesel fuel is a renewable fuel comprised of mono-alkyl esters of long chain fatty acids. It can be produced from a variety of feedstock, including common vegetable oils (soybean, cottonseed, palm, peanut, canola, sunflower, safflower, and coconut), animal fats (tallow), and sometimes waste cooking oil. Properties of biodiesel, like for any other fuels, are function of the fuel structure; moreover, biodiesel properties vary according to the origin feedstock, and are highly influenced by the molecular structures of the constituent organic compounds (Youssef, Agou, Paquet, & DeChamplain, 2012). Accordingly, many authors predict biodiesel properties either for a very specific feedstock, or for a single temperature. This narrow predictive range can certainly limit the usefulness of their studies.

The biodiesel used in the experimental part, is believed to be made from animal grease; however, the supplier (Rothsay Biodiesel, Canada) did not provide any data related to its composition. All the available information from the supplier are related to some commercial aspects, such as, the conformity with the ASTM standard (D6751-11a), and some certificates including the flash point, the cetane number, and some other properties that are irrelevant to the data needed for the definition of the numerical model. Consequently, an extensive research was performed. The author decided to choose the soybean based biodiesel, since it is widely well studied. Moreover, its properties are available in several publications, and it contains a high degree of unsaturated bonds, which is closer in nature to the animal grease based biodiesel used experimentally. The most common fatty acid methyl esters FAMEs present in the soy-based biodiesels are: methyl palmitate, methyl stearate, methyl oleate, methyl linoleate, and methyl linolenate (L.Huber, Lemmon, Kazakov, Ott, & Bruno, 2009). The reasonable procedure will be to obtain the properties of a soy-based B20 biodiesel blend, and implement them in FLUENT™, exactly as realised with the baseline case (N-C_7H_{16}). Unfortunately, such data for the B20 blend were not found in the literature. To confirm this argument, Professor Gerhard Knothe, who is considered as one of the pioneers in the biodiesel fuel domain, was contacted (Knothe, 2005). He confirmed to the author this lack of data for the B20, as well as, for the B50 blend (private communication though an email, December 2012).

In view of the above, a second approach was adopted, such that, the use of both B100 and heptane properties; then, mix them together using the liquid mixing laws in FLUENT™ based on the volumetric percentage of the fuel (to remember that, a B20 blend contains 20% biodiesel and 80% conventional diesel on a volumetric basis). Hence, the density of the liquid mixture will be treated with the volume weighted mixing law (with the incompressible assumption for a liquid), the viscosity, the surface tension, and the specific heat with the mass weighted law, and lastly, the vapor pressure with Raoult's law.

Soy-based B100 properties were gathered from three different sources, and integrated into the solver as piecewise functions over a range of temperature, from its pour point to its critical point, i.e. 270~780 K. The first source is Dr. Marcia from the National institute of standards and technology (NIST), because she developed a model for the prediction of the thermodynamic properties of a soy-based biodiesel (Huber, W.Lemmon, Kazakov, Ott, & Bruno, 2009). However, her article does not include biodiesel properties as function temperature; accordingly, she was contacted, and she voluntarily developed a bubble point curve containing the vapor pressure, the specific heat, and the viscosity for the B100 as a function of temperature. The second source is Rothsay Biodiesel (the supplier), who provided the density, and the flash point which will be used as the vaporization temperature. The last reference is a group of researchers, who predicted the properties of three different B100 biodiesels: Canola based B100, Palm based B100, and Soy-based B100 (Harun, et al., 2012). Their study was used to define surface tension, and binary diffusivity. ***Table 5***, ***Figure 29*** and ***Figure 30*** show a graphical summary of all the required properties for the numerical model.

Following the integration of both B100, and N-heptane properties, liquid fuel droplets will be treated as multi-component particles. The effects of the liquid droplet properties are mainly manifested inside the mass and energy equations. In order to understand how the solver works, and the difference between the droplet formulation used in the N-heptane case (single component case), and the multi-component formulation; the mass, and the energy equations will be presented when multi-component type particles are chosen.

Table 5 Soy-biodiesel fuel properties table

Soy-based B100 biodiesel liquid properties	Boiling temp.(K)	Density (kg/m^3) @ 300 K	Latent heat of vaporization @ boiling point (J/kg)	Binary diffusivity @ ambient conditions (m^2/s)	Molecular weight	Vaporization temp.(K)
Value	624	873	125 000	1e-8	N/A	450

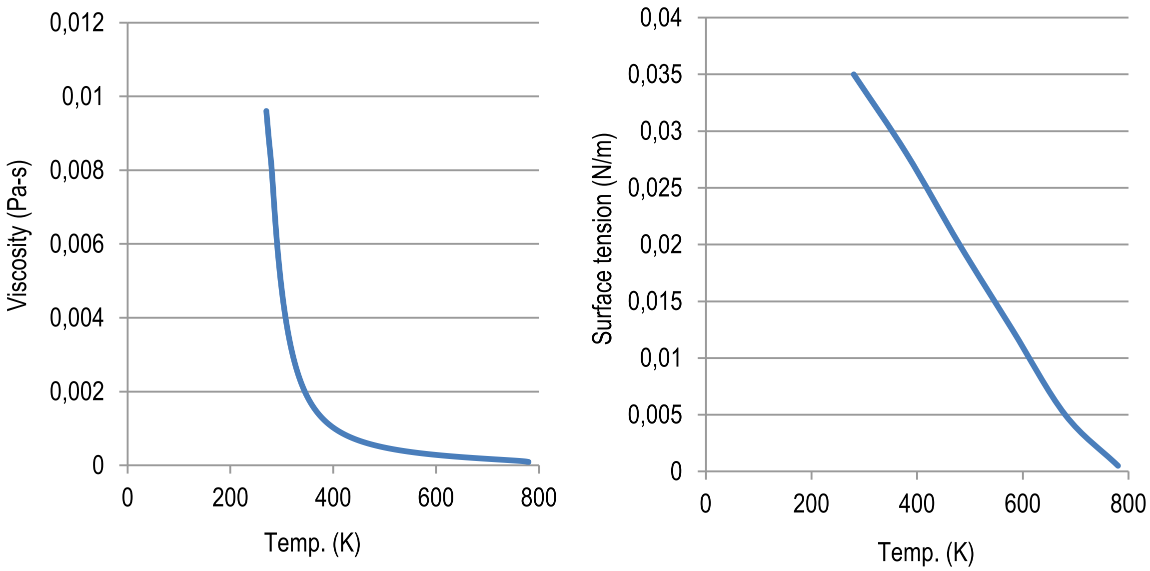

Figure 29 B100 fuel properties as a function of temperature viscosity, surface tension (from left to right)

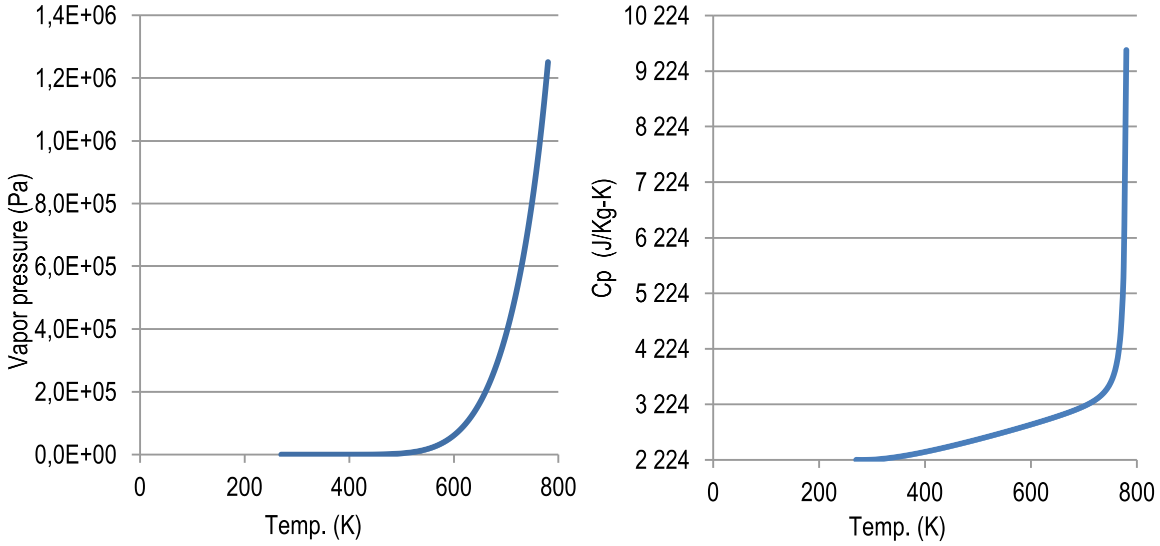

Figure 30 B100 fuel properties function of temperature, vapor pressure and specific heat (from left to right)

From equations(2.121), (2.123), and(2.125), when the droplet temperature is below the boiling point, equation (2.121) becomes :

$$\frac{Dm_i}{Dt} = K_{c,i} A_p \rho_{gas} \ln(1 + B_{M,i}) \tag{3.1}$$

where (m_i) is the mass of the component (i^{th}) in the droplet, ($K_{c,i}$) is determined from equation(3.2) and ($B_{M,i}$) from equation(3.3), as following:

$$Sh = \frac{k_{c,i} d_p}{D_{binary,i}} = 2 + 0.55 \operatorname{Re}_p^{1/2} \operatorname{Pr}^{1/3} \tag{3.2}$$

$$B_{M,i} = \frac{Y_{i,S} - Y_{i,\infty}}{1 - Y_{i,S}} \tag{3.3}$$

From these equations, it is observed that the vaporization rate of component (i^{th}) requires the component concentration, or its mass fraction at the droplet surface. This is achieved through Raoult's law, which is considered as the simplest form of the vapor-liquid equilibrium theory (ANSYS, 2011).

The definition of the starting point for the engagement of the boiling process in the multi-component theory differs from what was introduced in the single droplet. When multicomponent particles are defined, the boiling point of the components is used only as a reference temperature for the latent heat of vaporisation like in equation(2.124). Hence, the boiling starts when the sum of the partial pressures for each component at saturation reach the total fluid pressure. The definition of the saturation pressure curve is therefore, essential for the boiling in the theory for multicomponent particles. When the total vapor pressure at the droplet surface exceeds the cell pressure, the multicomponent droplet enters the boiling regime, accordingly, the boiling rate will be determined from:

$$\frac{Dm_i}{Dt} = x_i \frac{\pi d_p K_g}{c_{pg}} Sh \ln\left(1 + \frac{c_{pg}(T_\infty - T_p)}{h_{fg}}\right) \tag{3.4}$$

where (x_i) is the mole fraction of (i^{th}) component in the droplet, and (Sh) is the Sherwood number. The energy equation for the multi-component droplets is casted similarly to the single component particle energy equation:

$$m_p c_p \frac{DT_p}{Dt} = hA_p(T_\infty - T_p) + \varepsilon_p A_p \sigma (T_R^4 - T_p^4) - \sum \frac{Dm_i}{Dt} h_{fg} \tag{3.5}$$

The only difference is the summation term for the latent heat transfer. The (Dm_i/Dt) is computed from equation(3.1) or (3.4) subject to the boiling threshold, exactly as explained in the two-stage approach.

In FLUENT™ when the multi-component droplet type is chosen, the user will have to specify the mass fraction of the (i^{th}) component in the mixture, as well as, specifying the gas-phase species to be evaporated. This is essential for the solver, in order to be able to compute the species fractions involved in Raoult's law, mass weighted law, and volume weighted law, as well as, the equations shown above.

CHAPTER 4- MODEL DESCRIPTION

This part of the manuscript discusses the definition of the numerical model. The previous chapters aimed to prepare the reader to a better comprehension of the theoretical and numerical combustion processes. The goal is to fairly introduce the methodology of the various techniques used, and the parameters undertaken in the offered numerical simulation.

Spray wall interaction is considered in this study, and will be treated as a part of the boundary condition section. It should be noted that droplet collisions and coalescence are not encountered in this study. Based on a study by Reitz (Reitz & Diwakar, 1987), the droplet coalescence is less important in hollow cone sprays, due to the low spray density; and thus, this simplification is generally agreed on for such configuration (i.e. hollow cone sprays).

This section provides an overview of the different sub-models selected in the present study, which includes the real geometry, the configuration of the simulation domain (mesh), the boundary conditions, the numerical schemes, and the various sub-models describing turbulence effect, multiphase interaction, droplets breakup, evaporation, and combustion.

4.1. Geometry and Mesh

The experimental test rig consists of a combustor, made of quartz, having the shape of a cylindrical tube connected to a steel metal cone at the exit, as shown in ***Figure 31***. The cylindrical quartz tube was purchased from (Technical Glass Products Inc.); whereas, the exit cone was manufactured at Université Laval workshop, based on drawings from (Rolls-Royce Canada - RRC). The injector is mounted on a base plate at the inlet of the quartz tube, assembled, and confined inside a metal casing, which represents the main and only entrance of the air to the combustion chamber, as demonstrated in ***Figure 32***. Dry and filtered shop air is fed through a long inlet cone to prevent generation of any undesired flow disturbance at the combustor air inlet. In other words, the air participating in the combustion process is solely coming from the injector. This injector, namely the WLE T60 dual fuel injector, was developed for the injection of liquid and gaseous fuels. Further details about the injector cannot be disclosed, due to the patent protection agreement between the project partners.

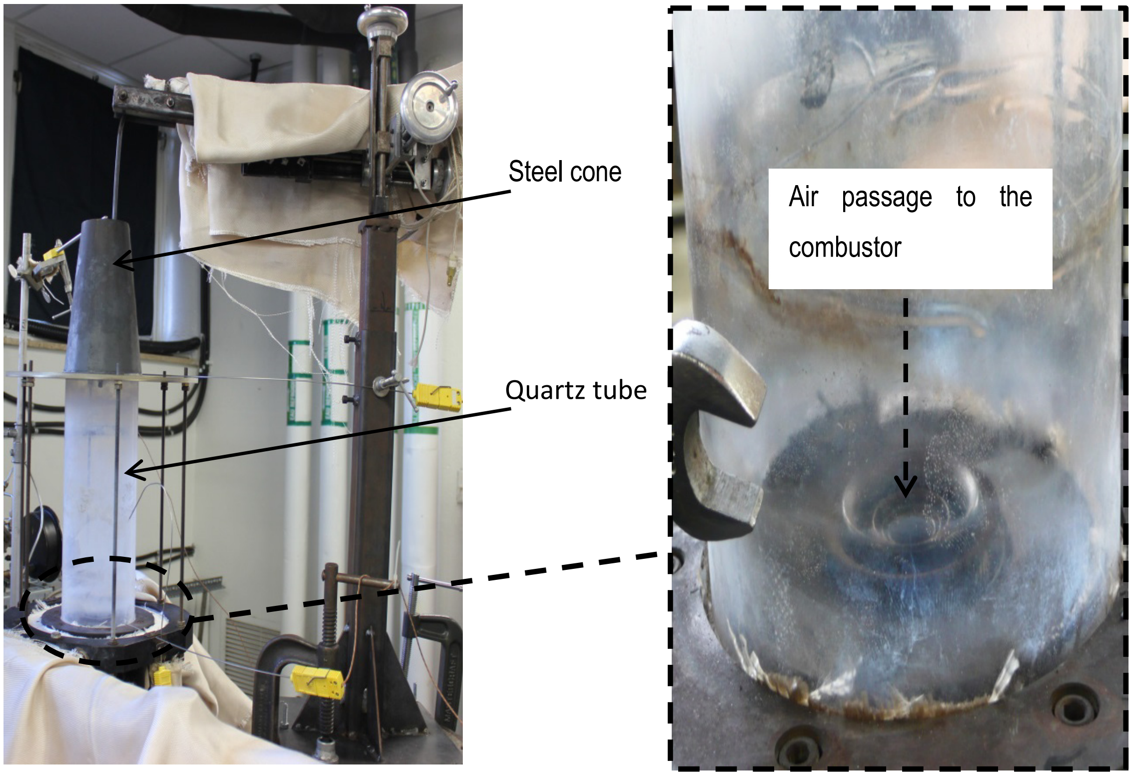

Figure 31 Experimental test rig configuration @ Ulaval laboratory, quartz tube, steel cone and the injector

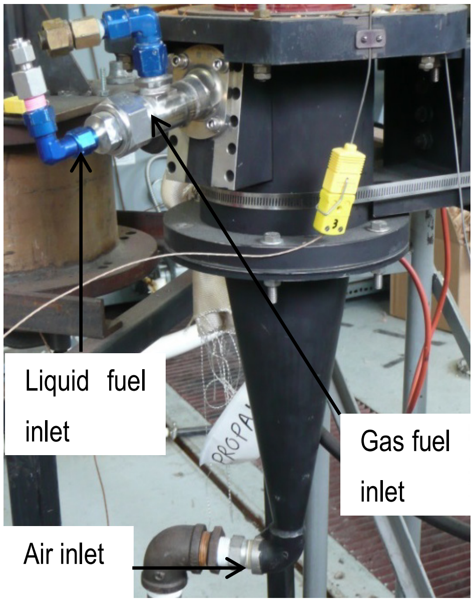

Figure 32 WLE T60 dual fuel injector and the air casing

Table 6 below summarizes the main dimensions, and the material properties of the combustor.

Table 6 Material properties and dimensions, Source: Technical Glass Products Inc., ANSYS FLUENT™ library.

Dimension /Properties	Quartz tube	Steel cone section
OD (mm)	115	122.7
ID (mm)	110	110
Exit diameter (mm)	110	60.5
Length (mm)	300	188
Thickness (mm)	2.5	6.35
Density (kg/m^3)	2 200	8 050
Thermal conductivity @ 20 °C (W/m -°C)	1.4	16.27
Specific heat (J/kg -°C)	670	502.5
Material emissivity	0.93	0.85

Properties from ***Table 6*** above are used during the definition of the boundary conditions to model the combustor wall. Density, thermal conductivity, specific heat, emissivity, and the thickness of the steel sheet, as well as, the quartz tube are of a great importance to the radiation sub-model.

The computational domain was created using GAMBIT™, which is a mesh generating software. The real geometrical dimensions were used, without any scaling for the injector, quartz tube, or the exit cone. The 3D generated mesh has (5.3 million) elements, with a total volume of (0.005443 m^3), and was generated with two schemes. The first scheme is the Tet/Hybrid un-structured mesh, leading to a tetrahedral volume elements used to model the injector. As for the rest of the combustor, the cooper scheme was integrated, and Hex/Wedge elements were obtained, which is a structured type mesh. The zones close to the injector vicinity were fairly refined. Thereafter, the grid is progressively coarsened up to the chamber exit, with a growth rate of (1.1). ***Figure 33*** shows total and partial views of the meshed grid in 3D, and 2D. ***Table 7*** summarizes the main parameters describing the mesh grid used.

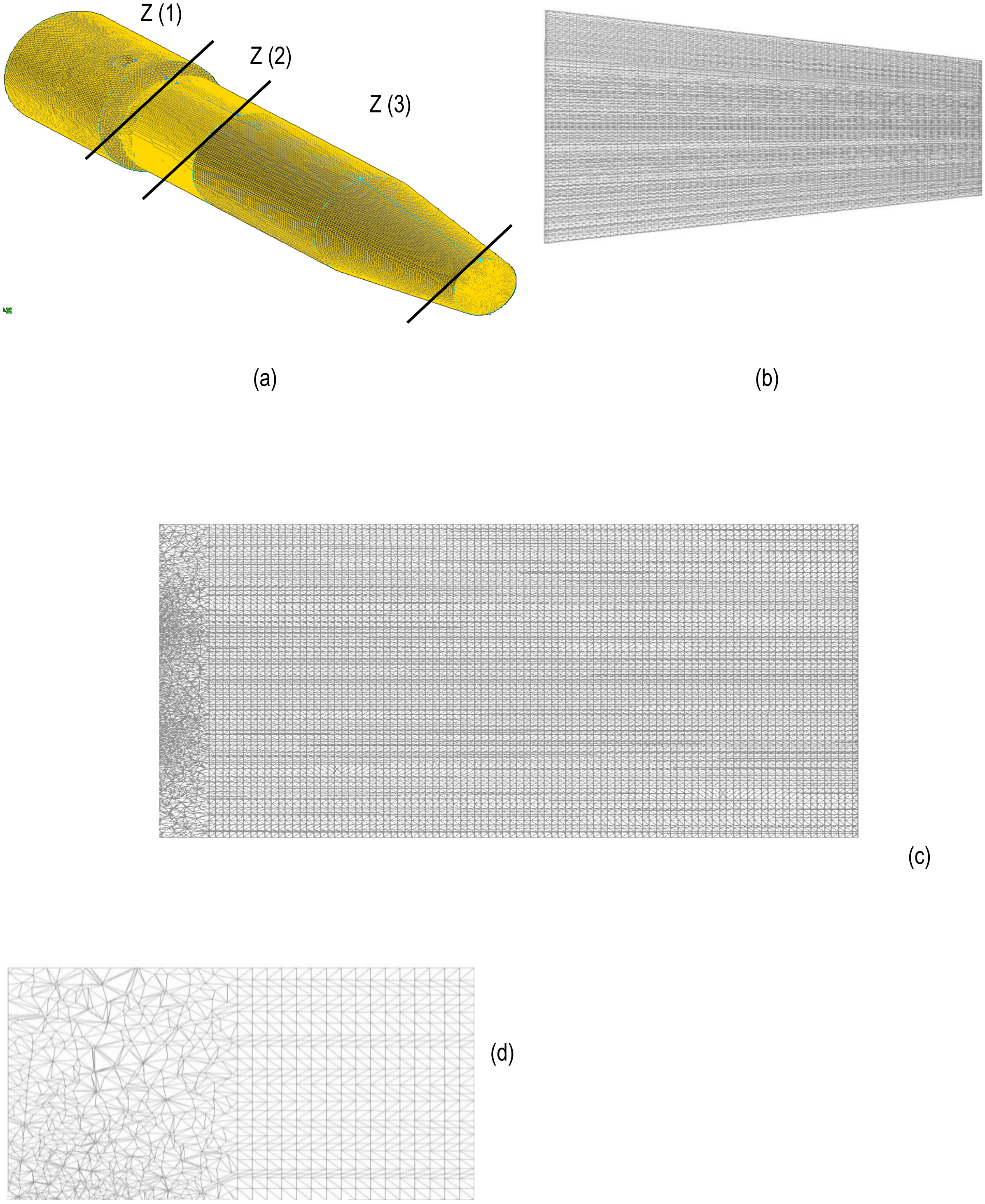

(a)

(b)

(c)

(d)

Figure 33 Different views of the meshed grid: (a) the entire 3D computational domain, (b) the structured mesh for the cone at the exit, (c) the combustor with the interface between the structured and un-structured mesh and (d) Zoom-in on the interface

Table 7 Parameters describing the meshed grid

Parameter		Values
Number of cells		5 325 109
Number of nodes		1 483 414
Element size	Zone (1)	1 mm
	Zone (2)	2 mm
	Zone (3)	3 mm

In principle, the desired level of numerical accuracy can be obtained by using a sufficiently fine grid. Nevertheless, care must be taken to avoid any significant increase in computational time associated with unnecessary refined grids. Usually, it is recommended to perform the same simulations using different levels of grid resolutions, while, keeping the geometry and boundary conditions unchanged. This practice allows the assessment of the overall performance of the computational domain, as well as, the investigation of the grid independence.

However, this practice is time and resources consuming processes, given the fact that the overall mesh size exceeds 5 million cells. In view of the above, the author decided to rely on the conventional quality pre-mesh measurement tools that are already integrated in FLUENT i.e. aspect ratio, skewness, and smoothness. This decision based on previous experience considerably affected the duration for all numerical calculation.

4.2. Flow configuration and Boundary conditions.

The overall matrix of the numerical calculations is summarized as following:

- Non-reacting flow case: This case is performed using the n-heptane fuel as a surrogate for conventional diesel. It is a preliminary case, during which the author can be familiarized with the various injection techniques available in the solver. FLUENT™ offers two categories for the atomization process within the discrete phase model DPM. The first and the simplest is the injection technique with no atomization, which can be modeled through five different injection sub-models: (a) single injection point, (b) group injection, (c) hollow cone, (d) solid cone, and lastly, (e) surface injection model. The choice among one of these sub-models depends on the degree of accuracy required, and the available information for the spray. The injection technique no atomization requires accurate knowledge of the spray, in terms of particle velocities (axial, radial, and tangential), droplet mean diameter (D10), droplet distribution, and spray cone angle. Hence, it is usually implemented when PDPA or PIV data are available for a specific injector and type of fuel. Due to its easiness, this technique is widely used, especially, when the coupling with combustion is necessary. However, due to the lack of the above mentioned information on the performance of the WLE T60 injector operated with biodiesel, the atomization technique with the first and secondary breakup mechanisms was chosen. This technique is considered more complicated than with the no atomization one, and it was mainly developed to validate the atomization process for liquid jets. One of its main advantages, as shown in the modeling theory (see § 2.4.3.1) for the combined (RT-KH) model, is the semi-empirical correlations and analogies used; thus, the interference no user input is required, i.e. limiting as much as possible any inputs from the user.

- Reacting flow cases: ***Table 8*** below summarizes the reacting flow cases, which involve the combustion of conventional diesel, and biodiesel blends. These cases are used for the validation of emissions, and wall temperature profiles, with the experimental test results.

Table 8 Test matrix for the reacting flow cases

Case reference	Case (1)	Case (2)	Case (3)	Case (4)
Fuel type	n-C_7H_{16}	n-C_7H_{16}	B20	B20
Overall (ϕ)	1	0.8	1	0.8

In order to ensure an accurate validation of the experimental test results, experimental operating conditions for each of the reacting cases were acquired, and used for the numerical model. ***Table 9*** shows the commonly used operating conditions for all the cases.

Table 9 Oxidizer operating conditions

Oxidizer	Combustor pressure drop ($\frac{\Delta P_{3-4}}{P_3}$)	P_3, P_4 (Pa)	(T_3) Inlet air temp. (K)	Mass flow rate (g/s)
Air	3.6%	105 000, 101 325	300	23

Values for the combustor pressure drop, the air inlet temperature, and the (P_4) were agreed on with RRC engineers, and they are related to the design criteria of the injector as well as, the test rig. The value of (P_3) is determined from the combustor press drop percentage ($P_3 - P_4 / P_3$), and the air mass flow rate is calculated from the basic equation of the flow through a hole (Lefebvre, 1998):

$$\dot{m} = (AC_D)\sqrt{2\rho_{air}(P_3 - P_4)} \tag{4.1}$$

where the product (AC_D) is the effective area acquired from RR internal data report, and the density of air ($\rho_{air} = P_3 / R_{air}T_3$).

For simplicity and to avoid repetition of the listed data, only the calculating sequence to obtain the operating conditions of the fuel for the n-heptane case at (ϕ=1) will be presented; and then, the differences between the numerical cases will be highlighted correspondingly.

The balanced global reaction mechanism for the n-C_7H_{16} at stoichiometry, without dissociation, can be expressed as:

$$C_7H_{16} + (11O_2 + 41.36N_2) \rightarrow 7CO_2 + 8H_2O + 41.36N_2 \qquad (4.2)$$

Using equation(4.2), the $(A/F)_{stoic}$ can be calculated from equation(2.71), and it is equal to (15.6). Consequently, if the value of the equivalence ratio (ϕ), and the operating air mass flow rate are known, the fuel mass flow rate can be determined from equation(2.72) . ***Table 10*** summarizes these conditions, which will depend mainly on the chemical kinetic mechanism used (to obtain the fuel composition), and the equivalence ratio according to the test matrix. Indeed, the air inlet pressure, temperature, and mass flow rate will be maintained at (105 000 Pa, 300 K and 23 g/s) for all the numerical cases, this was fixed to preserve the overall pressure drop. Thus, the only variable will be the fuel mass flow rate.

Table 10 Fuel operating conditions for the reacting flow cases

Fuel Type	Global (ϕ)	Fuel inlet temp.(K)	Calculated fuel mass flow rate (g/s)	Injected fuel pressure (Pa)	Fuel velocity (m/s)
n-C_7H_{16}	1	300	1.509	101 434	0.565
n-C_7H_{16}	0.8	300	1.208	101 394	0.452
B20	1	300	1.509	101 391	0.388
B20	0.8	300	1.208	101 367	0.312

It should be highlighted that for the B20 cases, the above mentioned values should not be similar the n-heptane cases. Because, the reaction mechanism is not the same (as it shall be described in section 4.3.1), the fuel and reactant compositions are not the same; and therefore, the $(A/F)_{stoic}$, as well as, the fuel mass flow rate should not to be equal. However, in the experimental test, due to some difficulties faced during the determination of the actual B20 fuel composition, equal mass flow rates were assumed. Accordingly, to ensure matching the experimental boundary conditions, the CFD followed this assumption. Concerning the calculation of the injected fuel pressure, the flow number equation was used, such that:

$$FN = \frac{Q}{\Delta P_{inj.}^{0.5}}, \text{ and } Q = \dot{m}_f \big/ \rho_f \qquad (4.3)$$

where (Q) is the volume flow rate, and $\Delta P_{inj.} = (P_{fuel} - P_4)$. The values of the injected fuel pressure, will serve in the calculations of the fuel velocity magnitude, which in return, will be used to calculate the relative velocity, between the fuel and the air, required by the solver during the injection sub-model definition.

4.2.1. Model set up

The parameters to set up the model are presented in the form of a tutorial. This methodology is used, to simplify the offered data, and to make it useful for any future research. ***Table 11*** below addresses the main solver parameters for the non-reacting flow case, using the N-heptane at (ϕ =1). Choosing this case to represent the solver parameter is justified, by the fact that, several parameters used in this case were commonly shared between all the numerical cases. The remaining differences, between the various reacting flow cases, will be mainly in the combustion sub-model, and the composition of the mixture.

Table 11 Solver parameter for the non-reacting flow case

Case Setup	Tab		Setting
General	Solver		Steady fashion, 3D, Pressure solver, Double precision.
Model	Chemistry		Species transport $\Rightarrow$ For the non-reacting flow. Steady laminar flamelet approach $\Rightarrow$ For the reacting flow.
	Turbulence model		Realizable (*k-ε*), Standard wall function, Default model constant.
	Radiation		N/A for the non-reacting case $\Rightarrow$ Adiabatic system P1 radiation model $\Rightarrow$ For the reacting flows
	Discrete phase	Interaction	Interaction with the continuous phase $\Rightarrow$ On Number of continuous phase interactions per (DPM) iteration : 20

		Tracking	Max. number of steps : 1e+7 Length scale : 8e-4 (m), this represents 8% of the smallest element size	
		Drag Law	Dynamic drag law	
		Particle Treatment (1)	Unsteady Tracking Particle time step size : 1e-4 ⟹ For non-reacting flow Number of time step size : 1	
		Physical	Two way turbulence coupling(2) Pressure dependent boiling	
		Breakup	Combined RT-KH (with the default sub-model constants)	
		Numerics	Tolerance: 1e-6 Max. Number of refinements : 20	
Materials	Mixture		Heptane–air ⟹ For non-reacting flow PDF ⟹ for the reacting flow cases	
	Fluid		Air	
	Solid	Combustor	Quartz (for physical properties refer to ***Table 6***)	
		Injector and exit cone	Steel (for physical properties refer to ***Table 6***)	
	Droplet material		Single component ⟹ Liquid heptane Multicomponent ⟹ B20 blends	
Boundary Condition (BC)	Air mass flow inlet (Total 23 g/s)	Main air inlet	Mass flow rate : 19.7	Turbulence intensity : 10% DPM: escape BC
		Flare cooling holes	Mass flow rate : 3.3 (16% of the total air flow rate goes through the cooling	

			holes of the injector)	
	Pressure outlet	Combustor exit	Backflow Turbulence intensity : 10% DPM : escape BC	
	Walls	Combustor	DPM BC: wall-film(3), no-slip walls	
		Injector	DPM BC: reflect(4), no-slip walls	
Solution	Pressure discretization		Coupled algorithm	
	Spatial discretization		2nd order for all equations	
	Flow solving fashion		Pseudo transient (with the default under relaxation factors)	
	DPM under relaxation factor		0.1	
Injection	Injection Type		Air-blast atomizer	
	Particle type		Droplet Multicomponent	
	Turbulent dispersion		Discrete random walk model, random eddy lifetime	
	Half spray angle(5)		15 degree	
	Fuel flow rate (g/s)		As per ***Table 10***	
	Injection position		9 mm from the real injector nozzle tip ***Figure 34***	

	Relative velocity(6)	Subject to the calculation refer to equation (4.5)
	Primary breakup model	Solver defaults (7)
	Evaporating species particle material(8)	For N-heptane cases : n-C_7H_{16} For B20 Cases : 20% n-C_7H_{16} + 80% B20

Most of these settings will remain unchanged for the rest of the cases, unless otherwise specified. Some of the above mentioned parameters were calculated, while, others were chosen based on FLUENT™ User's guide & best practice. In both situations, the reader can clearly identify almost all these parameters, as they were already detailed in the previous sections. In the following sub-section we will review the most important ones.

(1)Particle treatment: The discrete phase is solved in a Lagrangian frame; hence, particle trajectory equations, and any auxiliary equations describing mass, momentum, and heat transfer to/from the particles, are solved with stepwise integration over discrete time steps. Therefore, the accuracy of the discrete phase calculation highly depends on the time accuracy of the integration, as well as, the degree of coupling with the continuous phase. There is no best practice or calculation method to define these parameters, as they highly depend on the physics of the problem. However, large time step sizes, or large number of time steps, will allow faster penetration of particles in the domain. For the diesel cases the time step size was set to (0.1), whereas, for the biodiesel cases it was set to (0.01) to allow sufficient residence time of droplets inside the domain. Indeed B20 blends will need more time to evaporate than the conventional diesel fuels, because their flash points, density, and surface tension are higher.

(2)Two way turbulence coupling: Particles can damp or create turbulent eddies; this option allows the subtraction, of the work done by the turbulent eddies on the particles, from the formulation of the turbulence kinetic energy (ANSYS, 2011).

(3)& (4) DPM boundary condition: Based on some visual results from the experimental test rig, the fuel was observed highly colliding with the combustor wall, forming a thin film. This occurs certainly at the start-up, where the temperature is not high enough to evaporate all the fuel. To capture this phenomenon, the walls of the combustor were modeled as wall-film walls. Implementing numerically this technique, allows the spray impingements, forming a thin film layer based on their impact energy. This assumption is not valid in the simulation of the reacting flow cases; instead, the wall-jet type will be adapted. Wall-jet boundary condition is more suitable when droplets impact a hot surface, preventing it from forming a thin film layer, but rather, reflected or stuck to the wall, depending on their velocities, and directions.

(5)Half spray angle ($\alpha/2$): This angle is required to set the initial trajectory of the film as it leaves the injection orifice, as shown previously in (***Figure 4 b***). Since, in our model the injector nozzle tip exit is confined inside the inner injector wall, the liquid film leaving the injector is expected to follow this inner surface, due to the centrifugal force, as well as the Coanda effect. Due to this reason, the half spray angle was measured from the geometry of the injector as highlighted schematically in ***Figure 34***.

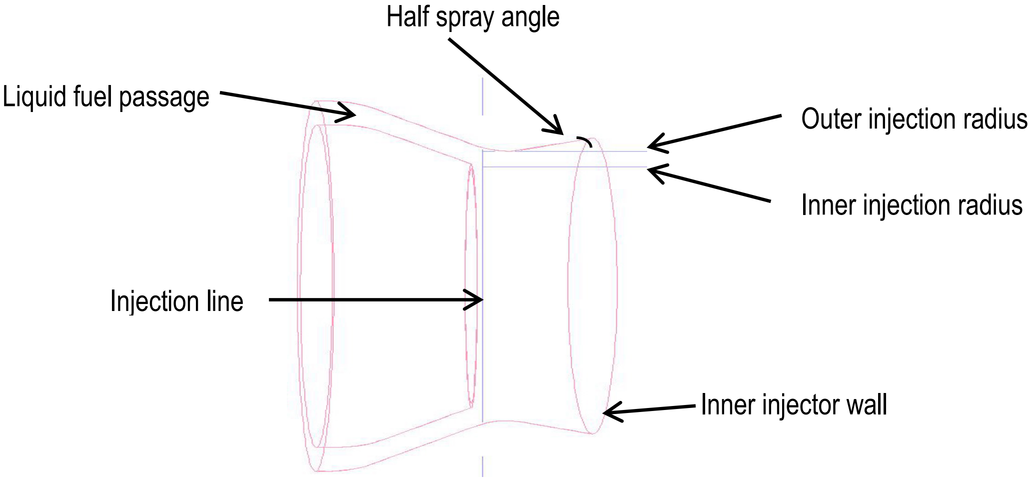

Figure 34 Schematic section of the injector

(6)Relative velocity: The atomization sub-models is capable of predicting the droplet velocities, diameter, and distribution. For realistic simulation of atomization, this model uses the parameters from actual physical atomizers, such as but not limited to, fuel mass flow rates, orifice diameters (OD and ID), and injection relative velocity. The relative velocity between the injected fuel and the surrounding was calculated from the classical law of momentum conservation:

$$\dot{m}_f U_f + \dot{m}_g U_g = (\dot{m}_f + \dot{m}_g) U_{mixture} \tag{4.4}$$

Fuel and air mass flow rates are known, the injected fuel velocity can be determined from the ($\Delta P_{inj.}$) using Bernoulli's equation. The (U_g) was acquired from a cold flow simulation performed only with air, as a result, the air velocity profile at the injector tip was obtained as highlighted in ***Figure 35*** . Therefore, the only unknown in equation(4.4) is the ($U_{mixture}$), which is the relative velocity required for the injection definition. In fact, the cold flow simulation case used to measure the (U_g) is not a special numerical case, it is simply the converged solution of the cold flow using only the flow, the (*k*) and (ε) equations, prior to activate the rest of the numerical sub-models. In practice, it is always better to start the simulation from a converged cold flow solution, to ensure that the velocity and the pressure field were properly captured, before engaging further complex sub-models.

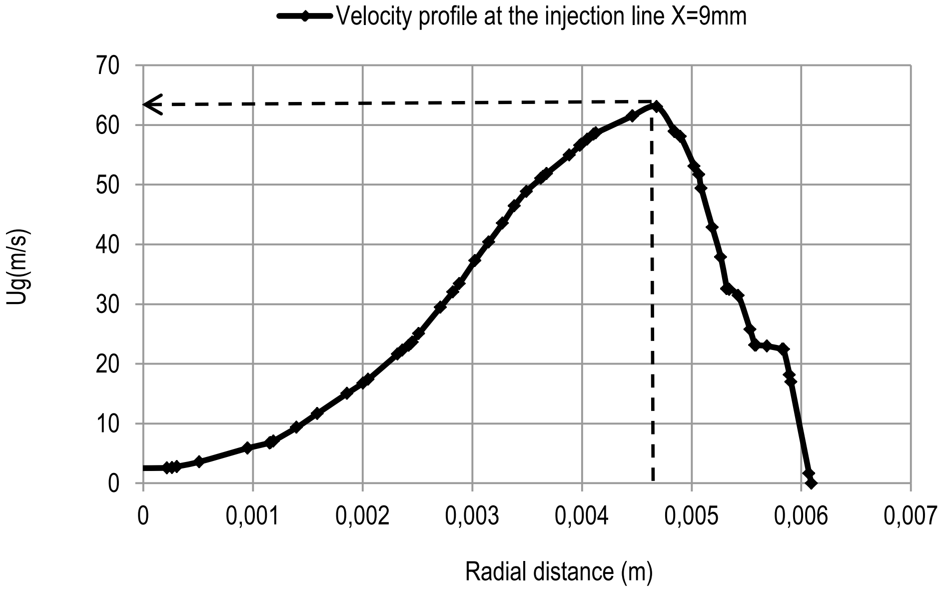

Figure 35 Air velocity profile from the cold flow simulation

The (U_g) found (~ 65 m/s), and the (U_f) ~ (0.565 m/s) for the heptane case (ϕ=1). This low value of (U_f) was expected, since in the air-blast atomizers, the quantity and velocity of the air are the major drive forces for the breakup of the fuel; consequently, the injected fuel pressure and the fuel velocity are relatively small. Sometimes, the term containing the product ($\dot{m}_f U_f$) in equation(4.4) can be neglected, which will lead to the following equation developed by (Lefebvre, 1989) for this type of injector:

$$U_R = \frac{U_g}{(1 + \frac{\dot{m}_f}{\dot{m}_g})} \tag{4.5}$$

Both equations gave almost the same values, that is, (U_R ~61 m/s) for the (ϕ=1) cases, and (U_R ~ 62 m/s) for the (ϕ=0.8) cases.

(7)Primary breakup model constants: The primary breakup mechanism in FLUENT™ is based on the LISA model, explained in the sheet atomization model for hollow cone spray (see § 2.4.3.1). The four main parameters needed to initiate the calculations are: the diameter and thickness of the ligaments, the breakup length, and the initial dispersion angle. Equations used to determine the primary breakup, and their related constants, are based on empirical correlations, and deemed to give representative description of the spray behaviour. In FLUENT™, these equations differ slightly form the LISA preciously mentioned formulations. The first input parameter is the sheet breakup constant (the ratio of $\ln\left(\eta_b/\eta_0\right)$ in equation(2.31)), and it is set by default to the value of (12). Regarding the ligament diameter, FLUENT™ replaces equation(2.32) by the following:

$$d_L = \frac{2\pi C_L}{Ks} \tag{4.6}$$

where (C_L), namely the ligament constant is equal to 0.5 by default. For the ligament thickness, equation (2.33) is used. Lastly, the specification of the initial dispersion angle is also required, by default it is (6°); the initial velocities of droplets are varied within this dispersion angle.

(8)Evaporating species: For biodiesel, as stated in the last paragraph of section (3.2), for the multicomponent theory, the user has to manually specify the evaporating species, as well as, the liquid mass fractions of the multicomponent particles. Based on the surrogate mechanism used for the B20 blends cases, the methyl decanoate (MD) is chosen to represent the biodiesel (reactions, mixture compositions, and chemical mechanisms will be detailed in the coming section). To define the B20 blend, 20 % of MD ($C_{11}H_{22}O_2$) will be mixed with 80 % of n-heptane (n-C_7H_{16}) on a volumetric basis. ***Table 12*** shows the liquid mass fractions defined in FLUENT™ for the B20 cases. Regarding the n-heptane cases, the user has to choose only the evaporating species for the solver library.

Table 12 Mass fraction calculations for the B20 blend cases

Species	Molecular weight (g/mol)	Molar fraction for the B20	Mass of the species based on the molar fraction (g)	Mass fraction input to the solver
$C_{11}H_{22}O_2$	186	20 %	186 × 0.2 = 37.2	0.317
n-C_7H_{16}	100	80 %	100 × 0.8 = 80	0.683
Sum			∑=117.2	∑=1

Lastly, before ending the model set up section, two major steps were performed in all five numerical cases. The DPM affects the continuous fluid flow by being integrated into the flow solver; this can create many instabilities from the numerical point of view, especially, when the main continuous flow solver is based on a steady-state algorithm, and the DPM solver is treated with an unsteady state fashion. These effects can be remedied through the following two steps:

[1] The activation of the Beta-feature, which will give the access to enabling the second step below :

[2] The averaging Node, the averaging DPM source term, and the feature to integrate averaging steps.

These options will allow a stable distribution of the droplet effects on the neighboring mesh nodes; and hence, reduces the grid dependency of the discrete phase model, allowing improvement of the convergence. These features are available only as a text user interface command in ANSYS FLUENT™ v.14, and were highly recommended by ANSYS engineers technical support team.

4.3. Chemical kinetics and Flamelets

Turbulent combustion is then modeled using the steady laminar flamelet approach, which is one of the three techniques available in FLUENT™ for the non-premixed combustion category. This procedure employs mainly two sequences:

- Flamelet generation, and
- Probability density function (PDF) generation/tabulated chemistry approach.

In the flamelet approach, the turbulent non-premixed flame is viewed as an ensemble of thin, laminar, and locally 1D reaction zone flamelets, embedded within the turbulent flow. These flamelets are continually displaced, and stretched within the turbulent medium. The formulation of the flamelet structure is introduced through a coordinate system, where the physical space (*X*) is transformed to the mixture fraction (*Z*) space; in which, (*Z*) itself is transported by convection and diffusion within the flame. Temperatures, species mass fractions, and density will be expressed as a function of the mixture fraction. Flamelet are then embedded into the overall turbulent flame using the probability density function approach. Consequently, an accurate prediction of the mixture fraction field which will lead to the determination of the species concentration in the flame structure will depend on the accuracy and the level of the detail kinetics described in the reaction mechanism.

In the laminar diffusion flamelet model, it is assumed that the structure of the turbulent flame is locally equal to that of a laminar diffusion flame at the same instantaneous mixture fraction (Z_{st}), and the instantaneous scalar dissipation (χ_{st}). The scalar dissipation is used to quantify the departure from equilibrium due to the aerodynamic straining. That is, when the scalar dissipation tends towards zero; the chemistry tends towards the equilibrium. The PDF captures the range/distribution of the time that the fluid spends in the vicinity of the state (*Z*). The PDF describing the temporal fluctuations of (*Z*) in the turbulent flow can be used to compute averaged values of variables that depend on (*Z*) such as: weighted-density, mean species mass fractions, and temperatures (ANSYS, 2011).

One of the main advantages of the laminar flamelet concept is its ability to include detailed chemical kinetics into the calculation of the turbulent flames. FLUENT™ solver has limited the usage of a detailed chemical kinetic mechanism to 300 species and 1 500 reactions, which is satisfactory for a wide range of applications. However, it should be mentioned that the PDF integration is directly proportional to the degree of complexity of the chosen mechanism. Consequently, care should be taken during the choice of the kinetic mechanism, this latter should not be too reduced to allow good prediction of a wide range of the species involved in the reaction, nor too detailed to avoid unmanageable PDF table sizes, and computational time.

4.3.1. Chemical Kinetics/ Reaction mechanisms

The conventional diesel case proved challenging for the acquisition of a mechanism that represents the winter diesel ($C_{12}H_{23}$) used in the experimental part; the reason being mainly, the number of reactions involved in the mechanisms, which exceeds 1 500 reactions. Moreover, the introduction of the surrogate principle has encouraged research to redirect their studies to elaborate adequate surrogates for complex diesel fuels to.

The UC San Diego combustion laboratory has developed a reliable reduced mechanism for the n-heptane; the same was revised and updated on the (7th of July 2012). It is a reduced mechanism that contains 55 species and 277 reactions, and it is valid for our range of operation, in terms of temperature and pressure, i.e. ambient conditions. This mechanism was used during the definition of the conventional diesel cases.

Regarding the biodiesel case, the choice of a mechanism was a crucial step, due to the complexity of these fuels. Biodiesel is a mixture of fatty acid alkyl esters, and contains large hydrocarbons (C_8 to C_{18}), whether, it is a blend or pure. For this reason, the chemical kinetics of biodiesel combustion is highly complex, and usually lead to a large size detailed mechanism (can reach up to 3 000 species and 10 000 reactions). 3D engine simulations with such a large mechanism are too prohibitive, and unfeasible; especially, for industrial and engineering applications (Pitz, et al., 2012). The research team at McGill University (Professor Jeffrey Bergthorson and PhD student Benjamin Akih Kumgeh), has successfully developed a surrogate mechanism for biodiesel as a part of their project mandate with RRC. It is a dual component surrogate mechanism, composed of methyl butanoate (MB), and n-heptane, containing 93 species and 709 reactions. However, while integrating this mechanism in FLUENT™, the solver generated some error messages, suggesting the presence of 22 reactions with mass imbalance rates. Despite, the uncertainty of these reactions impact on the chemistry; a decision was made to search for a new mechanism. This decision was also supported by the fact that, the dual component surrogate methyl butanoate/n-heptane mechanisms are considered the simplest mechanisms for biodiesels, due to its short chain length (C_5) compared to the actual biodiesel fuels. William Pitz (Pitz, et al., 2012) has investigated the (MB/n-C_7H_{16}) biodiesel surrogates, and they found that the (MB) is inadequate to accurately represent the physicochemical properties of biodiesels; moreover; its mechanism cannot accurately predict the flame lift-off, or emissions characteristics from biodiesel combustion. S.K. Aggarwal (Aggarwal & Han, 2013) cited that previous studies have demonstrated that the combustion, and emission of biodiesel fuels, is mostly determined by the hydrocarbon chain length, the number, and location of the unsaturated bonds in their molecular structure.

In favor of the above, the methyl decanoate (MD) surrogate mechanism for biodiesel was chosen. MD was recently recognized as a more viable surrogate for biodiesels; since it features both long hydrocarbon chains (C_{11}) and different esters groups. William Pitz (Pitz, et al., 2012) successfully developed a skeletal tri-component biodiesel surrogate mechanism, consisting of n-heptane, methyl decanoate, and methyl-9-decanoate. This mechanism contains 115 species, and 460 reactions, obtained by reducing the comprehensive mechanism created from Lawrence Livermore Nation Laboratory, which contains 3 299 species and 10 806 reactions. This substantial reduction was achieved using the direct relation graph (DRG), the isomer lumping, and the DRG-aided sensitivity analysis (DRGASA) techniques. This reduced mechanism was validated experimentally for our operating conditions, i.e. ambient conditions, and was reported by other researchers (Aggarwal & Han, 2013).

4.3.2. Flamelets generation

In order to generate flamelet libraries using FLUENT™, the following data must be supplied to the solver:

- File containing a description of the reaction mechanisms occurring in the gas phase, and
- File containing thermodynamic data for all the chemical species involved in the reaction.

The output file, namely the flamelet file, will contain species mass fractions, and temperatures of the ensemble of multiple laminar flamelets, as a function of the mixture fraction space (*Z*). Each flamelet in the library is associated with an instantaneous scalar dissipation value (χ_{st}). The initial (χ_{st}) is specified by the user, as well as, the time step for the calculation of the next flamelet in the library. The solver will progress correspondingly until (χ_{st}) exceeds a critical value (χ_q), at which the flamelet extinguishes. The extinguished flamelet is omitted from the overall flamelet library.

Because each steady flamelet is calculated by iteration over a time-stepping Fourier transformation, the convergence of each flamelet occurs only, when the maximum absolute change in the mass species fraction and temperature at any discrete mixture fraction point, is less than the user specified tolerance value for flamelet convergence. Thereafter, a new flamelet calculation will start, and a new value of (χ_{st}) is assigned. This process is controlled by the user through the Flamelet controls tab in FLUENT™, in which, the user can assign the initial Fourier number, flamelet convergence tolerance, and other various mathematical parameters related to the equation solution. Another important parameter linked to the resolution accuracy of generated flamelet is the number of mixture fraction grid points distributed between ($Z_{Oxidizer}$= 0 & Z_{Fuel} =1), in the flamelet. Increasing this number will provide a higher accuracy in the calculations of species, and temperatures inside the (Z) space; however, it will significantly impact the cost in computational time for the flamelet library. In FLUENT™ the minimum number of allowed grid points in the flamelet is eight, and the maximum being 64. However, the solver offers an option called the Automated Grid Refinement method (AGR), in which, an adaptive algorithm inserts grid points around the stoichiometric mixture fraction value, i.e. around the location of peak temperature. Once the refined flamelet is converged, the refinement process is repeated until no further change in values is obtained.

To assess the flamelet control, and the resolution parameters, a preliminary flamelet generation trial was performed on a simple and smaller mechanism. During this trial, the famous GRI 3.0 methane and natural gas mechanism, developed by the research team at the University of California at Berkeley, was tested; it contains 53 species and 325 reactions. Various flamelet libraries were generated with various different solver parameters. In conclusion, the best combination of these parameters was determined. Table 13 summarizes the main solver parameters used during the flamelet creation of both n-heptane, and B20 blend fuels.

Table 13 Flamelet control parameters

Control parameters	AGR	Fourier initial number	Fourier multiplier	Flamelet convergence tolerance
Values	Activated	1	1.1	1e-05

These parameters represent the best compromise for accuracy and computational time cost as observed by the author.

4.3.2.1. N-heptane flamelets

After implementing both the reaction mechanism, and the thermodynamic files, into the solver, the user is required to define the gaseous streams for the fuel and oxidizer. For the n-heptane cases, the fuel stream is made up of n-C_7H_{16} ($X_{n-C_7H_{16}} = 1$) at (300 K and 101 325 Pa), and the air stream consists of ($X_{N_2} = 0.79, X_{O_2} = 0.21$) at (300 K and 101 325 Pa). These are the operating conditions used in the experimental test rig, and thus, applied during the flamelet generation. The generated flamelet results are summarized in ***Table 14***.

Table 14 N-heptane flamelet library

Parameter	Maximum number of generated flamelets	Initial scalar dissipation (s^{-1})	(Z_{st})	Scalar dissipation increment step (s)	Scalar dissipation prior to flamelet extinction (s^{-1})	Strain rate value at χ_q (s^{-1})
Calculated value	16	0.01	0.06546	5	66	3 245

The strain rate value at extinction was computed from equation(2.105), using the values of (Z_{st}= 0.06546 and χ_{st} = 66) from the generated flamelets. No solution was obtained for a value greater than (66 s^{-1}), as a consequence, it is estimated that the extinction occurs immediately beyond this value. To the author knowledge no published literature was found for the extinction limits of the n-heptane at the ambient operation conditions (300 K and 101 325 Pa). Accordingly, validation of the obtained values of strain rates, and scalar dissipation could not be achieved. Estimated extinction occurred at a temperature of (1 790 K), after that the flame temperature falls suddenly to (300 K). The exact extinction limit cannot be fully assessed in FLUENT™, since the extinguished flamelets are omitted from the library; this is certainly a topic that needs some investigations.

The following ***Figure 36***, shows the predicted temperature profile as a function of the mixture fraction in an opposed flow laminar diffusion flame at different strain rates. Graphical representations for all the 16 flamelets were not included to simplify the graph. The generated flamelet library contains 16 laminar diffusion flames from a strain rate value of (0.5 to 3 245 s^{-1}). It can be observed that, as the strain rate increases the maximum temperature reduces till the flame extinguishes. The peak temperature falls off linearly from (2 275 to 1 790 K), for strain rate values between (0.5 - 3 245 s^{-1}, respectively), and then the flame suddenly extinguishes.

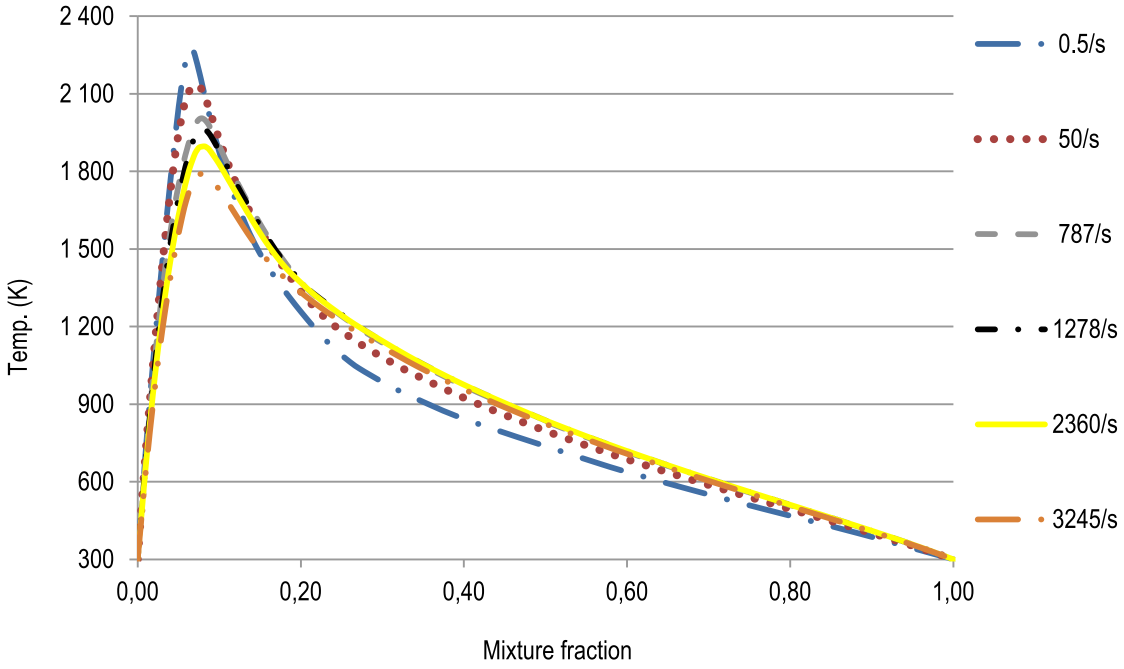

Figure 36 Temperature versus mixture fraction at various strain rates

To verify the pertinence of the obtained peak temperature value, the flame adiabatic temperature at equilibrium for n-heptane was computed using the combustion equilibrium software (GASEQ). Using this software, the adiabatic temperature found at stoichiometry was (2 282 K). This is plausible, since the obtained value of (2 275 K) in FLUENT™, was calculated for the first flamelet in the library, i.e. at the smallest scalar dissipation (0.01 s^{-1}), whereas, (GASEQ) computes the temperature at the full equilibrium, i.e. ($\chi = 0$).

In order to make sure that the generated flamelets render a reasonable combustion profile, some of the major species mass fractions were sketched as a function of the mixture fraction at chosen strain rate values. ***Figure 37*** shows the decrease of the (N_2) concentration towards the fuel rich side ($Z \sim 1$) from the first generated flamelet in the library, i.e. strain rate of (0.5 s^{-1}). ***Figure 38*** shows the concentration of the major combustion products (CO_2, H_2O, CO and O_2) from the last flamelet at a strain rate of (3 245 s^{-1}), prior to the predicted flame extinction. ***Figure 39*** indicates that as the strain rate increases, the concentration of the CO also increases. This is expected, since as explained above, the increment of the strain rate is an indication of the departure from the equilibrium; thus, all species far from equilibrium as the CO, will exhibit such tendency.

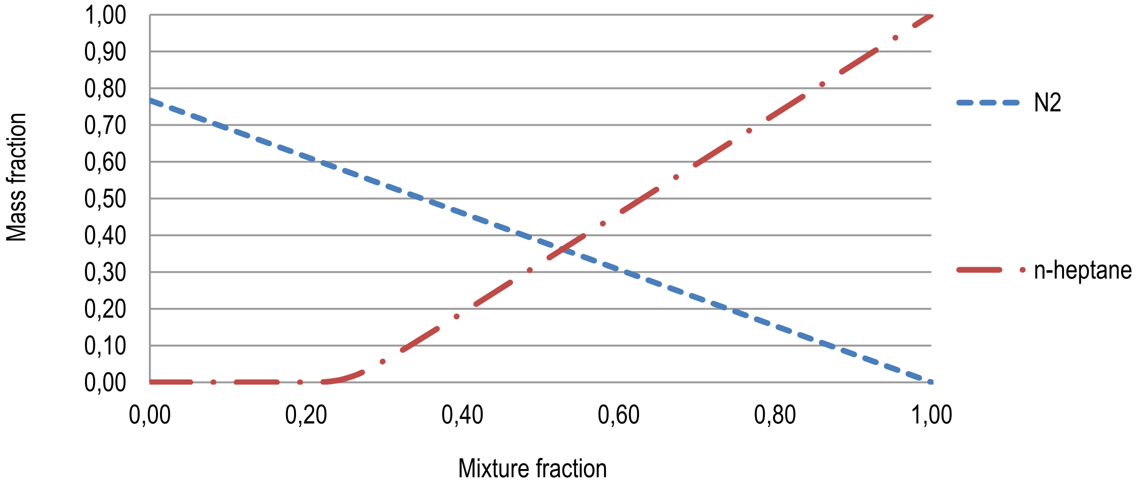

Figure 37 Fuel and N_2 mass fraction versus mixture fraction at a strain rate of 0.5/s

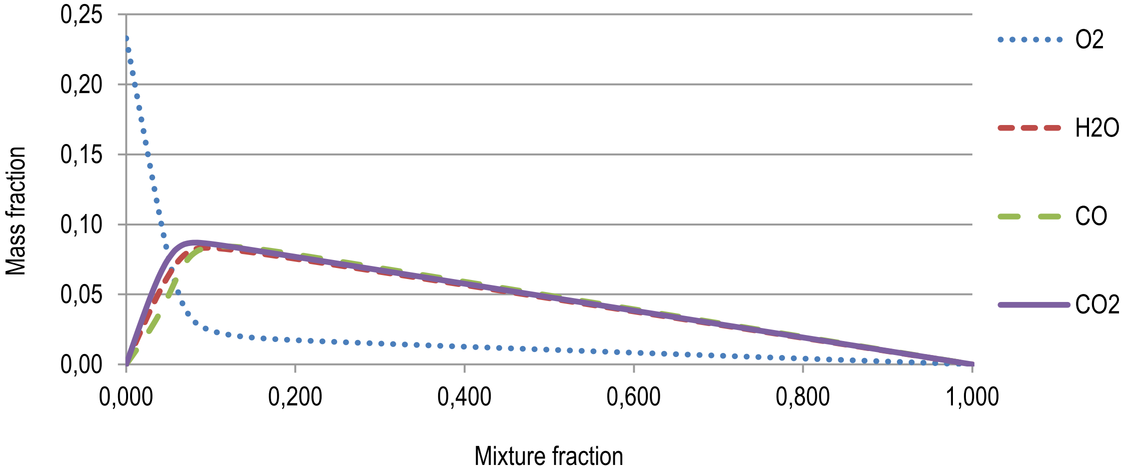

Figure 38 Major species mass fractions versus mixture fraction at a strain rate of 3 245/s

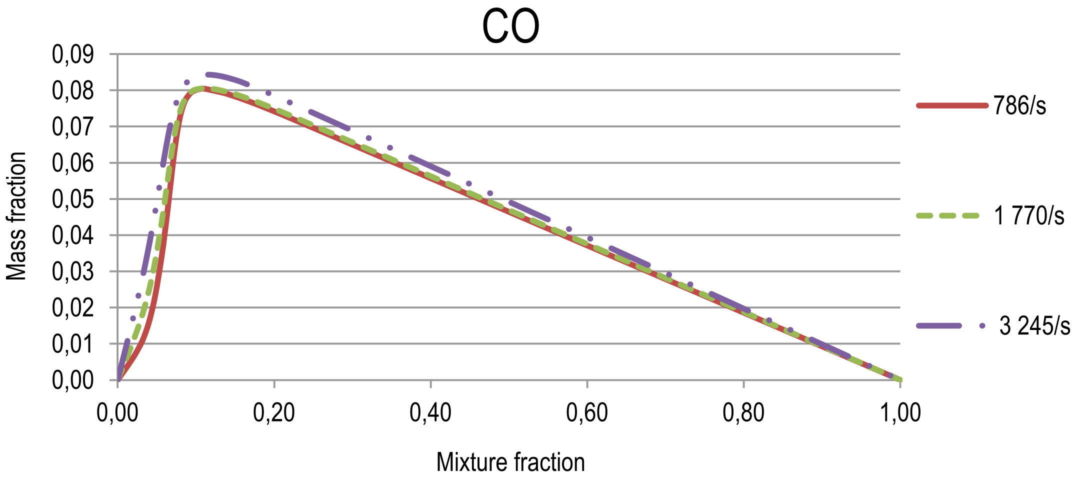

Figure 39 CO mass fraction versus mixture fraction at various strain rates

4.3.2.2. B20 blends flamelets

Regarding the biodiesel configuration, the fuel stream is made up of 50 % n-C_7H_{16} ($X_{n-C_7H_{16}} = 0.5$), 25 % methyl decanoate ($X_{C_{11}H_{22}O_2} = 0.25$), and 25 % methyl-9-decanoate ($X_{C_{11}H_{19}O_2} = 0.25$), at (300 K and 101 325 Pa), and the air stream consists of ($X_{N_2} = 0.79, X_{O_2} = 0.21$), at (300 K and 101 325 Pa). These percentages were recommended by the developer of the mechanism, since the validation of their reduced mechanism was achieved according to these species distribution in the fuel stream side. The generated flamelet results are summarized in ***Table 15***:

Table 15 Methyl decanoate flamelet library

Parameter	Maximum number of generated flamelets	Initial scalar dissipation (s^{-1})	(Z_{st})	Scalar dissipation increment step (s)	Scalar dissipation prior to flamelet extinction (s^{-1})	Strain rate value at χ_q (s^{-1})
Calculated value	58	0.01	0.077	1	83	4 760

Flamelet results from the MD mechanism will be addressed similar to the n-heptane cases. The MD flamelet library contains 58 flamelets; indeed, the number of generated flamelets is almost tripled compared to the n-heptane case, because the scalar dissipation time step was reduced. The scalar dissipation value of (83 s^{-1}) is estimated as the extinction limit. The mixture fraction value at stoichiometry (Z_{st}) for the first flamelet, which is the closest to the equilibrium found (0.077), is at a maximum temperature of (2 282 K). To assess the general behaviour of the generated MD flamelets, the mixture fraction profile at various strain rates was sketched in ***Figure 40***. ***Figure 41*** shows the behavior of the (N_2) and the tri-components fuel stream mass fractions with the mixture fraction, from the first flamelet, i.e. strain rate (0.57/s). ***Figure 42*** highlights the major combustion products species mass fractions (CO_2, H_2O, CO and O_2) for the last generated flamelet prior to the predicted extinction, i.e. at strain rate of (4 760/s). Lastly, the CO behaviour was verified at three different strain rates as shown in ***Figure* 43**, and the similar tendencies to the n-heptane case were observed.

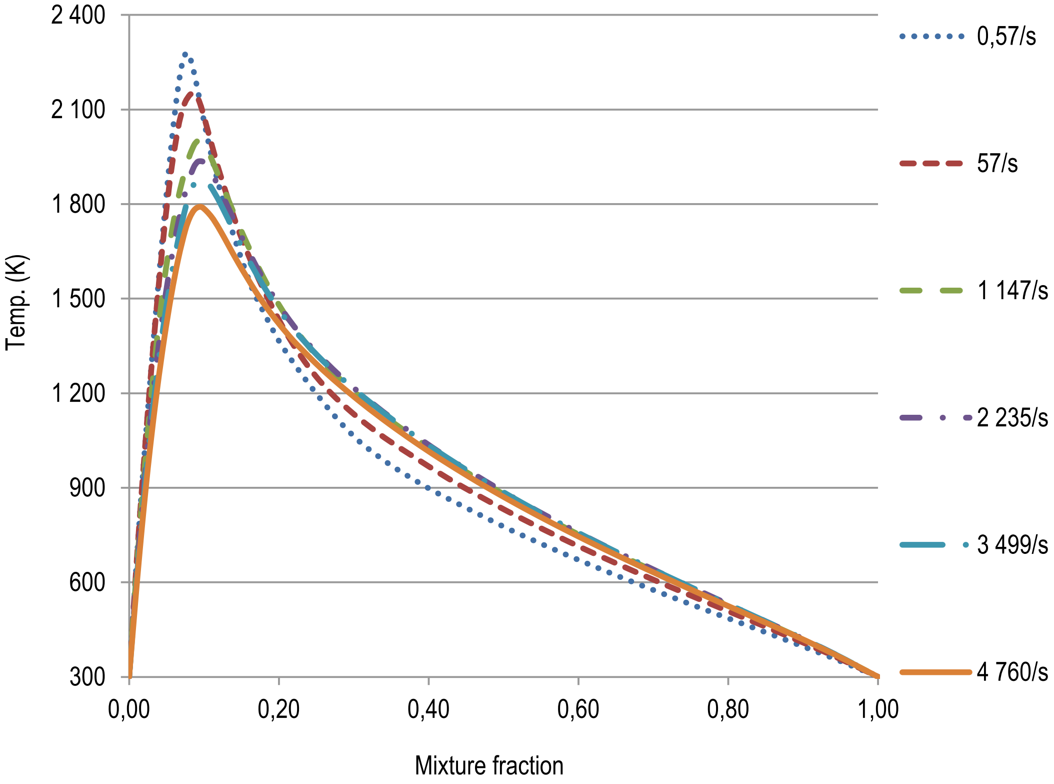

Figure 40 Temperature versus mixture fraction at various strain rates

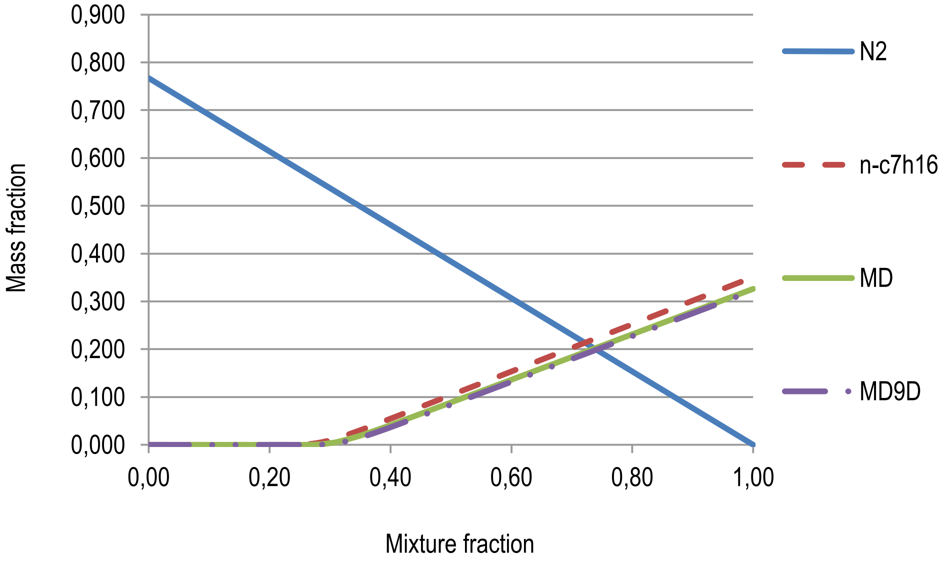

Figure 41 Fuel and N_2 mass fraction versus mixture fraction at a strain rate of 0.57/s

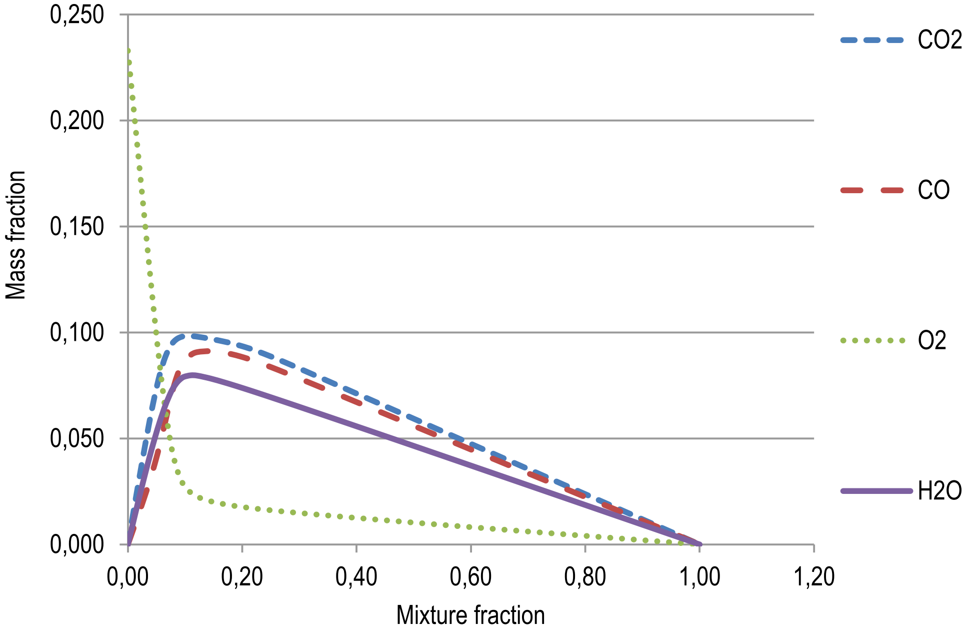

Figure 42 Major species mass fractions versus mixture fraction at a strain rate of 4 760/s

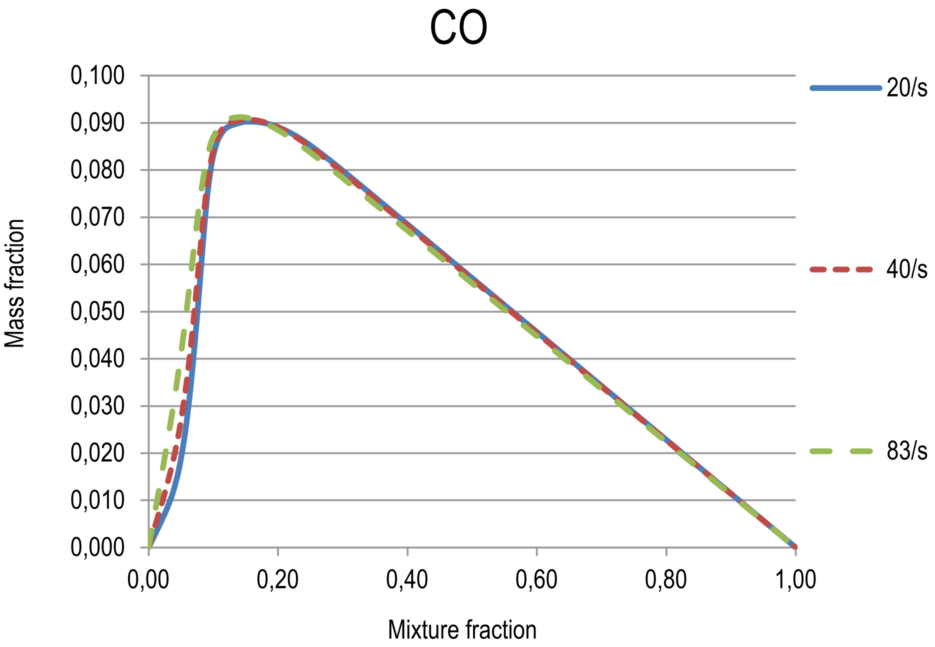

Figure 43 CO mass fraction versus mixture fraction at various strain rates

CHAPTER 5- RESULTS AND DISCUSSION

This section captures the results obtained from the numerical simulation of conventional diesel, and the biodiesel blends. Gas velocities, flame shape, flame temperature field, and wall temperatures are analysed. CFD results are then validated with the available experimental data acquired at Université Laval. Emission studies for the four reacting cases are presented, and a selective comparison between the combustion of diesel, as well as, biodiesel fuels is performed; highlighting all the major differences observed and the general emission trends.

This chapter begins, with a preliminary investigation on the cold flow non-reacting case (e.g. the atomization case using n-heptane), followed by a qualitative examination of the main spray characteristics, such as, droplet mean properties, which covers size, distribution, dispersion, and wall interactions. Impact of the spray on the continuous phase is also addressed, in terms of mixing, velocities, and temperatures, in the subsequent sub-sections.

5.1. N-heptane non-reacting flow case & Atomization results

Resolving details of the atomization process is not the primary objective of this study, and it is not within Université Laval mandate. Although PDPA measurements were attempted by Concordia University, data obtained experimentally at Université Laval, do not include the droplet size distribution, droplet mean diameters, or velocities. Consequently, extracting this information from the numerical model, and presenting them within this frame of work, is judged impractical. However, one key aspect of the spray was observed during the experimental test, that is, the fuel droplets were subject to wall impingements. Thus, it was necessary for the CFD model to be able to capture this phenomenon; because, it will certainly affect the aerodynamic of the combustor, and thus the combustion process.

Initially, it was important to verify the pertinence of choosing the (RT-KH) atomization model. Moreover, it was essential to validate the suitability of the parameters used during the definition of the injection module, such as but not limited to: the measurement of the initial half spray angle from the geometry, the introduced relative velocity, and the choice of time step. RR internal data performed some experimental tests for the determination of the spray cone angle, using a conventional diesel fuel. Their study is used to qualitatively validate the CFD results obtained, which were obtained from the cold flow non-reacting atomization case with n-heptane at ($\phi = 1$).

The test was carried at ambient conditions, using the same pressure drop (3.6%) as Université Laval test rig and the numerical model. The major difference between both RR internal report and Laval test rigs is that, the first is an unconfined test, i.e. no wall boundaries existed. In ***Figure 44,*** the left hand side shows the shape of the fuel cone spray, generated using the conventional diesel at RR internal data test facility, on the right hand side results from the non-reacting flow case are presented. From these figures, two main points can be concluded. The first is the presence of fuel mist at the outer area of the jet, which will likely help the ignition of the diesel at start-up; in other words, this observation highlights the high atomization capacity of the dual fuel WLE injector. The second point is related to the spray cone angle, which as illustrated, is well captured by the CFD model. This wide cone angle is expected to allow a high dispersion of the droplet inside the combustor.

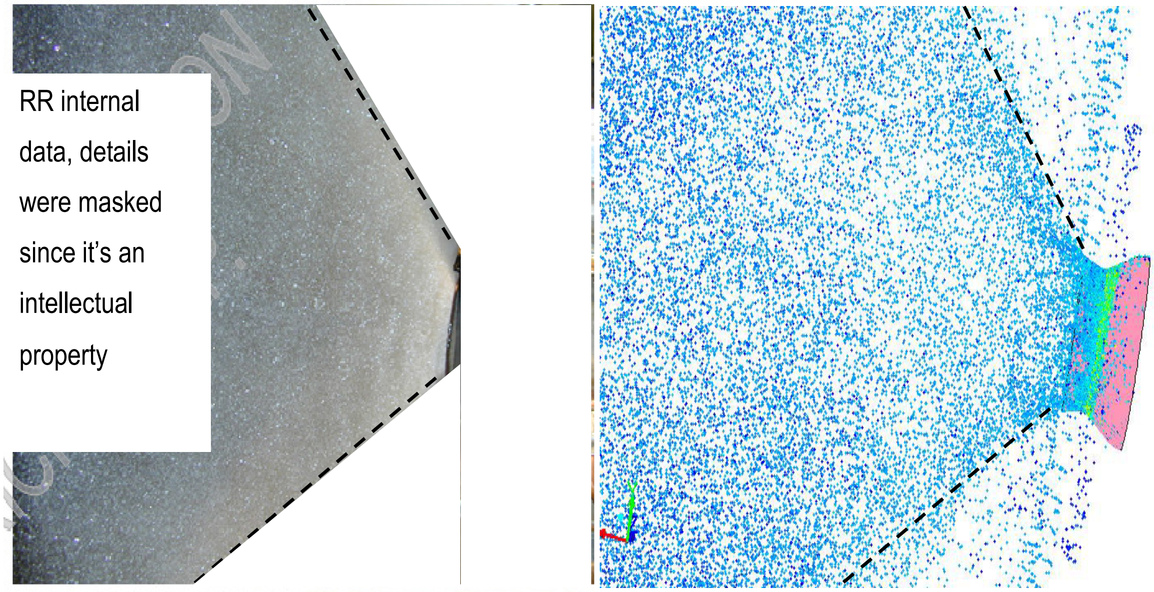
RR internal data, details were masked since it’s an intellectual property

Figure 44 Qualitative comparison between RR internal data l.h.s atomization test, and the CFD modeling r.h.s

Regarding droplet impingements on the combustor wall, ***Figure 45*** shows droplets impacting the combustor inner wall during the real experimental test on the left hand side with the CFD results shown in the right hand side. In order to capture the same phenomena, it was necessarily to use the wall film boundary condition for the combustor wall, as explained previously. This high impact, as it will be presented later, has a significant effect on the combustion process, and emissions. In liquid fuel combustion, droplet residence time needs to be long enough for the vaporization time, and the mixing time as well. Ideally, this high impingement is an indication of the short residence time of the liquid droplets. This is a crucial parameter for the overall combustion efficiency.

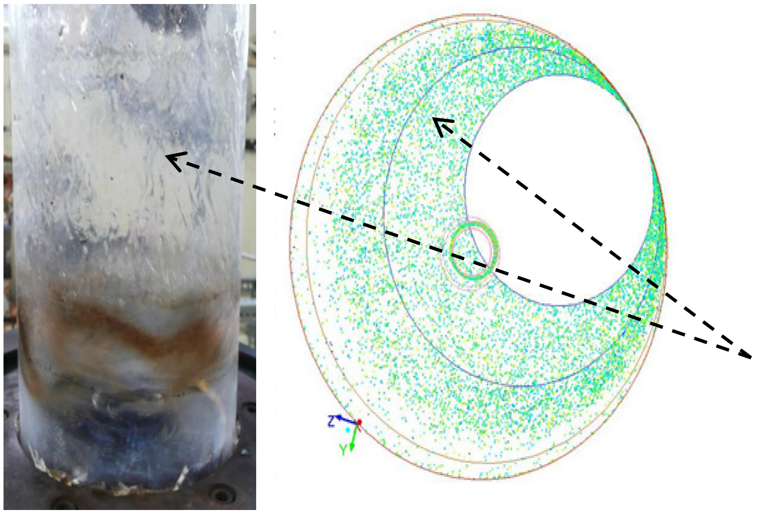

High wall impingement for droplets at test start-up using conventional diesel, the same thing was captured by the CFD model.

Figure 45 Qualitative comparison between the experimental test at Ulaval l.h.s, and the numerical model r.h.s for the droplet wall impingements

To verify the hollow cone shape expected from these types of injectors, a section in the middle of the computational was drawn, as illustrated in ***Figure 46***. This clearly shows that the droplets enter the combustion chamber as a hollow cone spray, because of the absence of droplets inside the core of the spray.

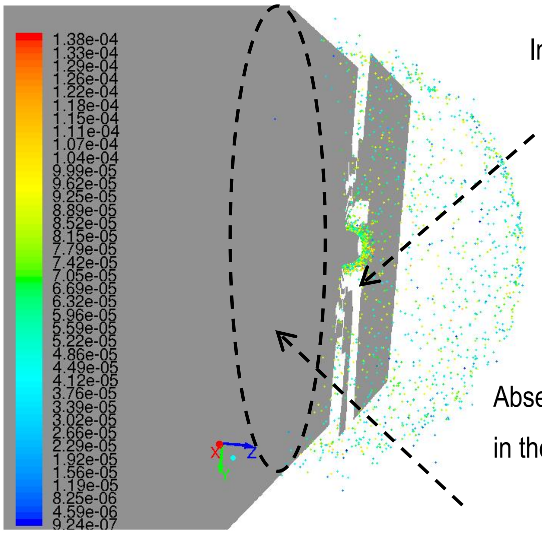

Injection point

Absence of droplets in the spray cone

Figure 46 Symmetrical plan section view, for the qualitative representation of the droplets distributions inside the domain

The effect of droplet dispersion and wall impingement on combustion is addressed during the analysis of the four reacting flow cases in the following subsections.

The overall Sauter mean diameter (SMD) from this non-reacting flow injection case was found at ($\sim 60\,\mu m$). No size and velocity distribution histograms are offered in this study, since experimental test results are not available for validation purposes.

5.2. Continuous phase (Gas) velocity field

This section reports the effect of the spray on the continuous phase, showing droplets having an impact on the recirculation zone and the axial velocity profile at various distances from the injector. The cold flow data treated, herein, are carried out without introducing the fuel spray. A comparison between the axial velocity profiles from the cold flow, and one of the reacting flow cases will be addressed. Indeed, both the cold flow and the reacting flow case, will share the same operating conditions, in terms of fuel and oxidizer mass flow rates, inlet temperatures, inlet pressures, boundary conditions, and turbulent intensity. The selected case to represent the reacting flow for this analysis is the first case (1) using n-heptane ($\phi = 1$); refer to ***Table 10*** for the operating condition. It should be reminded that the cold flow simulation is the converged solution of the cold flow using only the flow, (k) and (ε) equations, prior to activate the injection and the combustion sub-models. Before presenting the results, it should be also noted that all the values were normalized, i.e. the extracted values from the solver in (m/s) were divided by a reference velocity. Moreover, any figures, sketches, contours representing the injector, were omitted from this manuscript, as requested by the project partners for confidentiality of the offered data.

Figure 47 shows the normalized contours for axial velocity vectors observed at the convergence of the cold flow solution, which was obtained after 10 000 iterations. This contour shows the size of the recirculation zone, the flow stagnation points (points A and B), the location of the vortices, and the direction of the flows inside and outside the recirculation zone. This information is vital for the understanding of the aerodynamics of the combustor, which will have a significant effect on the atomization, the fuel vapor distribution, and thus the mixing and combustion processes.

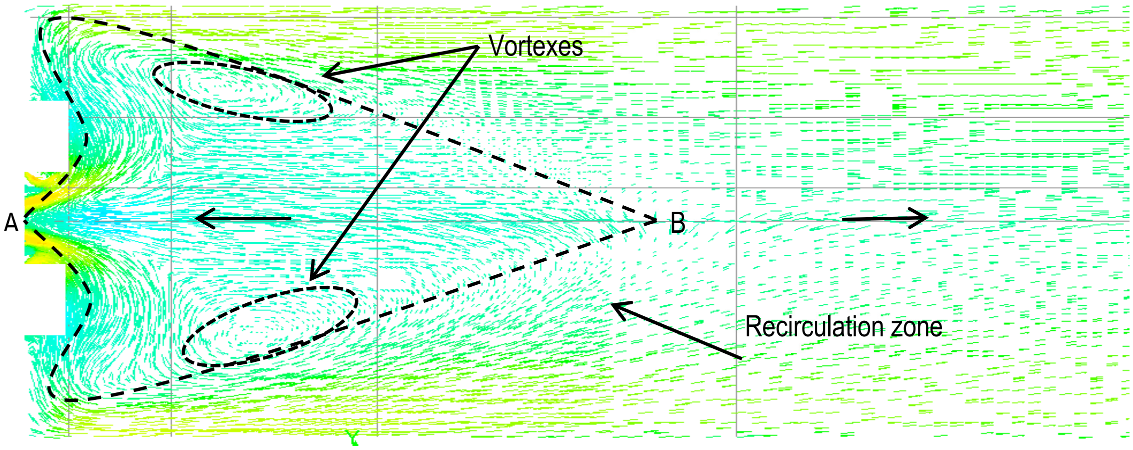

Figure 47 Axial velocity vectors at the symmetrical plan, from the injector tip to the exit plane of the combustor or inlet of the steel cone. The arrows indicate the direction of the flow.

Figure 48 shows the comparison between the normalized axial velocity profiles of the cold flow solution, and the reacting flow case solution, i.e. with injection and combustion, at various distances from the injector.

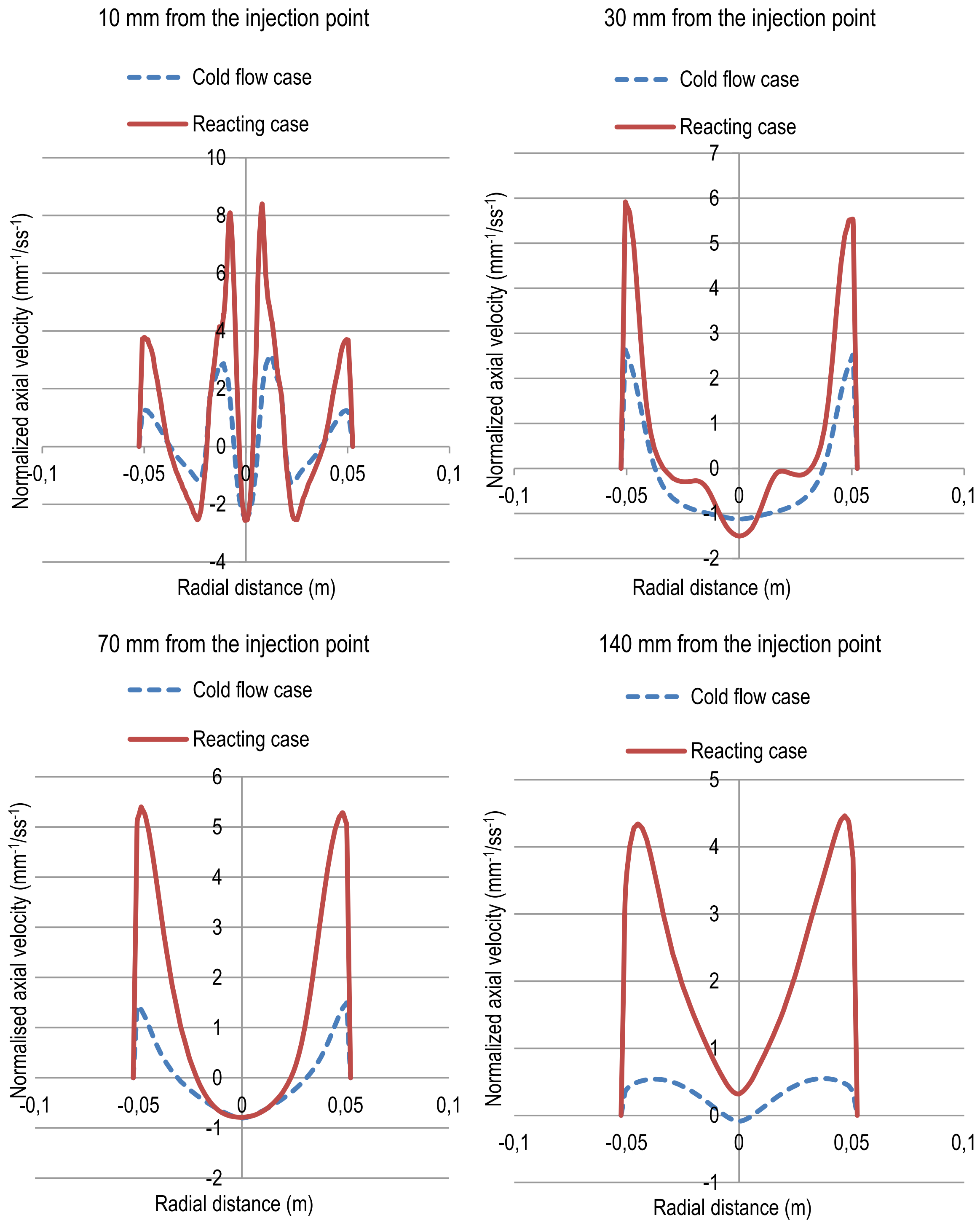

Figure 48 Radial distribution of axial velocity profiles at various distances from the injector

As expected, the reacting flow case exhibits a higher axial velocity profile than the cold flow case regardless of distance from the injector. This is mainly due to two different mechanisms. The first occurs prior to the full development of the high temperature field caused by combustion; in such situation; the non-evaporated droplets are responsible for the air velocity increment, since they will entrain the air as they travel downstream. The second mechanism is associated with the expansion of the hot gases related to the combustion process, which in return, will add a significant impact on the gas phase density, and the momentum of the gaseous flow.

To further expand the understanding of the key parameters that affect the velocity profile of the hot gases, the axial velocity profiles from the reacting flow case are drawn at five different distances from the injector, as shown in ***Figure 49***.

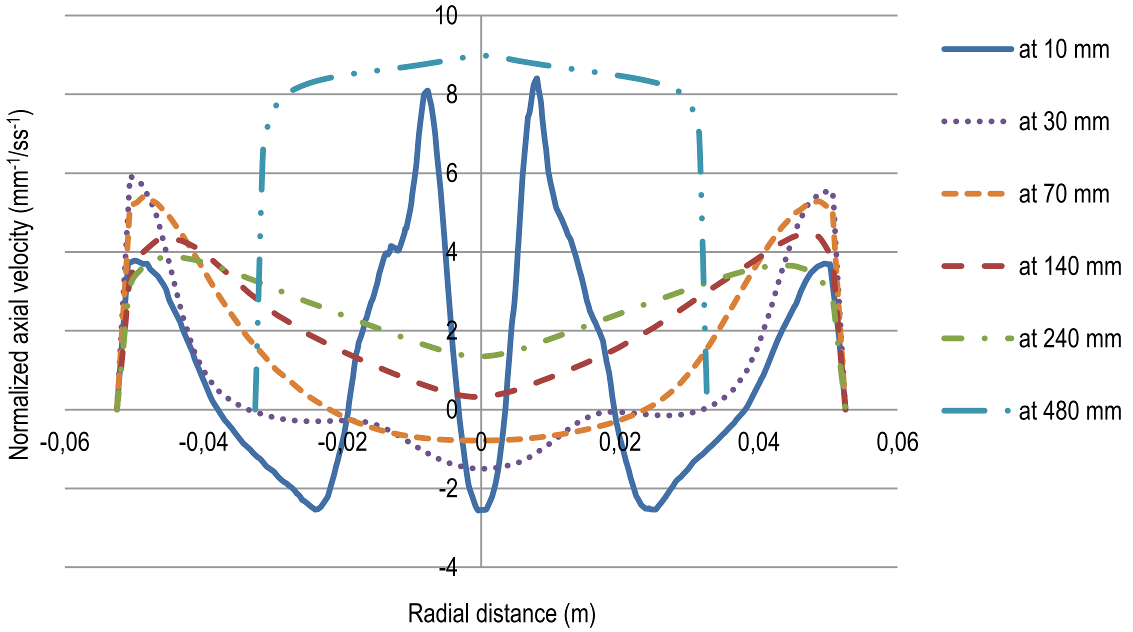

Figure 49 Radial distribution of the normalized axial velocity profile at various distance from the injection point for the n-heptane case at ($\phi = 1$)

In the vicinity of the injector nozzle, at a distance of (10 mm) from the injection point, the gaseous flow field displays negative axial velocity at the spray centerline. This behaviour results from the high reverse flow coming from the recirculation zone as illustrated in the axial velocity vector contour ***Figure 50***. Moving radially, a peak in the axial velocity is observed at a radius of (8 mm), which can be attributed to the spray momentum, and the heat released from the flame. Indeed, this will cause an acceleration of the gas velocity through the droplets effect on the gas density and the air entrainment. Furthermore radially, at a radius of (23 mm) and (50 mm) a drop followed by an increment in the axial velocity can be observed, respectively. This is due to the aerodynamic of the combustor, where mainly the vortices are dominating the flow field. Lastly, at the wall, the velocity falls to zero due to the no-slip wall boundary condition.

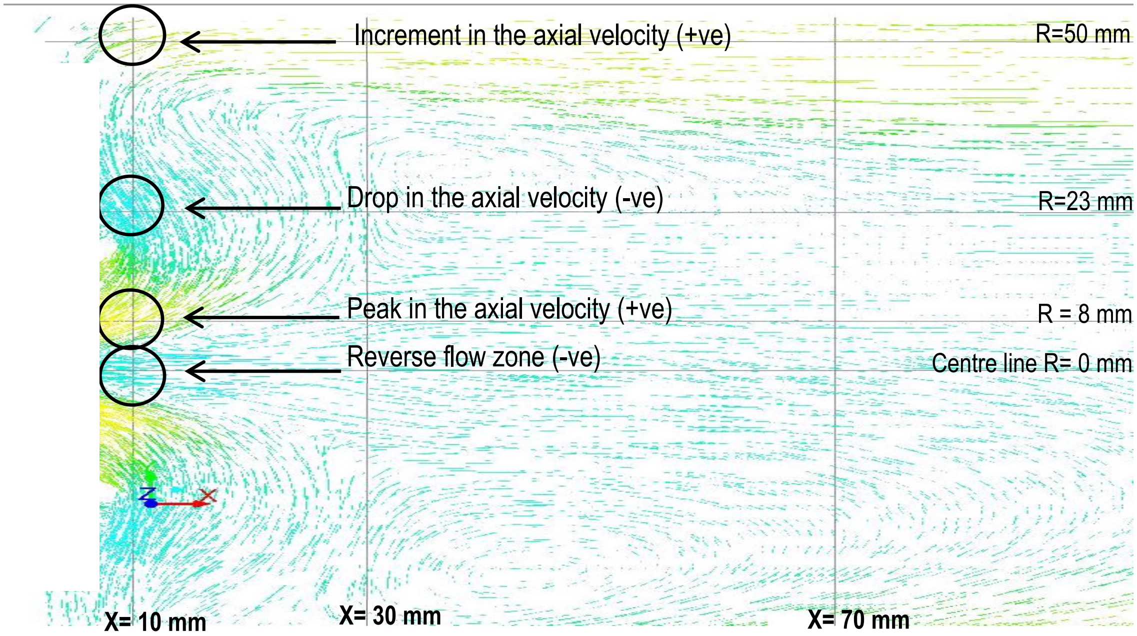

Figure 50 Vector contour of the axial velocity flow field identical to (Figure 47) above; with indicative panels to support the clarifications

A similar trend with less negative velocity intensity is observed at (30 mm) from the injection point, this is due to the high liquid loading; and thus, the high momentum exchange between both phases which have a significant impact on the gas flow field as can be clearly seen in ***Figure 51*** where the axial velocity vectors are superimposed on the DPM mass source contour.

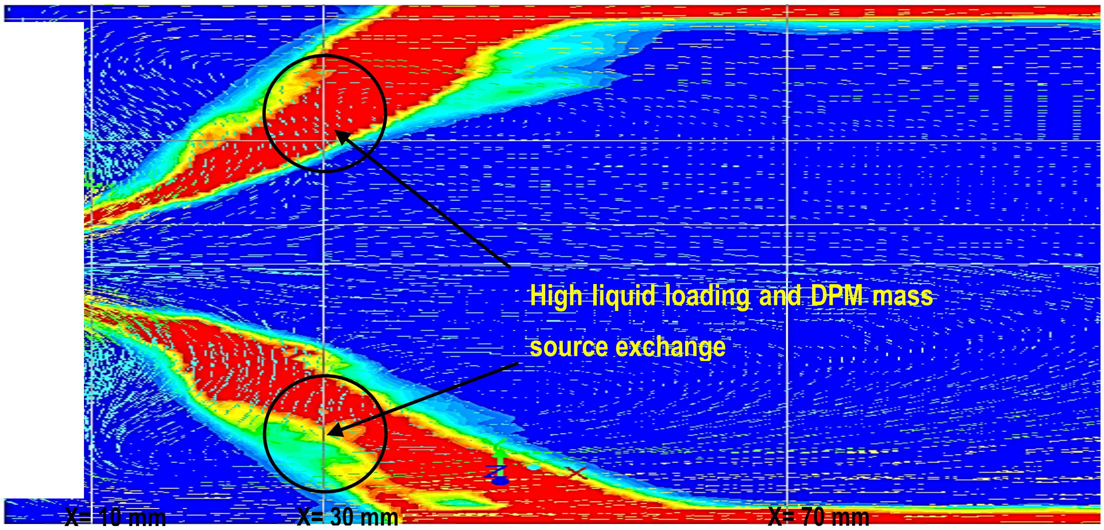

Figure 51 Axial gas velocity vectors superimposed on the DPM mass source to highlight the momentum exchange effects on both phases (gas, liquid spray)

The axial velocity magnitude at this location, i.e. X= 30 mm, is lower than the values exhibited at the axial distance of (10 mm). This is due to the shape of the spray (hollow cone with the high droplet dispersion observed), which will affect mainly the flow that exists in the outer area of the jet.

The DPM mass source contour quantifies the amount of mass exchange/interaction between both phases, accordingly, it can be thought as a sensor to the evaporation process. In others words, the highlighted two circles in ***Figure 51*** at (30 mm) from the injector can give an indication of the amount fuel vapor present locally in the cell.

Moving further axially in the downstream direction (i.e. X= 70,140 and 240 mm), the axial velocity profile shows a progressive increment at the spray centerline. This is probably related to the presence of the burnt gas in this region (as it will be revealed in the coming section). In this region the burnt gas velocities are governing the flow field, and hence, the swirling effect and the droplet presence are less dominant.

At a distance of (240 mm), the flow is still not fully recovered from the strong vortex, which explains the weak axial velocity at the centerline. However, further downstream at a distance of (480 mm) from the injection point, the flow can be considered fully developed, and the axial velocity will become very close to a top–hat velocity profile. This location corresponds to a vertical plan at the centre of the exit steel cone, almost (15 mm) from the end of the computational domain.

Velocity field analyses from the other three reacting flow cases, i.e. n-heptane lean condition, and both B20 cases, revealed a quite similar tendency to what is shown above in (***Figure 49***, ***Figure 50*** and ***Figure 51***), in terms of contours, profile, and overall trends. Indeed, there are slight differences in the magnitude, but again, not significantly.

5.3. Gas temperature field and Flame structure

The analysis in this sub-section begins with the computed structure of the n-heptane flame at ($\phi = 1$). It can be observed from ***Figure 52*** that, the flame once ignited is anchored in the surrounding area of the injector tip. This shape is initially dictated by the injected liquid hollow cone pattern, as well as, the convective/diffusion effects of the hot gases arriving from the recirculation zone.

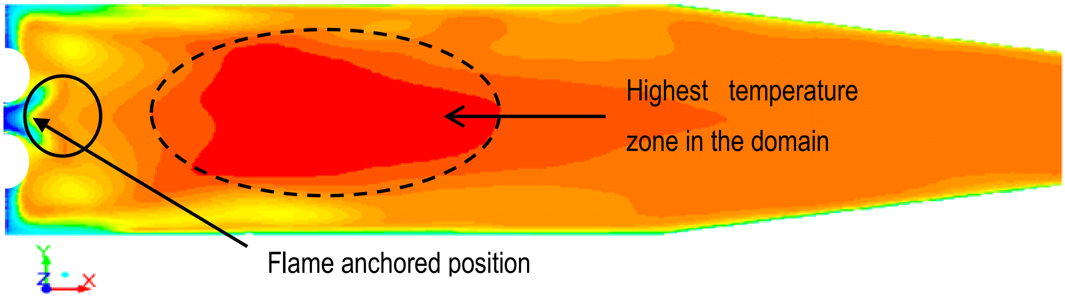

Figure 52 Normalized temperature contours at the symmetrical plan of the domain.

The anchored position of the flame is situated at (14 mm) from the injection point, and the highest temperature zone in the domain was observed in the middle of the quartz tube (the combustor). In order to investigate the flame structure and the temperature field; the radial distribution of the temperature profiles, and their corresponding local equivalence ratios, at three different axial distances from the injection point are examined. The selected axial and radial positions for the analysis are illustrated in ***Figure 53*** for clarification.

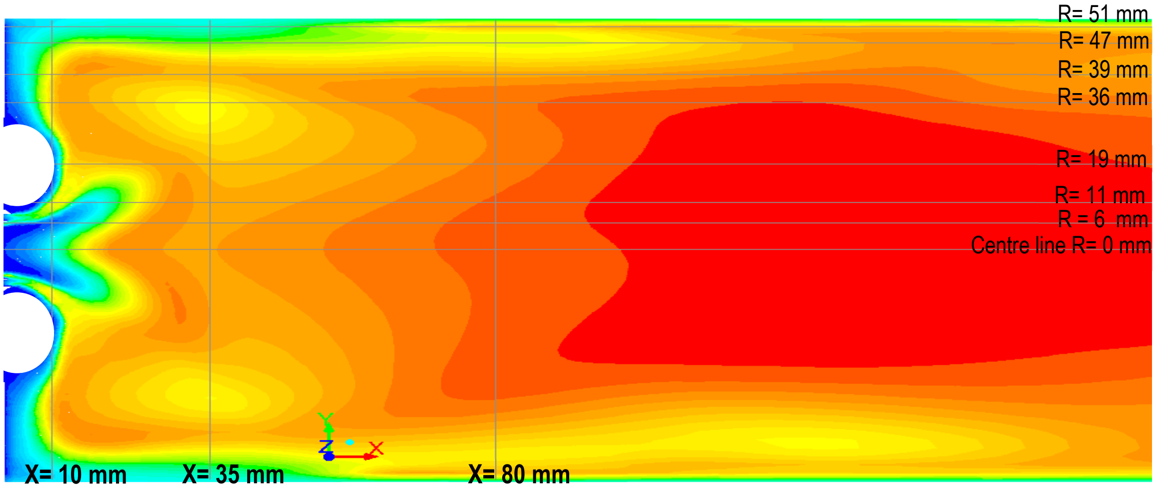

Figure 53 Normalized Temperature contours for a portion of the domain, highlighting the various selected axial and radial positions

The cited temperature values are normalized, i.e. the extracted values in (K) from the solver are divided by a reference temperature in K. Therefore a normalized temperature in SI unit (KK^{-1}) is assigned to the value during the discussion.

At an axial distance of (10 mm) from the injection point as shown in ***Figure 54***, the value of the normalized temperature at the centerline is found at around (2.7 KK^{-1}) which is due to the hot gas carried out by the reversed flow. Moving up radially at a radius of (6 mm) a drop in the temperature is observed, this is probably caused by the cooling effect of the spray on the gas phase, since it would locally act as a heat sink. Indeed, at this region, high presence of fine droplets (the mist) is expected (also demonstrated during RR internal data tests refer to section § 5.1). These fine droplets will mostly evaporate, but still not all of them are sufficiently mixed and ready to ignite. At a radius of (11 mm) the temperature jumps to (4.96 KK^{-1}) and the corresponding equivalence ratio found close to (2.7), suggesting that the mixture is on the rich side of the stoichiometry. The fact that the fuel is burning too rich in the vicinity of the nozzle can be related to the presence of a high concentration of fuel vapor in this area, which is solely caused by the vaporization. Consequently, rich mixing of the fuel vapor with the air occurs. In fact, this air is arriving at a high temperature from the recirculation zone, and thus, will further increase the vaporization rate. Further radially at a radius of (19 mm), the temperature falls again to (1.1 KK^{-1}), because this point as illustrated in ***Figure 53*** is outside the flame reaction zone. In other words, there is an absence of fuel in this region and this calculated temperature value reflects simply hot gases coming back from the recirculation zone as seen in ***Figure 50***. At a radius of (36 mm), the temperature rises again to (5.67 KK^{-1}) with the equivalence ratio found at around (1.1), this is due to the presence of a sufficient amount of fuel vapor mixed with the air. Indeed at this region the majority of the fine droplets are vaporized and mixed with the oxidizer, moreover, the fact that this region is near the eye of the vortex will enhance the mixing rate.

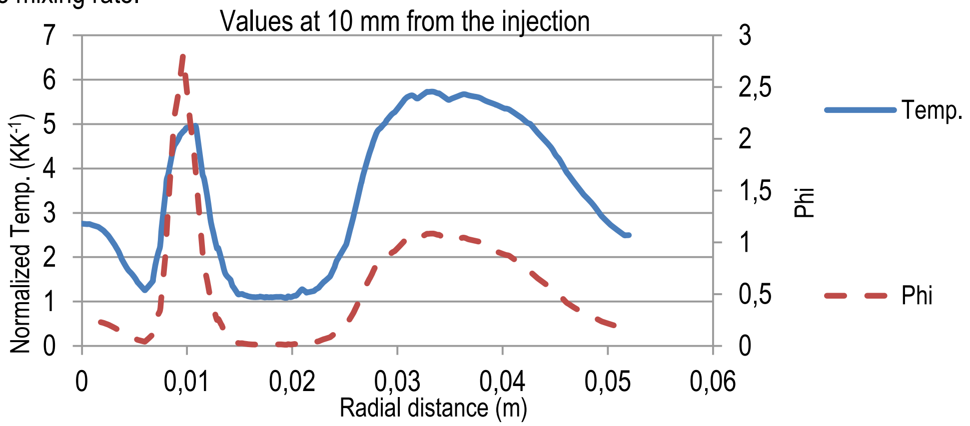

Figure 54 Profiles of radial distributions for temperature and (ϕ) at 10 mm from the injection point, the primary axis on the left represents the normalized temp., the secondary axis on the right represents (ϕ)

Moving to the second axial position (X= 35 mm) from the injection point, the radial temperature distribution has a trend that differs from that observed at (X= 10 mm), as illustrated in ***Figure 55***.

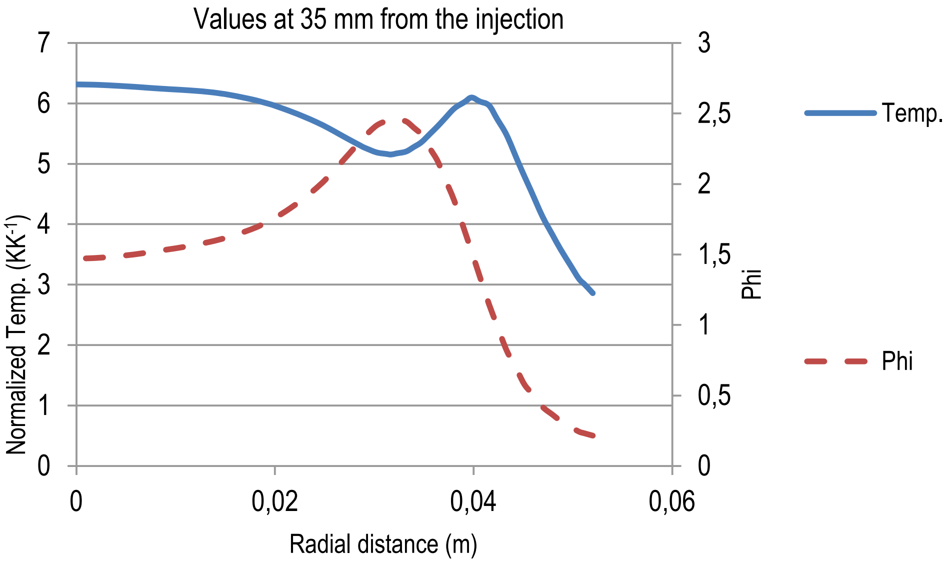

Figure 55 Profiles of radial distributions for temperature and (ϕ) at 35 mm from the injection point, the primary axis on the left represents the normalized temp., the secondary axis on the right represents (ϕ)

A peak temperature of (6.5 KK^{-1}) is observed at the centerline (core of the flame), followed by a drop in the temperature (5 KK^{-1}) at a radius of (36 mm), which is the centre of the as vortex seen at ***Figure 53***. The equivalence ratio corresponding to this area shows a value of (2.2), indicating a highly rich mixture. This is demonstrated through the local molar concentration ($kmol/m^3$) and the evaporating DPM contours of n-heptane at the same radius. ***Figure 56*** represents the planar contours of the molar concentration and the evaporating DPM source at the eye of the vortex (R= 36 mm). It can be seen that that there is a high fuel vapor concentration at this location, which can be attributed to two main mechanisms. The first is most likely, due to the concurrence of the vortex with the stream path of the evaporated fuel from the fine droplets at this location, and consequently the vorticity will trap the fuel vapour in this recirculating zone. The second, being the high volatility of n-heptane, as seen in the properties section it has a flash point of (262 K) and a boiling point of (371 K) which will enhance the vaporization rate, allowing a high fuel vapor concentration without sufficient mixing time. Beyond a radius of (36 mm), the temperature begins to build-up as the mixture is moving away from the eye of vortex, approaching the leaner side of stoichiometry. However at a radius of (47 mm), the temperature starts to fall again till it reaches its lowest value at the wall boundary. By examining both the molar concentration ***Figure 56*** and the local equivalence ratio ***Figure 55***, it can be concluded that there is insufficient fuel vapor in this area to sustain combustion. As a result the mixture becomes very lean. Indeed in this region, almost all the fine droplets can be considered evaporated and thus the remaining droplets are the ones having a bigger size, and thus, a higher momentum that allows them to penetrate deeper inside the domain. These bigger droplets require more time to be evaporated, and will also act a heat sink in the domain, this is beside the fact that, the majority of them will collide with the wall. All these parameters will act together to prevent sufficient evaporation and mixing time to sustain combustion in this region.

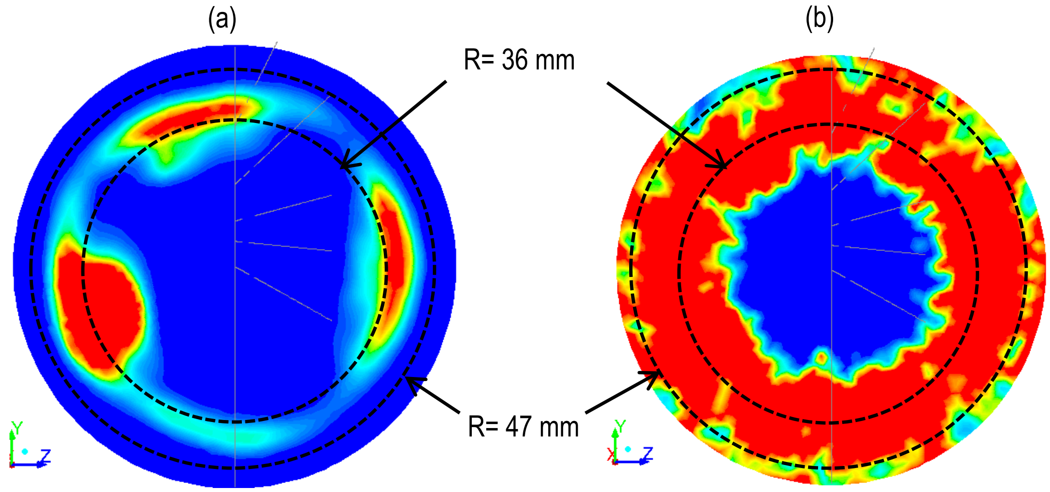

Figure 56 (a) Planar contours of the molar concentration for n-heptane at X=35 mm, (b) Local DPM contours for evaporation at X=35 mm (circular cross section)

At an axial distance of (80 mm) from the injection point, a similar trend for the radial temperature distribution at (X= 35 mm) was observed as illustrated in ***Figure 57***, except that the temperature tends to be more uniform in the radial direction.

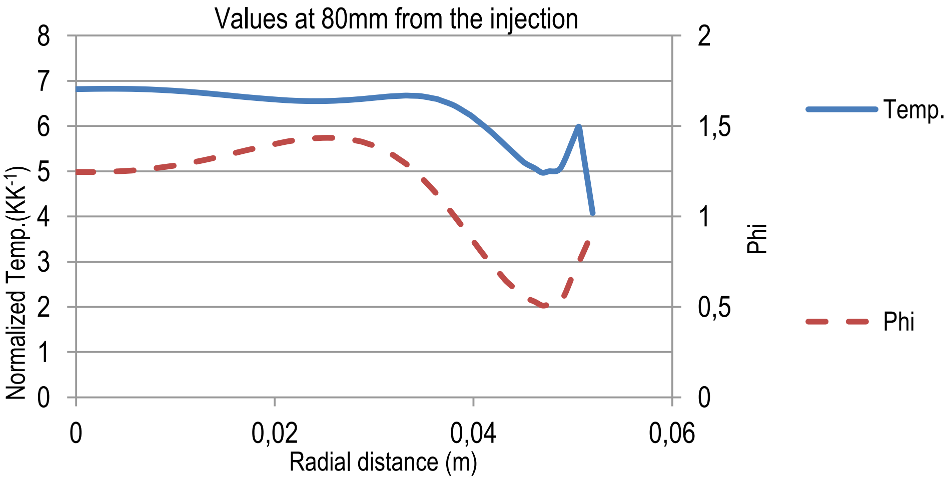

Figure 57 Profiles of radial distributions for temperature and (ϕ) at 80 mm from the injection point, the primary axis on the left represents the normalized temp., the secondary axis on the right represents (ϕ)

At a radius of (47 mm) the temperature falls to (5 KK^{-1}), followed by a rise till a radius of (51 mm) and then steeply falls again to (4 KK^{-1}). The first drop at (R= 47 mm) is related to the lean nature of the mixture in this region as indicated by the equivalence ratio ***Figure 57*** as well as both the molar concentration and the evaporating DPM contours ***Figure 58*** . After a radius of (R= 50 mm), an interesting phenomena occurs, temperature decreases down from (5.7 KK^{-1}) to (4 KK^{-1}) despite the increment in the corresponding local equivalence ratio from (0.7) to (0.95).

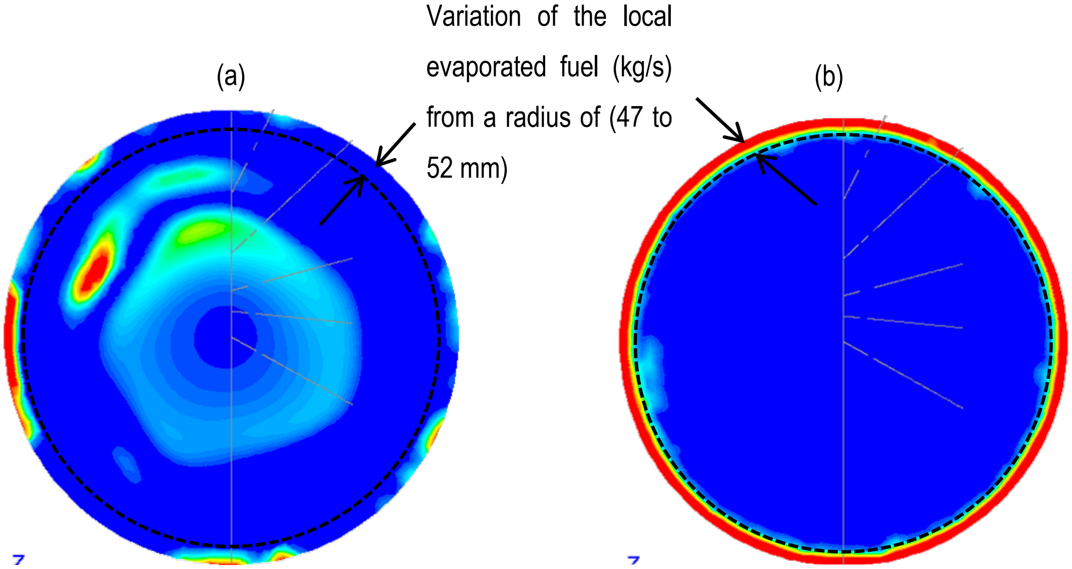

Figure 58 (a) Planar contours of the molar concentration for n-heptane at X= 80 mm, (b) Local DPM contours for evaporation at X= 80 mm (circular cross section)

Regarding the observed decrease of the temperature in the vicinity of the wall boundary, it is judicious to relate it to the wall cooling effects caused by radiation, since, all the combustor walls are simulated as non-adiabatic walls. Moreover, it would be reasonable to assume that at an axial distance of (80 mm) from the injection point, the bigger droplets are dominating and thus their presence is expected, which will certainly create a quenching effect. This is also validated experimentally through the droplet impingements on the wall ***Figure 45***, and predicted numerically through ***Figure 58***.

Concerning, the observed divergence of temperature from the equivalence ratio which tends to the stoichiometric value of ($\phi \sim 1$), whereas the corresponding temperature is the lowest in the domain instead of being the highest; this can be related to local scalar dissipation/strain rate effects caused by the aerodynamics. As explained previously, the calculated flamelets are parameterized by the scalar dissipation and ranked into the flamelet library. During the calculations, the solver will pick a particular flamelet from the calculated flamelets library based on the local value of the scalar dissipation/strain rate, computed from the following equation(5.1):

$$\chi = 2D\left(\frac{\partial \tilde{Z}}{\partial x_i}\right)^2 = C_\chi \frac{\tilde{\varepsilon}}{\tilde{k}}\widetilde{Z''^2} \text{, or in terms strain rate } a_s = \frac{\tilde{\varepsilon}}{\tilde{k}} \qquad (5.1)$$

The proposed formulation for modeling the strain rate as shown in equation (5.1) was introduced by Bray (Bray & Peters, 1994). The same definition was integrated as a user defined field function in FLUENT™, to help in obtaining the local strain rate distribution in the domain.

The idea is simple, based on the local value of (a_s or χ), the solver will determine which flamelet to be used. Seeing that, the temperature distribution versus the mixture fraction is not the same for all the 16 flamelets as seen at ***Figure 36***, it will not be surprising to have different temperature values at the same equivalence ratio, since it depends on the local scalar dissipation value (recall Temp. is a function of (Z, χ)). ***Figure 59*** shows both radial distributions for the local temperature and the local strain rate at (80 mm) from the injection point, it can be clearly seen that the steep fall in the temperature observed between a radius of 50 mm till the wall boundary as circled below, corresponds to high values of strain rates, suggesting that this area contains highly stretched flamelets.

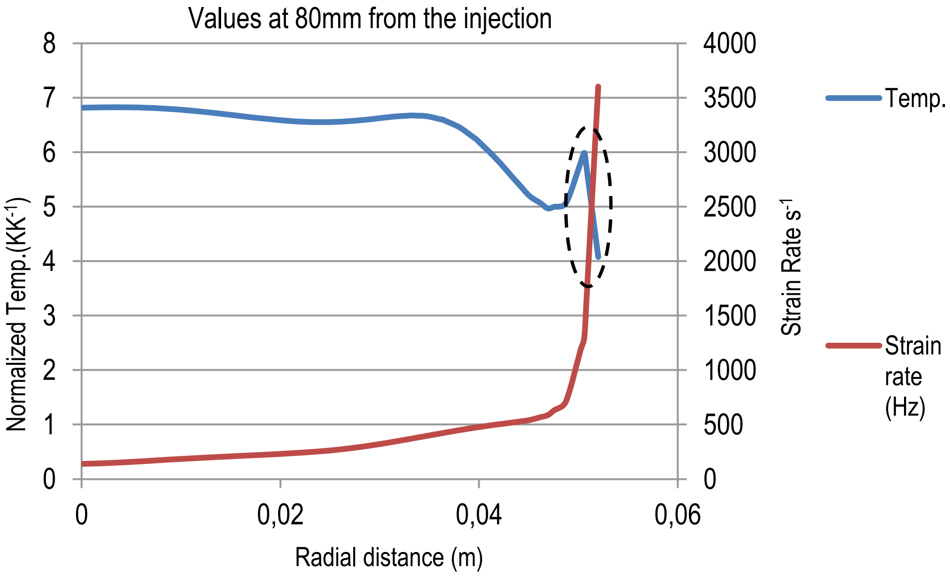

Figure 59 Profiles of radial distributions for temperature and strain rate profiles at 80 mm from the injection point, the primary axis on the left represents the normalized temp., the secondary axis on the right represents strain rate

All of the above mentioned analyses were systematically performed on the other three reacting flow cases. In terms of the combustor aerodynamics, the flame overall shape and trends for the radial distribution of the observed temperatures, there was no major changes found between the four reacting flow cases. Indeed, an order of magnitude difference is present, but the tendencies are almost the same. The differences observed between the various numerical cases are mostly manifested in the formation process for emissions and pollutants, as well as the outer wall temperatures. This shall be detailed for each case in the subsequent sections. In view of that, the analyses performed above for the n-heptane case (1) will not be repeated, but instead a graphical comparison for some contours between the remaining CFD cases will be addressed below. ***Figure 60*** represents the selected contours for case (2); the reader is referred to ***Table 8*** for more details.

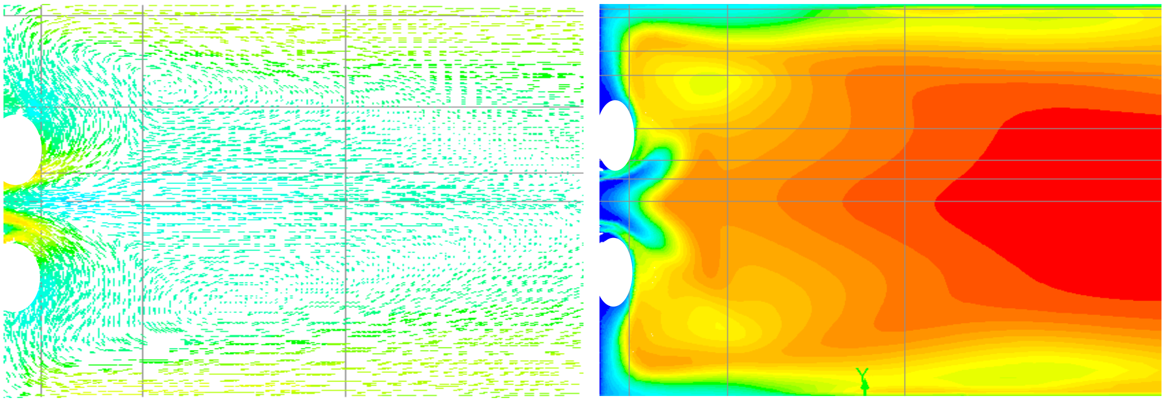

(a) Axial velocity vectors

(b) Normalized temperature contours

(c) DPM mass source contours superimposed on the axial velocity vectors

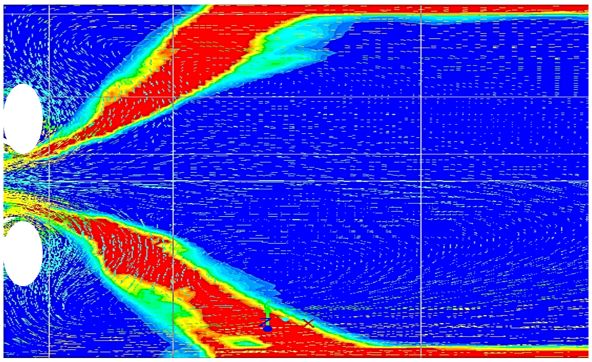

Figure 60 Selected contours of various flow variables for the case with n-heptane at a leaner condition.

Figure 61 shows different contours of the flow variables for both cases with B20 at stoichiometric and leaner conditions, respectively. It can be seen that the B20 exhibited almost similar tendencies as the n-heptane. The similarity in the velocity profile is mainly associated to the aerodynamics of the combustor, which in return is controlled by two parameters, the first is the operating conditions of the injector and the second is spray shape.

These two parameters have almost the same configuration for both n-heptane and B20 cases as seen in (***Table 9***, ***Table 10***, and ***Table 11***). Concerning the temperature profile and the flame shape, the similarity arises from the fact that the surrogate mechanism for B20 contains 50% n-heptane by volume; moreover, the liquid mass fractions for the B20 multicomponent particles were dominated by the presence of n-heptane as shown in ***Table 12***.

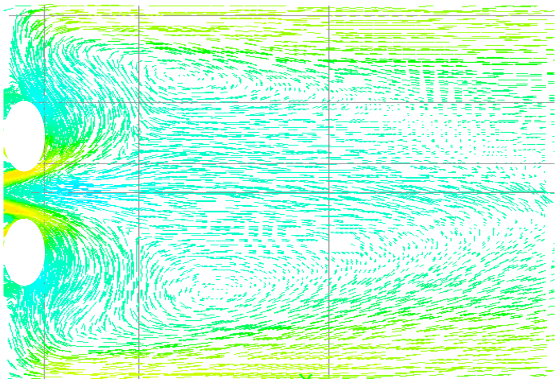

(a) Axial velocity vectors (ϕ =1)

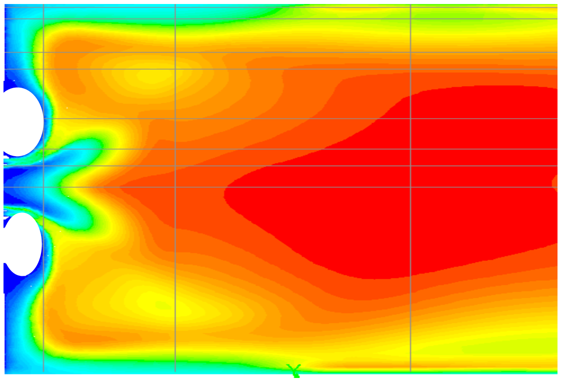

(b) Normalized temperature contours (ϕ =1)

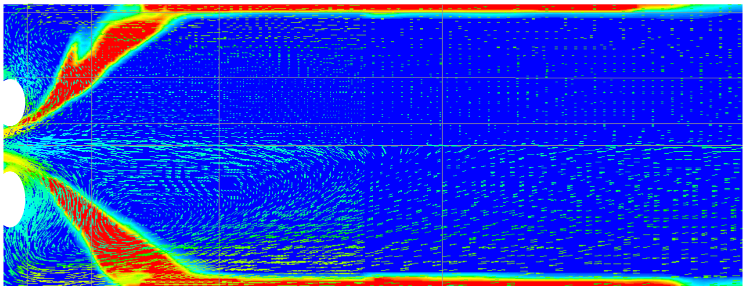

(c) DPM mass source contours superimposed on the axial velocity vectors B20 (ϕ =1)

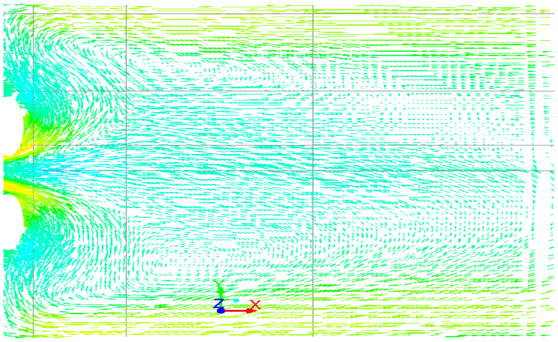

(d) Axial velocity vectors (ϕ =0.8)

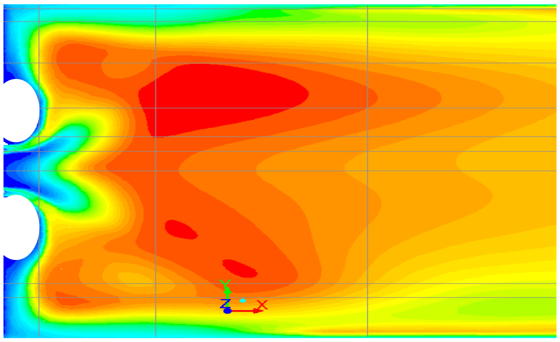

(e) Normalized temperature contours (ϕ =0.8)

(f) DPM mass source contours superimposed on the axial velocity vectors B20 (ϕ =0.8)

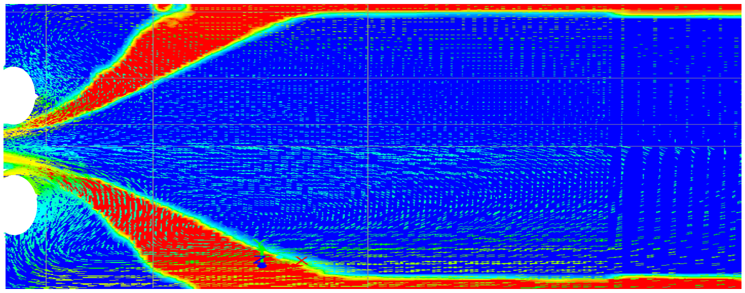

Figure 61 Selected contours for the biodiesel cases: (a), (b), and (c) are the contours for the stoichiometric B20 case (3), whereas, (d), (e), and (f) represent case (4) i.e. B20 at (ϕ =0.8)

5.3.1. Outer wall temperatures

The available outer wall temperatures obtained from the experimental test are compared to the CFD results. Experimentally these values were measured at three different axial locations as indicated in ***Figure 62***. These measurements were performed only for the baseline case and for the diesel case at a leaner condition i.e. (cases 1 and 2); accordingly, CFD validation for these two cases will be presented.

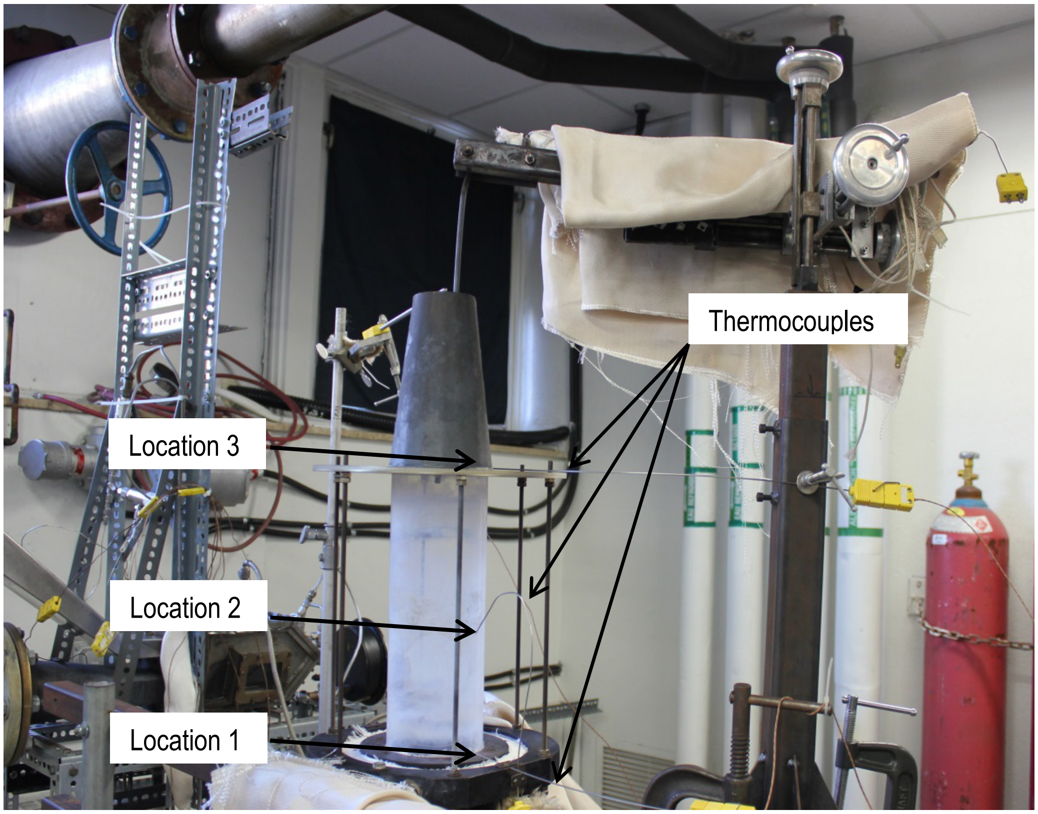

Figure 62 Positions of surface mounted thermocouples for temperature measurements of the combustor wall: locations (1), (2), and (3) correspond to the entry, middle and exit of the quartz tube, respectively.

For the baseline case (1), ***Figure 63*** shows that a very good agreement between both the CFD and the experimental values was obtained. At the inlet of the quartz tube, the difference in temperature does not exceed (~ 20 K) which is less than a 3 % error. At the middle position, the difference went to (~ 130 K) which corresponds to a 15 % error. At the exit of the quartz tube, the observed difference is (~ 30 K).

For the leaner diesel case (2), the outer wall temperature also exhibited a very good agreement with the CFD as illustrated in ***Figure 64***. Almost the exact trends as in case (1) were observed, low deviation between the measured and the predicted outer wall temperatures at the inlet and the exit of the quartz tube, however, the CFD slightly over-estimated the temperature at the middle position of the combustor. This is most likely due to the fact that, during the experimental test, the middle of the quartz tube was subject to high droplet impingements, which can certainly affect the thermocouple measurements.

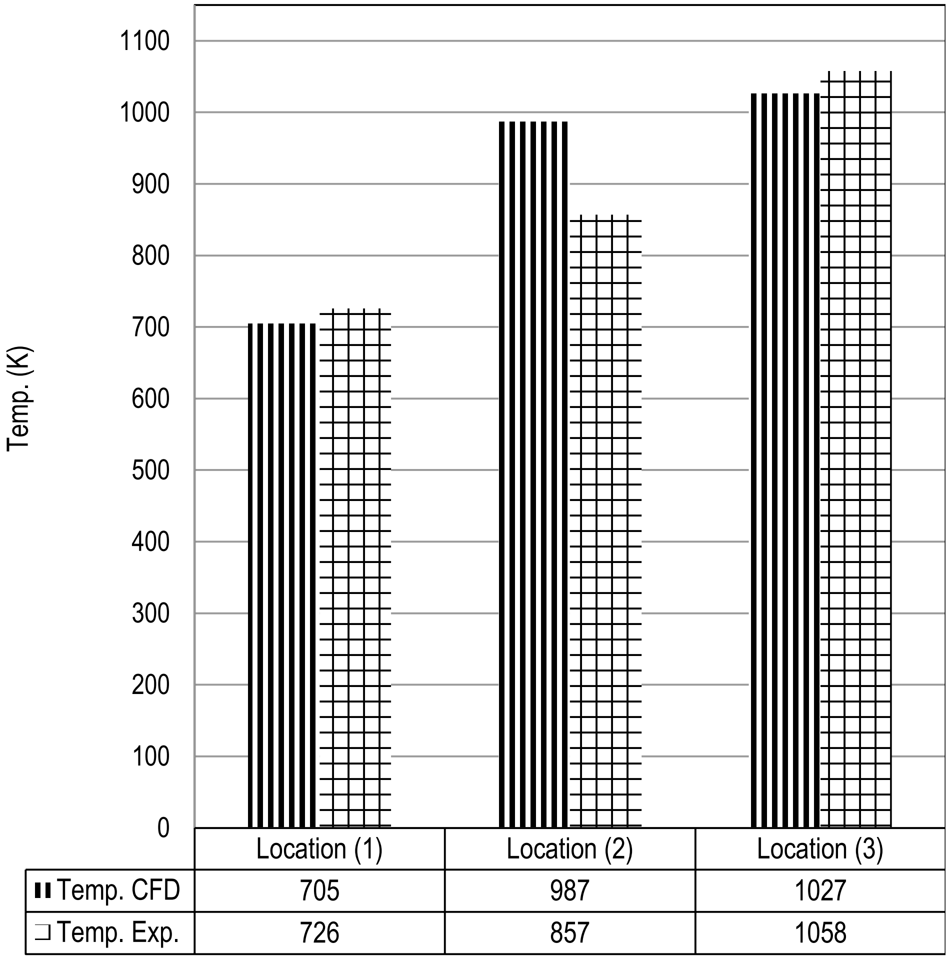

	Location (1)	Location (2)	Location (3)
▮ Temp. CFD	705	987	1027
❑ Temp. Exp.	726	857	1058

Figure 63 Comparison between the experimental and CFD-predicted outer wall temperatures for the n-heptane case (1)

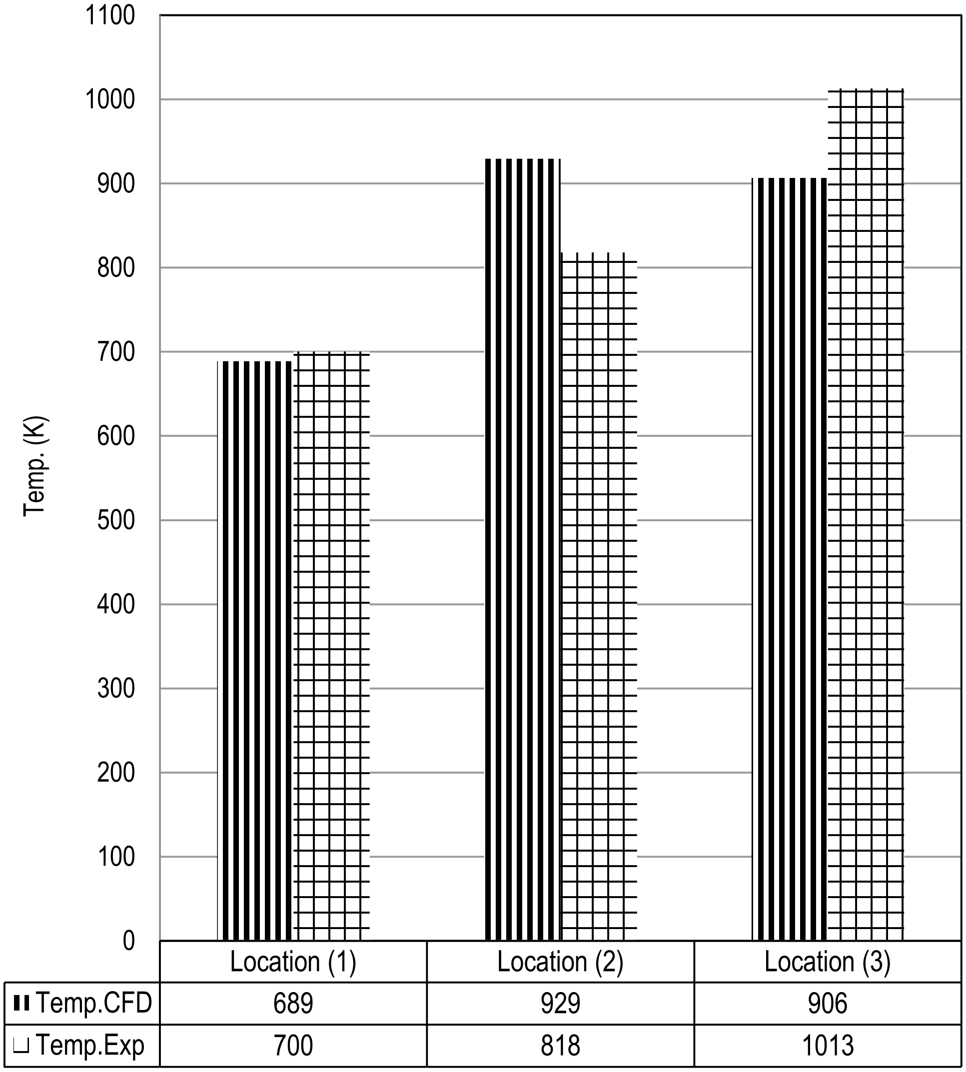

	Location (1)	Location (2)	Location (3)
▮ Temp.CFD	689	929	906
⊞ Temp.Exp	700	818	1013

Figure 64 Comparison between the experimental and CFD-predicted outer wall temperatures for the n-heptane case (2)

5.4. Emissions and Major combustion products

This section will treat the emissions trends obtained from the combustion of conventional diesel and B20 blends at two different equivalence ratios ($\phi = 1$ and 0.8). The results cover the major combustion products such as: H_2O, CO_2, and O_2; as well as the CO as pollutant, other pollutants such as (SO_X) and NO_X are not discussed. Concerning the (SO_X) formation, this latter was not measured experimentally and thus, treating it numerically will not be constructive. For the NO_X formation, a decision was made to omit it from the numerical calculations, even if it was measured experimentally. In fact in ANSYS FLUENT™, NO_X is post-processed from a combustion simulation and the software solves four additional transport equations for the NO_X formation mechanism. It is therefore evident that, an accurate flow field and a reliable combustion solution are the prerequisite for a consistent NO_X prediction. The theory guide for ANSYS FLUENT™ clearly states that under such circumstances trends in NO_X variation can be reasonably predicted, but the NO_X value cannot be used in absolute term (ANSYS, 2011). This statement was also confirmed by RRC engineers who concluded the same way, based on their large experience with the numerical simulations. To be realistic, solving four additional transport equations for four different numerical cases would certainly be time consuming with little chances to accurately quantify this pollutant.

Based on the experimental test protocol, the measuring plane for emissions is located at the exit of the quartz tube at a distance of (300 mm) from the injector. The measuring probe samples hot exhaust gases from five different points situated in that exit plane over a radius of (20 mm) from the geometrical centre of the quartz tube as sketched in ***Figure 65***. Local emission values were sampled in a cross pattern with each point labelled for clarity purposes with cardinal references such as: East, North, West, South and Center.

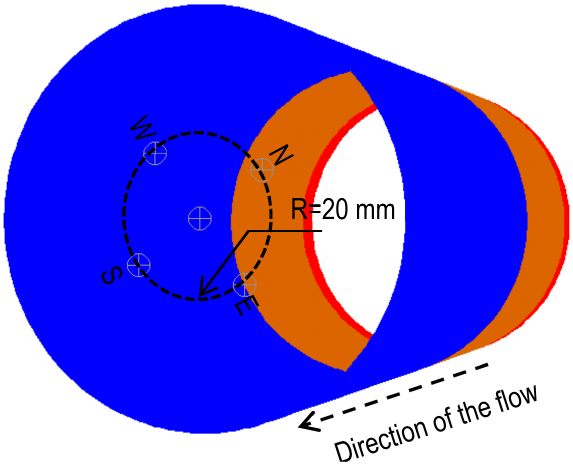

Figure 65 Sketch showing the location of the five measured points

5.4.1. N-heptane case (1)

Emission comparisons between the CFD results and the experimental measurements at the five locations are illustrated in ***Figure 66*** and ***Figure 67***. The CFD model shows a fair prediction of the main combustion products H_2O, CO2, and O_2; however, it seems that the laminar flamelet model has over-estimated the CO values. In order to investigate the reliability of the numerical model, equilibrium calculation was performed using the commercial code (GASEQ) to show how far the numerical combustion model is from equilibrium. Moreover, the local temperatures at their corresponding equivalence ratios are drawn in ***Figure* 68**; but, no experimental values for the local temperature distributions are available for the validation.

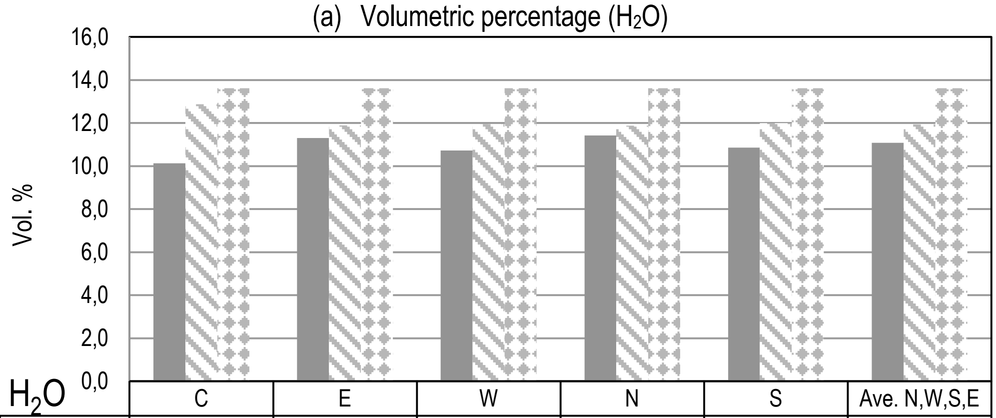
(a) Volumetric percentage (H_2O)

H_2O	C	E	W	N	S	Ave. N,W,S,E
■ Exp.	10,1	11,3	10,7	11,4	10,9	11,1
▧ SD 16	12,9	11,9	12,0	11,9	12,0	11,9
◆ Equilibrium	13,6	13,6	13,6	13,6	13,6	13,6

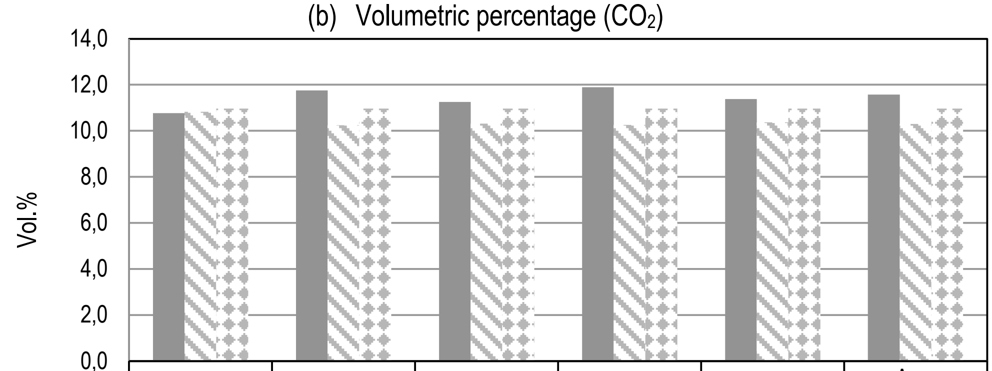
(b) Volumetric percentage (CO_2)

CO_2	C	E	W	N	S	Ave. N,W,S,E
■ Exp.	10,8	11,8	11,3	11,9	11,4	11,6
▧ SD 16	10,8	10,2	10,3	10,3	10,4	10,3
◆ Equilibrium	11,0	11,0	11,0	11,0	11,0	11,0

Figure 66 (H_2O) and (CO_2) measurements from the experimental tests, the San Diego mechanism with 16 flamelets (SD 16) and the (GASEQ) equilibrium calculations, respectively.

(a) Volumetric percentage (O_2)

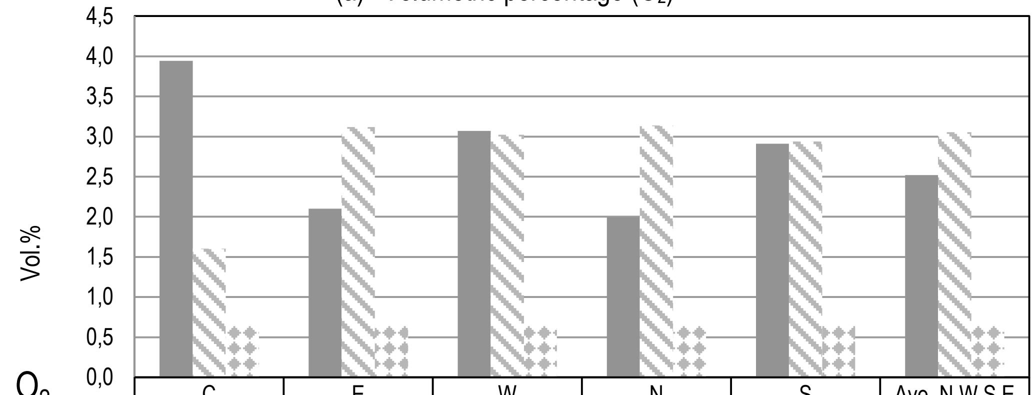

O_2	C	E	W	N	S	Ave. N,W,S,E
■ Exp.	3,9	2,1	3,1	2,0	2,9	2,5
▨ SD 16	1,6	3,1	3,0	3,1	2,9	3,1
◆ Equilibrium	0,6	0,6	0,6	0,6	0,6	0,6

(b) ppm concentration of (CO)

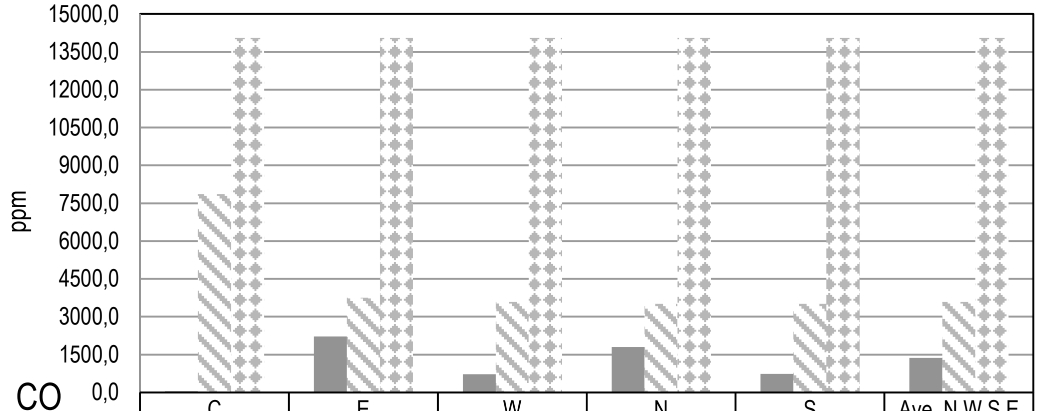

CO	C	E	W	N	S	Ave. N,W,S,E
■ Exp.	46,3	2216,9	719,3	1796,1	737,8	1367,5
▨ SD 16	7857	3756	3584	3515	3516	3593
◆ Equilibrium	14050	14050	14050	14050	14050	14050

Figure 67 (a) the (O_2) and (b) the (CO in ppm) measurements from the experimental tests, the San Diego mechanism (SD 16) and the (GASEQ) equilibrium calculations, respectively.

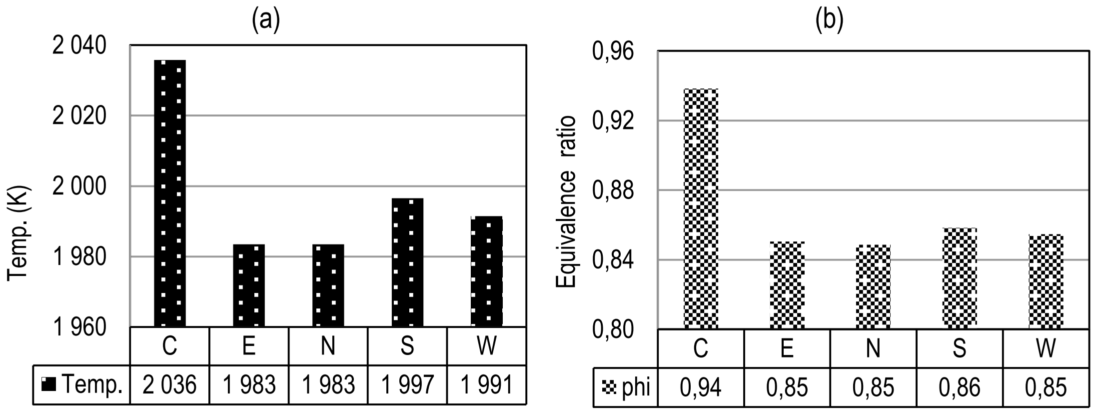

Figure 68 (a) Predicated local temperature and (b) Predicated local phi distributions, respectively

Both experimental and CFD results agreed that there is locally a slight excess amount of air at the measuring points as shown from the predicted local equivalence ratio distributions, as well as, the volumetric percentage of O_2, this is in conflict with the values predicted from the equilibrium theory. In fact, as mentioned above the measuring plane is located at the exit of the quartz tube (300 mm) from the injector, which is almost (3/5) of the computational domain after including the length of the steel cone (190 mm). Indeed at this location the assumption that the chemistry is relaxed and will tend towards equilibrium is not fully suitable, this explains the discrepancy observed with the equilibrium calculations. Concerning the small differences in the value of O_2 between the CFD and the experimental measurement, it should be noted that the values of O_2 obtained from the experimental tests were calculated rather than being measured, since, the analyzer provides a module for the O_2 measurement but it could not be operated for safety reasons. The calculated O_2 values came from a mass balance using the measured equivalence ratio for the reactants and the other measured combustion products but not including the unburned carbon cumulated on the combustor wall .This can add a certain level of uncertainty to the given experimental values.

Regarding the CO, there is a high degree of discrepancy between the CFD, the experimental and the equilibrium calculations; furthermore, there is a high inconsistency in the values obtained from the experimental test, in terms of the order of magnitude at the five points as shown in (***Figure 67 b***). ***Figure 69*** indicates the presence of a massive amount of soot (20 to 50 mm in thickness) during the real combustion test of the diesel at (ϕ=1), which will definitely affect the emission measurements. The presence of quenched carbon atoms on the combustor walls shows that the carbon atoms have not been properly consumed during the combustion process, leaving high carbon traces and leading to an excess of oxygen in the calculated value. Additionally, the quenched carbon distributions are not uniform; which explains the inconsistence of the CO values at the five points. The relation between the CO and the excess of O_2 is demonstrated by both the

CFD and the experimental measurements; for instance, through the point at the centre from the experimental data, at which the CO is at its minimum whereas the O_2 jumps to its maximum.

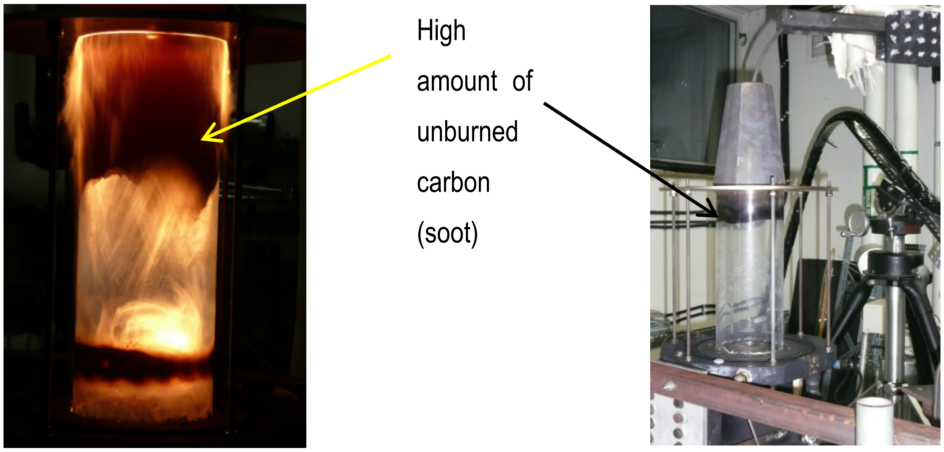

Figure 69 Elevated level of soot accumulation on the combustor wall for the baseline case

In the numerical model, no presence of soot is reported, since the soot sub-model is not activated, accordingly, the four cardinal points show a better consistence in terms of CO values, except for the point at the centre, where the CO concentration is almost doubled. By checking the local temperature distributions and their corresponding equivalence ratios ***Figure 68***, it can be seen that the local predicted value at the centre is closer to a stoichiometric value, which explains the peak in the temperature, and thus the rate of production of the CO by chemical dissociation of CO_2 starts to be significant. Actually, this should not be surprising, because the same trend in CO with temperature is shown through the calculated values using the equilibrium theory (e.g. at ϕ =1, $T_{max.}$ = 2 282 K, CO = 14 050 ppm). Lefebvre has investigated the influence of the equivalence ratio on the CO formation (Lefebvre & Ballal, 2010); his study shows the variation of CO with the equivalence ratio for three different inlet air pressure values ***Figure 70***. It can be observed that, the CO concentration reduces with the increment of the equivalence ratio till (ϕ =0.8) above which any further increment of the equivalence ratio will create a rise in the (CO), sometimes referred to as the famous CO kink. The high levels of CO at low equivalence ratios are due to the slow rates of oxidation, associated with low combustion temperatures. An increase in the equivalence ratio raises the flame temperature, which accelerates the rate of oxidation so that the CO emission declines. A further increase in the equivalence ratio will lead to higher temperatures, which will trigger the chemical dissociation of the CO_2, resulting into an increment of the CO concentrations.

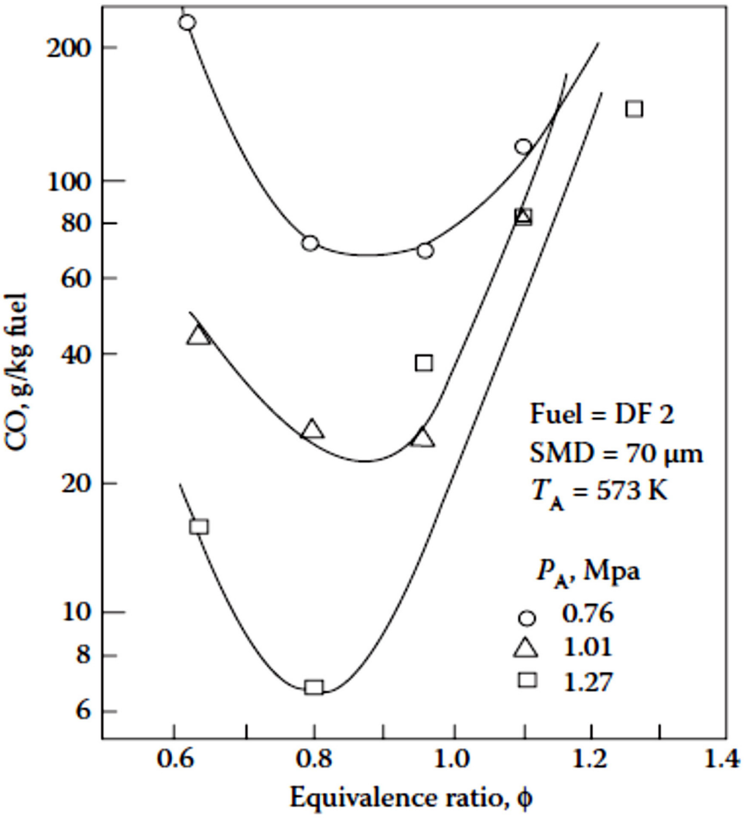

Figure 70 Influence of the air inlet pressure and the equivalence ratio on the CO formation **(Lefebvre & Ballal, 2010)**

5.4.2. N-heptane case (2)

This case is the leaner condition of case (1), in which the global equivalence ratio is set to (0.8). Emissions from the simulation of case (2), shows a better agreement with the experimental data and the equilibrium calculations using the (GASEQ) code, than those observed in case (1). ***Figure 71***, and ***Figure 72*** show, the emission concentrations of the H_2O, CO_2, O_2, and CO.

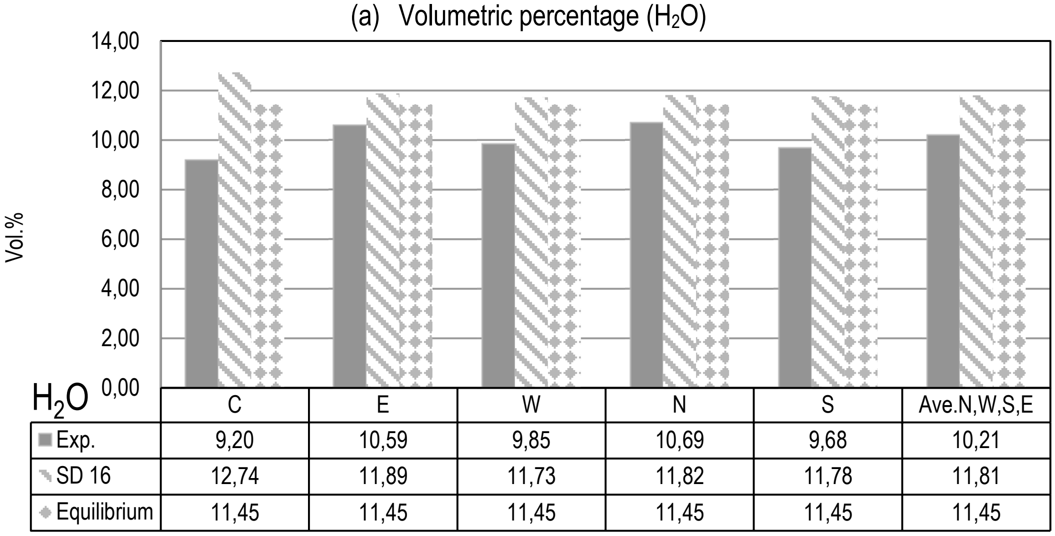
(a) Volumetric percentage (H_2O)

	C	E	W	N	S	Ave.N,W,S,E
■ Exp.	9,20	10,59	9,85	10,69	9,68	10,21
▨ SD 16	12,74	11,89	11,73	11,82	11,78	11,81
◆ Equilibrium	11,45	11,45	11,45	11,45	11,45	11,45

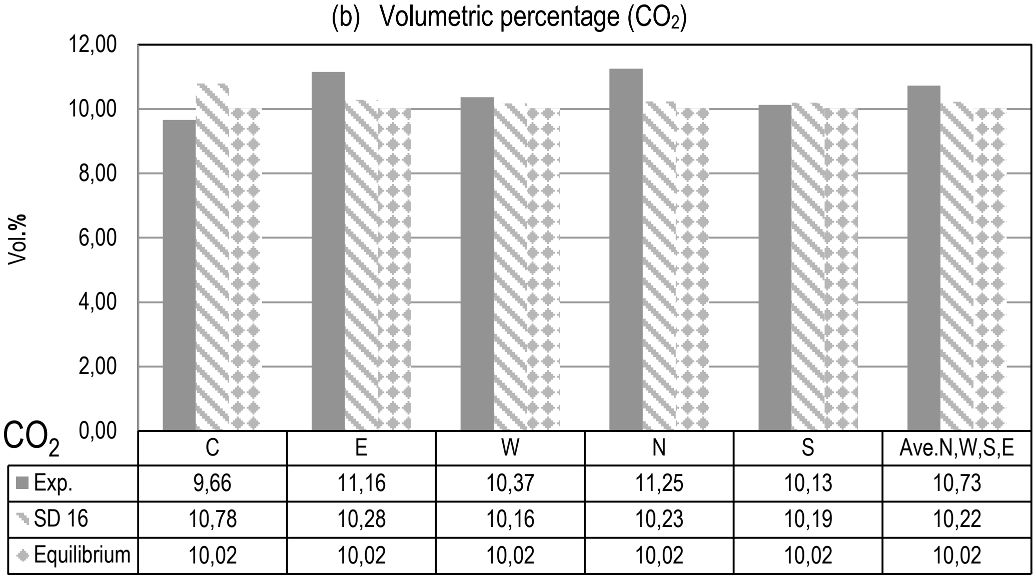
(b) Volumetric percentage (CO_2)

	C	E	W	N	S	Ave.N,W,S,E
■ Exp.	9,66	11,16	10,37	11,25	10,13	10,73
▨ SD 16	10,78	10,28	10,16	10,23	10,19	10,22
◆ Equilibrium	10,02	10,02	10,02	10,02	10,02	10,02

Figure 71 Emission concentrations (a) (H_2O) and (b) (CO_2) measurements from the experimental tests, the San Diego mechanism (SD 16) and the (GASEQ) equilibrium calculations, respectively

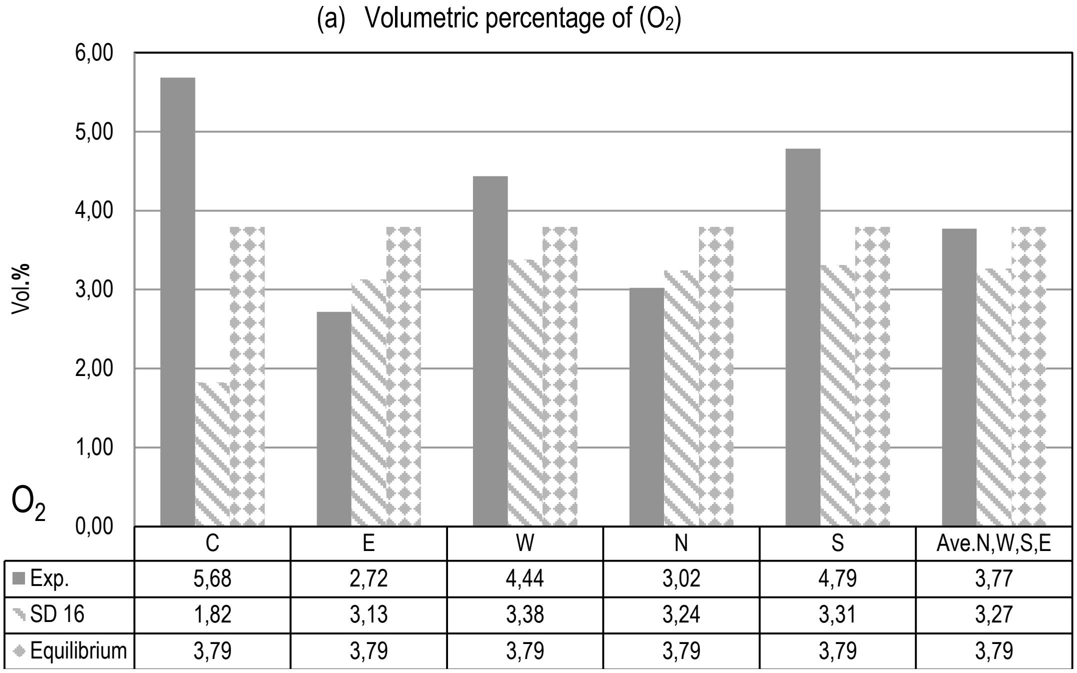

(a) Volumetric percentage of (O_2)

	C	E	W	N	S	Ave.N,W,S,E
■ Exp.	5,68	2,72	4,44	3,02	4,79	3,77
▨ SD 16	1,82	3,13	3,38	3,24	3,31	3,27
◆ Equilibrium	3,79	3,79	3,79	3,79	3,79	3,79

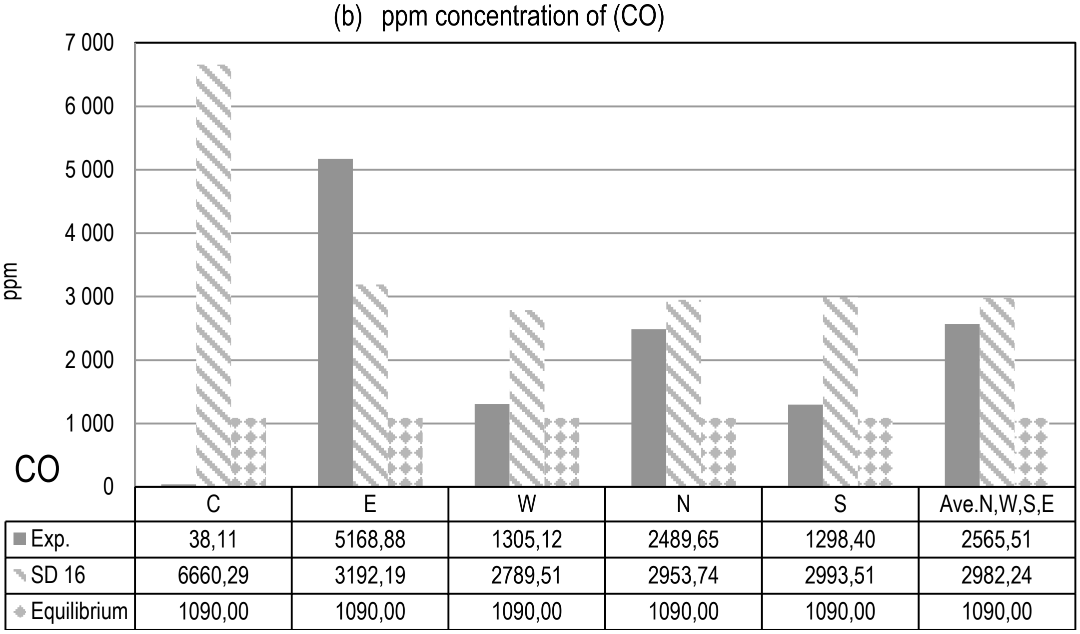

(b) ppm concentration of (CO)

	C	E	W	N	S	Ave.N,W,S,E
■ Exp.	38,11	5168,88	1305,12	2489,65	1298,40	2565,51
▨ SD 16	6660,29	3192,19	2789,51	2953,74	2993,51	2982,24
◆ Equilibrium	1090,00	1090,00	1090,00	1090,00	1090,00	1090,00

Figure 72 Emission concentrations (a) (O_2) and (b) (CO) measurements from the experimental test, the San Diego mechanism (SD 16) and the (GASEQ) equilibrium calculations, respectively.

The agreement observed between both CFD and experimental results can be mainly related to the strong reduction in the concentration of the quenched carbon atoms on the combustor walls, as seen in ***Figure 73***.

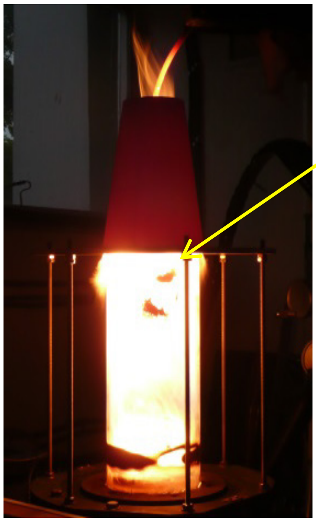
Significant soot reduction compared to case (1)

Figure 73 Photo of the test rig during combustion of n-heptane at a leaner condition

This remark further substantiates the author point of view that the experimental measurements, as well as, the O_2 calculations become more reliable when the amount of the quenched carbon atoms is considerably reduced. **Figure 74** shows a better local equivalence ratio prediction than the one observed at case (1), the gap is considerably reduced with respect to the global equivalence ratio. Except for the point at the centre, in which a relatively high local equivalence ratio is observed, explaining the jump in the CO concentration at this point.

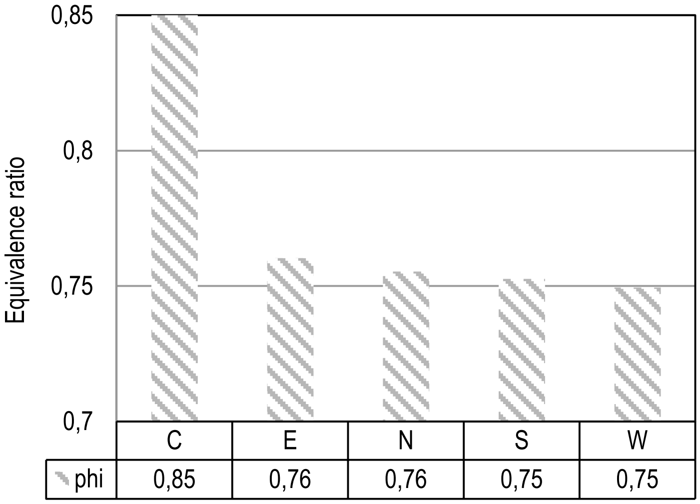

Figure 74 CFD prediction of the local equivalence ratio profile at the cardinal points

This point has always shown an odd trend compared to the other four, in both the CFD and the experimental tests. From the experimental point of view, this point is very close to the measuring probe, and thus a certain level of flow disturbance is expected, leading to an increase in the data acquired error at this particular location. However, it is unreasonable to assume the same for the CFD, because simply, the probe does not exist in the numerical domain. Yet, the reasoning of the flow disturbance at this point hold valid for both the CFD and the experimental test. For the CFD this disturbance occurred in a small scale for some cells located in the asymmetric axis from the exit of the quartz tube till the exit of the domain, due to the so called numerical backflow. This backflow is associated with the type of boundary condition chosen in the present numerical model, which is the pressure outlet type. It is usually manifested in the far downstream cells close to the exit of the domain due to high pressure gradient in the last cells; however, it seems that the introduction of the steel cone has influenced the pressure field, allowing the propagation of the backflow to some cells existing at the quartz tube exit plane.

In view of the above, the average of the cardinal four points is considered as the most reliable representative for both the CFD and the experimental data, ***Table 16*** shows the deviation between the CFD and the experimental for both n-heptane cases at (ϕ = 1 and 0.8) at the average of the four cardinal points. This table can be used to conclude that the gap between the CFD and the experimental results was reduced at the leaner condition.

Table 16 Percentage of the deviation between the CFD and the experimental for the conventional diesel cases

Parameter	Location	ϕ = 1	ϕ = 0.8
H_2O emission	Ave. N, W,S,E	7 %	15 %
CO_2 emission	Ave. N, W,S,E	11 %	5 %
CO emission	Ave. N, W,S,E	162 %	16 %
O_2 emission	Ave. N, W,S,E	24 %	13 %
Local phi	Ave. N, W,S,E	15 %	5 %

5.4.3. Biodiesel B20 blend cases (3 and 4)

This sub-section is grouping emissions for both the B20 cases at (ϕ = 1 and 0.8, respectively). For the biodiesel blend B20 at (ϕ = 1) i.e. case (3) as illustrated in ***Figure 75*** an emission trend similar to the conventional diesel case at (ϕ = 1) is observed. Where the H_2O and the CO_2 are in good agreement with the experimental values, the O_2 is moderately within the range and the CO is out of the range. It is believed that this is due to the same explanation proposed for the n-heptane case (1). Indeed this is not surprising, since as demonstrated in the gas temperature field section (see § 5.3) both fuels exhibited almost the same flame shape, temperature field, and reactivity; the differences are however, in the order of magnitude of the flow field variables and the emissions. In fact, one of the current objectives in this study is to demonstrate that the biodiesel B20 blends can be used as a drop-in fuel. This implement the usage of these non-convention fuels as a replacement for the conventional ones, without modifying the combustion chamber, and also to verify their superiority over conventional fuels in improving pollutant emissions. Additionally, this similarity arises from the chemical mechanism which contains (25% MD, 25% MD-9-D, and 50 % n-C_7H_{16}).

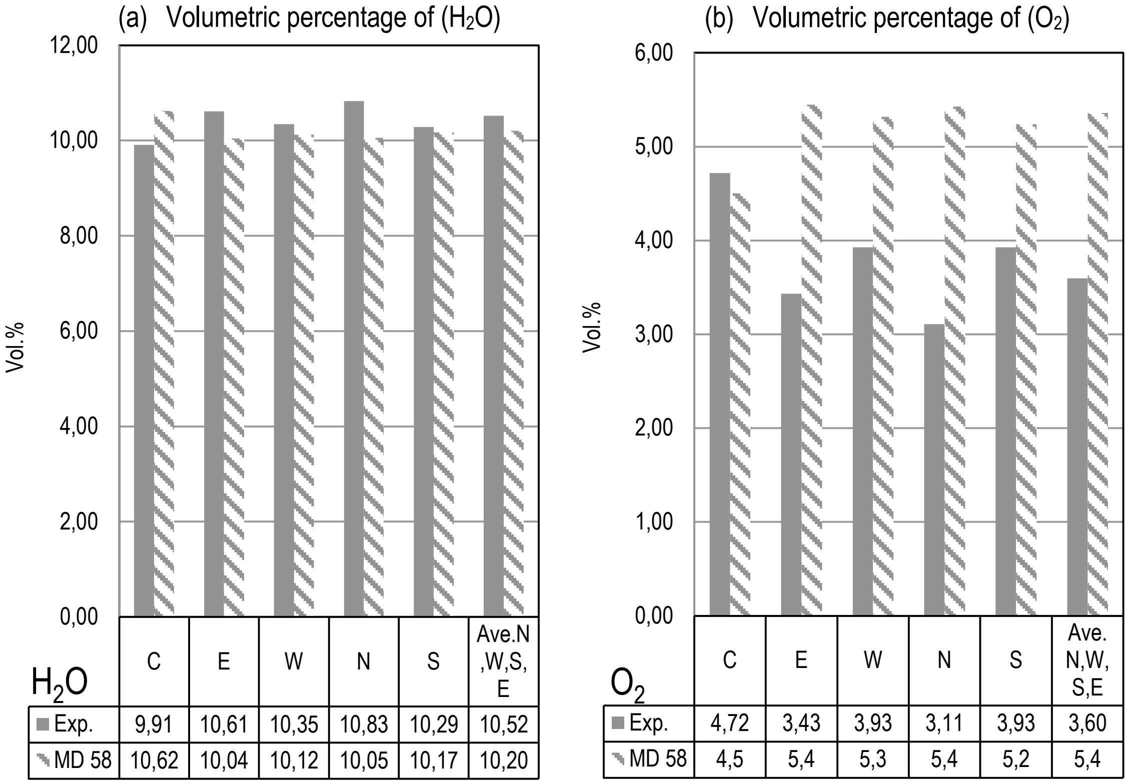

H_2O	C	E	W	N	S	Ave.N ,W,S, E
■ Exp.	9,91	10,61	10,35	10,83	10,29	10,52
▧ MD 58	10,62	10,04	10,12	10,05	10,17	10,20

O_2	C	E	W	N	S	Ave. N,W, S,E
■ Exp.	4,72	3,43	3,93	3,11	3,93	3,60
▧ MD 58	4,5	5,4	5,3	5,4	5,2	5,4

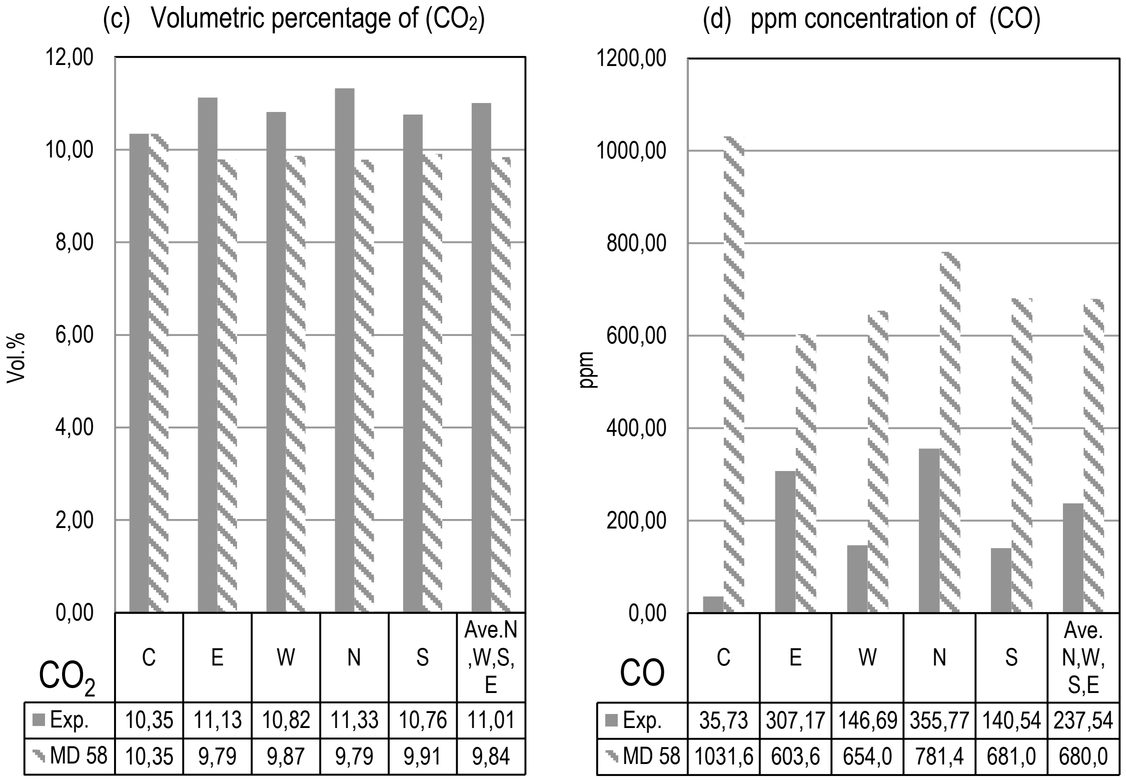

CO_2	C	E	W	N	S	Ave.N,W,S,E
■ Exp.	10,35	11,13	10,82	11,33	10,76	11,01
▨ MD 58	10,35	9,79	9,87	9,79	9,91	9,84

CO	C	E	W	N	S	Ave. N,W, S,E
■ Exp.	35,73	307,17	146,69	355,77	140,54	237,54
▨ MD 58	1031,6	603,6	654,0	781,4	681,0	680,0

Figure 75 Emissions for the B20 case (3) from the experimental results and the predicted values using the methyl decanoate mechanism with 58 flamelets (MD 58).

The CO concentration from the combustion of biodiesel not only shows that an improvement in the pollutant emissions is achieved, but also, the gap between the CFD and the experimental results is considerably reduced. From ***Figure 76*** it can be observed that the amount of quenched carbon atoms is drastically reduced compared to the conventional diesel case at the same operating condition.

Figure 76 Soot formation during the combustion of the B20 blend at (ϕ = 1)

These unburnt carbons were further reduced (almost vanished) during the combustion of the B20 blend case (4) at (ϕ = 0.8) as indicated at ***Figure 77***. Actually, our discussion is related to the soot accumulations observed at the measuring plane; the effects of soot formation in the vicinity of the injector, i.e. upstream were not investigated.

Figure 77 Soot formation during the combustion of the B20 blend at (ϕ = 0.8)

Accordingly, emissions from the B20 blend case (4) have also displayed a fair correspondence to the obtained experimental results as shown in ***Figure 78***.

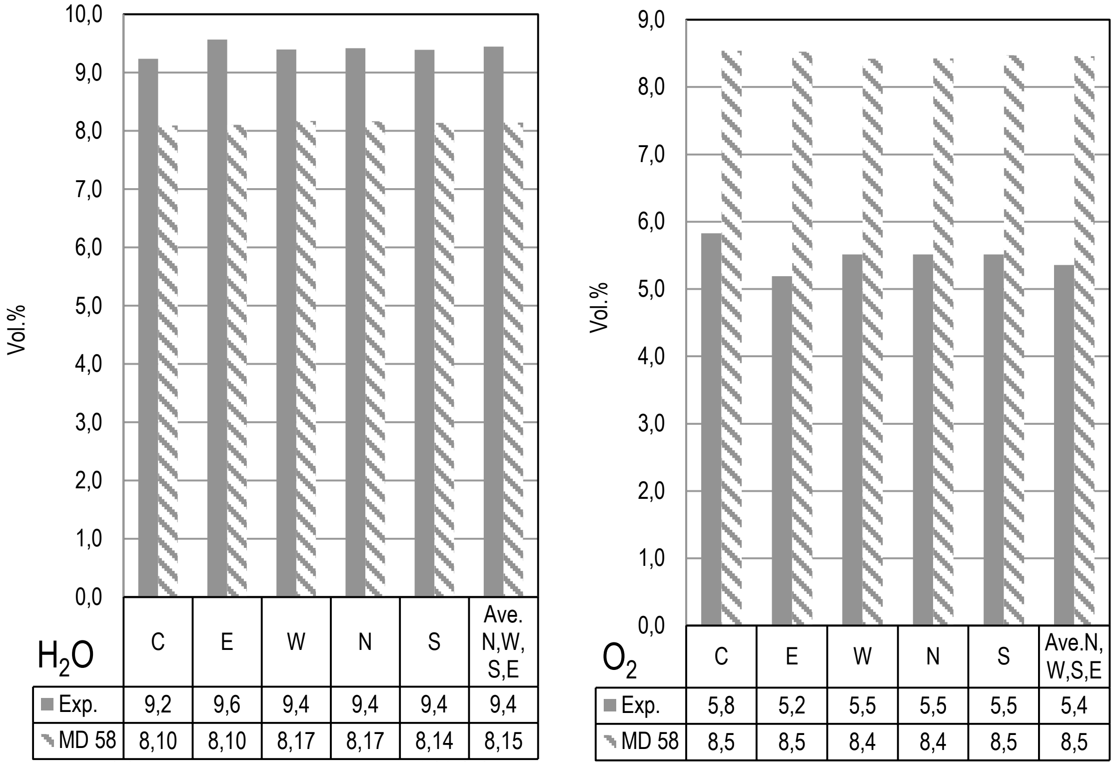

(a) Volumetric percentage of (H_2O)

(b) Volumetric percentage of (O_2)

H_2O	C	E	W	N	S	Ave. N,W, S,E
▨ Exp.	9,2	9,6	9,4	9,4	9,4	9,4
▧ MD 58	8,10	8,10	8,17	8,17	8,14	8,15

O_2	C	E	W	N	S	Ave.N, W,S,E
▨ Exp.	5,8	5,2	5,5	5,5	5,5	5,4
▧ MD 58	8,5	8,5	8,4	8,4	8,5	8,5

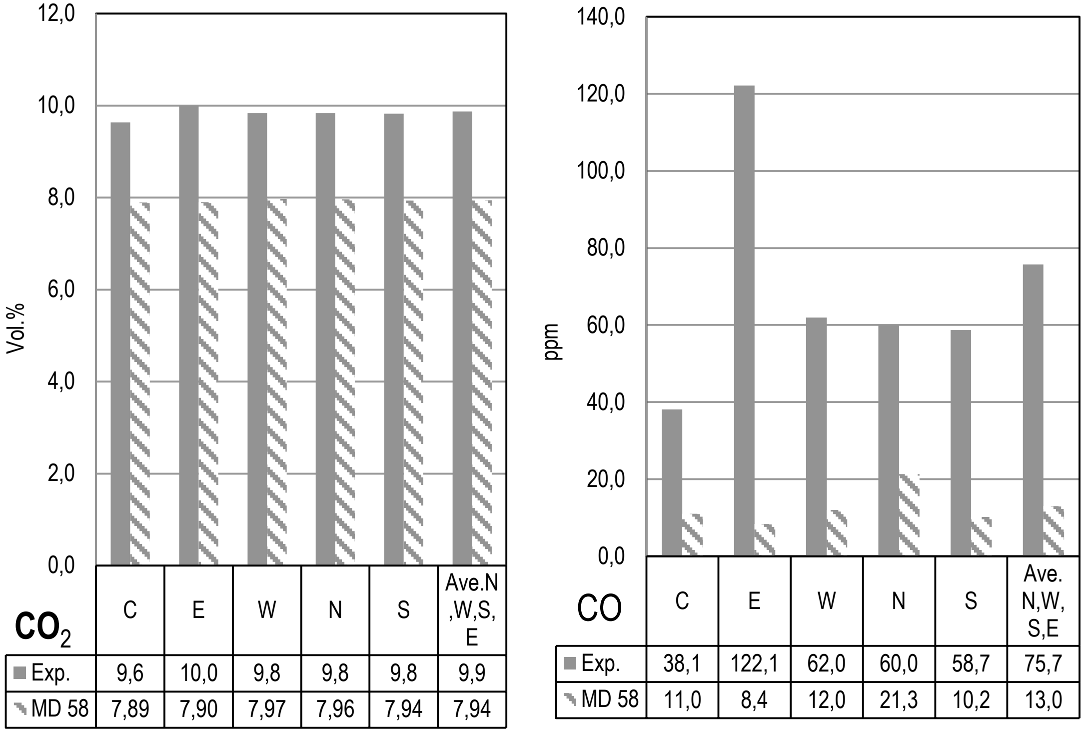

(c) Volumetric percentage of (CO_2)

(d) ppm concentration of (CO)

CO_2	C	E	W	N	S	Ave.N ,W,S, E
▨ Exp.	9,6	10,0	9,8	9,8	9,8	9,9
▧ MD 58	7,89	7,90	7,97	7,96	7,94	7,94

CO	C	E	W	N	S	Ave. N,W, S,E
▨ Exp.	38,1	122,1	62,0	60,0	58,7	75,7
▧ MD 58	11,0	8,4	12,0	21,3	10,2	13,0

Figure 78 Emissions of the B20 case (4) from the experimental results and the predicted values using the methyl decanoate mechanism with 58 flamelets (MD 58).

Despite the fact that, the deviation gap between the CFD and the experimental results increased for the B20 cases, especially for the B20 at the leaner condition as shown in ***Table 17*** which is the opposite of what was observed in the conventional fuel cases, the general trends are in good agreement. Both the CFD and the experimental results show that CO emissions from combustion of the B20 blend were considerably reduced compared to the conventional fuel cases; this can be clearly seen in ***Figure 79***.

Table 17 Percentage of the deviation between the CFD and the experimental for the B20 cases

Parameter	Location	ϕ = 1	ϕ = 0.8
H_2O emission	Ave. N, W,S,E	3 %	13 %
CO_2 emission	Ave. N, W,S,E	10 %	20 %
CO emission	Ave. N, W,S,E	186 %	83 %
O_2 emission	Ave. N, W,S,E	50 %	57 %

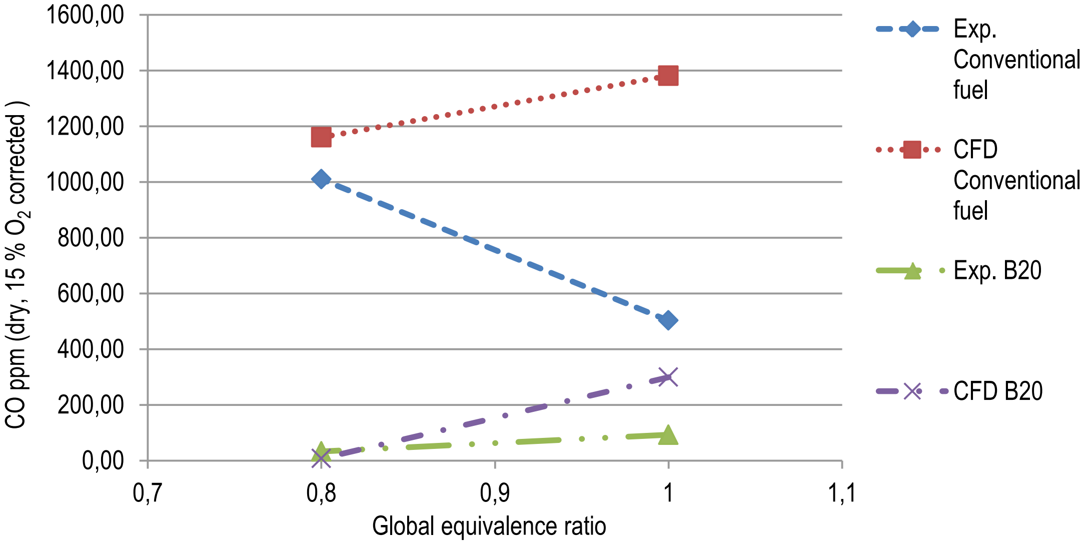

Figure 79 (CO) emissions from the four cases at the various global equivalence ratios

First, before explaining the above mentioned CO graph, it should be noted that the CO concentrations expressed in (ppm, dry and corrected) in ***Figure 79*** are different from the previously used units (wet ppm). Representing the data in terms of (dry, corrected 15 % O_2) is a commonly used practice in the gas turbine industry. The author has chosen to introduce it specifically in this graph, because it contains a correction factor that damps the order of magnitude of the presented values, hence simply, will allow a more reasonable graphical comparison between the CFD and measured values.

Several conclusions can be gained from this graph, initially, that the CFD has always over-predicted the CO values. Secondly, the deviation between the CFD and the experimental results are in good agreement at leaner conditions, whereas, the gap jumps near stoichiometric conditions. Thirdly, which is the most important, is the lower CO concentration of the B20 blends detected by both the CFD and the experimental values. In fact, the low CO emissions and lower soot formation demonstrated from the combustion of the biodiesel blends were widely investigated by many researchers. For example, Jaime (Jaime, Parthasarathy, & Gollahalli, 2010) suggested that the presence of fuel bound oxygen in the ester function group of the fuel molecule aids the oxidation process and suppresses the soot precursors, while, Nozomu (Hashimoto, Ozawa, Mori, & Yuri, 2008) related that to the absence of aromatic ring molecules in the biodiesel chains.

To summarize, the experimental data using the conventional fuel cases showed that the CO concentration at (ϕ = 0.8) is higher than that at (ϕ = 1), this is in contrast to the commonly understood CO trends. It is believed that this uncertainty rises from the high accumulation of the quenched carbon atoms, which can certainly affect the measured CO values. Consequently, the calculated O_2 values can be affected, because the O_2 was derived from a mass balance from the other measured combustion products. To this end, the CFD over-prediction cannot be fully justified.

Concerning the biodiesel cases, an emission enhancement was observed by both the CFD and the experimental from combustion of these fuels, this was found in agreement with the studies performed by other researchers. Yet, the CFD validation for the (CO) emissions was not as successful as in the conventional cases. With the absence of an equilibrium calculation as performed in the conversational cases, it was difficult to quantitatively evaluate the obtained emission results from both the CFD and the experimental values.

5.5. General observations

This section will highlight five main observations/remarks related to the flamelet approach in general, and its implementation within ANSYS FLUENT™ in particular.

The first observation is related to the ability of the flamelet model to capture the flamelet extinction. As previously mentioned, flamelets at extinction are not accounted for in the calculated flamelet library. This assumption might have a significant effect on the flame shape and temperature profile in regions where the local strain rate is elevated and consequently local extinction is expected. In order to evaluate the consequences of this assumption, the radial distribution for temperature is drawn against the local strain rate. ***Figure 80*** shows the response of temperature to the local aerodynamic strain/stretching at (10 mm) from the injection point during the combustion of n-heptane at global (ϕ = 1).

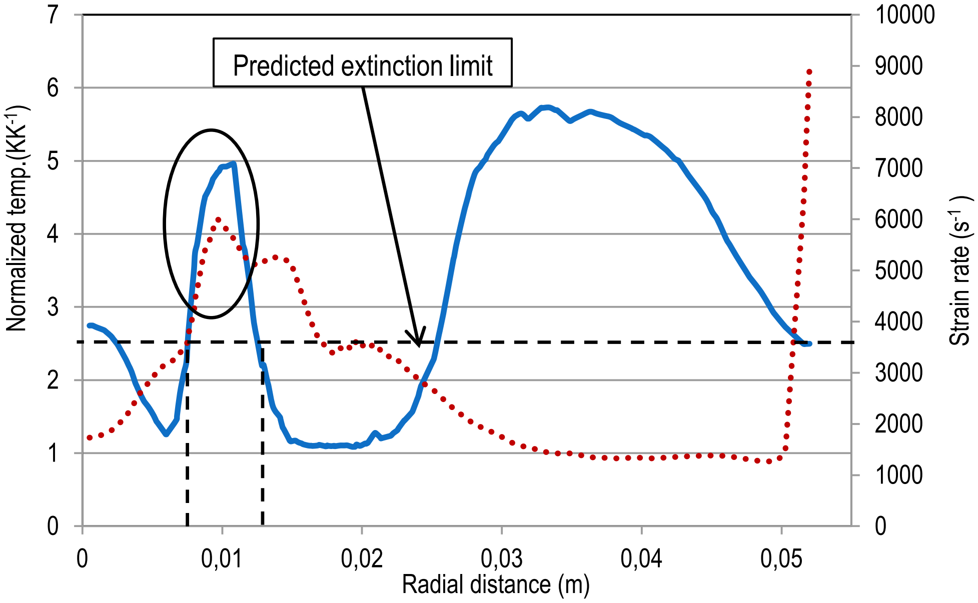

Figure 80 Radial temperature distribution (solid line) vs. local strain rate (--- dotted line) at (10 mm) from the injection point, from case (1)

The highlighted circle demonstrated clearly that at a radial distance of (10 mm) from the centreline the temperature peaks despite the locally elevated aerodynamic strain rate (~ 6 000 s^{-1}), which is almost double the estimated extinction limit of the calculated n-heptane flamelets (e.g. 3 245 s^{-1}). Obviously, at such excessive strain rate, a drop in temperature should be expected to match this flame quenching. Other authors (Rochaya, 2007) have reported the same observation with the laminar flamelet approach, but no explanation was proposed. It is believed that this odd trend is related to the deliberate choice in excluding the flamelets at extinction from the library generated in FLUENT™. Under such condition, one of the following two procedures can be employed, either the solver imposes an arbitrary temperature value corresponding to the initial boundary condition (i.e. 300 K in our case), or the solver will choose an alternative flamelet such as the last calculated flamelet in the library prior to extinction. The first suggestion is far from being right, since as seen in (***Figure 80*** vertical dashed lines) the radial range from (8 mm to 12 mm) is subject to varying elevated temperature values. The second suggestion seems more reasonable, by checking the distribution for mixture fraction from the flamelet prior to the extinction i.e. the flamelet at (66 s^{-1}), the (*Z*) value at this specific location (10 mm from the injection point and at a radius of 10 mm from the centreline) is found at around (0.15) with a corresponding normalized temperature of (5 KK^{-1}). This means, an overprediction of the temperature field in the highly strained regions, and also it can be interpreted as an over-estimation of the flamelet extinction. Accordingly, this can be considered as one of the drawback of the steady laminar flamelet model in predicting the local flame extinction.

The second observation is related to the major assumptions that are responsible for the derivation of the simplified steady flamelet equations (see § 2.7.4.1), and are summarized below:

- The omission of the transient term (unsteady term in the flamelet equation): This hypothesis relies on the assumption that the time scales for chemical kinetics are much shorter than the time scales of convection and diffusion. Nevertheless, some phenomena, such as pollutant formation (e.g. NO_x, and CO) are slow processes compared to the chemical time scales and can have a characteristic time scale on the same order of magnitude as the convective or diffusive ones. Additionally, Peters (Chen, Pitsch, & Peters, 1998) reported that the scalar dissipation, which can significantly influence the flamelet solution, can decrease by (x^{-4}) along the axis, if (*x*) is the distance from the nozzle, thus, in order to consider the rapid changes of the scalar dissipation profiles and to be able to account for the radiation heat transfer, the unsteady term should be retained. Therefore, a flamelet that is transported downstream has to undergo strong changes. The steady flamelet model is formulated by omitting the unsteady term which gives rise to its over-prediction capacity for pollutants (Claramunt, Cònsul, & Carbonell, 2006).

- The omission of the term that involves the (*Z*) derivative: In equation(2.103) the last term was neglected, as mentioned before, Peters suggested that this approximation can be accepted since this term is small compared to the source term. But (Claramunt, Cònsul, & Carbonell, 2006) argued that this term is very important for an accurate temperature prediction.

- The omission of the radiative heat loss term (Q_R / C_p): This term is a controversial parameter, in general, simplified equations for steady state flamelet have shown some problems in adequately predicting the temperature field since an overestimate of the radiation heat loss is present because of the negligence of this term (Claramunt, Cònsul, & Carbonell, 2006). However, (Pitsch, 2006) found that this term can be neglected without any compromises on the solution accuracy. In fact, he even promoted the negligence of this term, proving that his results are substantially improved by not considering the radiative heat losses, since the interaction of the radiation time with the residence times becomes only important for low scalar dissipation rate (e.g. close to the equilibrium zones).

- Unity Lewis number in the flamelet equations: The usage of the unity Lewis number certainly reduces the very expensive calculation of the binary/multicomponent diffusion coefficients, which are required to evaluate non-constant Lewis numbers for the chemical components. However, this assumption has been widely investigated by several authors (Pitsch & Peters, 1998). The conclusion was the reporting of large changes in the temperature, species profiles, and the extinction limits.

Eventually, the steady laminar flamelet can be considered pertinent under the assumption of the relatively fast chemistry, however, when it comes to deep non-equilibrium effects and slow chemistry, the steady flamelet approach is incapable of faithfully representing such phenomena. Due to several simplifications performed in the derivation of the flamelet equations, the model fails in situations where the local extinction is important. On the other hand, combustion modeling using the steady laminar flamelet model is beneficial, when qualitative trends are required. This approach shows a good ability in predicting the main flame trends i.e. temperature field, global flame shape, main species and major radicals (Claramunt, Cònsul, & Carbonell, 2006). The other advantageous feature of the steady flamelet approach is related to the fairly low computational costs associated with this model. In this study for example, a good degree of convergence was obtained for the reacting flow cases after only (31 000) iterations with reasonable trend predicted from most emissions.

To overcome the limitations of the steady flamelet assumption, the unsteady flamelets can be taken into account. In other words, the transient term in the complete flamelet equations(2.102), and (2.103) is retained. Several authors (Claramunt, Cònsul, & Carbonell, 2006), (Chen, Pitsch, & Peters, 1998) and (Peters, 2000) have reported the superior capabilities of the unsteady model over the steady flamelet one. In this model, the chemical flamelet structure can follow rapid changes of the scalar dissipation. This will improve the temperature field, and the species mass fraction predictions. In the cadre of another project performed between both McGill and Laval Universities with Pratt & Whitney Canada, both unsteady and steady flamelets were implemented. The results show that the temperature profiles and species concentrations were relatively enhanced using the unsteady model ((Fossi.A, Dechamplain, & Paquet, 2013), internal report).

As previously highlighted, the mixing process is an essential parameter for diffusion flames, moreover, the key aspect of the flamelet formulation, which is the scalar dissipation, depends mainly on the turbulence and flame straining due to the aerodynamics. To this end, the author of this thesis believes that the use of a superior turbulence model such as the LES can strongly enhance the results. The use of the LES model for the reacting flows was validated by many authors, and was proven to be more accurate than the RANS model (Poinsot & Veynante, 2005) and (Fossi, DeChamplain, Ghazlani, Paquet, & Kalla, 2014). Additionally, the formulation of the scalar dissipation in RANS, i.e. equation(2.112), was altered in the LES model, to take into consideration both the molecular and the turbulent diffusivities (Moin & Pierce, 1998), which can certainly add a higher degree of accuracy in predicting the scalar dissipation field. Unfortunately, simulations using the LES could not be achieved in this project due to the tight time frame of the work, since it can add a significant increase in the computational time.

CHAPTER 6- CONCLUSIONS

The combustion process in gas turbine combustors is very complex, and involves many variables acting simultaneously to process the fuel /air mixture in a limited space, with very stringent emission standards. Reasonably accurate Computational Fluid Dynamics (CFD) tools for liquid-phase combustion should be able to account for parameters such as: atomization, evaporation and diffusion of the fuel droplets, turbulence aerodynamics, mixing, and finally turbulence–chemistry interaction.

The present study was motivated by the high relevance of developing a numerical model for liquid spray combustion, and that could be capable of overcoming the difficulties related to existing numerical modeling techniques. The complexity of nowadays numerical models arises from the complex nature of the various processes involved during liquid fuel combustion. Moreover, the increasing market demand towards more greener, as well as, more environmental friendly fuels, lead this project to exploit the combustion of non-conventional fuels.

This thesis describes a model for spray combustion, using a combination of existing numerical theories and sub-models, without the introduction of any user define functions or external modifications. This can help any future developments, particularly in relation to biodiesel fuels.

The 3D fluid computational code FLUENT™ v.14 was used for the simulation of five different numerical configurations in accordance with the experimental tests performed in the facility of Université Laval. The choice of using FLUENT™ was inspired from its robustness, as well as, its large use by several industrial and engineering firms. The injector geometry and boundary conditions were acquired from Rolls–Royce Canada, based on their WLE T60 dual fuel injector, which can be considered as an air-blast atomizer with high swirl intensity. The experimental combustor represents only the primary zone of a gas turbine combustion chamber. The overall meshing domain was created using the software GAMBIT™, both, structured and unstructured schemes were utilised to generate the grid of the combustor, and the injector, respectively.

The RANS, Realizable ($k-\varepsilon$) formulation was chosen for the turbulence model closure of the continuous phase, which is an Eulerian-approach. The Lagrangian discrete phase model (DPM) was integrated to account for the liquid fuel injection, atomization, vaporization and evaporation. Tracking was performed based on the stochastic theory, and turbulence effects on the spray were accounted for using the Random Walk technique. Modeling the injection of the liquid spray included both the primary, and the secondary breakup mechanisms, through the hybrid Rayleigh-Taylor/Kelvin-Helmholtz breakup model. The dynamic drag feature was integrated, for its known capacity in providing realistic results. Droplet collisions were not addressed; however, droplets-wall interactions were considered using the wall film, and wall jet boundary conditions. The Multiphase aspect was calculated using the Eulerian-Lagrangian approach, with the two-way coupling technique, to account for mass, momentum, and heat exchange between the discrete phase and the continuous phase. Radiation was considered through the P1-radiation model.

The computational study began with a confined, adiabatic, and non-reacting n-heptane spray and was performed to assess qualitatively the atomization process. Graphical comparisons between the CFD prediction and the experimental results were presented. Main spray features, such as, the hollow cone nature of the spray, the dispersion of droplets, spray cone angle, and the droplet-wall impingements, were satisfactorily captured. The essential outcome from this non-reacting case with atomization was to validate the massive droplet impingements on the combustor wall, which was observed during the experimental test.

The reacting flow cases covered the liquid combustion of both, n-heptane, and B20 biodiesel blends, at two different global equivalence ratios (ϕ = 0.8 and 1), for each type of fuel used. The numerical combustion was realized using the simplified steady laminar flamelet formulation, and the turbulence-chemistry interaction was achieved through the presumed joint β-PDF closure in its non-adiabatic form, i.e. effects for heat loss/gain were taken into consideration.

For the conventional diesel cases, the Flamelet computation, used a reduced mechanism developed for n-heptane (n-C7H16) by UC San Diego laboratory, and it was implemented to account for the chemistry of the winter diesel used in the experimental part. The thermo-physical properties for the n-heptane were introduced in the solver as piecewise linear functions of temperature. This is an important step to accurately predict the spray evaporation.

Regarding the biodiesel cases, a surrogate skeletal mechanism for methyl decanoate, methyl-9-decanoate, and n-heptane was integrated. In order to capture the B20 blend, a multicomponent particle type was chosen, and both, methyl soya, and n-heptane properties was implemented. The mixing was performed using universal mixing laws, such that Raoult's law for vapor pressure, liquid volume weighted mixing law for density, and mass weighted mixing law for viscosity, and specific heat. The acquired thermo-physical properties were integrated as a piecewise linear function of temperature.

It was found during this study that, experimental results are characterized by a relatively elevated degree of discrepancy for the liquid spray combustion, leading to a high degree of uncertainty for CO; additionally that the actual test rig is not sufficiently adequate for the liquid fuel combustion. As shown, the presence of massive impingements of the droplets on the combustor wall definitely affected the combustion process with occasional large fuel pooling dripping along the wall. At the exit, as well as, in the vicinity of the injector, high accumulations of quenched carbon atoms were observed, which affected the emission measurements. The working conditions for the fuel injector are far too from the design point and prevented getting PDPA data to characterise the atomization process using the T60 injector that subsequently limited the CFD study. These parameters contributed to the experimental uncertainty that has not yet been fully assessed. It is believed that the dimension of the actual test rig should have been modified, in order to allow sufficient residence time, yielding a more efficient combustion.

Regarding the CFD part, both the n-heptane and the B20 biodiesel blends, have shown similar combustion characteristics, in terms of global flame shape, gaseous velocity profiles and temperature distribution. This validates the common belief that the B20 biodiesel blends can be used a as drop in fuel to replace conventional diesel. In term of emissions, the comparison between the CO emissions of n-heptane, and B20 biodiesel, shows good agreement in conjunction with the work done by different authors, as manifested by the notable reduction of the emitted CO from the biodiesel fuels. The numerical models have successfully captured the main combustion products, such as, H_2O, and CO_2. The outer wall temperatures were accurately validated with the available experimental data at three different locations.

The laminar flamelet approach failed to predict the local flame extinction in regions with high strain rates; this has certainly affected the flame shape, the location of peak temperatures, and the predicted emissions. Moreover, there are ambiguities related to the code assumption for the exclusion of the extinguished flamelets in the flamelet library; however, no further explanations could be obtained. Additionally it was shown that the simplified flamelet equations were subject to extensive simplifications, which has certainly limited their capacity to the category of ‘departure from non-equilibrium models. Consequently, if significant non-equilibrium phenomenon is to be expected, someone cannot expect to predict it accurately using the steady laminar approach.

For instance, based on the literature, as well as, a parallel numerical project performed by Université Laval on turbulent diffusion flames, the unsteady flamelet model can be thought of as the first choice to remedy the weakness of the steady laminar flamelet approach. In addition, further improvement can still be achieved with a more robust turbulence model such as LES that would be more appropriate for a highly swirled flow frequently combined with gas turbine fuel injectors to promote better fuel-air mixing and flame stability.

Benefits for method described here include its applicability to a wide range of combustion systems, its ability to predict emissions for a variety of pollutants, and its speed to render generic combustion trends.

Finally, subject to Poinsot's classification for non-premixed models (Poinsot & Veynante, 2005), the steady laminar flamelet approach falls under the primitive variable method category; accordingly, this model has to be validated numerically against other combustion models within this particular class, such as, the CMC, in order complete a fair assessment of its overall range of applicability, and capacity.

REFERENCES

Abramzon, B., & Sirignano, W. (1989). Droplet Vaporization Model for Spray Combustion Calculations. *ELSEVIER*.

Aggarwal, S., & Han, X. (2013). A Numerical Investigation on Counterflow Flames of Biodiesel/Diesel Surrogate Blends. *ASME*.

Altimira, M., Rivas, A., & Ramos, J. C. (2011). Disintegration Regime of Industrial Fan-Spray Atomizers through CFD Simulations. *Proceeding of ILASS-Europe*.

ANSYS. (2011). *Fluent Theory Guide.* All ANSYS Inc.Products.

ASTM 6751-11b, A. (2011, July). Standard Specification for Biodiesel Fuel Blend Stock (B100) for Middle Distillate Fuels. *ASTM Journal*, 1-9.

Baumgarten, C. (2006). *Mixture Formation in Internal Combustion Engines* (Vol. I). Berlin: Springs.

Baxter, L., & Smith, P. (1993). Turbulent Dispersion of Particles: The STP Model. *Energy&Fuels, 7*.

Bekdemir, C. (2008). *Numerical Modeling of Diesel Spray Formation and Combustion.* Eindhoven: Eindhoven University of Technology.

Board, N. B. (2013). *www.nbb.org*. Retrieved from www.biodiesel.org: www.biodiesel.org

Boussinesq, T. (1877). *Theorie de l'ecoulement Tourbillonnant* (Vol. XXIII). Paris: Mem.Pres.Acad.Sci.

Bray, K., & Peters, N. (1994). Laminar Flamelets in Turbulent Flames. In P. A. Libby, & F. A. Williams, *Turbulent Reaction Flows.* Academic Press.

Bray, N. (2011). *Turblent Premixed Flames.* New York: Cambrige University press.

Burke, P., & Schumann, W. (1928). *Diffusion Flames.* Swampscott, Massachusetts: The first Symposium on Combustion.

Chen, M., Pitsch, H., & Peters, N. (1998). Unseady Flamelet Modeling of Turbulent Hydrogen-Air Diffusion Flames. *ELSEVIER*.

Claramunt, K., Cònsul, R., & Carbonell, D. (2006). Analysis of the Laminar Flamelet Concept for Non-Premixed Laminar Flames. *ELSEVIER*.

Crowe, C., Schwarzkopf, D., Sommerfeld, M., & Tsuji, Y. (2012). *Multiphase Flows with Droplets and Particles* (Vol. II). Chigago: CRC Press Taylor & Francis Group.

Crowe, C., Troutt, R., & Chung, N. (1996). Numerical Models for Two-Phase Turbulent Flows. *Annual Reviews Fluid Mechanics. XXVIII.* Washington: Annual Reviews Fluid Mechanics.

Dwyer, A., & Sanders, B. (1984). Detailed Computation of Unsteady Droplet Dynamics. *ELSEVIER*.

E.Farvardin, M.Johson, H.Alaee, A.Martinez, & A.Dolatabati. (2013). Comparative Study of Biodiesel and Diesel Jets in Gaseous Crossflow. *JOURNAL OF PROPULSION AND POWER*, 1292-1302.

Faeth, G. (1987). Mixing, Transport and Combustion in Sprays. *Progress in Energy and Combustion Science, 13*.

Fossi, A., DeChamplain, A., Ghazlani, A., Paquet, B., & Kalla, S. (2014). Large Eddy Simulation of a Turbulent Swirling Jet-A1 Spray Flame Incorporating Chemical Non-Equilibrium Effects Through the Flamelet Model. *Proceedings of ASME Turbo Expo 2013*, 13.

Fossi.A, Dechamplain, A., & Paquet, B. (2013). *Laminar Flamelet Concept and its Application to The Multidimensional Numerical Simulation of Non-Premixed Flames: Particular Case of Spray Flames.* Quebec: Private source.

Ghassemi, H., & Khan, Q. (2006). Experimental Study on Evaporation of Kerosene Droplets at Elevated Pressures and Temperatures. *Taylor&Francis*.

Gosman, A., & Ioannides, E. (1983). Aspects of Computer Simulation of Liquid-Fuelled Combustors. *Journal of Energy*.

Gupta, K., Rehman, A., & Sarviya, R. (2010). Bio-fuels for the Gas Turbine : A review. *ELSEVIER*(14), 2946-2955. doi:10.1016/j.rser.2010.07.025

Harun, M., Hoon Ng, K., Cheng, X., Gan, S., Lucchini, T., & Errico, G. (2012). Development of Thermophysical and Transport Properties for the CFD Simulations of In-Cylinder Biodiesel Spray Combustion. *Energy&Fuels*.

Hashimoto, N., Ozawa, Y., Mori, N., & Yuri, I. (2008). Fundamental Combustion Characteristics of Palm Methyl Ester (PME) as Alternative Fuel for Gas Turbines. *ELSEVIER*(87), 3373-3378.

Huber, M., W.Lemmon, E., Kazakov, A., Ott, L. S., & Bruno, T. J. (2009). Model for the Thermodynamic Properties of a Biodiesel Fuel. *Energy&Fuels*.

J.Haas, M., M.Scott, K., & L.Alleman, T. (2001). Engine Performance of Biodiesel Fuel prepared from Soybean Soapstock: A High Quality Renewable Fuel produced from Waste Feedstock. *Energy&Fuels*(15), 1207-1212. doi:10.1021/ef010051

Jaime, A., Parthasarathy, R., & Gollahalli, S. (2010). Atomization and Combustion of Canola Methyl Ester Biofuel Spray. *ELSEVIER*.

Jakobsen, H. (2008). Chemical Reactor Modeling. In M. Flow, *Chemical Reactor Modeling.* Berlin: Springer-Verlag.

Kadota, & Hiroyasu. (1976). Evaporation of a Single Droplet at Elevated Pressures and Temperatures. *Bulletin of JSME*.

Knothe, G. (2005). *The Biodiesel Handbook.* Illinois: AOCS Press.

Knothe, G. (2005). The History of Vegetable Oil-Based Diesel Fuels. In G. Knothe, *The Biodiesel Handbook* . Illinois: AOCS Press.

Kretschmer, D., & Odgers, J. (1986). Combustion des Gaz Pauvres Dans les Turbines a Gaz. *Taylor& Francis*.

Kristyadi, T., & Lemoine, F. (2010). Monodisperse Monocomponent Fuel Droplet Heating and Evaporation. *ELSEVIER*.

Kuo, K. K. (2005). *Principles of Combustionn* (Vol. II). New Jersy: John Wiley and Sons Inc.

Kuo, K. K., & Acharya, R. (2012). *Fudamentals of Turbulent and Multiphase Combustion* (Vol. III). New Jersy: John Wiley & Sons, Inc.

L.Huber, M., Lemmon, E. W., Kazakov, A., Ott, L. S., & Bruno, T. J. (2009). Model for the Thermodynamic Properties of a Biodiesel Fuel.

L.Prandtl. (1925). *Bericht über Untersuchungen zur ausgebildeten Turbulenz* (Vol. V). Z.A.M.M.

L.Yaws, C. (2013). *Yaws' Handbook of Thermodynamic and Physical Properties of Chemical Compounds.* Knovel.

Latlosz, R., & Leipziger, S. (1972). Investigation of Liquid Drop Evaporation in a High Temperature and High Pressure Environment. *ELSEVIER*.

Launder, B., & Jones, W. (1972). The Prediction of Laminarization with a Two-Equation Model of Turbulence. In *Int. J. Heat Mass Transfer* (Vol. XV, pp. 301-314). London: Pergamon Press.

Launder, B., & Sharma, B. (1974). Application of the Energy Dissipation Model of Turbulence to the Calculation of Flow Bear a Spinning Disc. In *Letters in Heat and Mass Transfer* (Vol. I, pp. 131-138).

Lefebvre, A. (1983). *Gas Turbine Combustion* (Vol. I). Indiana: Taylor&Francis.

Lefebvre, A. (1985). Ifluence of Fuel Properties on Gas Turbine Combustion Performance. *Air Force Wright Aeronautical Laboratories*.

Lefebvre, A. (1989). *Atomization and Sprays* (Vol. I). Indiana: Hemisphere Publishing corporation.

Lefebvre, A. (1998). *Gas Turbine Combustion* (Vol. II). Phiadelphia: Taylor & Francis.

Lefebvre, A., & Ballal, D. (2010). *Gas Turbine Combustion Alternative Fuels and Emissions* (Vol. III). Boca Raton: CRC Press.

Lin, R., & Tavlarides, L. L. (2012). Thermophysical Properties needed for the Development of the Supercritical Diesel Combustion Technology: Evaluation of Diesel Fuel Surrogate Models. *The Journal of Supercritical Fluids*.

Loth, E. (2000). Numerical Approaches for Motion of Dispersed Particles, Droplets, and Bubbles. *ELSEVIER, 26*.

MacInnes, J., & Bracco, F. (1992). Stochastic Particle Dispersion Modeling and The Tracer-Particle Limit. *AIP Publishing, IV*.

Maqua, C., Castanet, G., & Grish, F. (2008). Monodisperse Droplet Heating and Evaporation: Experimental Study and Modelling. *Heat&Mass Transfer*.

Marshall, R. (1952). Evaporation from Drops. *Chemical Engineering Process*.

Mashayek, F., & Pandya, R. (2003). Analytical description of Particle Droplet-Laden Turbulent Flows. *ELSEVIER, 29*.

Moin, P., & Pierce, C. D. (1998). *Large Eddy Simulation of a Coaxial Jet Combustor.* Air Force Office of Scientific Research.

Morin, C., & Dagat, P. (2004). Vaporization and Oxidation of Liquid Fuel Droplets at High Temperature and Pressure Application to n-Akanes and Vegetable Oil Methyl Esters. *Taylor&Francis*.

NIST. (2011). *NIST Chemistry webBook*. Retrieved from http://webbook.nist.gov/chemistry/

Peters, N. (1984). Laminar Diffusion Flamelet Models in Non-Premixed Turbulent Combustion. *ELSEVIER*.

Peters, N. (2000). *Turbulent Combustion* (Vol. I). England: Cambridge University press.

Peters, N., Barths, H., Brehm, N., & Mack, A. (1998). Simulation of Pollutant Formation in A Gas-Turbine Combustor Using Unsteady Flamelets. *ELSEVIER*.

Piffaretti, S. (2007). *Flame Age Model: A Transient Laminar Flamelet Approach For Turbulent Diffusion Flames.* Zurich: SWISS FEDERAL INSTITUTE OF TECHNOLOGY ZURICH.

Pilch, M., & Erdman, C. (1987). Use of Breakup Time Data and Velocity History Data to Predict the Maximum Size of Stable Fragements for Acceleration-Induced Breakup of a Liquid Drop. *ELSEVIER, 13*.

Pitsch, H. (2006). Creating a Flamelet Library for the Steady Flamelet Model or the Flamelet/Progress Variable Approach. *AIAA Aerospace Sciences Meeting and Exhibit*.

Pitsch, H., & Peters, N. (1998). A Consistent Flamelet Formulation for Non-Premixed Combustion Considering Differential Diffusion Effects. *ELSEVIER*.

Pitz, W. J., Plomer, M., Luo, Z., Lu, T., Som, S., & Longman, D. E. (2012). A Reduced Mechanism for Biodiesel Surrogates for Compression Ignition Engine applications. *ELSEVIER*.

Poinsot, T., & Veynante, D. (2005). *Theoretical and Numerical Combustion* (Vol. II). Philadelphia: R.T Edwards.

R.Turns, S. (2000). Introduction to Turbulence . In S. R.Turns, *An Introducion to Combustion:Concepts and Applications* (Vol. II). McGraw-Hill .

R.W.Bilger. (1980). *Turbulent Reacting Flows.* New Yourk : Springer-Verlag.

Reitz, D., Youngchul, R., Stuart, C., & McFarlane, J. (2008). Effects of Fuel Physical Properties on Diesel Engine Combustion using Diesel and Bio-diesel Fuels. *Int.J.SAE, I*(I).

Reitz, R., & Diwakar, R. (1987). Effect of Drop Breakup on Fuel Sprays. *Int.J.SAE*.

Rochaya, D. (2007). *Numerical Simulation of Spray Combustion using Bio-Mass Derived Liquid Fuels.* Cranfield: Cranfield University.

Rolls-Royce ©, p. (1996). *The Jet Engine* (Vol. V). Derby: Crapaci.

Sanchez, P. (2012). *Modeling the Dispersion and Evaporation of Sprays in Aeronautical Combustion Chambers.* Institut National Polytechnique de Toulouse.

Sarviya, R., & Rehman, A. (2010). Evaluation of Soya Bio-Diesel as a Gas Turbine Fuel. *Iranica Journal of Energy & Environment* , 205-210.

Sazhin, S. (2006). Advanced Models of Fuel Droplet Heating and Evaporation. *ELSEVIER*.

Shih, T., Liou, W., Shabbir, A., & Zhu, J. (1995). A New- Eddy-Viscosity Model for High Reynolds Number Turbulent Flows- Model Development and Validation. *NASA. Lewis Research Center, XXIV*, 227-238.

Shirolkar, J., Coimbra, C., & McQuay, M. (1996). Fundamental Aspects of Modeling Turbulent Particle. *ELSEVIER, 22*.

Sirignano, W. (1999). *Fluid Dynamics and Transport of Droplets and Sprays.* London: Cambridge University Press.

Som, S., Longman, D., Ramirez, A., & Aggarwal, S. (2010). A Comparison of Injector Flow and Spray Characteristics of Biodiesel with Petrodiesel. *ELSEVIER*(89), 4014-4024.

Spalart, P., & Allmaras, S. (1992). *A One Equation Turbulence Model for Aerodynamic Flows.* American Institute of Aeronautics and Astronautics.

Stan, G. (2000). *Fundamental Characteristics of Turbulent Opposed Impinging Jets.* Waterloo: University of Waterloo.

Steidley, R., & Knothe, G. (2005). Lubricity of Components of Biodiesel and Petrodiesel. *Energy&Fuels*(19), 1192-1200.

Subramaniam, S. (2013). Lagrangiane-Eulerian Methods for Multiphase Flows. *ElSEVIER*(39).

Tian, Z. (2006). *Numerical Modelling of Turbulent Gas-Particle Flow and its Applications.* Melbourne: RMIT University.

Tsuji, H. (1982). *Counterflow Diffusion Flames.* Progress in Energy and Combustion Science.

Tu, J., Yeoh, G., & Morsi, Y. (2010). A Study of Particle Rebounding Characteristics of a Gas-Particle Flow over a Curved Wall Surface. *Taylor&Francis*(38:7).

Veynante, D., & Vervisch, L. (2001). Turbulent Combustion Modeling. *Springer Link*.

Waynick, J. (1997). Evaluation of the Stability, Lubricity, and Cold Flow Properties of Biodiesel Fuel. *Proceedings of the 6th International Conference on Stability and Handling of Liquid Fuels, II*, 805-818.

Wilcox, C. (1998). *Turbulence Modeling for CFD* (Vol. II). California: KNI, Inc.

Wong, S., & Yang, J. (2002). An Experimental and Theoretical Study of the Effects of Heat Conduction Through the Support Fiber on the Evaporation of a Droplet in a Weakly Convective Flow. *ELSEVIER*.

Yakhot, V. O. (1986). Renormalization Group Analysis of Turbulence. *Springer Link, I*, 3-51.

Youssef, M., Agou, J., Paquet, B., & DeChamplain, A. (2012). Comparative Study for Biodiesel Properties and Standards for Gas Turbine. *The Combustion Institute Canadian Section*.

Zhang, H., Yang, W., Chan, C., & Lau, K. (2002). Comparison of Three Separated Flow Models. *Springer, 23*.

Zuckerman, N., & Lior, N. (2006). Jet Impingement Heat Transfer:Physics, Correlations, and Numerical Modeling. *ELSEVIER, XXXIX*.